FORM #2377-D

File with N76-19017

18549

NASA CR-132594

THE GARRETT CORPORATION
AiResearch Manufacturing Division
LOS ANGELES 45, CALIFORNIA

REPORT NO. AP-68-3429

HYPERSONIC RESEARCH ENGINE PROJECT - PHASE IIA INSTRUMENTATION PROGRAM

FOURTH INTERIM TECHNICAL DATA REPORT

24 NOVEMBER 1967 THROUGH 23 FEBRUARY 1968

DATA ITEM NO. 55-8.04

NASA CONTRACT NO. NAS1-6666

AP-68-3429 April 10, 1968

ISSUED January 1975

NO. OF PAGES 196

DATE April 10, 1968

PREPARED BY Engineering Staff

EDITED BY L. F. Jilly

APPROVED BY Henry J. Lopez

Henry J. Lopez
HRE Program Manager

REVISIONS				ADDITIONS			
PAGE	DATE	PAGE	DATE	PAGE	DATE	PAGE	DATE

U.S. GOVERNMENT AGENCIES & THEIR CONTRACTORS ONLY

FOREWORD

This Interim Technical Data Report is submitted to the NASA Langley Research Center by the AiResearch Manufacturing Company, Los Angeles, California. The document was prepared in accordance with the guidelines established by Paragraph 6.3.3.2 of NASA Statement Of Work L-4947-B.

Interim Technical Data Reports are generated on a quarterly basis for major program tasks under the Hypersonic Research Engine Project. Upon completion of a given task effort, a Final Technical Data Report will be submitted.

The document in hand presents a detailed technical discussion of the Instrumentation Program for the period 24 November 1967 through 23 February 1968.

ACKNOWLEDGMENTS

Acknowledgments for assistance in the completion of this document are extended to the following contributors:

N. Naves	Gas Sampling Probe and Double-Sonic Orifice Probe
G. Sawyer	Total Temperature Measurements
W. Flieder	Thrust Block Design Analysis
J. Pratt	Thrust/Drag System
R. Ranney	Thrust/Drag System Accelerometer
G. Sawyer	Gas Analyzer
D. Osborn	Engine Metals and Coolant Temperature Measurements
C. Pavone	Fuel-Coolant Weight Flow Rate Measurements
S. Cho	Heat Transfer Analyses
J. Tranter Roger Holland A. Saur	Pressures Measurements
A. Vigilante	Overall Responsibility

TABLE OF CONTENTS

TABLE OF CONTENTS (Continued)

ILLUSTRATIONS

ILLUSTRATIONS (Continued)

ILLUSTRATIONS (Continued)

LIST OF TABLES

LIST OF TABLES (Continued)

TABLE OF SYMBOLS

Section 3.2

Symbols

D_1	Outside diameter of probe at tip, ft
D_2	Outside diameter of probe at cylindrical section, ft
H	Enthalpy, Btu/lb
L	Overall probe length, ft
M	Mach number
m	Mass flux, equal to ρ V lb/ft^2-sec
Nu_X	Local Nusselt number
Nu_L	Average Nusselt number
p	Pressure, lb/ft^2
Pr	Prandtl number
R	Gas constant, ft/^{0}R
Re	Reynolds number
T	Static temperature, ^{0}R
T_T	Total temperature, ^{0}R
V	Flow velocity, ft/sec
X	Length measure probe tip, ft

Greek Symbols

γ	Ratio of specific heats
ρ	Density, lb/ft^3
μ	Viscosity, lb/ft-sec

Subscripts

1, 2, 3, 4, 5	Corresponding to regions in Figure 3.2-1
ad	Adiabatic condition

Section 3.2 (Continued)

L	Overall condition
s	Shoulder at base of cone section
T	Total conditions
tr	Transition point from laminar to turbulent flow
w	Wall condition
X	Local conditions at X

Section 4.1

Symbols

A_o	$A_1 + A_2$
A_1	Cross sectional area of wire, $in.^2$
A_2	Cross sectional area of tube, $in.^2$
A_{conv}	Area of J that receives heat from gas stream by convection $(in.^2)^2$
A_{rad}	Area of J that radiates heat, $in.^2$
h_o	Heat transfer coefficient
J	Thermocouple function shown in Figure 4.1-1
K_1	Coefficient of thermal conductivity of wire in center of probe
K_2 or K	Coefficient of thermal conductivity of tube comprising outside of probe
p	Perimeter of tube = outside diameter x π
q_1	Heat lost by J due to wire, Btu/sec
q_2	Heat lost by J due to tube, Btu/sec
q_{cond}	Heat lost by J due to conduction of heat through tube and wire to cooler areas, Btu/sec
q_{conv}	Convective heat transfer from gas stream to junction, Btu/sec

Section 4.1 (Continued)

q_{rad}	Net radiative heat lost by junction, Btu/sec
T	Temperature of tube at same particular point X, ^{0}R
t	Time, sec
T_j	Temperature of thermocouple junction shown in Figure 4.1-1, ^{0}R
T_T	Total temperature of gas stream. Static temperature plus temperature (^{0}R) due to relative translation between thermocouple and gas stream, ^{0}R
T_ω	Temperature of wall, ^{0}R
T.C.	Thermocouple
$\frac{dT_1}{dx_1} x = 0$	Temperature gradient of wire evaluated at X = 0, $^{0}R/in.$
$\frac{dT_2}{dx_2} x \overset{or}{=} 0$ $\frac{dT}{dX} X = 0$	Temperature gradient of tube evaluated at X = 0, $^{0}R/in.$

Section 4.3

Symbols

A	Nozzle throat area, ft^2
C_D	Discharge coefficient
d	Differential
P	Pressure, lb/ft^2
R	Universal gas constant, $\frac{ft\text{-}lb}{mole\ ^{0}R}$
T	Temperature, ^{0}R
∂	Partial differential

Subscripts

1	Conditions at first nozzle throat
2	Conditions at second nozzle throat

Section 4.3 (Continued)

c	Coolant
g	Gas
T	Total or stagnation conditions

Greek Symbols

Δ	Subtraction of two like measurands
γ	Ratio of specific heats

1.0 SUMMARY

During the fourth interim reporting period, 24 November 1967 through 23 February 1968, the Instrumentation program for the Hypersonic Research Engine (HRE) furthered the developments in each of the following categories:

- Thrust measurement
- Gas sampling
- Temperature measurements
- Pressure measurements
- Fuel-coolant measurements
- First qualification engine instrumentation

The following paragraphs describe the status of the principal categories of the HRE instrumentation development task.

1.1 THRUST MEASURING SUBSYSTEM

1.1.1 Summary

A revised stress analysis has resulted in a new block design, incorporating four flexures of increased width and using a different material. Heat transfer and temperature gradient analyses have established the requirement for temperature control of the thrust block assembly. A different accelerometer has been considered to determine the inertia forces offering a better accuracy and a self-checking facility. The major contributors to the overall analysis of error in the determination of internal thrust are the determination of drag, measurement of indicated thrust and inertia force, the estimated force due to differential thermal expansion of wishbone and engine, and the thermal effects on the deflection block. At maximum internal thrust conditions the 3σ error has been estimated as 2.55 percent. Further analyses will be performed on the design of the wishbone and rear suspension, heat transfer using the latest block material characteristics, and the design of suitable temperature control (presently conceived as being in the form of a radiation shield). Some design drawings have been made and fabrication and procurement of components for the block assembly are proceeding. To reflect the latest considerations of design and environment, the Development Plan will be updated, particularly in the early stages.

1.2 GAS SAMPLING SUBSYSTEM

1.2.1 Gas Analyzer

During the past quarter, the gas analyzer was moved to the North American Rockwell (NAR) facility at El Segundo and set up for use in the combustor tests.

Tests were made then to determine the resolution, the drift rates (zero and span), and the accuracy. The resolution is ±0.5 percent of full scale; the zero drift rate over a 30-min period was within the resolution (±0.5 percent); and the span drift rate was tentatively determined to be 1 percent of full scale.

When the species is between 10 and 100 volume percent, the accuracy is 1 percent or better of full scale. When the species is less than 10 volume percent, the accuracy is 0.5 percent or better of full scale.

1.2.2 Gas Sampling Total Pressure Probe

Fabrication of the backup probe is complete. Testing of the first probe has been initiated and will continue upon completion of the 2 in. by 6 in. combustor installation at North American Rockwell. During this reporting period the backup probe has successfully completed initial tests, including proof pressure and flow testing. Installation of the probe on-site at North American Rockwell has been completed and final checkout and precalibration tests are in process.

1.3 DOUBLE-SONIC ORIFICE TOTAL-TEMPERATURE PROBE

Fabrication of the double-sonic orifice probe is complete and the tests outlined in Subsection 1.2.2 above have been successfully completed. The probe will measure total temperature in the HRE combustor test rig and boilerplate engine by two independent methods; it also has the capability of measuring pitot- and stream-static pressures. The two independent temperature measuring methods are the double-sonic orifice technique and the calorimetric technique. The probe is designed to traverse the gas flow stream of any axial plane without significantly affecting the performance of the test rig.

A complete error analysis of the two temperature measuring techniques is included in Subsection 4.2.5 of this report.

Total-Temperature Thermocouple

During the past quarter, activity in obtaining a suitable probe for determining total-temperatures in the engine inlet and engine exhaust was resumed.

An error analysis was performed for determining the random error in T_{Tg} when the temperature gradient (in the axial direction) at the tip is known. A conceptional thermocouple design is shown for determining the

temperature gradient at the tip. Coating information is given for materials that may be used to extend thermocouple life.

1.4 ENGINE TEMPERATURE SUBSYSTEM

The temperature subsystem task has been reviewed and the constraints placed upon the system by accuracy requirements, measurement locations, structure build-up procedures, and the system's component and environmental limitations were considered.

Measurements, locations, and anticipated ranges and accuracies have been outlined and tabulated with the expected static errors.

Areas of major error sources are being investigated and approaches to minimize these errors are being studied.

1.5 FUEL-COOLANT MASS-FLOW RATE MEASUREMENTS

Analysis was started on the problem of measuring combustion fuel mass-flow rate accurately enough to determine the internal specific impulse of the engine to within ±5 percent or better. Since the direct measurement of combustion fuel flow using the injector ports as calibrated orifices is a method of unproven accuracy, it was decided to include an approach in which all flow measurements would be made by transducers of known or demonstrable accuracy. The method selected measures the total mass-flow rate to the pump and the total mass-flow rate of dumped fuel. The difference would be the combustion fuel mass-flow rate.

Present program plans include the experimental evaluation of both methods of measuring combustion fuel. Thus, there will be two redundant measurements of combustion fuel flow.

The difference in method by which total and dump flows are measured and subtracted has been analyzed for the special case of steady flow. Assuming that all systematic areas can be eliminated and that only random errors due to transducer effects remain, and assuming the use of best quality commercially available transducers, the random-related error in measuring combustion fuel flow is estimated to be 5.4 percent. The reduction of this error is being investigated.

1.6 FIRST QUALIFICATION ENGINE TEMPERATURE AND PRESSURE MEASUREMENT SUBSYSTEM

Design of the composite instrumentation system required for the first qualification engine continued. This instrumentation is composed of items for both flight testing and ground testing. The effort has concentrated on defining the system's requirements for accuracies, responses, environments, and on determining the system's pattern with respect to transducer types, cable routing, line and transducer responses, and general concepts.

2.0 THRUST/DRAG MEASUREMENT SYSTEM

2.1 PROBLEM STATEMENT

The objective of the thrust/drag measurement system is to determine both the internal thrust developed by the engine during powered flight, and the drag experienced during cold engine flight. The internal thrust of the engine is determined by assessing all extraneous loads due to drag, inertia, gravity, interface cabling, and fuel and coolant lines. The deflection block is the active portion of the system. Since it forms part of the engine suspension system, the deflection block must withstand both inertial and aerodynamic loads and extremes of vibration, shock,and temperature. System requirements are as follows:

	Flight Range	Remarks
Internal thrust	0 to 6000 lb	
Acceleration	+3 → -3 g	
Indicated thrust	0 → 7000 lb	(Thrust)
Indicated thrust	0 → 5000 lb	(Drag)
Frequency response	0 to 10 Hz	See below
3σ error in internal thrust	2.5 percent	See Paragraph 2.4.6
Temperature	-40°F → 200°F	Thrust block region
Altitude	85,000 ft	

The 0- to 10-Hz frequency response range is considered adequate for measurement during the quasi-steady-state conditions existing during flight engine test. The temperature range of -40° to 200°F is based on a recent heat-transfer analysis (see Paragraph 2.4.3).

2.2 TOPICAL BACKGROUND

Several factors influence the system design: the varying aerodynamic and inertial forces arising from maneuvering flight conditions of the X-15 release, engine start and unstart, and landing. Since the deflection block

forms one of the engine suspension parts, its structural integrity must be assured. The HRE must be compatible with the dynamic loading and jettison capabilities of the X-15 airplane.

Before the exact internal thrust can be computed, the external drag, frictional drag, aerodynamic drag, and resistance due to cabling fluid lines and additional engine suspension must be known; and temperature and suspension stiffness must be accurately determined. To compute the specific impulse, both the internal thrust and the rate of fuel consumption must be known. The allowable maximum error for determining the specific impulse governs the allowable errors in the internal thrust and fuel consumption rate measurements.

Since the thrust block is subjected to temperature extremes that are dependent on conduction and radiation from the engine and aerodynamically affected sources, temperature is an important consideration in selecting materials and components for the deflection block and the transducers associated with the thrust, drag, and inertial measurements close to the block.

2.3 OVERALL APPROACH

2.3.1 Analytical

The basic analytical approach remains the same as in previous Technical Data Reports and in Reference 2-1, and is detailed in the third Technical Data Report. Revisions have been made to the measurement requirements and contributing factors; the relationship of forces is:

$$T_{int} = T_{ind} + W\sin\theta + \ddot{W}x + D_E + F \qquad \text{(See Figure 2.3-1)}$$

The indicated thrust (T_{ind}) is the net thrust acting on the thrust-measurement block due to the major forces of internal thrust (T_{int}), engine external (D_E), engine inertia ($\ddot{W}x$), and gravity ($W\sin\theta$). The term F represents the secondary forces, and covers the forces appearing as an output from the thrust-measurement-block transducer due to effects of block distortion (thermal) interface structural forces misalignment, differential thermal expansion, vibration, etc.

Indicated thrust is measured by detecting the displacement of a linear spring system incorporated in the thrust block. A capacitive or strain-gage transducer system is used to convert this displacement to an electrical analog.

The external drag force will be determined using static pressure tap measurements.

Engine inertia and gravity forces will be measured using an accelerometer mounted on the thrust block. (The angle of pitch is not required since the accelerometer inherently measures the vectored sum of the gravity and inertia force.)

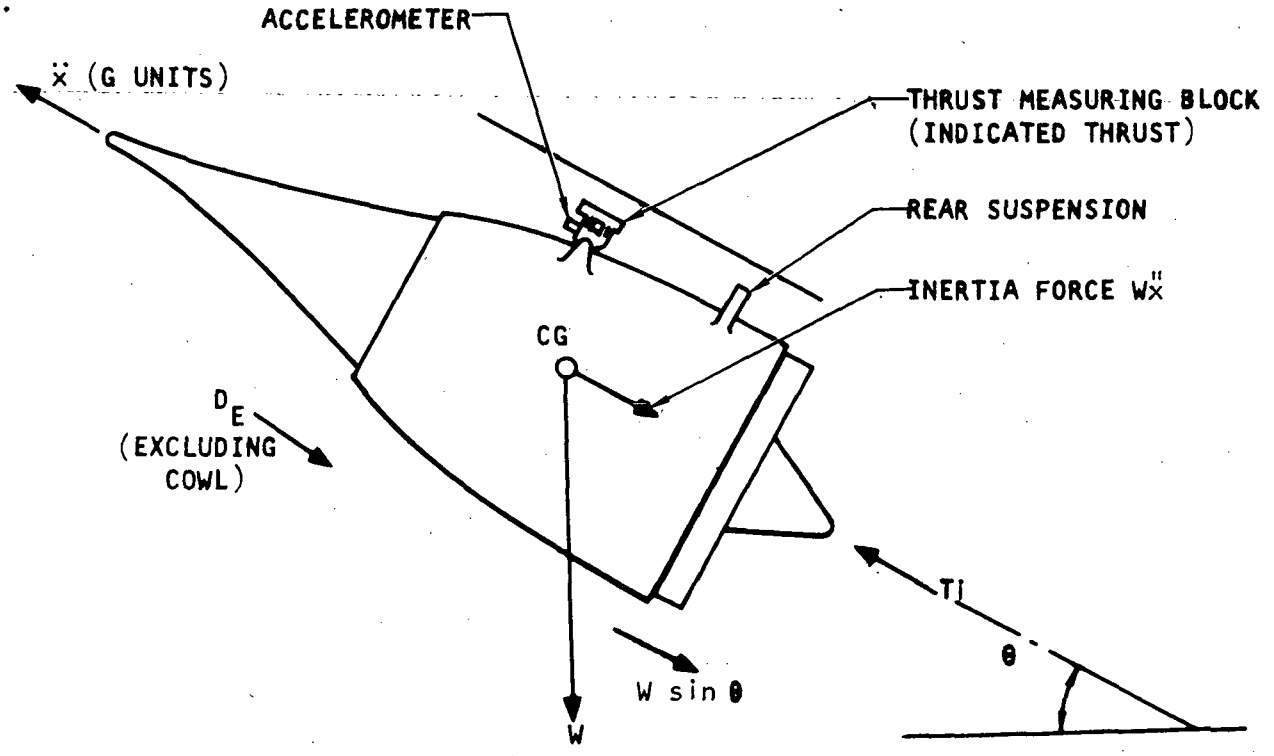

INTERNAL THRUST = INDICATED THRUST + RESOLVED WEIGHT + INERTIA FORCE + DRAG + SECONDARY FORCES

$$Ti = (T_{IND}) + (W \sin \theta + W\ddot{x}) + (D_E) + (F)$$

DEFLECTION BLOCK & DIFFERENTIAL CAPACITOR SENSOR (OR STRAIN GAGE)

ACCELEROMETER

PRESSURE CALCULATION

ESTIMATED MEASURED ERROR

A-34448

Figure 2.3-1. Determination of Internal Thrust

The secondary forces (F) are either evaluated by measurement or estimation, or both, or are ignored and treated as an error contribution. Assessment of some of these forces will be made during development ground testing; shielding of the block and accelerometer is to be considered for reducing thermal errors to a necessary minimum. In-flight measurements will be made during quasi-steady-state conditions and forces generated by actuator and spike translation will not appear in the computation.

2.3.2 Experimental

Full-scale models of the deflection block and transducers will be subjected to a test program that includes assessing the effects of high and low temperatures, differential temperature, dynamic and static characteristics, vibration under simulated engine loading, side loadings, and frequency response tests. To more thoroughly examine the effects of thermal gradients and three-axial loadings, the early part of the test program is being reconsidered.

2.4 ANALYTICAL DESIGN

2.4.1 Design of the Deflection Block

As stated in Reference 2-1, the thrust-block design analysis has been revised to meet the updated structural load and instrument range requirements. To meet these latest requirements, a block has been designed (see Figure 2.4-1) using an increased number of flexures, a wider block,and different material.

The new requirements together with a reevaluation of the stress equations have resulted in these design changes. The analysis report, now in a preliminary stage, is concerned principally with the design dimensions regarding instrument and maximum axial structural loading requirements. Calculations have checked the adequacy of the block under side and vertical loadings; it is considered satisfactory. However,a full report is to be issued covering stresses within the block as part of the engine support system of wishbone, rear supports, and thrust block. Design analysis of the wishbone and rear supports is in progress.

2.4.1.1 Summary of Preliminary Design Report

The guided cantilever flexure design had been previously determined. The flexure must provide a specified spring-rate, and must also fulfill the structural function of engine support from the wishbone framework. The design calculations performed earlier in the program showed the axial force to be the major design load. The present flexure is designed for a load capability of 14,000 lb (20 g times estimated supported wt = 700 lb).

The final formulation showed that the structural performance index by which different materials can be compared is:

$$\text{Structural Index} = \sigma^3/L^2$$

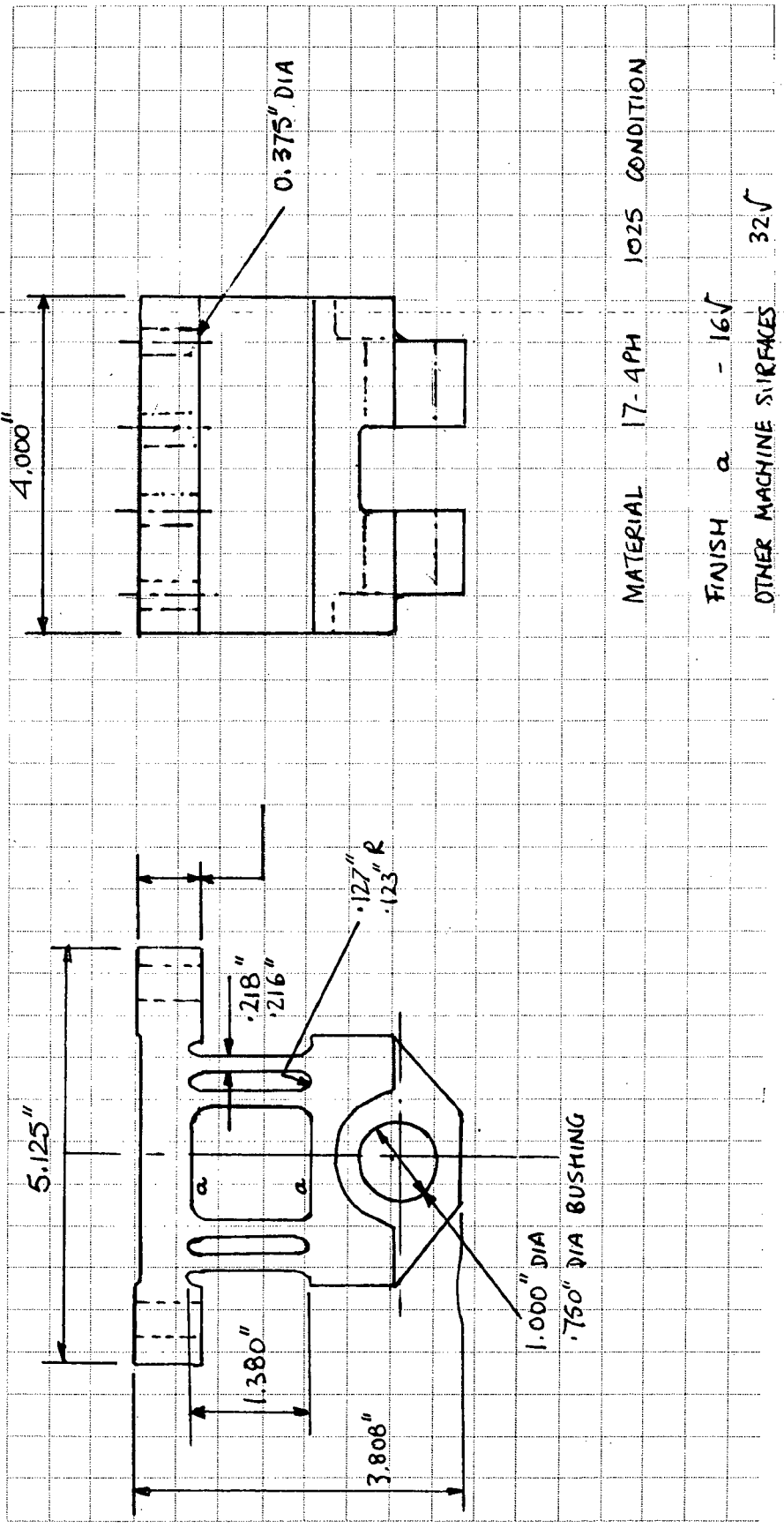

Figure 2.4-1. Development Prototype Thrust Block

In this expression, σ is the 10^7 cycles endurance stress. The principal materials investigated were:

Ni-Span-C (desirable for its outstanding thermoelastic coefficient (TEC))

Ti-6Al-4V (desirable for its low density)

Inconel 718

4340 Steel

17-4PH - Steel, Condition H-1025

17-7PH - Steel, Condition TH-1050

Inconel 718 and 17-4PH Steel were found to be the most suitable. Although they are about equal, the 17-4PH alloy has been chosen because of its slightly lower expansion coefficient.

2.4.1.2 Design Analysis

These symbols will be used in the discussion that follows:

E = Young's modulus, lb/in.^{2}

I = second moment of area, in.^{4}

σ = stress, lb/in.^{2}

b = width of flexure, in.

t = thickness of flexure, in.

d = deflection at end of flexure(s), in.

l = length, in.

P = applied load, lb

m = Poisson's ratio

Z = section modulus, in.^{3}

For cantilever beam (Figure 2.4-2a),

$$\delta = \frac{Pl^3}{12EI}$$

$$\sigma = \frac{Pl}{2Z}$$

For a flat plate beam as in Figure 2.4-2b, allowance must be made for cross stresses; the relationships are modified to include Poisson's ratio and to give P for n flexures (Figure 2.4-2c).

$$\delta = \frac{Pl^3}{12EIn} \cdot (1-m^2) \quad \text{and} \quad \sigma \frac{Pl}{2Z}$$

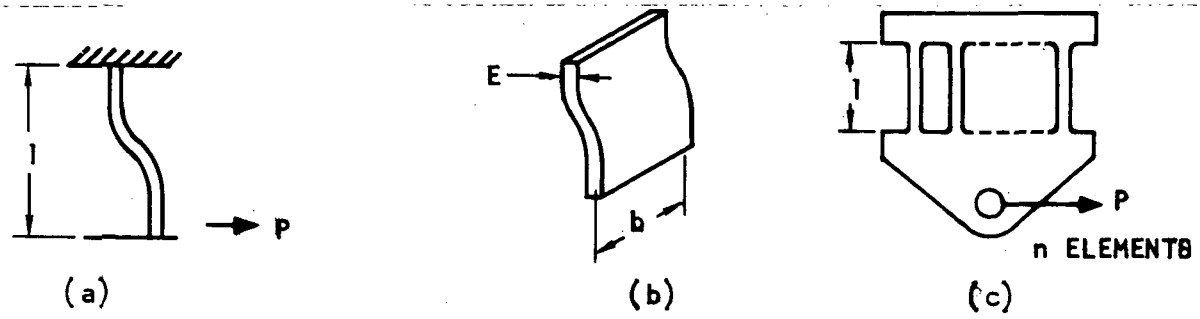

Figure 2.4-2. Load Diagrams A-34494

Substituting

$$I = \frac{bt^3}{12} \qquad \text{and } Z = \frac{bt^2}{6}$$

$$\delta = (1-m^2)\,\frac{P}{Enb}\,\left(\frac{l}{t}\right)^3 \tag{2.4-1}$$

$$\sigma = \frac{3Pl}{nbt^2} \tag{2.4-2}$$

Spring rate

$$k = \frac{P}{\delta}$$

$$k = \frac{Enb}{(1-m^2)\,(l/t)^3} \tag{2.4-3}$$

Manipulation yields

$$nbl^3 = \frac{27}{(1-m^2)^2} \times \frac{P^3}{k^2(\sigma^3/E^2)} \tag{2.4-4}$$

P and k are design constraints [7000-lb load for 0.003 in. determines k and

$$P = 14{,}000 \text{ lb}]$$

The most favorable material has the largest f^3/E^2, i.e.,

$$\text{structural index} = f^3/E^2$$

P = 14,000 lb and represents the vibration condition under 3 g input for magnification at a resonance between 6 and 7 (qualification testing).

σ is taken as the fatigue stress to 10^7 cycles. 30 min endurance at resonance is equivalent to around 270,000 cycles. Since fatigue stress curves begin to level off above 10^5 cycles, a safety margin of 10^7 cycles has been taken, rather than a safety margin on load.

Table 2.4-1 shows a comparison of six materials considered in the design analysis.

TABLE 2.4-1

COMPARISON OF DEFLECTION BLOCK MATERIALS

Material	E x 10^{-6}	10^7 Cycle Fatigue			σ_{all} * $=0.85\ \sigma_{un}$	σ^3/E^2	nbl^3	Remarks
		Unnotched	Kt=232	K=3.27				
Ni-Span-C	27.8	50	-	-	42.5	0.0995	166	Not possible
Ti-6Al-5V	15.2	55	35	-	46.75	0.442	37.4	
Inconel 718	29.6	91	-	-	77.3	0.527	31.4	Best on stress
4340	30.5	80	-	40	68	0.338	48.8	
17-4PH Condition H-1025	28.5	88	-	-	74.8	0.515	32.0	Close to 718 on stress -- use due to lower α
17-7PH Condition TH-1050	29.0	79	45	40	68.2	0.378	43.7	

*Based on estimate stress concentration factor in beam fillet radius

(σ_{all} = stress allowed, σ_{un} = unnotched stress)

The material choice was 17-4PH (Paragraph 2.4.1.1)

Then from Table 2.4-1 $nbl^3 = 32.0$

For l = 1.30 in. $nb = 14.5$

nb is taken as 16.0, giving

$$nbl^3 = 35.2$$

This corresponds to designing to a stress

$$\sigma \text{ design} = 74.8\sqrt[3]{\frac{32.0}{35.2}} = \frac{72{,}500 \text{ psi}}{(\text{compared with } 74{,}800 \text{ psi})}$$

To meet nb = 16.0, the block design will incorporate four beam members (n = 4),4 in. wide (b = 4)

From Equation (2.4-3)

$$\left(\frac{l}{t}\right) = \sqrt[3]{\frac{Enb}{(1-m^2)k}} = \sqrt[3]{\frac{(28.5\times10^6)(16)}{(.91)(2.33\times10^6)}} = 6.0$$

where $t = 1/6.0$, $t = 1.30/6 = 0.217$ in.

$E = 28.5 \times 10^6$ lb/in.^{2}

$nb = 16.0$ in.^{2}

$m = 0.3$

$k = 2.33 \times 10^6 \left[\text{from } k = P/\delta \text{ lb/in.} = \frac{7000 \text{ lb}}{0.003 \text{ in.}}\right]$

The actual length of the beam elements, including the effect of a fillet radius at the beam ends, must be obtained. A fillet radius of 0.125 in. will be used.

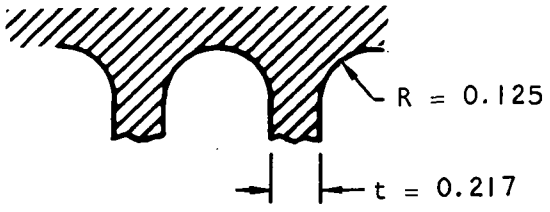

$R/t = 0.58$

The stress concentration factor in bending is about 1.18, which is consistent with using a stress of 0.85 σ_{all}. The fillet was broken into ten equal-length elements and the straight section length was computed to produce the same flexibility as an unfilleted guided cantilever 1.3 in. long. The total length including the fillets at each end was found to be 1.380 in. To control beam spring rates and stresses under load, the three critical dimensions of beam total length, beam thickness, and fillet radius should be held to ±1/2 percent tolerance limits on the nominal dimensions.

2.4.2 Thermal Analysis of Block

The choice of material for the deflection block is influenced not only by the structural and functional requirements, but also by the need to minimize error due to temperature in the indicated thrust. The following simplified analysis deals with the effect of temperature gradients within the block and concludes that limiting the (3σ) uncertainity error to 1 percent requires that gradients no greater than 25°F exist within the block during the period of measurement.

2.4.2.1 Error

A first step is to determine what error due to temperature can be tolerated.

The root-sum-square method is used to resolve the overall error in determination due to individual contributory errors. Since system errors are calibrated out, the overall error in determination is considered random.

The engine parameter to be determined by the thrust measurement is the internal thrust. Combined with the fuel flow through the injectors, the internal specific impulse is determined.

Let the absolute error in internal thrust, T_i, be ϵ_T

Let the absolute error in fuel rate flow, $\dot{\omega}_f$, be ϵ_w

Let the absolute error in internal specific impulse $I_{s,i}$, be ϵ_I

Then

$$I_{s,i} = \frac{T_i}{\dot{\omega}_f} \tag{2.4-5}$$

and

$$\epsilon_I = \sqrt{\left(\epsilon_T \frac{\partial I_{s,i}}{\partial T_i}\right)^2 + \left(\epsilon_w \frac{\partial I_{s,i}}{\partial \dot{\omega}_f}\right)^2} \tag{2.4-6}$$

From Equation (2.4-5) $\frac{\partial I_{s,i}}{\partial T_i} = \frac{1}{\dot{\omega}_f}$ and $\frac{\partial I_{s,i}}{\partial \dot{\omega}_f} = \frac{-T_i}{\dot{\omega}_f^2}$

Substituting and dividing both sides by $I_{s,i}$,

$$\frac{\epsilon_I}{I_{s,i}} = \sqrt{\left(\frac{\epsilon_T}{T_i/\dot{\omega}_f}\ \frac{1}{\dot{\omega}_f}\right)^2 + \left(\frac{\epsilon_w}{T_i/\dot{\omega}_f}\ \frac{-T_i}{\dot{\omega}_f^2}\right)^2}$$

$$\frac{\epsilon_I}{I_{s,i}} = \sqrt{\left(\frac{\epsilon_T}{T_i}\right)^2 + \left(\frac{\epsilon_w}{\dot{\omega}_f}\right)^2} \qquad (2.4\text{-}7)$$

Let e_I, e_T, e_w be the percentage of errors in $I_{s,i}$, T_i and $\dot{\omega}_f$, respectively.

Then from Equation (2.4-7)

$$e_I = \sqrt{e_T^2 + e_w^2} \qquad (2.4\text{-}8)$$

2.4.2.2 Application

I_{si} should be determined to within an error of 5 percent or less (Reference 2-2). In view of the uncertainties associated with measuring fuel flow rate (see Section 5), the error in T_i will be reduced as far as is practicable. Current error analyses suggest that an error (at full scale) of less than 2.7 percent can be obtained (see Paragraph 2.4.6)

from Equation (2.4-8) $\quad e_T^2 + e_w^2 = 25 \qquad (2.4\text{-}9)$

for $\quad e_T = 2.7$ percent, $e_w = 4.25$ percent

(Figure 2.4-3 plots the relationship of Equation (2.4-9)). On this basis, the thermal error maximum will be evaluated. The error e_T is composed of errors in indicated thrust, drag, acceleration, etc., and is estimated by the root-sum-square method as under Equation (2.4-6), extended to cover more variables.

The third Instrumentation Technical Data Report (Reference 2-1) shows the relationship between the internal thrust, T_i, and the following variables:

$$T_i = T_{ind} + W \sin\theta + W\ddot{x} + D_e + F_R + F_M + \Delta_F - F_I = R - F_E \qquad (2.4\text{-}10)$$

where T_{ind} = indicated thrust

W = effective engine weight

θ = angle of pitch

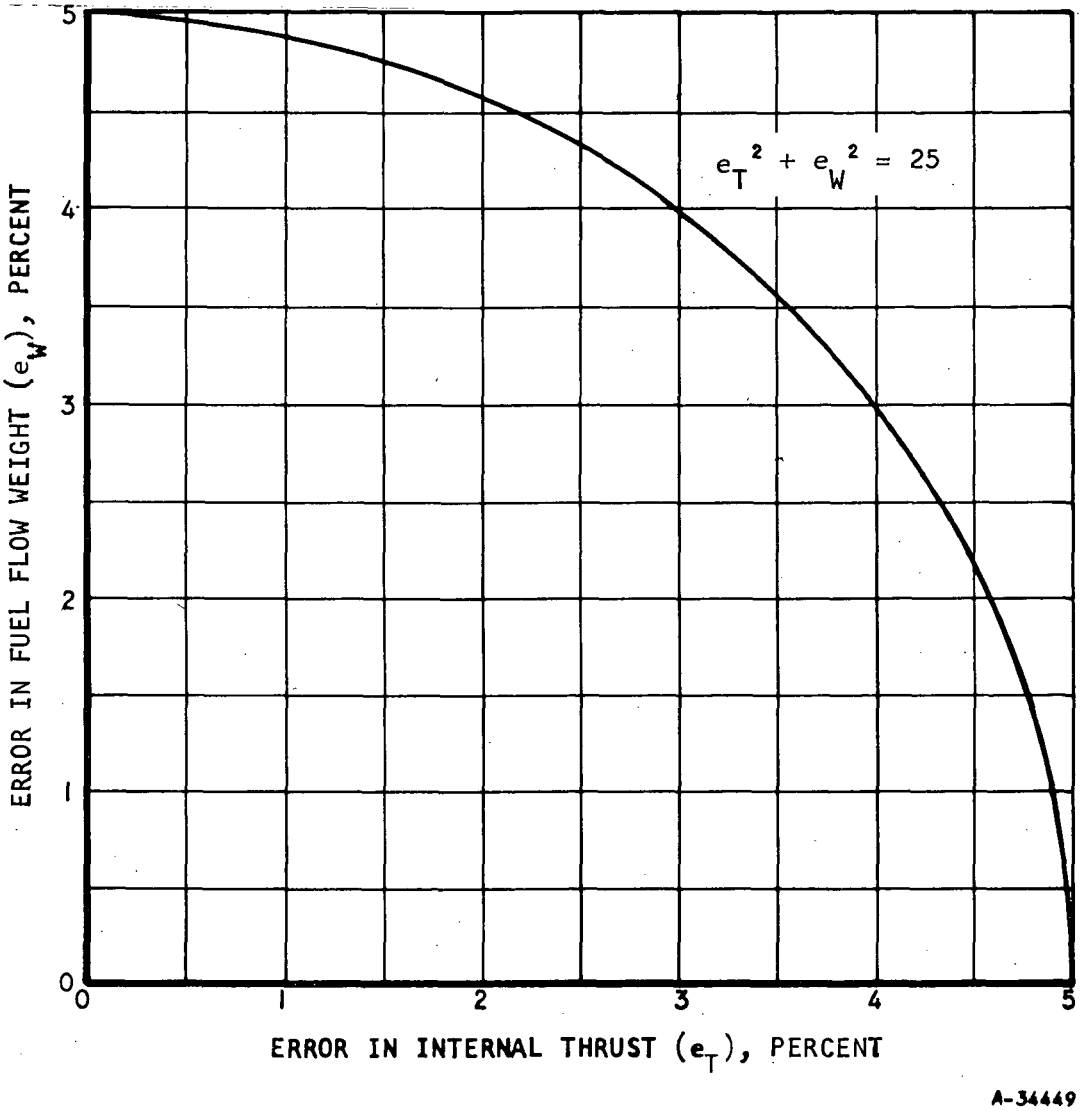

Figure 2.4-3. Error in Fuel Flow (Weight) Versus Error in Internal Thrust

$\ddot{x}$ = acceleration of engine along X-axis

D_e = external drag

F_R = parallel restraint force

F_M = effective force due to block moment (through friction)

Δ_F = capacitor area change equivalent force

F_i = resolved vertical force due to misalignment

R = resolved vertical force due to block deflection

F_E = thermal effects--equivalent force

NOTES:

(a) The force, F_E, corresponding to thermal movement in the deflection block assembly is to be examined for error.

(b) The accelerometer will inherently measure ($W\ddot{x}$ + W sin θ).

(c) The differential thermal expansion force, F_T, is taken with an assumed error at this stage.

(d) The external drag force, D_e, does not include cowl drag; the cowl is supported on the aircraft side of the thrust block.

Table 2.4-2 is a simplified error table based on the following relationship:

$$\epsilon_T = \sqrt{(\epsilon_1\omega_1)^2 + (\epsilon_2\omega_2)^2 + \ldots\ldots(\epsilon_n\omega_n)^2} \qquad (2.4\text{-}11)$$

where ϵ_T, ϵ_1, ϵ_2, ϵ_n are absolute errors

and ω_1, ω_2, ω_n are weighting factors

[(if $Q = \phi\ (A_1\ A_2\ A_3\ \ldots\ldots\ A_n)$ ϕ is a function.

Then $\omega_1 = \frac{\partial Q}{\partial A_1}$, $\omega_2 = \frac{\partial Q}{\partial A_2}$ .... $\omega_n = \frac{\partial Q}{\partial A_n}$]

TABLE 2.4-2

SIMPLIFIED ERROR TABLE

Factor	Symbol	Error, percent FS	Absolute Error ϵ_n	Weighting Factor ω_n	$\epsilon_n \cdot \omega_n$	$(\epsilon_n \omega_n)^2$
Indicated thrust	T_{ind}	1.10	77	1	77	5950
Accelerometer output	$W(\ddot{x} + \sin\theta)$	1.73	0.052 g	700	35.4	1250
Drag	D_E	12.5	88	1	88	7744
Parallel restraints	F_R	(small) estimate	2	1	2	4
Thermal expansion	F_T	estimate	50	1	50	2500
Resolved vertical force	F_I		8	1	8	64
Resolved vertical force	R		10	1	10	100
Resolved moment	F_M		10	1	10	100
Temperature effects	F_E		To be determined			-
					$\Sigma(\epsilon_n \omega_n)^2$	17,712
					$\sqrt{\Sigma(\epsilon_n \omega_n)^2}$	133

$T_{int_{(max.)}} = 5950$ Thus $e_T = \frac{133.100}{5950}$ excluding temperature effects.

$$e_T = 2.23 \text{ percent}$$

To meet $e_T = 2.7$ percent (including temperature effects)

then $2.7^2 = 2.23^2 + e_f$

e_F = env percent due to temperature effects

Thus $e_F = 1.5$ percent

For design purposes, e_F is taken at ±1.0 percent maximum.

2.4.2.3 Thermal Effects (Refer to Figure 2.4-4)

3.1 (E_1) Differential expansion between centers of outer plates (top) and center plate (bottom)

3.2 (E_2) Rotation of center plate due to differential expansion of flexures (top to bottom)

3.3 (E_3) Change of capacitance due to expansion (top to bottom)

3.4 (E_4) Change of capacitance due to transverse expansion

3.5 (E_5) Change of modulus of elasticity

3.6 (E_6) Change in capacitor gap due to differential expansion.

Each of the above thermal effects will be considered in the analysis which follows:

These effects are illustrated in the following diagrams:-

(E_1)

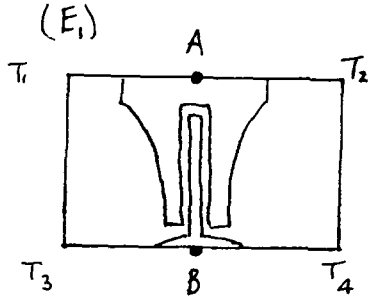

If $T_1 > T_2$ A will move to the right

If $T_3 > T_4$ B will move to the right

if $(T_1 \sim T_2) \neq (T_3 \sim T_4)$ A will move relative to B.

From Reference 2-1,

Relative deflection $\Delta_1 = \frac{\alpha x}{8}\left[(T_1 - T_2) - (T_3 - T_4)\right]$ ... (2.4-12)

Full-scale deflection is nominally .003", α = coefft. of thermal expansion of block.

Then % error $e_1 = +\frac{\alpha x}{24} \cdot 10^5 \left[(T_1 - T_2) - (T_3 - T_4)\right]$ .. (2.4-13)

(E_2)

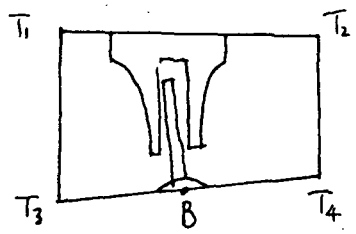

If $T_1 + T_3 > T_2 + T_4$ the flexures will have different lengths under expansion causing a displacement of the center plate to the left (assuming pivoting about B) Counteracting this will be a moment tending to keep the top and bottom parallel. This moment will effectively displace the center-plate to the right

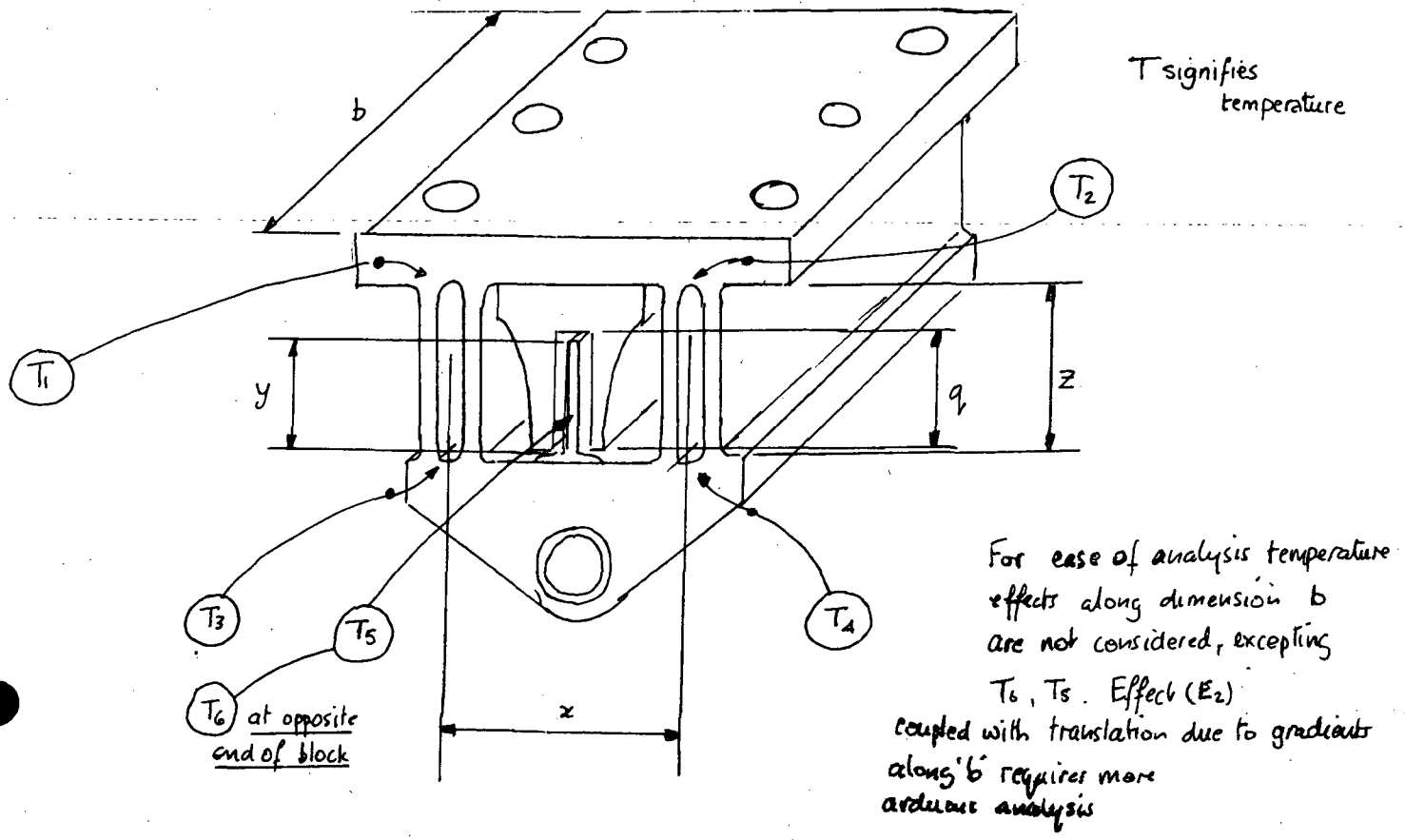

Figure 2.4-4. Deflection Block

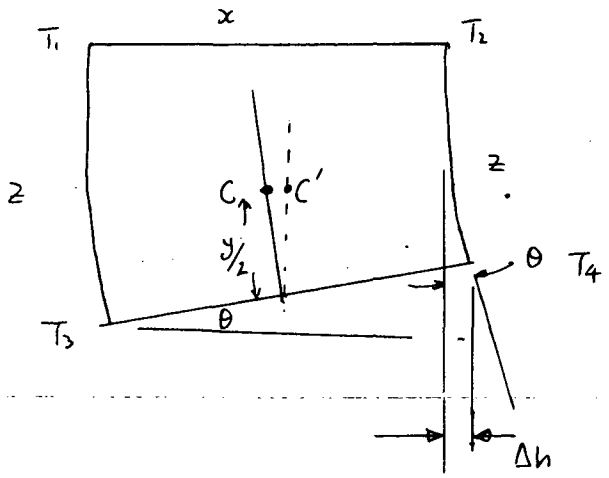

The block will deflect as shown

Let $cc' = \Delta_c$

Then relative displacement of centerplate

$$\Delta_2 = \Delta_c - \Delta h \quad \text{(to give positive error)}$$

Consider the beam

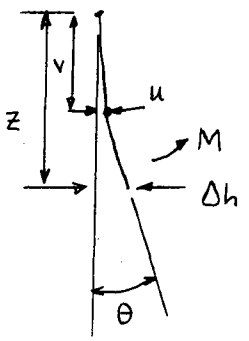

Then by simple beam theory

$$\frac{d^2u}{dv^2} = \frac{M}{EI}$$

$$\frac{du}{dv} = \frac{Mv}{EI} \quad (v=0, \frac{du}{dv}=0)$$

$$u = \frac{Mv^2}{2EI} \quad (v=0, u=0)$$

$$u = \frac{du}{dv} \cdot \frac{v}{2}$$

Hence $\Delta h = \theta \cdot z/2$

And $\Delta_c = \frac{y\theta}{2}$

Thus $\Delta_2 = \frac{\theta}{2}[y-z]$

But $\theta = \frac{z}{x}\alpha\left[\frac{T_1+T_3}{2} - \frac{T_2+T_4}{2}\right]$

$$\therefore \quad \Delta_2 = \frac{\alpha z}{4x}\left[(T_1-T_2)+(T_3-T_4)\right][y-z] \quad \text{.....(2.4-14)}$$

$$e_2 = \frac{\alpha z}{12x} \cdot 10^5 \left[(T_1-T_2)+(T_3-T_4)\right][y-z] \quad \text{.....(2.4-15)}$$

(E_3)

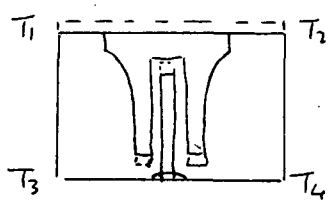

Expansion of the flexures, centerplate, and outerplates will alter the effective area of the capacitor plates.

From ref 55-8.03

$$e_3 = -100/y\,[T_A - T_c][\alpha z - \alpha_c y - \alpha_o q] \quad \text{...(2.4-16)}$$

where T_A = average temperature
T_c = calibration "
α_c = coefft. of exp. of centerplate
α_o = " " " " outerplate

(E_4)

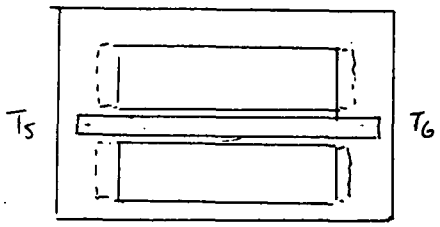

In the latest design the center plate will be longer than the outer plates. Tranverse differential expansion will occur, altering the effective area.

Then $e_4 = +100\alpha_o\left(\frac{T_S+T_G}{2} - T_C\right)$ ... (2.4-17)

(E_5) The modulus of elasticity will decrease with temperature

The spring constant 'k' of the flexures is dependent on the length, thickness 't' and elasticity modulus E and the width of the block 'b'

The relationship may be expressed as

$k/b = E\,(t/2)^3$ [ignoring the Poisson's Ratio Term see (2.4-3)]

Although the temperature differential along a flexure will give varying thickness, the length will increase also. The expansion is small and ignoring second order terms $t/2$ may be considered constant.

Thus the effective variables are b and E

Then $\Delta k = b\,(t/2)^3\,\Delta E + E\,(t/2)^3\,\Delta b$

$\Delta k = -b\,(t/2)^3 \cdot E\,\alpha_E\,(T_A - T_C) + E\,(t/2)^3\,b\,\alpha\,(T_A - T_C)$ α_E = modulus coefficient

$\Delta k = bE\,(t/2)^3\,(T_A - T_C)(-\alpha_E + \alpha)$

$\frac{\Delta k}{k} = (T_A - T_C)(\alpha_E + \alpha)$

$e_5 = +100\,(T_A - T_C)(\alpha - \alpha_E)$ ... (2.4-18)

(E_6)

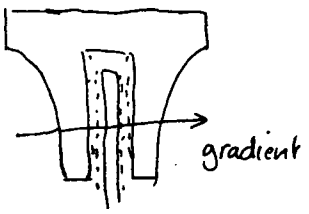

Temperature gradient across capacitor will cause differential expansion. Due to the low expansion coefficients this will be small (gradient low also) This effect is neglected.

If these thermal effects are not accounted for, they become systematic errors and must be added

Then the total error e_e becomes

$$e_e = \frac{\alpha x}{24} 10^5 \left[(T_1-T_2)-(T_3-T_4)\right] + \frac{\alpha z}{12x} 10^5 \left[(T_1-T_2)+(T_3-T_4)\right][y-z]$$

$$-\frac{100}{y}\left[T_A-T_c\right][\alpha z-\alpha c y-\alpha_0 q_1] + 100\alpha_0\left[\frac{T_5+T_6}{2}-T_c\right]+100\left[T_A-T_c\right][\alpha-\alpha_E]$$

Let $T_1-T_2 = \Delta T_1$ Substitute $x=2$ $b=4$

$T_3-T_4 = \Delta T_2$ $y=0.9$ $\alpha_c = 1\times10^{-6}/°F$ Invar

$T_A-T_c = \Delta T_3$ $z=1.38$ $\alpha_c = 1\times10^{-6}$ Alsimag

$\frac{T_5+T_6}{2}-T_c = \Delta T_4$ $q=0.9$

Then $$e_e = \frac{\alpha\times 2\times10^5}{24}\left[\Delta T_1-\Delta T_2\right] + \frac{\alpha\times1.38\times10^5}{12\times2}\left[\Delta T_1+\Delta T_2\right][-0.48]$$

$$-\frac{100}{0.9}\Delta T_3\left[1.38\alpha-2\times0.9\times10^{-6}\right]+100\times1\times10^{-6}\Delta T_4+100\Delta T_3(\alpha-\alpha_E)$$

This reduces to

$$e_e = \alpha\left[5570\Delta T_1-11{,}090\Delta T_2-53\Delta T_3\right]-100\alpha_E\Delta T_3+10^{-4}(\Delta T_4+2\Delta T_3) \quad (2.4\text{-}19)$$

A recent heat transfer analysis has been performed and reference is made to the report to obtain approximate temperatures. This analysis was performed using the properties of Ti-6Al-4V

Temperatures are taken at time 170 secs after launch

$T_1 = -22°F$

$T_2 = +40°F$

$T_3 = +12°F$

$T_4 = +70°F$

$T_5 = +23°F$ (estimated)

$T_6 = T_5 = 23°F$

T_c = calibration temperature 68°F

$T_A = \frac{T_1+T_2+T_3+T_4}{4}$ assuming no transverse gradients

$T_A = 25°F$

And $\Delta T_1 = -62°F$

$\Delta T_2 = -58°F$

$\Delta T_3 = -43°F$

$\Delta T_4 = -45°F$

Substituting values, the relationship becomes:-

$$e_e = -300,390\alpha - 4300\alpha_E + 0.0131$$

For $e_e = -1$ (%)

Then $\underline{300,390\alpha + 4300\alpha_E = 0.987}$ . . . . . (2.4-20)

This relationship is shown plotted in figure 2.4-5 (Applicable Ti-6Al-4V only)

However, consider a calibration temperature of 85°F

Then approximately $\Delta T_1 = \Delta T_2 = \Delta T_3 = \Delta T_4 = \Delta T$

Then the relationship becomes

$$e_e = -(5573\alpha + 100\alpha_E)\Delta T$$

ignoring the latter terms which are small comparatively

For $e_e = -1$

$$\underline{\Delta T(5570\alpha + 100\alpha_E) = 1} \quad \ldots\ldots\ldots\ldots\ldots\ldots (2.4\text{-}21)$$

This relationship is shown plotted for various values of ΔT in figure 2.4-6

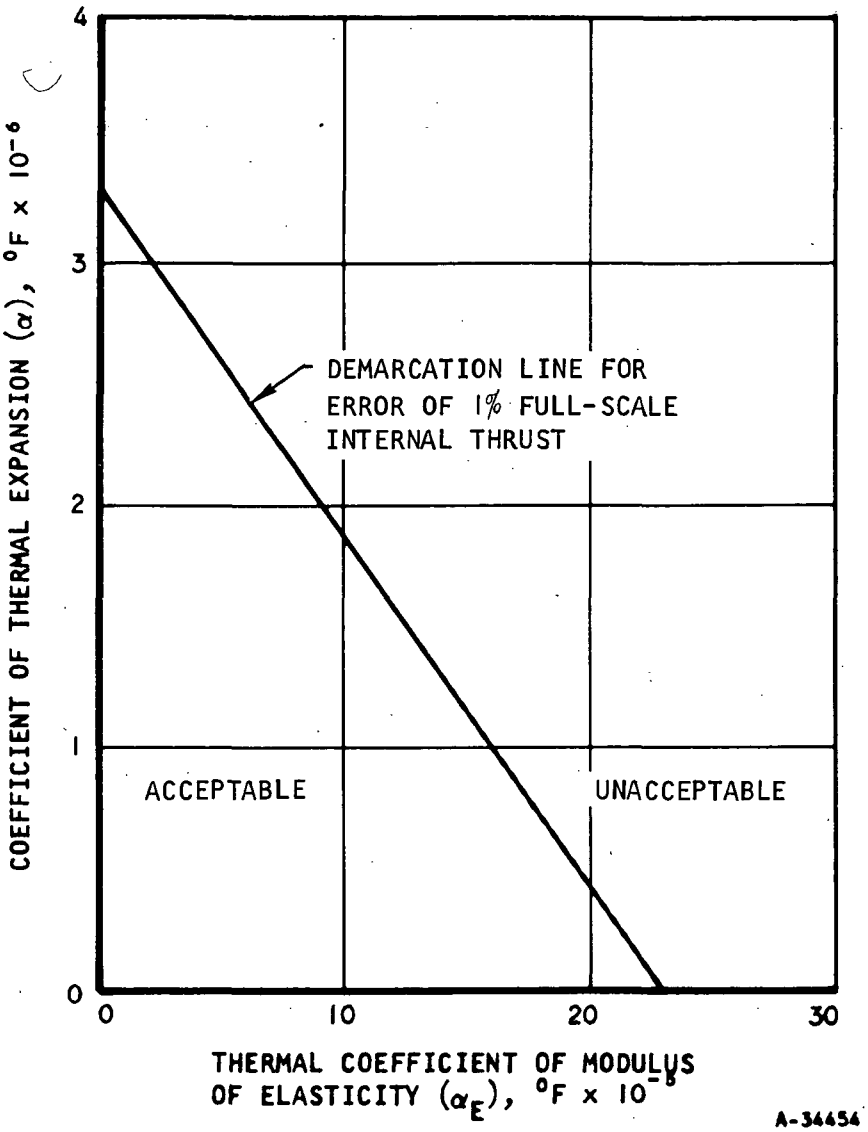

Figure 2.4-5. Relationship of α/α_E, Based on Analysis of Ti-6Al-4V Block

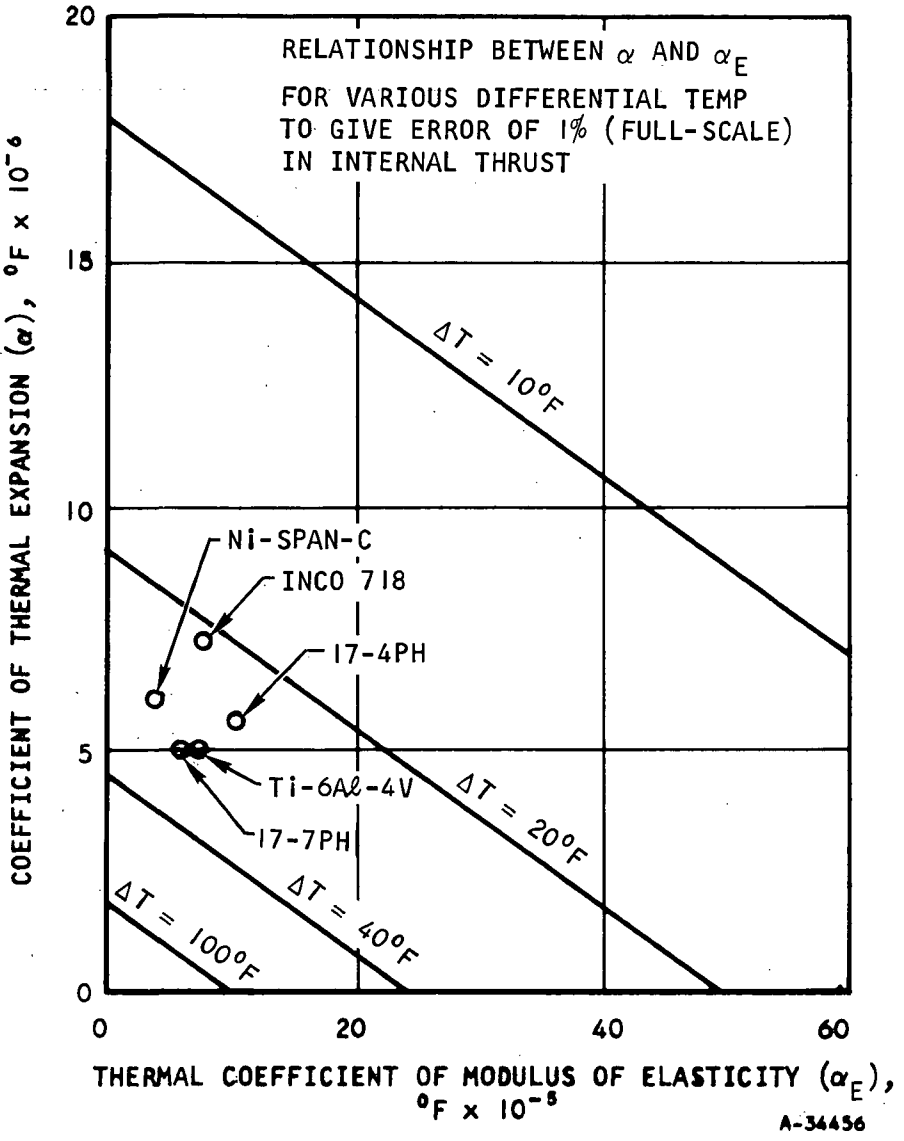

Figure 2.4-6. Relationship of α/α_E for Various Metals

2.4.2.4 Conclusions

The analysis has been simplified by assuming that no temperature gradients exist across the block, that all materials have similar gradient distributions, and that the gradients considered in the block remain sensibly equal for different gradient values.

Figure 2.4-6 and five of the six candidate materials considered (plotted in terms of their elasticity modulus and thermal expansion coefficients) are based on this simplification.

For the material chosen (17-4PH), the result suggests that temperature gradients within the block should be limited to 25^0F. In view of the heat transfer analysis (see Paragraph 2.4.3), some form of temperature control will be necessary. For a block of Ti-6Al-4V material, temperature gradients of approximately 60^0F are envisaged.

It is hoped that passive control will meet the requirements. Since the major heat input is by radiation, present thoughts are to use a radiation shield. Limitations of space and interface considerations affect the design of such a shield; active work on this problem is in process. Development tests will be undertaken to correlate the analysis.

2.4.3 Heat Transfer Analysis

2.4.3.1 Heat Sources and Sinks

The heat sources for the X-15/HRE interface structure under consideration are fuel-injector manifolds 1 and 2, outer-shell-coolant outlet manifold, turbine, and inner surfaces of the pylon. The heat sinks are the leading-edge inlet manifold for the H_2 coolant and the X-15 interior to which the top of the pylon is open. The thermal conditions of these sources and sinks are shown in Figures 2.4-7 and 2.4-8. A black-body assumption was made for these sources and sinks. During an X-15 test flight, thermocouple measurements were taken of the inner skin temperature of the ablatively cooled dummy HRE fuselage. These measurements were used as a representative temperature history of the inner skin of the pylon (also to be cooled ablatively) in the belief that the thickness of the ablator over the pylon is such that the temperature of inner skin is even.

The analysis did not cover the effect of natural convection of the air. A comparison indicates that due to natural convection, the heat-transfer rate from the outer-shell outlet manifold to the otherwise still air is about one-fifth of the radiative heat-transfer rate from the same manifold surface. This means that heat convection from the air will cause the lower part of the deflection block to have a somewhat higher temperature than that predicted by the present analysis. Because of small temperature differences between the air and the lower part of the block, the excess temperature over the predicted values is believed to be negligible. Also, since the rate of temperature rise due to radiation is much larger than that due to natural convection, the heat will flow from the block to the air for the latter part of the time, resulting

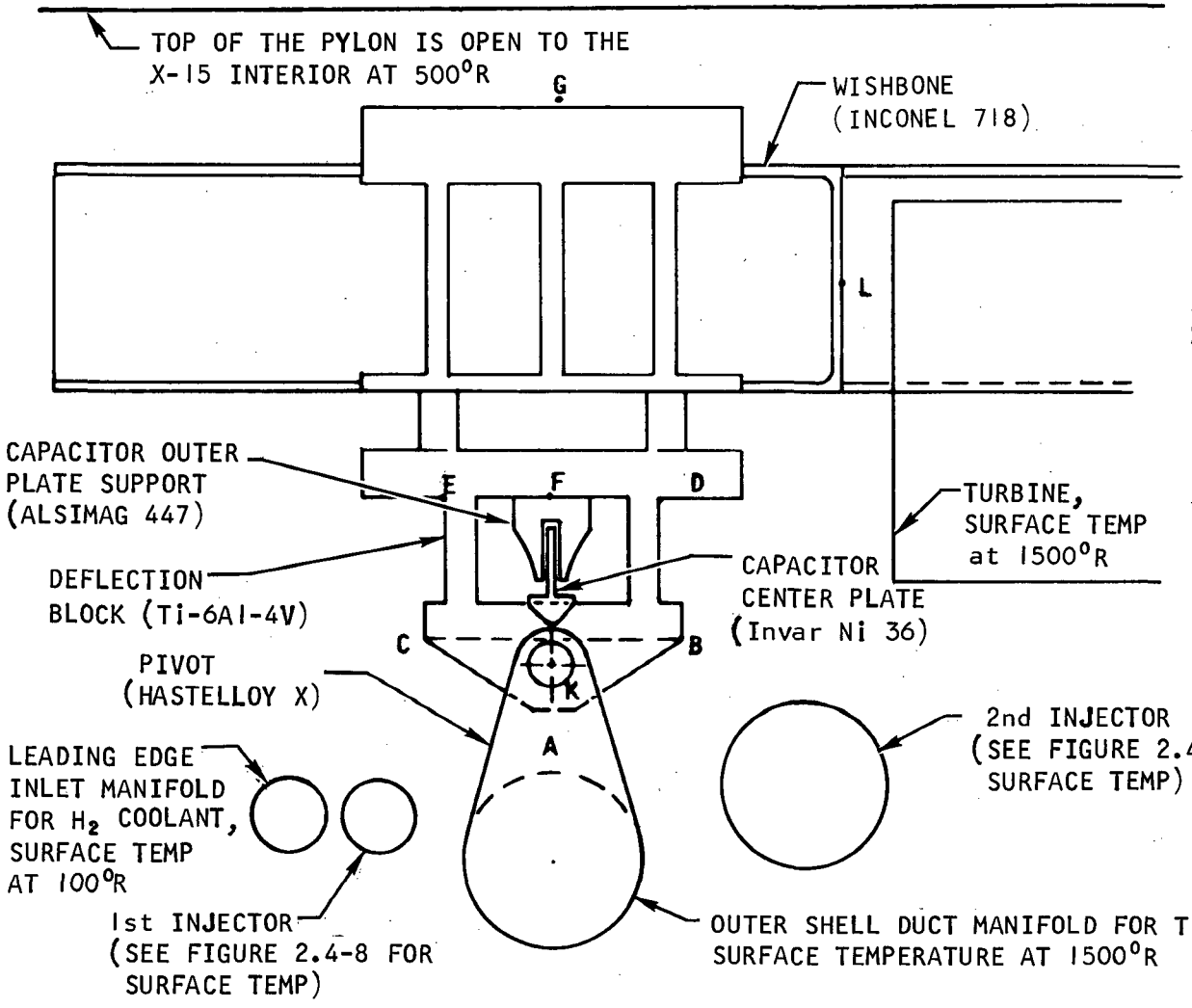

NOTES:

A: BOTTOM SURFACE OF DEFLECTION BLOCK

B,C: SIDE SURFACES OF LOWER PART OF D,B

D,E: SIDE SURFACES OF UPPER PART OF D,B

F: BETWEEN D AND E

G: UPPER SURFACE OF WISHBONE

H: PART OF D,B CONNECTED TO PIVOT THRUST PIN

K: UPPER PART OF PIVOT

L: PART OF WISHBONE FACING TURBINE

REFER TO REFERENCE 2-1 FOR DETAILED DRAWING

Figure 2.4-7. Deflection Block and Supporting Structure

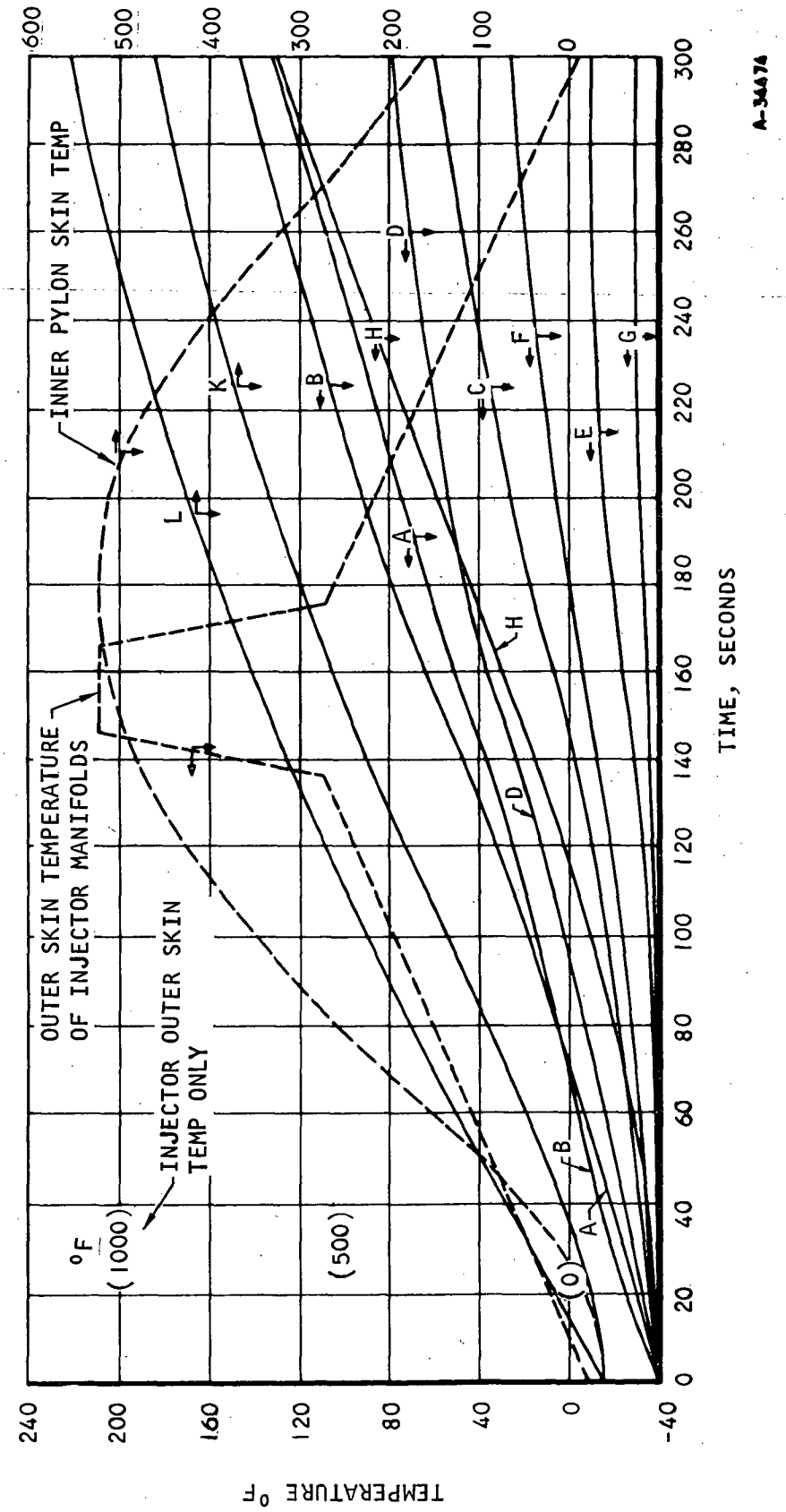

Figure 2.4-8. Temperature Versus Time

in a lower block temperature than predicted. Both the temperature difference and the effect of natural convection on the upper part of the block are believed to be negligible.

2.4.3.2 Comments

Table 2.4-3 lists the properties of the various materials used in this analysis. In Figure 2.4-8, the temperatures in the solid blocks are in the transient state during the period under consideration; the maximum temperature in the deflection block is about 155°F on the lower side surface. In Figure 2.4-7, Point B has a 160° to 180°F differential across the block from the engine mount to the aircraft mount (between A or B and F or G), and a 100°F differential fore to aft (between B and C), all at the end of the first and 300-sec flight of the X-15 aircraft. Also notice that the surfaces facing the turbine, which has an outer skin temperature of about 1500°R, have a higher temperature than those surfaces not facing the turbine. The upper part of the pivot (Point K in Figure 2.4-7), and the part of the wishbone facing the turbine (Point L in Figure 2.4-7) reach temperatures of 460° and 560°F at 300 sec, respectively. If necessary, insulation between the turbine and the deflection block can reduce both the maximum structure temperature and the temperature differential fore to aft. To predict temperatures beyond 300 sec, the curves in Figure 2.4-8 may be extrapolated.

The above results represent a summary of a revised analysis using a modified computer program. In contrast to the older computer program, which could handle only 50 radiation resistances, this program can handle up to 400. For the purposes of this analysis, 220 resistances were taken; it is considered that realistic results have been obtained.

2.4.4 Accelerometer

2.4.4.1 Range

The range of the accelerometer will be determined as a function of the acceleration envelope to which the accelerometer will be exposed. A mounting technique that filters the vibration inputs to the accelerometer would be ideal; however, since such a mount would involve too much mechanical complexity, another method must be considered. This approach will be used in place of that described in Reference 2-1 in which a 10-cps mechanical filter was proposed to remove high-level vibration inputs.

Consideration of a "force-balance" accelerometer has led to the comparison of the characteristics of a very accurate open-loop accelerometer with a typical force-balance model (see Table 2.4-4).

Because of the improved linearity of the Kistler model, there are relatively small increases in overall error with large increases in range (see Table 2.4-5). The accelerometer error analysis indicated only a 0.42- to 0.53-percent increase in error (expressed as a percentage of 3 g) for a change in range of from ±5 to ±20 g. Since the accelerometer uncertainty will be about one third to one fourth the total acceleration

TABLE 2.4-3

PROPERTIES USED IN PRESENT ANALYSIS

Item	Material	Thermal Conductivity, Btu-in. /ft²/hr/°F	Density, lb per cu in.	Specific Heat, Btu/lb/°F	Emissivity
Wishbone	Inconel 718	92	0.296	0.1	0.65
Deflection block	Ti-6Al-4V	42	0.159	0.14	0.65
Capacitor center plate	Invar Ni 36	72.6	0.288	0.123	0.25
Capacitor outer plates support	ALSIMAG 447	75	0.0646	0.2365	0.5
Pivot	Hastelloy Alloy X	88	0.297	0.105	0.2

TABLE 2.4-4

COMPARISON OF ACCELEROMETER CHARACTERISTICS

Specification	Accelerometer		Remarks
	Kistler Model 303B	Kaman Model KA-1100	
Range	As required	Fixed as ordered	KA-1100 requires separate Oscillator-Demod package
Natural frequency	550 to 700 cps	500 to 1000 cps	Kistler has adjustable range ±0.5 to ±50 g
Sensitivity	±5 v full range	0 to 5 v full range	
Resolution	0.00001 g	Continuous	
Nonlinearity	±0.05 percent full range	±0.5 percent full range	
Repeatability and resolution	±0.0005 g	0.1 percent of full range	
Noise	5 mv rms max.	--	8 MHz filtered in signal condition
Zero output	±0.05 g max.	Not specified	Will be biased out
Transverse sensitivity	0.002 g/g	0.005 g/g	
Zero shift	0.03 g/100°F	0.02 percent/°F full range	
Thermal sensitivity	0.015 percent/°F		
Size	1 in. dia by 2 in. length	1 in. dia by 0.675 in. length	Kaman requires a 7-oz Oscillator-Demod
Weight	3.3 oz	1.8 oz	
Temperature			
Operational	-65° to +180°F	-65° to +400°F	
Survival	-65° to +250°F	-65° to +400°F	
Shock	100 g 5 ms	500 g 10 ms	
Vibration	±20 g	--	
Acceleration	100 g	--	
Self test	yes	no	

TABLE 2.4-5

ACCELEROMETER ERROR ANALYSIS
KISTLER MODEL 303B
±5, ±10, AND ±20 g RANGES

Source	Value	Multiplier	Error	Error, percent of 3-g range			E^2		
				±5 g	±10 g	±20 g	±5 g	±10 g	±20 g
Resolution	0.00001 g		0.00001 g	0.0003	0.0003	0.0003	-	-	-
Linearity	0.05 percent		0.05 percent	0.08	0.16	0.32	0.0064	0.0256	0.103
Hysteresis repeat-ability	0.0005 g		0.0005 g	0.016	0.016	0.016	0.0002	0.0002	0.0002
Zero shift	0.03 g/100°F	2 20°F	0.006 g	0.20	0.20	0.20	0.04	0.04	0.04
Sensitivity shift	0.015 percent/°F	2 20°F	0.3 percent	0.30	0.30	0.30	0.09	0.09	0.09
Transverse sensitivity	0.002 g/g	1 3.16 g	0.006 g	0.20	0.20	0.20	0.04	0.04	0.04
						ΣE^2	0.1766	0.1958	0.2732
						$\sqrt{\Sigma E^2}$	0.42 percent	0.44 percent	0.53 percent

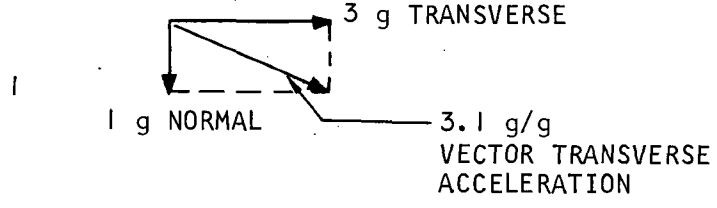

1

2 Temperature uncertainty is 20°F

uncertainty, it becomes apparent that the range, at least in the band of ±5 to ±20 g, is not a critical factor relative to the measurand. Table 2.4-6 presents an acceleration error analysis.

It is necessary to assess the spectral density function of random vibration on the deflection block so that the range of the accelerometer may be adjusted to include the envelope of peak amplitudes. This will reduce errors caused by distortion in the output due to over-range signals. In Reference 2-1, the spectral density function of the input vibration was assumed to be flat, with Gaussian amplitude distribution and the peak acceleration was computed by assuming the thrust block/engine system to be a single-degree-of-freedom system. Based on an input of 0.015 g^2/cps (Reference 2-3), an rms level of 6.5 g could be expected at the accelerometer mounting position with 3σ peaks to 19.5 g. An accelerometer range of ±20 g would thus seem applicable.

2.4.4.2 Temperature

Based on a recent heat-transfer analysis of the deflection block, the operating temperature and the maximum temperature for the acceleration transducer have been defined further. In the area where the accelerometer is to be mounted, the upper temperature limit of the block will be 200°F. The operating temperature will be from -40° to +80°F. The accelerometer will be instrumented with a thermocouple. It is anticipated that the uncertainty of the temperature accelerometer will be ±20°F. Temperature shielding of the block assembly is necessary and may need to include the accelerometer.

2.4.4.3 Error

Although not the most important source of error (see Section 2.4.6.1) the accelerometer does contribute significantly (especially at lower internal thrust outputs where drag is reduced and the inertia forces constitute a major portion of the indicated thrust measurement). Thus, the error should be minimized and should not be higher than 2.0 percent of full scale.

2.4.5 Secondary Forces

The origins and derivations of the secondary forces (F) were comprehensively covered in Reference 2-1, however, certain errors and omissions necessitate some revision.

2.4.5.1 Moment Thrust Pin Friction M_B (Paragraph 2.4.2.4 of Reference 2-1)

The friction between the pin and bushing will give rise to a torque on the block under the applied moment (M). This torque will reach a maximum of

$$T = \mu F_N R \qquad \mu = \text{coefficient of friction}$$

In the direction of moment shown in the following figure, Z_1 will extend and Z_2 will compress causing a rotation of the capacitor sensor center plate, and a displacement of the center of the plate to the left. This effect will appear as hysteresis and can be evaluated under test.

TABLE 2.4-6

ACCELERATION ERROR ANALYSIS

Source	Value, percent	E, percent of 3 g	E^2
Accelerometer (±20 g)	0.53	0.53	0.28
Vibration (0.001 g/g)	0.003 g*	0.1	0.01
System calibration	1.5 (est.)	1.5	2.25
Power regulation	±0.01	0.01	0.0001
Signal conditioning	±0.4	0.4	0.16
PCM system accuracy	±0.5	0.5	0.25
PCM calibration	±0.1	0.1	0.01
PCM resolution	±0.2	0.2	0.04
		ΣE^2	3.00
		$\sqrt{\Sigma E^2}$	1.73 percent

*Actual value

WIDTH OF BLOCK (THROUGH PAPER) = b

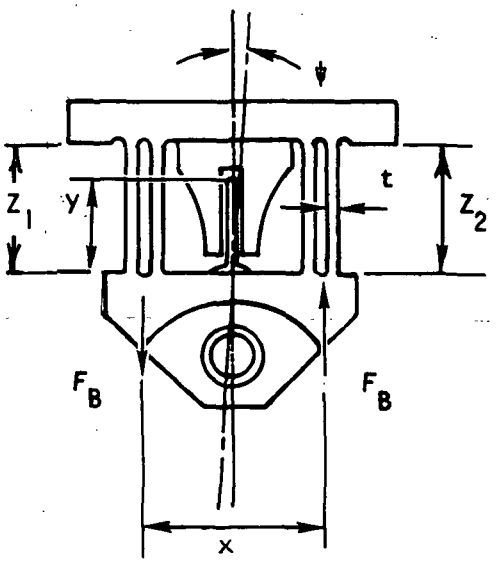

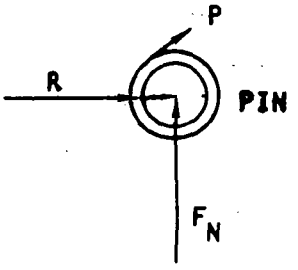

Now $F_B = T/x$

$$F_B = \frac{\mu F_N R}{x}$$

Strain = stress/E

$$= \frac{F_B}{xbtE}$$

Thus, the change of length of flexure = δz

$$= \frac{\mu F_N z}{2xbtE}$$

and $$\psi = \frac{Z_1 - Z_2}{x} = \frac{2\delta z}{x}$$

$$\psi = \frac{2F_N z}{2btEx^2}\mu$$

Displacement of center plate = $(y/2)\psi$

$$= \frac{yF_N zK}{2btEx^2}\mu$$

Equivalent force for spring constant = k

$$F_M = \frac{yF_N zK}{2btEx^2}\mu \qquad (2.4\text{-}22)$$

2.4.5.1.1 Determination of F_N

From Reference 2-4, the following load diagram may be drawn for the wishbone engine interface.

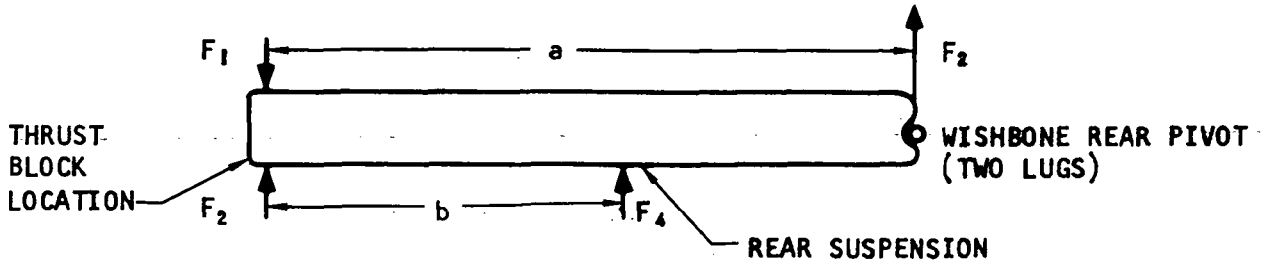

Forces shown are the reactions of the pylon on the wishbone.

From Table 5-V of Reference 2-4, condition 20 the values are

$F_1 = 3396$ lb

$F_2 = 2258 + 1758$

$F_2 = 4016$ lb

(F_2 adjusted for sign in above sketch.)

$a = 35$ in.

$b = 13.75$ in.

Resolving forces $F_1 + F_2 = F_3 + F_4$

By moments $bF_4 = aF_2$

By substitution $F_1 + F_2 = F_3 + a/b\ F_2$

$$F_3 = F_1 - F_2\ (a/b - 1) \qquad (2.4\text{-}23)$$

By substituting values, $F_3 = -3064$ lb

Table 5-V, Reference 2-4.

Condition 32 yields $F_3 = -3200$ lb

Taking $y = 1.0$ in.

$Z = 1.38$ in.

$x = 2$ in.

$t = 0.217$ in.

$E = 28.5 \times 10^6$

$k = 2 \times 10^6$

$b = 4$

$F_N = 5000$ lb (3200 lb calculated)

$\mu = 0.1$

Then $F_M = 7.1$ lb

2.4.5.2 Acceleration Error Due to Off-Center-of-Gravity Location of Engine

a_x = acceleration sensed by accelerometer in x direction

$\ddot{x}$ = aircraft acceleration in g's

r_1 = distance from aircraft c.g. to accelerometer (12.36 ft)

r_2 = distance from aircraft c.g. to HRE c.g. (13.27 ft)

θ = angle of attack

$\theta_1 = 15.7^0$, see Figure 2.4-9

$\theta_2 = 19.2^0$, see Figure 2.4-9

ω = pitch rate, 2^0/sec max., estimated from statement of work, (see Figure A-5 of Reference 2-3)

$\dot{\omega}$ = change g pitch rate, $0.2^0/\text{sec}^2$ max., estimated

$$a_x = \ddot{x} + \sin\theta + \frac{r_1}{g}\omega^2 \cos\theta_1 + \frac{r_1}{g}\dot{\omega}\sin\theta \qquad (2.4\text{-}24)$$

and

$$T_{int} = W\ddot{x} + W\sin\theta + T_{ind} + W\frac{r_2}{g}\omega^2\cos\theta_2\, W\frac{r_2}{g}\dot{\omega}\sin\theta_2 + D_E \qquad (2.4\text{-}25)$$

See Figure 2.4-9.

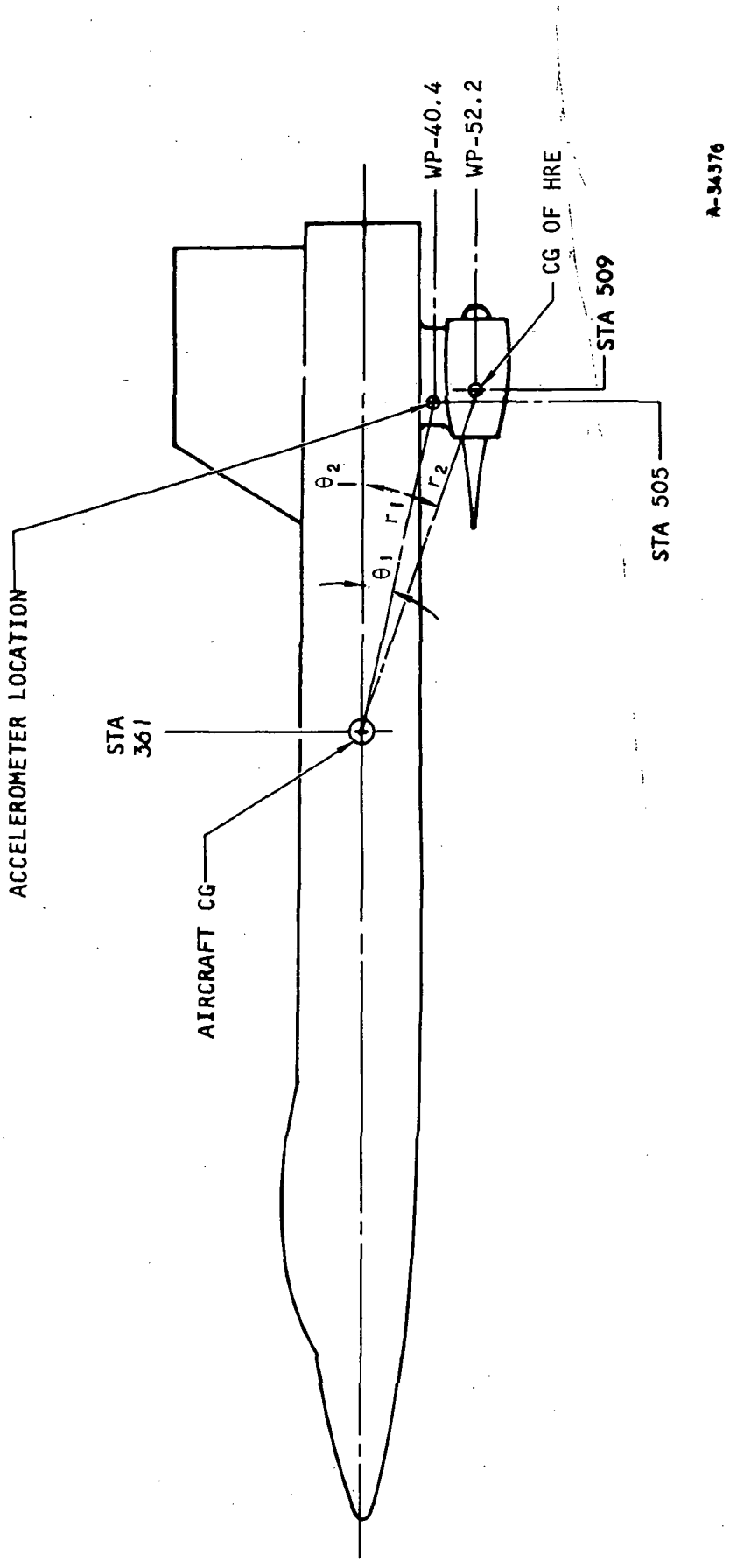

Figure 2.4-9. Accelerometer and HRE Center of Gravity Locations

Multiplying Equation (2.4-24) by W

$$Wa_x = W\ddot{x} + W \sin\theta + W \frac{r_1}{g} \omega^2 \cos\theta_1 + W \frac{r_1}{g} \dot{\omega} \sin\theta$$

then $$T_{int} = Wa_x + T_{ind} + \frac{W}{g} [\omega^2(r_2 \cos\theta_2 - r_1 \cos\theta_1) + \dot{\omega}(r_2 \sin\theta_2 - r_1 \sin\theta_1)] + D_E$$

$$T_{int} = T_{ind} + Wa_x + \frac{W}{g} [\omega^2(r_2 \cos\theta_2 - r_1 \cos\theta_1) + \dot{\omega}(r_2 \sin\theta_2 - r_1 \sin\theta_1)] + D_E$$

Evaluating the bracketed term:

$$\frac{W}{g} [\omega^2(r_2 \cos\theta_2 - r_1 \cos\theta_1) + \dot{\omega}(r_2 \sin\theta_2 - r_1 \sin\theta_1)] =$$

$$= \frac{700}{32.2} \left[\left(\frac{2}{57}\right)^2 (13.27 \times .945 - 12.36 \times .964) + \left(\frac{.2}{57}\right) (13.27 \times .33 - 12.36 \times .27) \right]$$

$$= 21.7 \left[12.3 \times 10^{-4}(.66) + 3.49 \times 10^{-3}(.93) \right]$$

$$= 21.7 \left[8.1 \times 10^{-4} + 3.2.5 \times 10^{-4} \right] = 21.7 \left[40.6 \times 10^{-4} \right]$$

$$= 885 \times 10^{-4} = .08 \text{ lb}$$

This error is negligible. (See Figure 2.4-9.)

2.4.5.3 Misalignment Error

Paragraph 2.4.2.1 of Reference 2-1 gives an expression for the resolved force along the thrust block sensitive axis based on vertical lift force (F_2), acceleration (N_2), and misalignment (angle β). The force to be considered should be the resolved portion of the pin-reaction force shown in Paragraph 2.4.5.1 of this report to be about 3000 lb.

This would give a resolved force of 3000 x .0175 = 52.5 lb/deg. This number is high; alignment to a reference axis should be aimed at better than 1/2 deg (unknown error). Misalignment will also reduce the internal thrust component acting on the block in its sensitive direction but since this error will be small, $(1 - \cos\beta)\, T_{int}$, it can be ignored.

2.4.5.4 Combined Vertical and Axial Loading of Block

The following sketch considers one of the four flexures under the action of the axial load (indicated thrust) and the vertical reaction force.

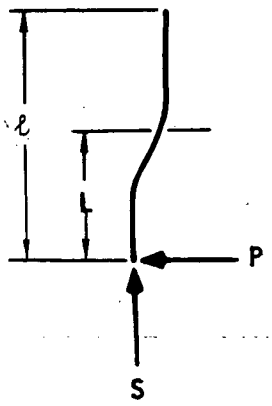

Let K_L = spring constant for portion of flexure, length L

Then from Reference 2-5 $K_L = \frac{EI\pi^4}{64L^3} - \frac{S\pi^2}{16L}$

Substituting $L = \ell/2$

Then $K = \frac{EI\pi^4}{8\ell^3} - \frac{S\pi^2}{8\ell}$

Therefore, error due to ignoring the effect of S is $\frac{S\pi^2}{8\ell} \Big/ \frac{EI\pi^4}{8\ell^3} .100$ percent

$$\text{Error} = \frac{S\ell^2}{EI\pi^2} .100$$

Substituting

$S = 800$ lb [3200 lb ÷ 4] (See Paragraph 2.4.5.1.1)

$I = bd^3/_{12} = \frac{4(.217)^3}{12} = 3.41 \times 10^{-3}$ in.^{4}

$E = 28.5 \times 10^6$

$\ell = 1.38$

Then

Error = 0.16 percent

2.4.6 System Error Analysis

The error in determining the value of the internal thrust has been estimated for several operating conditions. Values of internal thrust, acceleration, drag, etc. have been taken from a table of flight conditions and are summarized in Table 2.4-7, on the following page. The root-sum-square method of error assessment has been used with the derivation of errors as given in both Reference 2-1 and this report. Any discrepancies are considered insignificant, although consideration must be given to assessing the misalignment and resolved force factors. The drag error of 12.5 percent represents the latest

assessment of the drag measurement and is expressed as a percentage of the actual evaluation rather than of full scale.

TABLE 2.4-7

SUMMARY OF FLIGHT CONDITIONS

Internal Thrust, lb	Acceleration (Nx=$\ddot{x}$), g	Drag, lb	Mach No.	Pressure (q_∞), psf	Angle of Attack, deg
5950	-2.0	699	5.0	1800	8.8
4340	-3.0	769	8.0	1800	10.0
3310	-2.0	443	5.0	1800	-1.0
2740	-2.0	397	6.5	1800	-1.0
1900	-2.0	375	8.0	1800	-1.0

The error computations are shown in Tables 2.4-8 through 2.4-12. The error-versus-thrust curve is shown in Figure 2.4-10.

2.4.6.1 Significance of Individual Errors

Relationship Equation (2.4-11) is

$$\epsilon_T = \sqrt{(\epsilon_1\omega_1)^2 + (\epsilon_2\omega_2)^2 + \ldots\ldots(\epsilon_n\omega_n)^2}$$

ϵ_{T_1}, ϵ_1, $\epsilon_2 \ldots \epsilon_n$ are absolute errors (ϵ_T = error in internal thrust)

In terms of percentage of errors

$$e_T = \frac{1}{T_i}\sqrt{(e_1 F_1\omega_1)^2 + (e_2\omega_2 F_2)^2 + \ldots (e_n F_n\omega_n)}$$

F_1, F_2, F_n are the maximum values of the forces associated with e_1, $e_2 \ldots e_n$.

Then

$$\frac{\partial e_T}{\partial e_n} = \frac{1}{T_i}\,\frac{2e_n\omega_n{}^2F_n{}^2 \times \frac{1}{2}}{\sqrt{(e_1F_1\omega_1)^2 + \ldots (e_n\omega_n F_n)^2}}$$

This becomes

$$\frac{\partial e_T}{\partial e_n} = \frac{e_n}{e_T}\left(\frac{F_n}{T_i}\right)^2 \omega_n{}^2 \qquad (2.4\text{-}26)$$

TABLE 2.4-8

ERROR ANALYSIS

Measurand	Full-Scale Error, percent	Maximum Range	Absolute Error	Weighting Factor	Absolute Error Times Weighting Factor (AE·WF)	$\left(\text{Absolute Error Times Weighting Factor}\right)^2$ $(AE \cdot WF)^2$
Indicated thrust	1.1	7000 lb	77 lb	1	77	5940
$\ddot{x}$ (-2 g)						
θ 8.8° sin θ = .153						
$\ddot{x}$ + sin θ = 1.847	1.73	3 g	.0518 g	700	36.3	1320
Weight 700 lb	1.0	700 lb	7 lb	1.847	13	169
Drag #	12.5	700 lb	87.5 lb	1	87.5	7660
Differential thermal expansion	40	125 lb	50 lb	1	50	2500
Misalignment			15 lb	1	15	225
Resolved vertical due to deflection			20 lb	1	20	160
Transferred moment			11 lb	1	11	121
Block thermal effects	1.0	7000 lb	70 lb	1	70	4900
Parallel restraints			5 lb	1	5	25

q_∞ = 1800

M_∞ = 5.0

T_i = 5950

$\Sigma(AE \cdot WF)^2$	23,020
$\sqrt{\Sigma(AE \cdot WF)^2}$	151
Expected error percentage in T_i	2.55

#Error given as percentage of calculated value (includes measurand errors).

TABLE 2.4-9

ERROR ANALYSIS

Measurand	Full-Scale Error, percent	Maximum Range	Absolute Error	Weighting Factor	Absolute Error Times Weighting Factor (AE·WF)	$\left(\text{Absolute Error Times Weighting Factor}\right)^2$ $(AE \cdot WF)^2$
Indicated thrust	1.1	7000 lb	77 lb	1	77	5940
$\ddot{x} = -3$ g						
$\theta = 10^0$; $\sin\theta = .173$						
$\ddot{x} + \sin\theta = -2.83$	1.73	3 g	.0518 g	700	36.3	1320
Weight	1.0	700 lb	7 lb	2.83	20	400
Drag *	12.5	769 lb	96 lb	1	96	9230
Differential thermal expansion	40.0	125 lb	50 lb	1	50	2500
Misalignment			15 lb	1	15	225
Resolved vertical due to deflection			20 lb	1	20	400
Transferred moment			11 lb	1	11	121
Block thermal effects	1.0	7000 lb	70 lb	1	70	4900
Parallel restraints			5 lb	1	5	25

$\Sigma(AE \cdot WF)^2$	25,061
$\sqrt{\Sigma(AE \cdot WF)^2}$	158
Expected error percentage in T_i	3.65

$q_\infty = 1800$

$M_\infty = 8.0$

$T_i = 4340$

*Error given as percentage of calculated value (includes measurand errors).

TABLE 2.4-10

ERROR ANALYSIS

Measurand	Full-Scale Error, percent	Maximum Range	Absolute Error	Weighting Factor	Absolute Error Times Weighting Factor (AE·WF)	$\left(\text{Absolute Error Times Weighting Factor}\right)^2$ $(AE \cdot WF)^2$
Indicated thrust	1.1	7000 lb	77 lb	1	77	5940
$\ddot{x} = -2$ g						
$\theta - 1.0 \sin\theta = -.017$						
$\ddot{x} + \sin\theta = 2.017$	1.73	3 g	.0518 g	700	36.3	1320
Weight	1.0	700 lb	7 lb	2.017	14	196
Drag #	12.5	443 lb	55 lb	1	55	3250
Differential thermal expansion	40	125 lb	50 lb	1	50	2500
Misalignment			15 lb	1	15	225
Resolved vertical due to deflection			10 lb	1	10	100
Transferred moment			11 lb	1	11	121
Block thermal effects	1	7000 lb	70 lb	1	70	4900
Parallel restraints			5 lb	1	5	25

$q_\infty = 1800$	$\Sigma(AE \cdot WF)^2$	18,577
$M_\infty = 5.0$	$\sqrt{\Sigma(AE \cdot WF)^2}$	136
$T_i = 3310$		
	Expected error percentage in T_i	4.11

#Error given as percentage of calculated value (includes measurand errors).

TABLE 2.4-11

ERROR ANALYSIS

Measurand	Full-Scale Error, percent	Maximum Range	Absolute Error	Weighting Factor	Absolute Error Times Weighting Factor (AE·WF)	$\left(\text{Absolute Error Times Weighting Factor (AE·WF)}\right)^2$
Indicated thrust	1.1	7000 lb	77 lb	1	77	5940
$\ddot{x} = -2$ g						
$\theta = -1.0 \sin\theta = -.017$						
$\ddot{x} + \sin\theta = -2.017$	1.73	3 g	.0518 g	700	36.3	1320
Weight	1.0	700 lb	7 lb	2.017	14	196
Drag*	12.5	397 lb	49.5 lb	1	49.5	2460
Differential thermal expansion	40	125 lb	50 lb	1	50	2500
Misalignment			15 lb	1	15	225
Resolved vertical due to deflection			10 lb	1	10	100
Transferred moment			11 lb	1	11	121
Block thermal effects	1	7000 lb	70 lb	1	70	4900
Parallel restraints			5 lb	1	5	25
					$\Sigma(AE \cdot WF)^2$	17,787
					$\sqrt{\Sigma(AE \cdot WF)^2}$	133
					Expected Error Percentage in T_i	4.86

$q_\infty = 1800$

$M_\infty = 6.5$

$T_i = 2740$

*Error given as percentage of calculated value (includes measurand errors).

TABLE 2.4- 12

ERROR ANALYSIS

Measurand	Full-Scale Error, percent	Maximum Range	Absolute Error	Weighting Factor	Absolute Error Times Weighting Factor (AE·WF)	$\left(\text{Absolute Error Times Weighting Factor}\right)^2$ $(AE \cdot WF)^2$
Indicated thrust	1.1	7000 lb	77 lb	1	77	5940
$\ddot{x} = -2$ g						
$\theta = -1.0 \sin \theta = -.017$						
$\ddot{x} + \sin \theta = -2.017$	1.73	3 g	.0518 g	700	36.3	1320
Weight 700 lb	1.0	700 lb	7 lb	2.017	14	196
Drag *	12.5	375 lb	46.9 lb	1	46.9	2200
Differential thermal expansion	40	125 lb	50 lb	1	50	2500
Misalignment			15 lb	1	15	225
Resolved vertical due to deflection			10 lb	1	10	100
Transferred moment			11 lb	1	11	121
Block thermal effects	1	7000 lb	70 lb	1	70	4900
Parallel restraints			5 lb	1	5	25
					$\Sigma(AE \cdot WF)^2$	17,527
					$\sqrt{\Sigma(AE \cdot WF)^2}$	132
					Expected Error Percentage in T_i	6.95

$q_\infty = 1800$

$M_\infty = 8$

$T_i = 1900$

*Error given as persentage of calculated value (includes measurand errors.

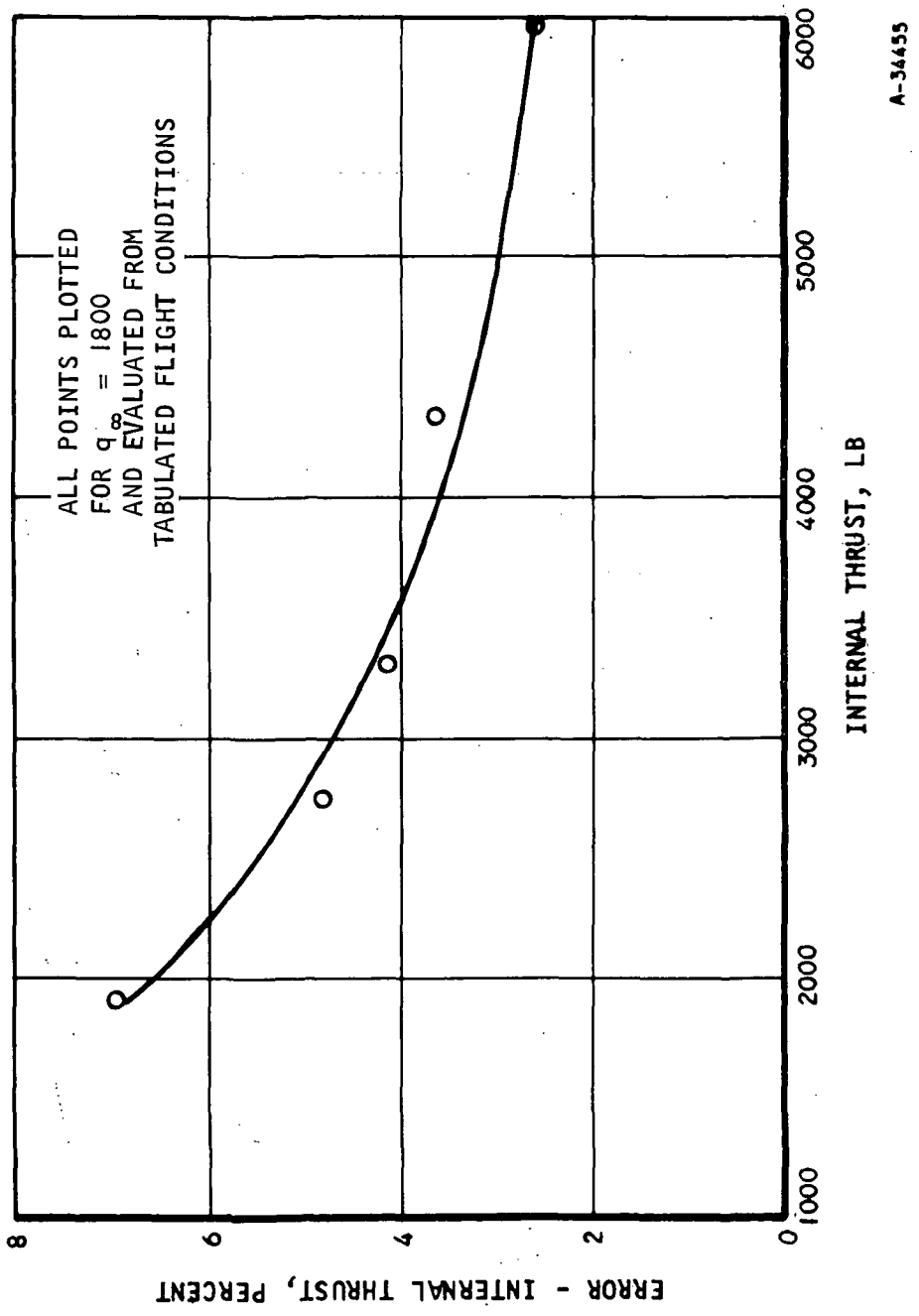

Figure 2.4-10. Error - Internal Thrust

The important errors are treated in Table 2.4-13. (For the condition T_{int} = 5950 lb, error in T_{int} = 2.55 percent, see Table 2.4-8). In Table 2.4-13, the figure of importance is defined as

$$\frac{\text{Error percent full-scale}}{\text{Error in source equivalent to 1 percent in } T_{int}}$$

On this basis, the error source are listed in order of importance

Drag	0.84
Indicated thrust	0.65
Block thermal effects	0.40
Differential thermal expansion	0.28
Acceleration	0.14

Note for T_{int} = 5950 only

2.4.7 Rear and Parallel Suspensions

The differential thermal expansion between the engine and the wishbone causes a deflection of the thrust-block flexures corresponding to an estimated force of 125 lb (see Reference 2-1, Paragraph 2.4.2.2). This force is significant and must be accounted for to within an error consistent with the desired accuracy of the internal thrust measurement. The less-stiff rear supports will undergo more deflection than the thrust block under the expansion force. During ground testing, this deflection will be measured with reference to the differential temperature. However, the structural behavior of the pylon, wishbone, and engine support; together with the uncertainty of the parallel stiffnesses of fuel lines, cables, etc., and of the temperature differential during flight, present difficulties in accurate correlation. Thus, if possible, parallel stiffnesses should be reduced to a level that allows 40 to 50 percent of this thermal force to be treated as an error in the internal thrust calculation.

Currently, analysis is in progress toward the design of the wishbone and rear-support system and a figure of 1000 lb/in. has been stipulated for all parallel stiffnesses.

Forces generated by the action of flow through the fuel pines are inputs to the thrust block and must be evaluated by testing.

TABLE 2.4-13

ERROR ANALYSIS

Error Source	Error, percent full-scale	Full-Scale Value $(min)^2$	Weighting Factor	$\partial_{eT}/\partial_{en}$	Error in Source, Corresponding to 1 Percent in T_{int}	Figure of Importance
Acceleration	1.73	3 g	700	0.084	12	0.14
Drag	12.5	700	1	0.067	15	0.84
Weight	1.0	700	1	0.010	100	0.01
Differential thermal expansion	40	125	1	0.007	140	0.28
Block thermal effects Misalignment	1.0	5950	1	0.39	2.5	0.40
Indicated thrust	1.1	7000	1	0.6	1.7	0.65

2.5 FABRICATION AND MATERIALS

2.5.1 Thrust Deflection Block

The recommended material for the block is 17-4PH in the 1025 heat-treated condition. This material is strong and corrosion resistant. After fabrication, heat treating to 1025°F gives optimum strength and ductility. To ensure freedom from microporosities, vacuum remelt is recommended. By reducing the oxygen content, this process also improves the cleanliness and reduces the hydrogen values by more than 300 percent. These reductions improve the elongation and reduction of area figures and increase the fatigue resistance. Vacuum remelt will be called out for the flight-type thrust block, but development of the item will proceed using a block of certificated steel that is subject to radiographic inspection. Although the design of the block calls for accurate machining, no problems are anticipated in fabrication. It is important that all four flexures are parallel and have the same spring constant. If this requires correction (for example, honing), a small difference in the nominal flexure thickness could be tolerated, although it is to be borne in mind that the thickness parameter operates as a square power in the stress relationship.

2.5.2 Capacitor Assembly

2.5.2.1 Capacitor Outerplate Support

To prevent the ingress of water, it is necessary to impregnate the capacitor outerplate support (manufactured from ceramic Alsimag 447). The technique used dehydrates and impregnates with Dow-Corning Silicone Varnish 997 applied per AiResearch Specification SR 152. This will allow for bonding by epoxy without detriment to the sealing. The inserts for securing to the block and the Invar outer plates will be bonded to the support using Expoxylite 5524. Special fixtures will be used to locate the inserts and plates during bonding; these items will be machined prior to assembly. The fixtures are expected to give the required tolerances or location and parallelism.

2.5.2.2 Diode Assembly

The diodes will be held in contact with the tabs on the capacitor outer plates through folded 80-mesh pads of platinum-iridium or gold-brass by means of coil springs. Epoxy will be used to retain the spring pressure pads and to contain the wiring leads

2.5.2.3 Fabrication

Capacitor outerplate supports have been fabricated (by America Lava Company); fabrication of the inserts and outer plates is in process.

2.5.3 Thrust Block Assembly Test Fixtures

Modification to the design of these fixtures to be used in the static load tests, temperature tests, and frequency response tests has been initiated. The design of a test fixture for vibration testing of the full-scale component engine to which the development prototype thrust block will be fitted also has started.

2.6 FUTURE ACTION

2.6.1 Heat Shield - Temperature Control

The feasibility and design concepts for using a heat shield to limit the temperature gradients within the block assembly is being studied. To evaluate the heat transfer and temperature distribution on the new block design, a revised heat analysis has been initiated. This analysis early development testings and interface restrictions affect the design of the temperature control system.

2.6.2 Electromagnetic Interference Shield

After the physical model has been tested, an electromagnetic (EMI) shield will be fitted to the block. The design of such a shield must not restrain the block in its operating direction. To prevent water from entering during ascent, however, the design of this shield may need to include a method of sealing the block cavity that houses the capacitor.

2.6.3 Development Plan

Immediate revision of the development plan is required to cover the new block design, temperature gradient effects, sealing of capacitor outer support, combined three-axial loading of the block, temperature control, and establishing of the accelerometer design.

3.0 GAS SAMPLING SUBSYSTEM

The gas sampling subsystem is designed to indicate the composition of the combustion gases. This subsystem is only to be used during ground tests in support of the 2 in. by 6 in. combustor development testing and Phase II boilerplate engine testing.

The gas sampling subsystem design effort is divided into two separate areas; the analyzer, and the probe. Each is discussed in Paragraph 3.1 and 3.2, respectively. The analyzer determines the composition of the gas received from the probe. The probe is used to capture a representative sample of gas from the supersonic combustion stream, reduce its velocity to subsonic speeds, and feed a continuous sample into the analyzer.

3.1 ANALYZER

3.1.1 Problem Statement

The NASA Statement of Work requires an analysis of the gases captured by the gas sampling probe to determine the extent hydrogen mixes into the main airstream.

The analyses are to be restricted to hydrogen, oxygen, nitrogen, and water vapor with direct readouts in volume percent or sufficient information to calculate the volume percents.

3.1.2 Topical Background

The Hypersonic Research Engine Program requires an on-line gas analysis capability for supersonic combustion tests. To fulfill this requirement, a sample will be taken from a burning hydrogen and air mixture, cooled, and then analyzed for H_2, O_2, H_2O, and N_2 species, which are expected to comprise at least 97 percent of the sample. From the resulting information, the atomic balance of hydrogen, nitrogen, and oxygen will be determined. It can then be determined if the hydrogen content increases due to hydrogen and air mixing in the combustor.

3.1.3 Overall Approach

The percentage of O_2, N_2, H_2O, and H_2 will be measured. During the 2-in. by 6-in. combustor and the Phase II boilerplate engine tests, all four gases will be measured, as independent percentages, with a mass spectrometer.

The mass spectrometer admits gas species, ionizes them, and sorts the ions on the basis of their mass-to-charge ratio. By inspection of the

oscillograph record, the resolution for all gases is about 0.5 percent. Because the scale is expanded the resolution of the oxygen content is about 0.1 percent.

The zero drift is determined by observing the oxygen or water vapor content when the sample contains neither of these gases. Although zero values range from -0.5 to +0.5, the zeros frequently repeat. On this basis, the zero drift is less than ±0.5 percent of full scale in 30 min.

The span drift is determined by observing the full-scale displacements of pure gases. Although the pretest calibration was not recorded, it is assumed to be exact. By observing the water vapor column (Table 3.1-1), the span drift is -1.0 percent in 30 min. By observing the hydrogen column of the same table, the span drift is -0.7 percent in 20 min. More data points on reading 100-percent gases are needed to obtain more confidence in these values. The minus 0.5 percent represents resolution errors and possible zero drift.

The accuracy is obtained by comparing the reported percentages with the percentages listed under the column "Composition as Indicated by Previous Analysis." The values in the column are a composite of values shown by the vendor's analyzed contents, and cross checks made by the writer. By referring to Table 3.1-1 and observing data point 2, it is seen that the values mismatch by 0.0 and 0.5 percent (percent of full scale). By observing data point 5, values mismatch by 0.2 and 0.7 percent. By observing data point 7, one value mismatches by being low 1.7 percent and the second by being high 1.5 percent. By observing data point 8, values mismatch by 0.2 and 0.3 percent. The calibration gas used in data point 7 should be rechecked. The resolution of the data from the oscillograph is such that the other mismatches may be due to resolution error of the oscillograph records; therefore, no recommendation is made that the mismatches be explained.

3.1.4 Experimental Effort

A test was performed to experimentally determine the resolution, drift, and accuracy of the Mass Spectrometer Gas Analysis Subsystem. During this test, a prerun calibration was made and a simulated test run was made. The time required for this test run was estimated to be more than 30 min.

During the pretest calibration, 100-percent span and zero gases were used to set the zero position and 100-percent span position (on the oscillograph, 10 cm = 100 percent) for each of the 4 channels, H_2, H_2O, N_2 and O_2. Helium was sometimes used as a zero gas for all channels. The calibration gases were admitted into the system by the scaning valve. Some mixed and some pure gases were used during the test run. The gold-leak pressure in each case was manually adjusted to 2.5 mm Hg before readings were taken. The information shown in Table 3.1-1 uses the last values determined for each data point. Table 3.1-2 shows all the data for each data point.

TABLE 3.1-1

GAS COMPOSITION FROM OSCILLOGAPH RECORD

Data Point Number	Composition As Indicated By Previous Analyses	Oscillograph Indicates Following Composition				
		Oxygen, O_2	Nitrogen, N_2	Water Vapor, H_2O	Hydrogen, H_2	Total, percent
1	100 percent N_2	0	100.0	0	0	100.0
2	51.5 percent N_2, 48.5 percent H_2	0	51.5	0.5	49.0	101.0
3	100 percent H_e	0	0.5	0.0	0.0	0.5
4	100 percent H_2	0	-0.5	-0.5	100.0	99.0
5	76.2 percent N_2, 23.8 percent H_2*	0.0	76.0	0.5	24.5	101.0
6	100 percent H_e	0	0.5	0	0	0.5
7	75.5 percent N_2, 24.4 percent O_2, 0.1 percent H_2	22.7	77	-0.5	-0.5	98.7
8	95.3 percent N_2, 4.7 percent O_2*	4.9	95.0	0	0.5	100.4
9	100 percent H_e	0	1 percent	0.5	0	1.5
10	100 percent H_2O	0	0	99.0	1.0	100.0

Reference: First Interim Technical Data Report AP-67-2203, dated 7 June 1967, page 3-23

*Simulated Test Run Data Summary of January 15, 1968

TABLE 3.1-2

SIMULATED TEST RUN DATA, COMPLETE JANUARY 15, 1968

Data Print Number	Composition As Indicated By Previous Analysis	Oscillograph Indicates Following Composition				
		Oxygen, O_2	Nitrogen, N_2	Water Vapor, H_2	Hydrogen, H_2	Total, percent
1	100 percent N_2	0	99.5	0	0	
		0	100.0	0	0	
		0	100.0	0	0	
		0*	99.8*	0*	0*	Total 99.8
2	51.5 percent N_2, 48.5 percent H_2	0	52.0	0.5	48.5	
		0	52.5	0.5	48.5	
		0	51.5	0.5	50.0	
		-	-	0.5	49.0	
		-	-	-	49.0	
		0*	52.0*	0.5*	49.0*	Total 101.5
3	100 percent H_e	0.0	0.5	0.0	0.0	
		0.0*	0.5*	0.0*	0.0*	Total 0.5
4	100 percent H_2	0	-0.5	-0.5	98.5	
		-	-	-	100.0	
		0*	-0.5*	-0.5*	99.3*	Total 98.3
5	23.6 percent H_2, 74.6 percent N_2	0.5	79.0	0.5	24.5	
		0.5	77.5	0.5	24.0	
		0.0	76.0	0.5	25.5	
		-	-	0.5	24.5	
		0*	77.5*	0.5*	24.6*	Total 102.6
6	100 percent H_e	0	0	-0.5	2.0	
		0	0	-0.5	0	
		0	1.0	0	-	
		0	0.5	0	0	
		0*	+0.4*	-0.25*	0.7*	Total 0.9
7	75.6 percent N_2	22.7	77	0	0.0	
	2.4.4 percent O_2	22.1	75	-0.5	-1.0	
		22.7	77	-0.5	-0.5	
		22.5*	76.3*	-0.3*	-0.5*	Total 98.0
8	95.4 percent N_2, 4.6 percent O_2	4.9	93.5	0	0	
		4.9	93.5	0	-	
		4.9	95.0	0	0.5	
		4.9	-	-	0.5	
		4.9*	94.0*	0*	0.3*	Total 99.2
9	100 percent H_e	0	1.0 percent	0.5	0	
		0*	1.0*	0.5*	0*	Total 1.5
10	100 percent H_2O	0.5	0	101	1.0	
		0.0	0	98.5	1.5	
		0.0	0	99	0.5	
		-	-	-	-	
		0.2*	0*	99.5*	1.0*	Total 100.7

*Average values

3.2 GAS SAMPLING/TOTAL-PRESSURE PROBE

3.2.1 Problem Statement

A device is needed to collect and distribute a sample of gas from the internal supersonic flow field of a hypersonic ramjet engine. The device must collect a representative sample from the gas stream, and must preserve the atomic balance of the constituents of the sample. The operating environments for this device in the effluent gases of an oxygen-hydrogen burner include temperatures to about 5800°R and velocities to about Mach 3. The device must be suitable for installation and use in both a fixed and traversing mode in a variety of test configurations associated with a hypersonic ramjet engine and component test program.

3.2.2 Topical Background

To determine oxygen-hydrogen combustor performance and how this performance is influenced by the injector geometry, jet penetration, and spreading; a probe must ascertain the mixing of the effluent gases at several points in the combustor. If the probe is too large, it will block the combustor flow and choke it. To have sufficient life, the probe and its support must be cooled.

The gas mixture will be sampled during component and engine tests. The main objective will be to determine the mixing efficiency of the hydrogen fuel and the airstream. To evaluate the extent of mixing, the atomic balances must be known. This approach is based on the consideration that the combustor performance is mixing limited in the supersonic combustion regime of greatest interest.

3.2.3 Overall Approach

It is difficult to get gas samples from a supersonic H_2-Air combustor. Cooling requirements for the probe and its support, plus the necessity for providing a coolant return that will exclude the addition of H_2O to the combustor flow, dictate a complex design. Other major problems include capturing a truly representative sample of the combustion gases from any desired point in the combustor and preserving its atomic balance while transporting it to a mass spectrometer for analysis.

To capture a representative sample of the gas stream, the detached bow shock which exists around the leading edge of any body immersed in a supersonic stream must be attached to the probe inlet. This prevents the segregation of the sample due to inlet spillage, and the deflection of the lighter mass particles away from the inlet that would occur in the subsonic region behind the shock. Maintaining the composition of the sample is limited to preserving its atomic balance of H_2, O_2, N_2, and H_2O. To preserve the atomic balance, the water vapor in the sample must not be allowed to condense on the walls of the probe or tubing that transports the sample to the gas analyzer.

With the above requirements and constraints, a preliminary design for a gas sampling probe was made and analyzed to ensure adequate cooling, structural integrity, ease of fabrication, and satisfactory aerodynamic performance.

3.2.4 Gas Sampling Probe Status

Fabrication has been successfully completed on both probes for the combustor test rig. The following calibration and development tests have been successfully completed:

Proof pressure and leak tests

Coolant circuit ΔP measurements over required range of flow rates

Gas flow measuring section calibration

System test with probe tip inserted in a "cold" supersonic stream of two molecularly mixed gases at a known mixture ratio. (Gas analyzer results indicated that the probe captured a sample of the gases of the same mixture ratio.)

Calibration tests of the turbine-type coolant flowmeters on distilled water at 70^0 and 200^0F.

Two tests are planned for the future. The first test will verify the cooling system design by exposing the entire probe to hot-gas conditions and comparing the actual coolant ΔT's with the predicted values. The second test will determine the range of probe back-pressure to stream total-pressure ratios as a function of the stream Mach number and specific heat ratio at which the bow shock, as an upper limit, will remain attached; and as a lower limit, will be on the verge of being completely swallowed. This test will be performed using cold air and a Schlieren system for viewing the shock.

3.2.5 Analytical Design

The following paragraphs contain the results and a discussion of the analysis for determining the effect of the bow shock at the probe tip on the flow field and the heat transfer coefficient.

3.2.5.1 Summary and Results

In addition to its primary function, the gas sampling probe, whose dimensions and cooling systems are shown in Figure 3.2-1 of Reference 3-1, may be used as a calorimetric-temperature-measuring device. This is accomplished by measuring the rise in coolant temperature for both cases of the internal gas flow on and off, and analyzing the energy level of the gas samples taken when the internal gas flow is on. This technique of measuring the energy or enthalpy level of the hot-gas stream requires the existence of a negligible difference between the heat loads on the external surface of the probe when the internal gas flow is on or off.

This analysis compares these external heat loads for presumably "worst" hot-gas conditions. Figure 3.2-1 shows the flow models for both cases of internal flow on and off. Since the higher the upstream Mach number, the stronger the bow shock in front of the probe, and the larger the difference in aerodynamic conditions between the two cases, the highest Mach number probe position was chosen along with the highest heat-flux conditions.

Based on the aerodynamic conditions along the probe surface for the selected upstream conditions, as shown in Figure 3.2-1, heat transfer calculations were made on the external surface of the probe for both cases. The results show that even though the difference in heat loads is about 7.7 percent for the cone section, the heat loads and coolant ΔT rise between the two cases differ by about 2.4 percent for an overall probe length of 12 in. This indicates that the shorter the cone section with respect to the overall probe length, the smaller the difference in the external heat load between the two cases.

3.2.5.2 External Heat Loads

Basic heat transfer equations used in the present study are:

$$Nu_x = c_1 \, Re_x^{\,n} \, Pr^{1/3}$$
$$Nu_L = c_2 \, Re_L^{\,n} \, Pr^{1/3} \qquad (3.2\text{-}1)$$

where c_1, c_2, and n are functions of the flow geometry with values as shown below.

Flow geometry	C_1	C_2	n
Laminar cone flow	0.575	0.767	0.5
Laminar flat plate flow	0.332	0.664	0.5
Turbulent flat plate flow	0.0296	0.036	0.8

The properties are to be evaluated at a reference temperature of

$$T^* = 0.28T + 0.22T_{ad} + 0.5\,T_w \qquad (3.2\text{-}2)$$

Based on static properties at X_s, the Reynolds number at the end of the cone section is

$$Re_{X_s} = \frac{\rho V X_s}{\mu} = \frac{55 \times 1.765}{0.375 \times 10^{-4} \times 12} = 2.16 \times 10^5$$

Since this is less than the transition Reynolds number of about 10^6, the flow over the cone should be laminar. The use of Equation (3.2-1) with the appropriate coefficients gives the following heat load on the cone for both cases of internal flow on and off.

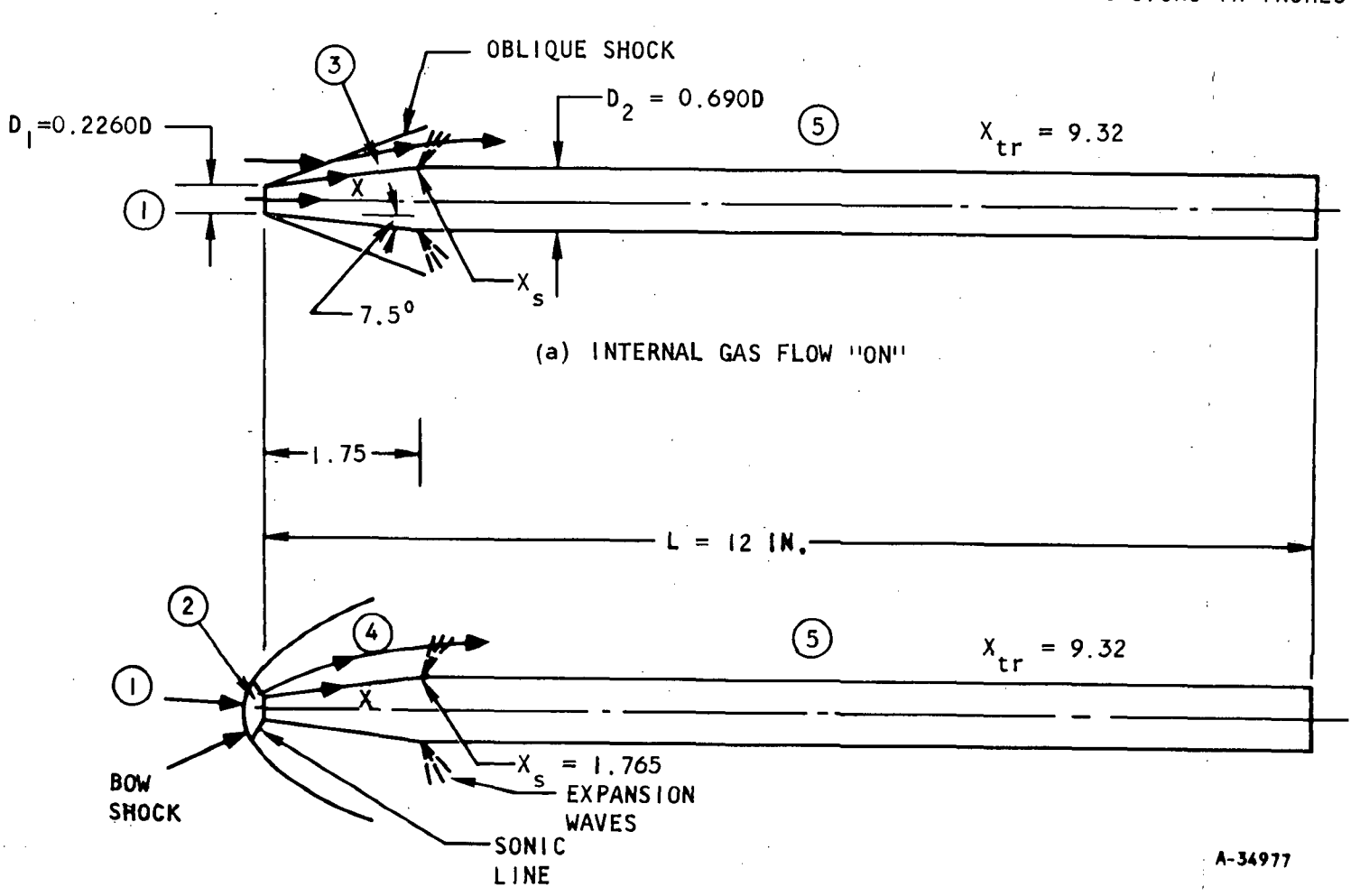

Figure 3.2.1. Flow Models and Aerodynamic Conditions

$$q_{ON(cone)} = Am_3^{0.5} X_s^{0.5} \quad (3.2\text{-}3)$$

$$q_{OFF(cone)} = Bm_4^{0.5} X_s^{0.5} \quad (3.2\text{-}4)$$

where

$$A = 0.767 \times \pi \times \frac{D_1 + D_2}{2} \times Pr^{-2/3} \mu^{1/2} (H_{ad} - H_w) \quad (3.2\text{-}5a)$$

with properties evaluated at T_3*.

$$B = 0.767 \times \pi \times \frac{D_1 + D_2}{2} \times Pr^{-2/3} \mu^{1/2} (H_{ad} - H_w) \quad (3.2\text{-}5b)$$

with properties evaluated at T_4*.

The transition point from laminar to turbulent flow occurs at $x = x_{tr} = 9.32$ in. with the transition Reynolds number of 10^6. This divides the flow over the cylindrical portion of the probe into two regions: the laminar region up to $x = x_{tr} = 9.32$ in., and the turbulent region thereafter. The use of flat-plate heat-transfer Equation (3.2-1) yields the following heat load on the cylindrical portion of the probe.

$$q_{ON(cylinder)} = q_{OFF(cylinder)}$$

$$= CM_5^{0.5} (X_{tr}^{0.5} - X_s^{0.5}) + DM_5^{0.8} (L^{0.8} - X_{tr}^{0.8}) \quad (3.2\text{-}6)$$

where

$$C = 0.664 \times \pi \times D_2 \times Pr^{-2/3} \times \mu^{1/2} \times (H_{ad} - H_w) \quad (3.2\text{-}5c)$$

$$D = 0.036 \times \pi \times D_2 \times Pr^{-2/3} \times \mu^{0.2} \times (H_{ad} - H_w) \quad (3.2\text{-}5d)$$

with properties evaluated at T_5*.

By adding Equation (3.2-2) or (3.2-4) to Equation (3.2-6) the total heat load on the external surface of the probe is obtained.

$$q_{T,ON} = AM_3^{0.5} X_s^{0.5} + CM_s^{0.5} (X_{tr}^{0.5} - X_s^{0.5}) + DM_5^{0.8} (L^{0.8} - X_{tr}^{0.8}) \quad (3.2\text{-}7)$$

$$q_{T,OFF} = BM_4^{0.5} X_s^{0.5} + CM_5^{0.5} (X_{tr}^{0.5} - X_s^{0.5}) + DM_5^{0.8} (L^{0.8} - X_{tr}^{0.8}) \quad (3.2\text{-}8)$$

Therefore,

$$\frac{q_{T,OFF}}{q_{T,\ ON}} = \frac{BM_4^{0.5} X_s^{0.5} + CM_5^{0.5} (X_{tr}^{0.5} - X_s^{0.5}) + DM_5^{0.8} (L^{0.8} - X_{tr}^{0.8})}{AM_3^{0.5} X_s^{0.5} + CM_5^{0.5} (X_{tr}^{0.5} - X_s^{0.5}) + DM_5^{0.8} (L^{0.8} - X_{tr}^{0.8})} \tag{3.2-9}$$

In terms of dimensionless quantities, Equation (3.2-9) may be written

$$\frac{q_{T,OFF}}{q_{T,ON}} = \frac{1}{Y_1} + \frac{1}{Y_2} + \frac{1}{Y_3} \tag{3.2-10}$$

where

$$Y_1 = \left(\frac{A}{B}\right)\left(\frac{M_3}{M_4}\right)^{0.5} + \left(\frac{C}{B}\right)\left(\frac{M_5}{M_4}\right)^{0.5} \left[\left(\frac{X_{tr}}{X_s}\right)^{0.5} - 1\right] + \left(\frac{D}{B} M_4^{0.3} X_s^{0.3}\right)\left(\frac{M_5}{M_4}\right)^{0.8} \left[\left(\frac{L}{X_s}\right)^{0.8} - \left(\frac{X_{tr}}{X_s}\right)^{0.8}\right] \tag{3.2-11a}$$

$$Y_2 = \frac{1}{\left(\frac{C}{A}\right)\left(\frac{M_5}{M_3}\right)^{0.5}\left[\left(\frac{X_{tr}}{X_s}\right)^{0.5} - 1\right]} + 1 + \frac{1}{\left(\frac{C}{DM_5^{0.3} L^{0.3}}\right)\left[\left(\frac{X_{tr}}{L}\right)^{0.5} - \left(\frac{X_s}{L}\right)^{0.5}\right]} - \frac{1}{\left(\frac{C}{DM_5^{0.3} X_{tr}^{0.3}}\right)\left[1 - \left(\frac{X_s}{X_{tr}}\right)^{0.5}\right]} \tag{3.2-11b}$$

$$Y_3 = \frac{1}{\left(\frac{D}{A} M_3^{0.3} X_s^{0.3}\right)\left(\frac{M_5}{M_3}\right)^{0.8}\left[\left(\frac{L}{X_s}\right)^{0.8} - \left(\frac{X_{tr}}{X_s}\right)^{0.8}\right]} + \frac{1}{\left(\frac{D}{C} M_5^{0.3} X_{tr}^{0.3}\right)\left[\left(\frac{L}{X_{tr}}\right)^{0.8} - 1\right]} - \frac{1}{\frac{D}{C} M_5^{0.3} X_s^{0.3}\left[\left(\frac{L}{X_s}\right)^{0.8} - \left[\left(\frac{X_{tr}}{X_s}\right)^{0.8}\right]\right]} + 1 \tag{3.2-11c}$$

Since changes of properties are not appreciable compared with changes of M from region 3 or 4 to region 5 , properties may be evaluated at a reference temperature of $T^* = 0.28 \times 3243^0R + 0.22 \times 5400 + 0.5 \times 800 = 2500^0R$ from Equation (3.2-2) where the static temperature was averaged in the whole flow field, the adiabatic wall temperature was approximately equated to the total gas temperature and the wall temperature of 800^0R was assumed.

Then

$$\left.\begin{aligned} A &= B \\ \frac{C}{A} &= \frac{C}{B} = \frac{1.73}{1 + \frac{D_1}{D_2}} \\ \frac{D}{B} M_4^{0.3} X_s^{0.3} &= \frac{0.0426}{1 + \frac{D_1}{D_2}} \times \left(\frac{M_4 X_s}{\mu^*}\right) \\ \frac{C}{DM \rho_s^{0.3} L^{0.3}} &= 18.4 \times \left(\frac{\mu^*}{M_5 L}\right)^{0.3} \end{aligned}\right\} \quad (3.2\text{-}12)$$

and Y_1, Y_2 and Y_3 contain probe dimensions and M_3, M_4 , and M_5 which are all shown in Figure 3.2-1. Substitution of appropriate values into Equations (3.2-10), (3.2-11a), (3.2-11b), (3.2-11c) finally yields

$$\frac{q_{T,OFF}}{q_{T,ON}} = 1.024$$

This shows the heat loads on the external surface of the probe with the internal gas flow on and off differing by 2.4 percent.

A comparison of the heat loads on the cone surface alone gives

$$\frac{q_{OFF}(cone)}{q_{ON}(cone} = \left(\frac{M_4}{M_3}\right)^{0.5} = 1.077$$

If the probe consisted of the cone section alone, the heat load on the external surface of the probe with the internal gas off would be 7.7 percent greater than that with the internal gas flow on.

3.2.6 Design Effort

No further design effort was performed during this reporting period.

3.2.7 Manufacturing

Primary effort during this reporting period was directed toward the fabrication of the backup gas-sampling probe that was completed during December 1967.

3.2.8 Testing

The preliminary tests that were performed on the initial probe and outlined in Reference 3-1 were also successfully performed on the backup probe.

3.2.9 Future Action

To demonstrate mechanical integrity of the probe, adequate cooling, freedom from flutter, and verification of tip design development tests will be performed. Calibration tests will be performed on the entire gas analyzing system and on the probe to determine the backpressure necessary to attach the bow shock over the required operating range of stream Mach numbers.

4.0 ENGINE GAS TEMPERATURE MEASUREMENT

The measurement of engine gas temperatures may be made by the double-sonic orifice, the calorimetric, or the thermocouple-type total-temperature probe. These three probes have different applications.

Total temperature must be determined in two distinct areas: the free-stream or uncontaminated flow, and the exhaust flow from the engine proper.

With exhaust flow, either the exhaust products may be fully reacted in equilibrium, or combustion may be incomplete. In addition, the exhaust temperature of the engine is influenced by the method of cooling the structure. In a regeneratively cooled system, there is no energy deficiency in the exhaust and the heat of reaction appears in total temperature of the exhaust. In a water-cooled system, there is an energy deficiency equal to the temperature rise of the coolant. This energy deficiency results in a decrease in the exhaust total temperature from that computed for the ideal case (even assuming 100-percent combustion).

For freestream measurement, or measurement of the exhaust temperature for the water-cooled case (assuming 100-percent combustion efficiency), thermocouples, double-sonic orifice probes, and calorimetric probes are applicable. For a water-cooled system, an average mixed temperature may be calculated from knowledge of the energy removable from the system, but the temperature profile is unobtainable by this method. Thermocouples, double-sonic orifice probes, and calorimetric methods are applicable for determining the total temperature and for checking the energy balance between the engine stream and the water jackets. As in the freestream case, selection of the probe should be based on accuracy requirements and/or life.

The double-sonic orifice probes and the calorimetric probe techniques are not applicable for incomplete combustion. Since it is not possible to quench the reactions within these probes, there will be an inherent error that cannot be adequately evaluated. The thermocouple, however, is suitable for this measurement. Since the transient flow over the thermocouples is small there will be little reaction over that which would be normally occuring. Therefore the thermocouple appears capable of determining the exhaust temperature in a flow where combustion is incomplete.

Present state-of-the-art techniques are adequate for measuring gas temperatures up to 3200^{0}F. All three measurement techniques (thermocouple, calorimetric, and couble-sonic orifice) are reasonable methods for determining temperatures higher than 3200^{0}R for the HRE Project.

The total-temperature thermocouple is discussed in Paragraph 4.1 and the double-sonic orifice probe is discussed in Paragraph 4.2.

4.1 TOTAL-TEMPERATURE THERMOCOUPLE

4.1.1 Problem Statement

The objective of the total-temperature thermocouple program is the development of a thermoelectric device of sufficient accuracy and life to determine engine exhaust total temperatures and engine inlet total temperature.

The major areas of concern are the response, accuracy, and life of the thermocouple. The thermocouples operate in atmospheres ranging from oxygen-rich (oxidizing) to oxygen-poor (reducing).

(a) Thermocouple materials ideally suited for the task are not available. Available thermocouple materials have a limited life in such a hostile operating environment and improved models are desired.

(b) Methods are required to reduce the thermocouple uncertainty errors associated with the hot-gas probe heat-transfer mechanisms during the variable gas flow conditions.

4.1.2 Topical Background

Investigations show that the tungsten on tungsten and 26-percent rhenium combination have the overall characteristics best suited to the HRE task. Coatings are frequently applied to tungsten and tungsten alloys to increase its resistance to oxidation at high temperatures. Coatings are discussed in Paragraph 4.1.7.

Iridium versus iridium-rhodium alloy (Ir/Ir Rh) combinations can operate in oxidizing environments for longer periods and show promise in application where the actual junction temperature is purposely lowered by using a design where heat is removed from the junction by radiation and conduction.

4.1.3 Overall Approach

To assure sufficient probe life for the application, the total-temperature thermocouple task combines materials and developes fabrication techniques. This approach must consider the necessity of certain forced tradeoffs of objectives due to the severe operating environment for the sensor.

A test facility is available for the thermocouple development program. The following approximate gas temperatures can be obtained with the energy available for sensor testing: 5600°F with an oxygen and hydrogen combination; 4700°F with a hydrogen and air combination, and more than 5600°F with an oxygen and acetylene combination. The gas mixtures can be controlled to permit a broad range of temperatures and conditions. Supporting equipment includes strip chart recorders, a radiometer, an optical pyrometer, and other temperature-measuring equipment. Although this facility cannot duplicate all the operational engine conditions that the probe will encounter, it does provide the means to subject sensors to heat fluxes and temperature levels similar to those encountered in actual service.

4.1.4 Overall Status

During the past quarter, it has been decided that a total-temperature thermocouple probe will be developed for measuring engine inlet total temperature.

To aid in design optimization, the probe shown in Figure 4.1-1 will be tested in various configurations at the test facility for thermocouple development. This particular probe will be evaluated for:

(a) Life versus stream composition and temperature

(b) Recovery factor

(c) Radiation and conduction error assessment

(d) Dynamic error

(e) Emissivity versus temperature

(f) Response rate

4.1.5 Basic Design Considerations

The thermocouple junction temperature T_j is always less than the total gas temperature T_T (see Figure 4.1-2). During flight, the total-temperature thermocouple probe will be exposed to a temperature range from 1080^0 to 4700^0R.

The thermocouple may be designed so that T_j is as near T_{T_g} as possible (see Figure 4.1-2a), and Δt, the difference, is as small as possible. The advantage of this design is that with a single measurement (T_j), the total temperature (T_{T_g}) may be approximated.

To keep it from melting or to make it last longer, the thermocouple may be designed to make Δt large (see Figure 4-2b).

Since T_{T_g} is not measured, but is determined by measuring T_j and calculating Δt, the uncertainty in knowing the true value of T_{T_g} depends on the certainty in T_j and Δt. Determining the uncertainty in T_{T_g} is the subject of the following section.

4.1.6 Error Analysis of a Total-Temperature Thermocouple Probe

This section presents an error analysis and details how this error analysis is used in maximizing the accuracy of the total-temperature determination. Reference 4-1 presents an error analysis that includes the transient case; an error analysis of the static case follows. When measuring the total temperature with a thermocouple in a supersonic gas stream, the thermocouple is not as hot as the total temperature of the gas stream. This is because the thermocouple

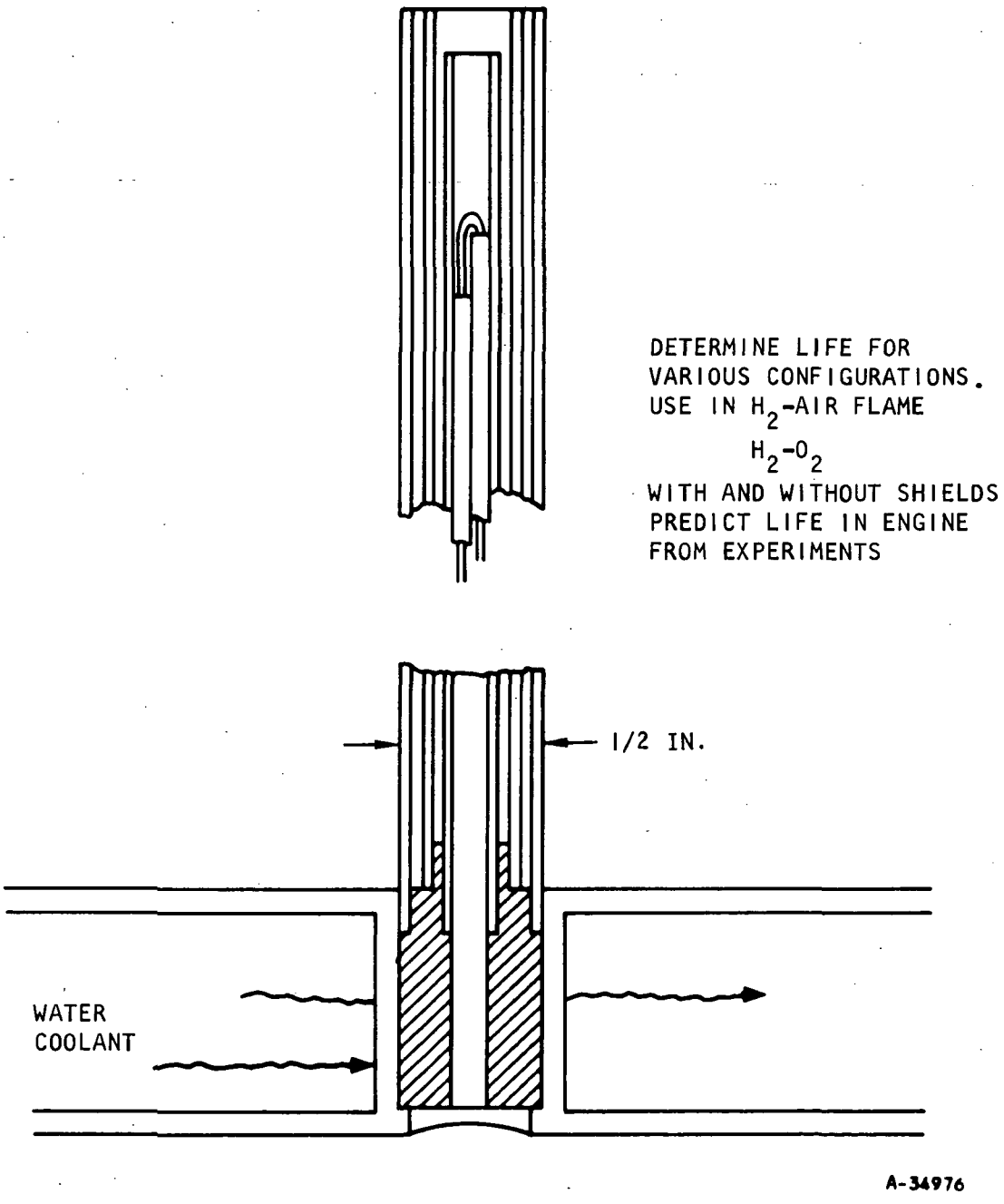

Figure 4.1-1. Total Temperature Probe to be Used for Design Optimization

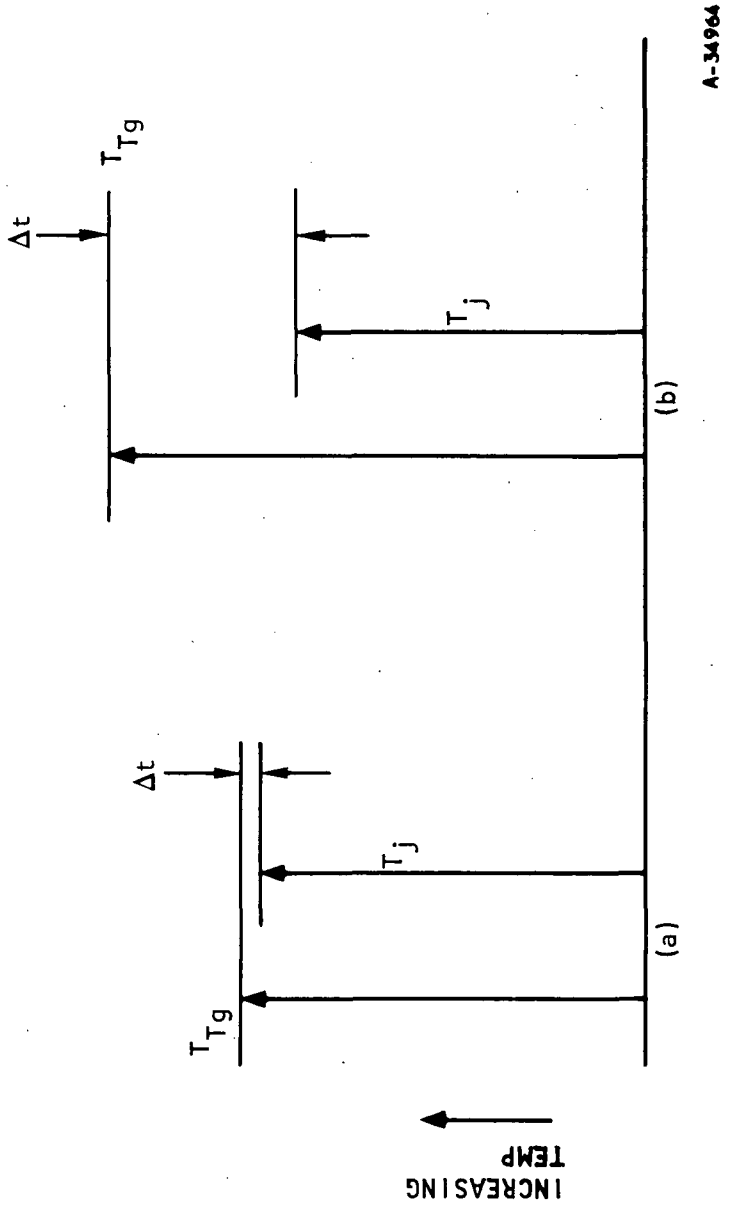

Figure 4.1-2. Total Temperature Measurement with Thermocouple

continually loses heat by radiation, by the support draining heat from it by conduction, and because all the energy of translation of the gas stream is not transferred to the thermocouple. An advantage of using the thermocouple is that the total temperature is always at least as hot as the thermocouple. Thus, a lower limit of the total temperature of the gas is established without further knowledge of gas stream properties, heat transfer coefficients, etc.

In determining the total temperature of the gas stream, it is necessary to determine how hot the thermocouple would have been if losses, mentioned above, were not present.

Because of the varied aerodynamic conditions along the probe and because of geometric complexity, a transient analysis of such a probe is difficult to obtain explicitly. For these reasons, the whole probe is divided into about 100 elements, and the transient response of all elements, and therefore of the entire probe, is obtained. With the aid of a nodal analysis program, this is accomplished by writing the energy conservation equations of all the discrete elements and solving them simultaneously on a digital computer after the various heat-transfer coefficients, etc., along the probe surface are computed.

In designing a total-temperature thermocouple probe or in using data from an existing probe, it is important to know how much each term in the analysis for a particular model contributes to a total-temperature random error. The information is useful in optimizing the design of a physical model, and in reducing data from an existing model.

When using the thermocouple model shown in Figure 4.1-3 and Equation (4.1-4), it is assumed that the model adequately describes a real thermocouple, and that the equations adequately describe the model. After referring to Figure 4.1-3 and 4.1-4, and the disc (the material forward of the thermocouple junction) at the tip of the thermocouple labeled T_j in the figure, the following preliminary analysis assumptions were made:

(a) The thermocouple junction has a uniform temperature for all internal points. (It is a perfect heat conductor.)

(b) The recovery factor $\simeq 1.0$.

Other assumptions that were made are:

(a) The emissivity of the surface does not vary with temperature

(b) Radiation from walls is not absorbed by the gas stream

(c) Radiation from hot-gas stream to thermocouple is zero

(d) The heat-transfer coefficient along the tube is constant

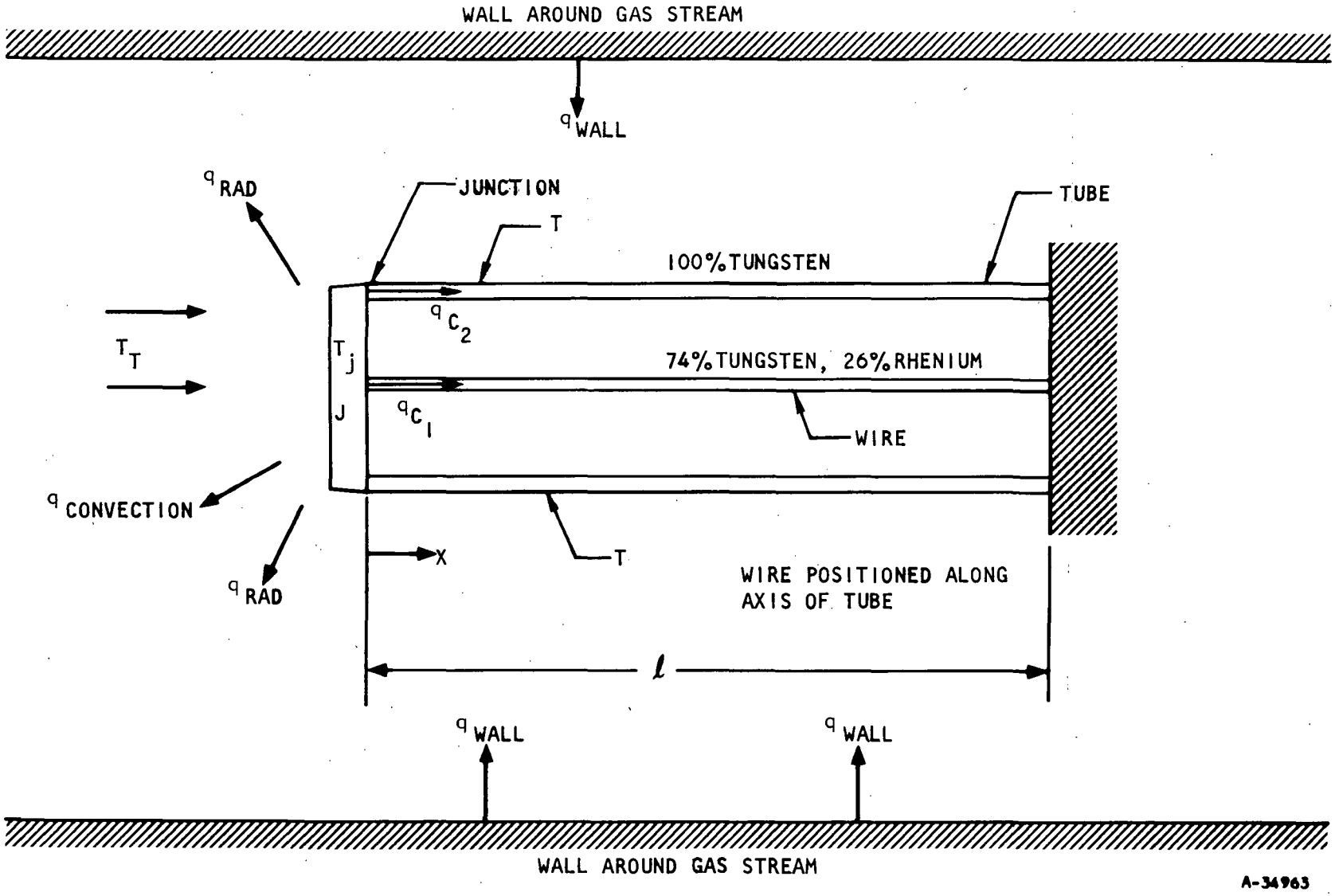

Figure 4.1-3. Cross Section of a Coaxial Thermocouple

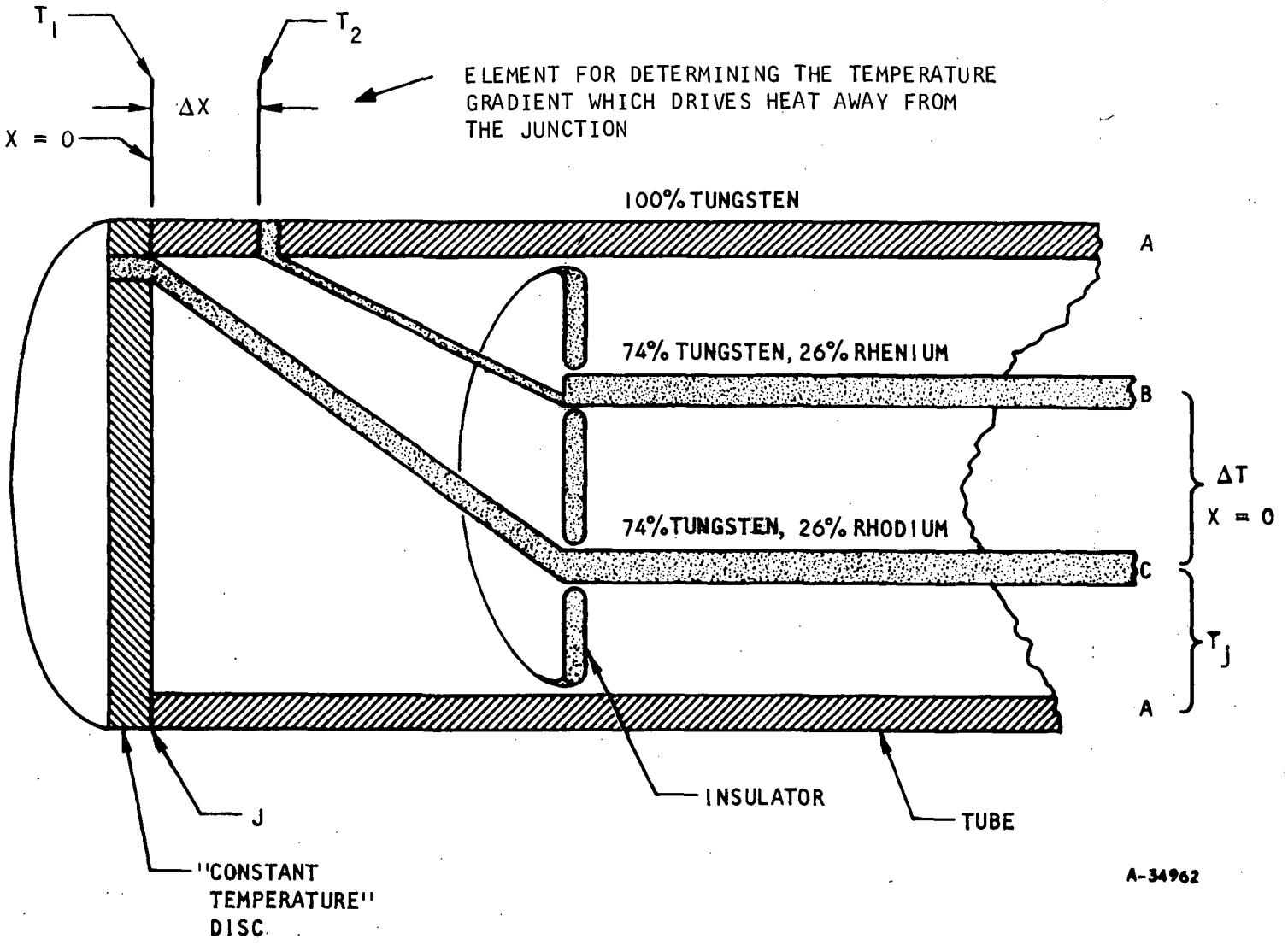

Figure 4.1-4. Cross Section of Three-Element Thermocouple

Heat is added to the junction by convection from the hot-gas stream and is removed from the junction by radiation; some heat is added to the junction by radiation from the enclosure. Heat is lost from the junction by conduction down the tube walls and down the center wire. These variations are expressed below.

$$q_{convective} = h_o A_{conv}(T_T - T_j) \qquad (4.1\text{-}1)$$

$$q_{radiative} = \epsilon\sigma A_{rad}(T_j^4 - T_\omega^4) \qquad (4.1\text{-}2)$$

$$q_{conduction} = K_1 A_1 \left(\frac{dT_1}{dx_1}\right)_{x=0} + K_2 A_2 \left(\frac{dT_2}{dx_2}\right)_{x=0} \qquad (4.1\text{-}3)$$

Terms are defined in Figure 4.1-2.

Equation (4.1-2) assumes that the emissivity of the wall = 1.0, that the wall completely surrounds the tip, and that the probe is small compared to the enclosure.

The heat into the wire and the heat out of the wire may be equated, producing the following results:

$$q_{conv} = q_{rad} + q_{cond_1} + q_{cond_2}$$

$$h_o A_{conv}(T_T - T_j) = \epsilon\sigma A_{rad}(T_j^4 - T_\omega^4) + K_1 A_2 \left(\frac{-dT_1}{dx_1}\right)_{x=0} + K_2 A_2 \left(\frac{-dT_2}{dx_2}\right)_{x=0} \qquad (4.1\text{-}4)$$

Assuming the temperature gradient of the center wire adequately approximates the temperature gradient of the tube, and that an equivalent area of $A_1 + A_2$ equals A (which takes into consideration the difference of thermal conductivities of the wire and tube), the above formula is modified to

$$h_o A_{conv}(T_T - T_j) = \epsilon\sigma A_{rad}(T_j^4 - T_\omega^4) + K A_o \left(\frac{-dT}{dx}\right)_{x=o} \qquad (4.1\text{-}5)$$

$\left(\frac{-dT}{dx}\right)$ is unknown; if it can be determined, then Equation (4.1-5) may be solved for T_T.

By considering a thin slice taken perpendicular to the axis of the tube, an equation may be written, stating that the heat into and out of this element is equal to zero, because in steady-state conditions $\left(\frac{dT}{dx}\right) = 0$. A further assumption is that the emissivity does not vary with temperature.

$$K_2 A_2 \frac{d^2T}{dx^2} = Ph_c(T_T - T) - \epsilon\sigma T(T^4 - T_\omega^4) = 0 \qquad (4.1\text{-}6)$$

by solving Equation (4.1-6), determine $(\frac{dT}{dx})_{x=o}$.

This value can be plugged into the last term of Equation (4.1-5), however, except by repeated approximations or using a computer, the resulting equation cannot be solved. Equation (4.1-5) can be solved, provided $\frac{dT}{dx}$ is considered to be a variable that can be determined by an independent method and a specific value of $\frac{dT}{dx}$ is used. A small value of x is desired so that the temperature gradient thus determined will apply to the point where the tube is joined to the end plate, or "J" (Figure 4.1-2). At this location, x=o.

Several possibilities exist

(a) Determine $\frac{dT}{dx}$

1. Optical pyrometer

2. Thermocouple with three elements

(b) Eliminate the term $\frac{dT}{dx}$ by making it equal to zero by special probe design

(c) Design the probe so $\frac{dT}{dx}$ is minimized

Two methods are suggested for determining $\frac{dT}{dx}$.

The first method uses an optical pyrometer to determine the temperature difference between the point where the probe tip joins the tube (x=o) and a point near there where x equals a small value. For the $\frac{dT}{dx}$ value to apply to the point where x=o, the distance, x, needs to be small. To minimize errors, the same pyrometer should be used to measure the temperature of the two adjoining points. The temperature difference is obtained by subtracting one temperature value from the other.

The second method determines the temperature difference directly. A ΔT thermocouple is used at a location where $x \cong o$. By referring to Figure 4.1-2, it can be seen that T_j is measured between A and C; and that ΔT is measured between B and C. By extrapolation of the curve to a point closer to x=o than can be done with the third element as shown, additional elements could be used along the inside of the tube to allow useful temperature-versus-x curve.

To determine accurately, Δx and ΔT should be measured; the effect of the temperature gradient $\frac{dT}{dx}$ on accuracy is discussed in a following section. When the value of $(\frac{-dT}{dx})_{x=o}$ is determined by an independent means (as by the model

shown in Figure 4.1-2), T_T is determined by simple operations starting with Equation (4.1-5) and resulting in

$$T_T = \frac{\varepsilon\sigma}{h_o}\left(\frac{A_{rad}}{A_{conv}}\right)\left(T_j^4 - T_\omega^4\right) + \frac{K}{h_o}\left(\frac{A_o}{A_{conv}}\right)\left(\frac{-dT}{dx}\right) + T_j \qquad (4.1\text{-}7)$$

Radiation and Convection | Conduction and Convection | Thermocouple

The expression is further simplified when the temperature gradient $\left(\frac{dT}{dx}\right)$ approaches zero; the entire conduction term then drops out. Corollaries immediately follow: The contribution by the conduction term to T_T can be minimized by reducing K or $\left(\frac{A_o}{A_{conv}}\right)$, or by increasing the heat-transfer coefficient, h_o.

The contribution by the radiation term to T_T can be reduced by increasing the heat-transfer coefficient (h_o), or by reducing the emissivity ε, the ratio $\left(\frac{A_{rad}}{A_{conv}}\right)$, or by increasing the wall temperature T_ω. Providing single or multiple shields is equivalent to increasing the wall temperature. When T_T is fixed, T_j must rise as the radiation or conduction terms decrease.

Because of material limitations, it may be desirable to design the thermocouple probe so that T_j is purposely less than T_T, and to know accurately what the difference is so that T_T may be determined accurately and so that the thermocouple will live in the environment.

To design a thermocouple probe to realize the greatest accuracy, it is necessary to determine how much the error in each parameter contributes to error in T_T. Large errors in the values of certain parameters, may have less contribution to errors in T_T than small errors in other parameters. An error analysis will show the relative importance of errors in each term.

In the following analysis, a general treatment will be given first. A few particular solutions follow.

In general terms, T_T depends on some relationship of ε, σ, h_o, $\left(\frac{A_{rad}}{A_{conv}}\right)$, T_j, T_ω, K, $\left(\frac{A_o}{A_{conv}}\right)$, $\left(\frac{dT}{dx}\right)$, and T_j. By substituting $T_T = Z$, and $\varepsilon = z_1$, $\sigma = z_2$, etc., and assuming that the values z_1, z_2, z_3, etc. are independently observed

parameters, that the errors in these parameters have equal chance of being positive or negative, and that repeated measurements would yield a normal distribution curve.

The error in Z in actual degrees Rankine, is

$$\Delta Z = \sqrt{\left(\frac{\partial Z}{\partial z_1} \cdot \Delta_{z_1}\right)^2 + \left(\frac{\partial Z}{\partial z_2} \cdot \Delta z_2\right)^2 \ldots\ldots \left(\frac{\partial Z}{\partial z_n} \cdot \Delta z_n\right)^2} \qquad (4.1\text{-}8)$$

where the partials are taken at nominal values of the various parameters.

If the error in each of the observed quantities (Δz_1, Δz_2, etc.) is given in percent of the nominal value.

$$\nabla Z_{(\text{in. }\%)} = \frac{1}{Z}\sqrt{\left(\frac{\partial Z}{\partial z_1} \cdot z_1 \ \nabla z_1\right)^2 + \left(\frac{\partial Z}{\partial z_2} \cdot z_2 \cdot \nabla z_2\right)^2 \ldots\ldots \left(\frac{\partial Z}{\partial z_n} \cdot z_n \cdot \nabla Z\right)^2} \qquad (4.1\text{-}9)$$

∇ indicates that the error is given in percent of the nominal value. For example, if the nominal value of $Z_2 = 150$, and the error in Z_2 is 1-1/2, then $\Delta Z_2 = 1.0$.

Equation (4.1-9) will be applied to a real case where T_T is to be determined by assigning values to each parameter. Also, the error in T_T in percent (or ∇T_T)of the nominal temperature will be determined and it will be shown which errors are important and which are not. This is important because it shows that time spent improving smaller error items will be wasted effort on the overall accuracy.

The following nominal values are assigned to the quantities in Equation (4.1-7):

T_j = 4230 (^{0}R)

T_ω = 1000 (^{0}R)

ϵ = 0.5 (no units)

σ = 3.3×10^{-15} (Btu/sec in.^{2} R^4)

h_o = 1.0×10^{-3} (Btu/sec in.^{2} ^{0}R)

$\left(\frac{A_{rad}}{A_{cond}}\right)$ = 1.0 (no units)

K = 0.22×10^{-4} (Btu/sec in ^{0}F)

$$\left(\frac{A_o}{A_{conv}}\right) = 0.5 \text{ (no units)}$$

$\left(\frac{dT}{dx}\right)$ = zero, 1000°/in., or 2000°/in. (°R/in.)
value to be assigned for these examples
and to be determined for real cases

h_o depends on T_T. A value of h_o is first selected for an estimated T_T and on this basis a T_T is determined. From this value of T_T, a better value of h_o can be determined. By using these numerical values in Equation (4.1-7) to determine nominal values for T_T,

$T_T = 4760$ at $\frac{-dT}{dx} = 0°R/in.$ (530 Radiation, 0 Conduction, 4230 Thermocouple)

$T_T = 5860$ at $\frac{-dT}{dx} = 1000°R/in.$ (530 Radiation, 1000 Conduction, 4230 Thermocouple)

$T_T = 6960$ at $\frac{-dT}{dx} = 2000°R/in.$ (530 Radiation, 2200 Conduction, 4230 Thermocouple)

The percent error in the total temperature, as determined from Equation 4.1-7) by the method of Equation (4.1-9), is given in Figure 4.1-5. To better see what the effect of each error is on the error of T_T in percent, Equation 4.1-9 is rearranged to

$$Z(\text{in percent}) = \sqrt{\left(\frac{\frac{\partial Z}{\partial z_1} \cdot z_1 \cdot \nabla z_1}{Z}\right)^2_{①} + \left(\frac{\frac{\partial Z}{\partial z_2} \cdot z_2 \cdot \nabla z_2}{Z}\right)^2_{②} \cdots \left(\frac{\frac{\partial Z}{\partial z_n} \cdot z_n \cdot \nabla z_n}{Z}\right)^2_{ⓜ}} \quad (4.1\text{-}10)$$

The subscripts ① , ② , etc. refer to terms that will be discussed later. This formula is now in a form where the nominal values may be substituted, and the coefficient of each error written down. Equation (4.1-10) is evaluated by using values located between Equations (4.1-9) and (4.1-10). Equation (4.1-11) is a listing of errors when the gradient equals 2000°F/in.

$$\Delta T \text{ in percent error} = \sqrt{\underbrace{\left[\frac{\sigma\epsilon}{h_o}\left(\frac{A_{rad}}{A_{conv}}\right)(T_j^4 - T_\omega^4)\,\nabla\epsilon\right]^2}_{T_T\ (1)} + \underbrace{\left[\frac{\epsilon\sigma}{h_o}\left(\frac{A_{rad}}{A_{conv}}\right)\frac{(T_j^4 - T_\omega^4)\nabla h_o}{T_T}\right]^2}_{(2)}}$$

$$+\underbrace{\left[\frac{\epsilon\sigma}{h_o}\left(\frac{A_{rad}}{A_{conv}}\right)\frac{(T_j^4 - T_\omega^4)}{T_T}\nabla\left(\frac{A_{rad}}{A_{conv}}\right)\right]^2}_{(3)} + \underbrace{\left[\frac{\epsilon\sigma}{h_o}\left(\frac{A_{rad}}{A_{conv}}\right)\frac{4T_j^4\,\nabla T_j}{T_T}\right]^2}_{(4)}$$

$$+\underbrace{\left[\frac{\epsilon\sigma}{h_o}\left(\frac{A_{rad}}{A_{conv}}\right)\frac{(-4T_\omega^4)\nabla T_\omega}{T_T}\right]^2}_{(5)} + \underbrace{\left[\frac{K}{h_o}\left(\frac{A_{tube}}{A_{conv}}\right)\left(\frac{dT}{dx}\right)\frac{\nabla K}{T_T}\right]^2}_{(6)}$$

$$+\underbrace{\left[\left(\frac{K}{h_o T_T}\left(\frac{A_{tube}}{A_{conv}}\right)\left(\frac{dT}{dx}\right)\nabla\left(\frac{A_{tube}}{A_{conv}}\right)\right]^2}_{(7)} + \underbrace{\left[\frac{-K}{h_o T_T}\left(\frac{A_{tube}}{A_{conv}}\right)\left(\frac{dT}{dx}\right)\nabla h_o\right]^2}_{(8)}$$

$$+\underbrace{\left[\frac{K}{h_o T_T}\left(\frac{A_{tube}}{A_{conv}}\right)\frac{dT}{dx}\nabla\left(\frac{dT}{dx}\right)\right]^2}_{(9)} + \underbrace{\left[\frac{T_j}{T_T}\Delta T_j\right]^2}_{(10)}$$

where

$$\nabla T,\ \nabla\epsilon,\ \nabla h_o,\ \nabla\left(\frac{A_{rad}}{A_{conv}}\right),\ \nabla T_j,\ \nabla T_\omega,\ \nabla K,\ \nabla\left(\frac{A_{tube}}{A_{conv}}\right)$$

are all given in percent of the nominal values.

Figure 4.1-5. Expanded Error Expression

Errors When Gradient Equals 2000°F/in.

①, ② etc. indicate the term number for reference

∇T_T = when temperature gradient at tip equals 2000°F/in.

Radiation	① .006 $(\nabla\epsilon)^2$	$\nabla\epsilon$ = ± 30 percent	5.4 percent^2	4.1-11
	② + .006 $(\nabla h_o)^2$	∇h_o = ± 50 percent	15.0	
	③ + .006 $\left(\nabla \frac{A_{rad}}{A_{conv}}\right)^2$	$\left(\nabla \frac{A_{rad}}{A_{conv}}\right)$ = ± 5 percent	.15	
	④ + .09 $(\nabla T_j)^2$	(∇T_j) = ± 1 percent	.09	
	⑤ + 1 x 10^{-6} $(\nabla T\omega)^2$	$(\nabla T\omega)$ = ± 1 percent	10^{-6}	
Conduction	⑥ + 0.1 $(\nabla K)^2$	(∇K) = ± 1 percent	0.1	
	⑦ + 0.1 $\left(\nabla \frac{A_{tube}}{A_{conv}}\right)^2$	$\left(\nabla \frac{A_{tube}}{A_{conv}}\right)$ = ± 5 percent	2.5	
	⑧ + 0.1 $(\nabla h_o)^2$	(∇h_o) = ± 50 percent	250.0	
	⑨ + 0.1 $\left(\nabla \frac{dT}{dx}\right)^2$	$\left(\nabla \frac{dT}{dx}\right)$ = ± 20 percent	40.0	
Thermocouple	⑩ + 0.37 $(\nabla T_j)^2$	(∇T_j) = ± 1 percent	$\frac{.4}{314}$ = the sum square error	

The coefficients in this column indicate the sensitivity of the total-temperature error to a 1-percent error in the parameter

The values in this column show the percent error the writer has assigned to each parameter.

The values in this column show the result when values in the second column are inserted in the first column.

∇T_T *in percent* = 17.7 percent

Referring to Equation (4.1-11), the total of the figures in the last column is 314 and is the sum square error (SS error). The square root of this total is 17.7 percent. This is the root sum square error (or RSS error) in T_T. By noting the terms that contribute to the error, it is evident that the error is mostly due to the error in h_o in the terms (8) plus (2). The error in T_T, therefore, could be reduced if the error in h_o could be reduced. This error determination for T_T was performed for the case when the temperature gradient at the tip was 2000°F/in. Two other error determinations are made for temperature gradients of 1000°F/in. and 0°F/in. Details are given in the following two paragraphs. The results are later summarized in Table 4.1-1.

Errors When Gradient Equals 1000°F/in.

Square errors and sum square errors for $\frac{dT}{dx}$ = 1000°F/in.:

∇T_T in percent						
①	$0.008\ (\nabla\epsilon)^2$	Radiation	$\nabla E = \pm 30$ percent	7.2	percent²	
②	$0.008\ (h_o)^2$		$\nabla h_o = \pm 50$ percent	20.0		
③	$0.008\left(\nabla \frac{A_{rad}}{A_{conv}}\right)^2$		$\nabla \frac{A_{rad}}{A_{conv}} = \pm 5$ percent	0.2		27.4
④	$0.013\ (\nabla T_j)^2$		$\nabla T_j = \pm 1$ percent	0.013		
⑤	$\sim 10^{-6}\ \nabla T_\omega$		$\nabla T_\omega = \pm 1$ percent	$\sim 10^{-6}$		
⑥	$0.035\ (\nabla K)^2$	Conduction	$\nabla K = \pm 1$ percent	0.035		
⑦	$0.035\left(\nabla \frac{A_{tube}}{A_{conv}}\right)^2$		$\nabla \frac{A_{tube}}{A_{conv}} = \pm 5$ percent	0.87		
⑧	$0.035\ (\nabla h_o)^2$		$\nabla h_o = \pm 50$ percent	87.5		
⑨	$0.035\left(\nabla \frac{dT}{dx}\right)^2$		$\nabla \frac{dT}{dx} = \pm 20$ percent	14.0		102.4
⑩	$0.52\ (\nabla T_j)^2$	Thermocouple	$\nabla T_j = \pm 1$ percent	0.52		0.5
			Sum square error	130.3		

The coefficients in this column indicate the sensitivity of the total-temperature error to a 1-percent error in the parameter

The values in this column show the present error the writer has assigned to each parameter

The values in this column show the result when values in the second column are inserted in the first column

∇T_T in percent = 11.4 percent RRS error

TABLE 4.1-1

SUMMARY OF ERRORS WHEN TEMPERATURE GRADIENTS ARE 2000°, 1000°, AND 0°F PER IN.

Term No.	Parameter		Nominal	Parameter, 3σ Error, percent	Square Errors Degrees F/in., percent		
					2000	1000	0
①	ϵ	Emissivity	0.5	$\nabla\epsilon = \pm 30$	5.4	7.2	11.2
	σ	Radiation constant	3.3×10^{-15}	$\nabla\sigma = \pm 0$	0	0	0
②	h_o	Heat transfer coefficient	1.0×10^{-3}	$\nabla h_o = \pm 50$	15.0	20.0	31.0
③	$\frac{A_{rad}}{A_{conv}}$	Area ratio	1.0	$\nabla \frac{A_{rad}}{A_{conv}} = \pm 5$	0.15	0.2	0.3
④	T_j	Thermocouple junction temperature	4230°R	$\nabla T_j = \pm 1$	0.09	0.013	0.2
⑤	$T_{(t)}$	Wall temperature	1000°R	$\nabla T_{(t)} = \pm 1$	10^{-6}	$\sim10^{-6}$	2×10^{-6}
⑥	K_1	Coefficient of thermal conductivity	2.2×10^{-3}	$\nabla K = \pm 1$	0.1	0.035	0
⑦	$\frac{A_{tube}}{A_{conv}}$	Area ratio	0.5	$\nabla \frac{A_{tube}}{A_{conv}} = \pm 5$	2.5	0.87	0
⑧	h_o	Heat transfer coefficient	1.0×10^{-3}	$(\nabla h_o) = \pm 50$	250	87.5	0
⑨	$\frac{dT}{dx}$	Temperature gradient along wall at tip	2000°F/in.	$\nabla \frac{dT}{dx} = \pm 20$	40	--	--
		Temperature gradient along wall at tip	1000°F/in.	$\nabla \frac{dT}{dx} = \pm 20$	--	14.0	--
		Temperature gradient along wall at tip	0°F/in.	$\nabla \frac{dT}{dx} = \pm 20$	--	--	0
⑩	T_j	Thermocouple	4230°R	$\nabla T_j = \pm 1$	0.37	0.52	0.8
	Sum of squares of errors (total)				314	130	43.5
	Root sum of squares of errors				17.7	11.4	6.6
	Total temperature T_t				6960°R	5860°R	4760°R

Errors When Gradient Equals $0^{0}F/in.$

Sum square errors for $\frac{-dT}{dx} = 0^{0}F/in.$

$\nabla T_T =$	① $0.012\ (\nabla\varepsilon)^2$	Radiation	$\nabla\varepsilon = \pm 30$ percent	$= 11.2$ percent
	② $0.0124\ (\nabla h_o)^2$	Radiation	$\nabla h_o = \pm 50$ percent	$= 31.0$ percent
	③ $0.0124\left(\nabla \frac{A_{rad}}{A_{conv}}\right)^2$	Radiation	$\left(\nabla \frac{A_{rad}}{A_{conv}}\right. = \pm 5$ percent	$= 0.3$
	④ $0.203\ (\nabla T_j)^2$	Radiation	$\nabla T_j = \pm 1$ percent	$= 0.2$
	⑤ $2 \times 10^{-6}\ (\nabla T_\omega)^2$	Radiation	$\nabla T_\omega = \pm 1$ percent	$= 2 \times 10^{-6}$
	⑥ 0	Conduction	0	$= 0$
	⑦ 0	Conduction	0	$= 0$
	⑧ 0	Conduction	0	$= 0$
	⑨ 0	Conduction	0	$= 0$
	⑩ $0.8\ (\nabla T_j)^2$ (Thermocouple)		$\nabla T_j = \pm 1$ percent	$= 0.8$

Sum square error 43.5

∇T_T in percent = 6.6 percent RSS error

5.6 percent RSS error if no error in emissivity

For the case shown, the error in T_T is due mostly to the error in the heat-transfer coefficient.

Figure 4.1-6 shows the complete computer program printout for the orifice-probe error analysis.

To determine what should be done to decrease the error in T_T, the individual errors may be reduced in the contributing parameter, or the multiplier of the contributing parameter may be decreased. For example, if reduction in the T_T error due to an error in the emissivity value is desired, the first term (indicated by ①) of the formula given in Figure 4.1-5 is examined because this is the only term in which the emissivity error (indicated by $\nabla\epsilon$, where ϵ is the percent error of the nominal emissivity) appears. To reduce the error due to emissivity error in T_T, either the emissivity error ($\nabla\epsilon$) must be determined more accurately or the multiplier of $\nabla\epsilon$ must be reduced. The multiplier may be reduced by increasing the wall temperature (T_ω) or by artificially increasing the wall temperature by providing shields around the thermocouple so that T_ω is effectively raised. σ is a constant that cannot be varied. The emissivity (ϵ) should be reduced as much as possible or selected so as to be made as reflective as possible.

In all examples used, the heat transfer coefficient is the biggest contributor to error in T_T of any of the parameters. The heat transfer error h_o appears in terms ② and ⑧ (see Figure 4.1-5). The magnitude of the error due to error in heat-transfer coefficient in T_T, is shown in Table 4.1-1. (Table 4.1-2 shows sensitivity of T_T to errors in parameters.) Again h_o appears in terms ② and ⑧. By inspection of these terms in the formula for error, it can be readily seen that term ② could be substantially reduced if the thermocouple can be made with a material that has a high reflectivity (or a low ϵ). Term ⑧ need not be reduced by decreasing ϵ but may be reduced by reducing the temperature gradient ($\frac{dT}{dx}$), or may be decreased by making the tube of thinner material, thus reducing $\frac{A_{tube}}{A_{conv}}$, or by increasing h_o by selecting one shape factor as superior to another.

To reduce significant errors, other errors are similarly examined as shown in the previous two paragraphs. General comments may be made about errors of the thermocouple of these examples.

> The most significant factor leading to T_T errors is the uncertainty in knowing the heat-transfer coefficient. This can be reduced by reducing ϵ.
>
> If $\frac{dT}{dx}$ can be either made equal to zero or accurately determined, the error in the emissivity becomes the most significant. If materials or coatings with low emissivity are selected, this error can be reduced.

```
// JOB T
// FOR
*IOCS(CARD,1132 PRINTER)
*LISTALL
C       ORIFICE PROBE TT CALCULATION ERROR ANALYSIS
        DIMENSION HEAD(20)
   99 READ (2,5) HEAD
      READ (2,2) N
      READ (2,1) CD1,CD2,A1,A2
      READ (2,1) DTT2,DPT1,DPT2,DCD1,DCD2,DA1,DA2
      READ (2,1) DMC,DTCN,DTCF
      WRITE (3,6) HEAD
      WRITE (3,7) CD1,CD2,A1,A2
      WRITE (3,8) DTT2,DPT1,DPT2,DCD1,DCD2,DA1,DA2,DMC,DTCN,DTCF
      WRITE (3,3)
      AN=N-1
      TTB=2900.0
      AMC=8.0*62.5/448.0
      DO 90 I=1,N
      AI=I
      AM=(AI-1.0)/AN
      PT1=280.0-220.0*AM
      PT2=225.0-184.0*AM
      TT2=900.0+460.0*AM
      D2TC=12.0+10.0*AM
      TTB=TTB+AM*2500.0
   15 GAM1=1.382-0.00008*TTB
      GAM2=1.516-0.00004*TTB
      R1=25.8+0.00948*TTB
      R2=40.888+0.00428*TTB
      A=SQRT(GAM1/R1*(2.0/(1.+GAM1))**((1.+GAM1)/(GAM1-1.0)))
      B=SQRT(GAM2/R2*(2.0/(1.+GAM2))**((GAM2+1.)/(GAM2-1.0)))
      TT=TT2*(PT1*CD1*A1/(PT2*CD2*A2))**2.0*A/B
      IF(ABS(1.0-TT/TTB)-0.001)30,30,20
   20 TTB=0.5*(TTB+TT)
      GO TO 15
C       DOUBLE SONIC ORIFICE TECHNIQUE
   30 DA=DTT2/TT2
      DB=DPT1/PT1
      DC=DPT2/PT2
      DD=DCD1/CD1
      DE=DCD2/CD2
      DF=DA1/A1
      DG=DA2/A2
      EDS=SQRT(DA*DA+4.0*(DB*DB+DC*DC+DD*DD+DE*DE+DF*DF+DG*DG))*100.0
C       CALORIMETRIC TECHNIQUE
      TTA=2900.+2500.*AM
   40 GAM2=1.516-0.00004*TTA
      R2=40.888+0.00428*TTA
      CPG=R2/((1.-1.0/GAM2)*778.0)
      CPC=0.03965
      CAY=CD2*SQRT(GAM2*(2.0/(GAM2+1.0))**((GAM2+1.)/(GAM2-1.0))/(32.16*
     1R2))
      AMG=CAY*PT2*A2*5.01/SQRT(TT2)
      TT1=TT2+CPC*AMC*D2TC/(CPG*AMG)
      IF (ABS(1.0-TT1/TTA)-0.01 )50,50,45
   45 TTA=0.5*(TTA+TT1)
```

Figure 4.1-6. Double-Sonic Orifice Probe Error Analysis Computer Program

```
      GO TO 40
   50 CA=DMC/AMC
      CB=DTC*/D2TC
      CC=DTCF/D2TC
      CD=DPT*/PT2
      CE=DA2/A2
      CF=DCD2/CD2
      CG=(TT1+TT2)*DTT2*0.5/(TT2*(TT1-TT2))
      EC =(1.0-TT2/TT1)*SQRT(CA*CA+CB*CB+CC*CC+CD*CD+CE*CE+CF*CF+CG*CG)
     1*100.
      WRITE (3,4) TT ,EDS,PT1,PT2,TT2,TT1,EC,AMG,R2,GAM2
   90 CONTINUE
      GO TO 99
    1 FORMAT (8F10.0)
    2 FORMAT (8I10)
    3 FORMAT (3X'------------- DOUBLE SONIC ORIFICE TECHNIQUE ----------
     1---'3X, '---------------- CALORIMETRIC TECHNIQUE ----------------'
     2/   6X,'TT1'9X,'ERROR'8X,'PT1'8X,'PT2'9X,'TT2'9X,'TT1'9X,'ERROR'9X
     3'MG'10X'R2'9X,'GAM 2'/)
    4 FORMAT (10F12.3)
    5 FORMAT (20A4)
    6 FORMAT (1H1,20A4)
    7 FORMAT (1H0,'INPUT DATA'/' CD1 ='E12.5,3X'CD2 ='E12.5,3X'A1  ='E12
     1.5,3X,'A2  ='E12.5)
    8 FORMAT (' DTT2='E12.5,3X'DPT1='E12.5,3X'DPT2='E12.5,3X,'DCD1=',
     1E12.5,3X,'DCD2='E12.5/' DA1 ='E12.5,3X'DA2 ='E12.5,3X,'DMC ='E12.5
     2,3X,'DTC*='E12.5,3X'DTCF='E12.5/)
      END
```

Figure 4.1-6. Continued

ORIFICE PROBE TT1 ERROR ANALYSIS

INPUT DATA

CD1 = 0.964000E 00 CD2 = 0.980000E 00 A1 = 0.295000E-01 A2 = 0.202000E-01
DTT2= 0.136000E 02 DPT1= 0.580000E 01 DPT2= 0.480000E 01 DCD1= 0.462000E-02 DCD2= 0.460000E-02
DA1 = 0.148000E-03 DA2 = 0.101000E-03 D/C = 0.160000E 00 DTCR= 0.164000E 01 DTCP= 0.120000E 01

DOUBLE SONIC ORIFICE TECHNIQUE					CALORIMETRIC TECHNIQUE				
TT1	ERROR	PT1	PT2	TT2	TT1	ERROR	MG	R2	GAM 2
2476.921	6.188	260.000	225.000	980.000	1119.645	4.583	0.003	45.683	1.471
3271.157	7.159	256.000	188.300	992.000	1398.029	5.109	0.010	46.469	1.463
3539.106	8.652	192.000	151.600	1084.000	1542.489	5.862	0.007	47.496	1.454
3951.721	11.134	148.000	114.900	1176.000	1863.218	6.952	0.005	48.868	1.441
4436.657	15.924	104.000	78.200	1268.000	2375.799	8.666	0.003	51.064	1.420
5389.837	28.701	60.000	41.500	1360.000	3483.651	12.346	0.001	55.511	1.376

Figure 4.1-6. Continued

TABLE 4.1-2

SENSITIVITY OF T_T TO PARAMETER ERRORS

$$\nabla T_T = \left\{ \begin{array}{llll} \textcircled{1} & [0.006 & \text{or } 0.008 & \text{or } 0.012\ ] \ (\nabla\epsilon)^2 \\ \textcircled{2}\ \textcircled{8} & [0.106 & \text{or } 0.043 & \text{or } 0.0124] \ (\nabla h_o)^2 \\ \textcircled{3} & [0.006 & \text{or } 0.008 & \text{or } 0.0124] \left(\nabla \frac{A_{rad}}{A_{conv}}\right)^2 \\ \textcircled{4}\ \textcircled{10} & [0.46 & \text{or } 0.65 & \text{or } 1.003\ ] \ (\nabla T_j)^2 \\ \textcircled{5} & [1 \times 10^{-6} & \text{or } 1 \times 10^{-6} & \text{or } 2\times10^{-6}] \ (\nabla T_\omega)^2 \\ \textcircled{6} & [0.1 & \text{or } 0.035 & \text{or } 0\ ] \ (\nabla K)^2 \\ \textcircled{7} & [0.1 & \text{or } 0.035 & \text{or } 0\ ] \left(\nabla \frac{A_{tube}}{A_{conv}}\right)^2 \\ \textcircled{9} & [0.1 & \text{or } 0.035 & \text{or } 0\ ] \ \nabla \frac{dT}{dx}^2 \\ & 2000^\circ F \text{ per in.} & 1000^\circ F \text{ per in.} & \text{zero } ^\circ F \text{ per in.} \end{array} \right\} \quad (4.1\text{-}12)$$

NOTE: Similar terms $\left[(\nabla h_o)^2 \text{ and } (\nabla T_j)^2\right]$ are combined.

Source: Equation (4.1-11)

As a consequence of these suggestions, the thermocouple of Table 4.1-1 was figuratively modified to change ϵ from 0.5 to 0.1 maintaining the emissivity error of ±30 percent of the nominal value of the emissivity. As a result, the calculated error in T_T change ϵ from 6.6 percent to 1.4 percent for the case where $\frac{dT}{dx}$ equals zero. Notice this happens even when a ±50-percent error in h_o is present.

Because the amount of heat lost by conduction depends on the product of $\frac{dT}{dx}$ times (the coefficient of thermal conductivity) and not on the term $\frac{dT}{dx}$ alone, it would probably be more convenient to use the product and not $\frac{dT}{dx}$ alone. Thus, a 2000°F/in. temperature gradient may be very important in a tungsten material and may be totally insignificant in a poorer heat-conductor material.

Omitting wall temperature (T_ω) entirely creates an error of only 0.3 percent in T_T. The exact value of the radiative and conductive area is relatively unimportant.

4.1.6.2 Analysis of High-Temperature Thermocouple Probe

A total-temperature thermocouple probe of coaxial design is analyzed in Reference 4-2 to estimate the time response as well as the difference in temperature between the total temperature of the gas (T_T) and the thermocouple junction temperature (T_j). The thermocouple is made of tungsten versus tungsten rhenium. A sketch of this probe is shown in Figure 4.1-7. In Reference 4-2, the thermocouple junction temperature is determined for two designs from given upstream conditions. Both transient and steady-state thermocouple temperatures are determined. In this case, the treatment uses nominal values for a heat-transfer coefficient and for the emissivity.

The treatment for the case where the heat-transfer coefficient or the emissivity may be either 20 percent higher or 20 percent lower than the nominal value as given in Reference 4-3. A different heat-transfer coefficient is used for three zones along the probe. An error in coating thickness is also considered.

The results of Reference 4-3 are summarized as follows: (Given gas velocity is at Mach 3.02, total temperature (T_T) is at 5850°R, and the static pressure is at 1.67; nominal emissivity is 0.60, and nominal coating thickness is 0.04 in. "A" refers to the nominal heat-transfer coefficient tip, "B" to nominal coefficient near the tip, and "C" to coefficient along the shank of the probe; Figure 1 of Reference 4-3 shows the areas to which "A", "B", and "C" refer.)

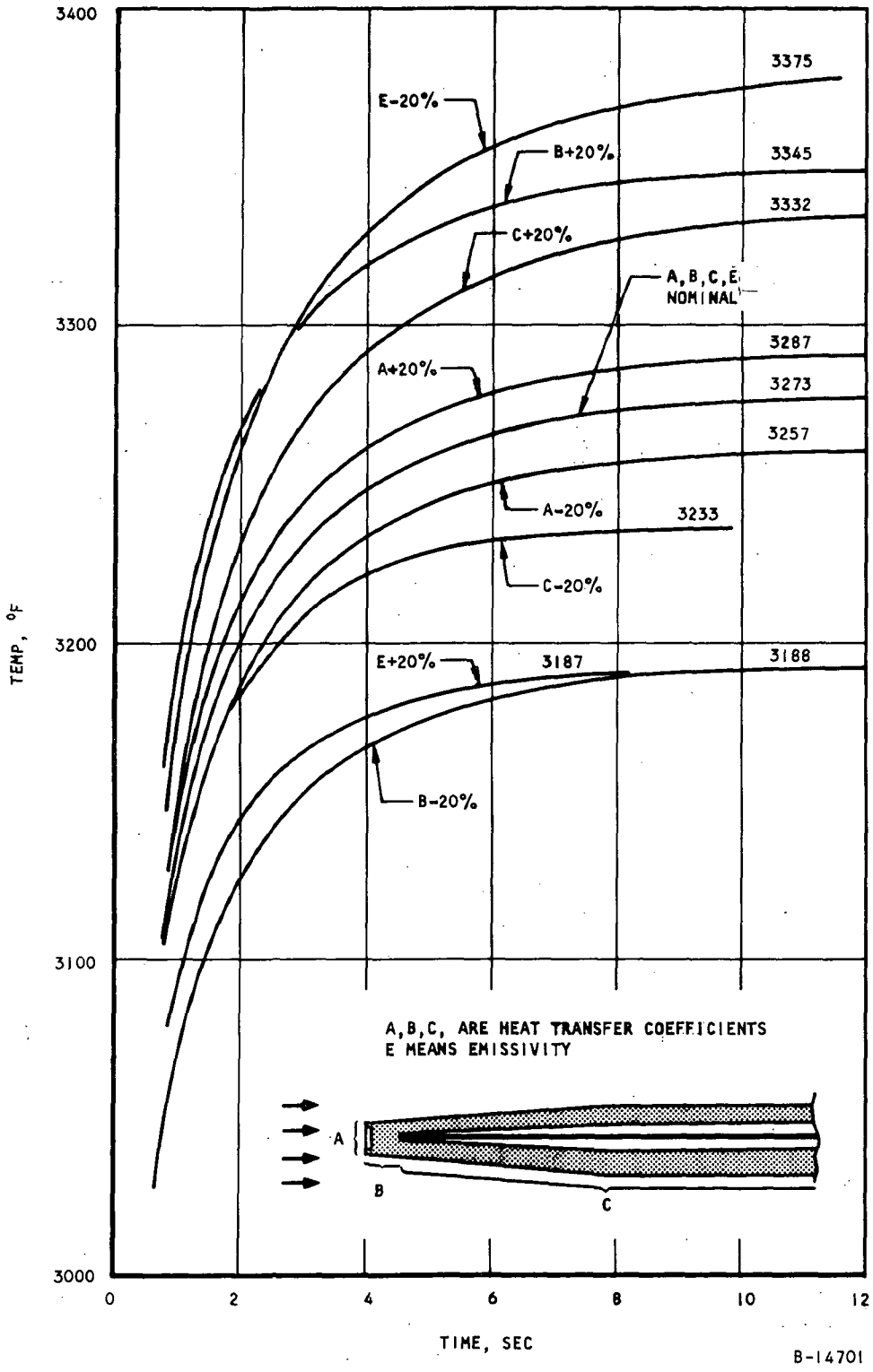

Figure 4.1-7. Effect of 20-Percent Change in Heat-Transfer Coefficients: Thermocouple Temperature Versus Time

(a) An error of 20 percent in the nominal emissivity results in an error of about 2.7 percent in T_J.

(b) An error of 20 percent in the nominal coating thickness results in an error of about 0.5 percent in T_J.

(c) An error of 20 percent in the nominal heat-transfer coefficient at "A" results in an error of about 0.4 percent in T_J.

(d) An error of 20 percent in the nominal heat-transfer coefficient at "B" results in an error of about 2.1 percent in T_J.

(e) An error of 20 percent in the nominal heat-transfer coefficient at "C" results in an error of about 1.5 percent in T_J.

4.1.7 Coating Considerations

Dickinson, et al., have the following to say about "Protective Coatings for Tungsten" in the October 1963 Journal of Metals (Reference 4-4):

"A number of formidable problems must be overcome before the full potential of tungsten and tungsten-base allows as structural materials for use at high temperatures can be realized. On a strength-to-weight basis, these materials are particularly promising for use at temperatures about 1500°C and are possibly the only metallic materials that have reasonable strength at 2000°C and above. However, many potential applications call for long service lives in oxidizing environments, therefore, their poor high-temperature oxidation resistance is a severe limitation.

"Considerable attention is being paid to the development of protective coatings for very high-temperature use. Some coatings already developed can confer protection for considerable periods at temperatures up to 1800°C, but so far none are able to withstand temperatures in excess of 2000°C for reasonable times. In addition to technological difficulties, such as the development of techniques for the application of adherent, pore-free coatings, some of this lack of success may be due to the poor definition of the phenomena that are of primary importance in determining the behavior of coating at high temperatures.

"An ideal coating forms a solid (or extremely viscous), inert, impermeable barrier between the oxidizing environment and the protected substrate. Although easy to state, the combination of properties needed to achieve this ideal coating are complex. Many types of coatings have been investigated, and the types found to be more successful than the others for most environmental conditions are metal coatings, particularly intermetallic compounds, diffusion-bonded to the protected substrate. These compounds are usually composed of metals of widely differing reactivities, the protection being conferred through the oxidation characteristics of the more reactive metal.

"Intermetallic coatings are successful even though they are not inert. Upon exposure to air, any metal surface becomes covered by oxide layers. Also some reaction between the coating and the substrate is a necessity if good adherence is to be obtained. It is highly desirable, therefore, that the products of the coating-environment and coating-substrate reactions should be solids or extremely viscous liquids at operational temperatures. In addition to chemical reactions, purely physical processes, such as vaporization, may proceed at significantly rapid rates at high temperatures and therefore must be considered. In principle, the rate of gaseous permeation is also important, but it may be ignored in practice, except in a few special cases. These departures from the ideal rule out the possibility of developing an infinitely durable simple coating consisting of an inert layer.

"Because of coating-environment and coating-substrate reactions, the structures of actual protective-coating systems are complex. Multilayer coating systems are often found to be most successful and, in practice, even single-layer coatings become multi-layer during service due to coating-substrate and coating environment reactions. Both the oxide scale and the additional substrate layers formed by these reactions thicken with time and, eventually, the initial coating reservoir will be consumed entirely. Knowledge of the rates of consumption of the original coating material by these reactions is necessary for a complete analysis of coating behavior.

"Three vaporization processes can affect the behavior of a coating system: (1) vaporization of the protective external oxide film, (2) reaction with the environment to produce volatile products, and (3) vaporization from an internal layer.

"Vaporization at an internal interface is harmful to coating stability, since it may cause disruption of protective external oxide layers. Two types of vaporization can occur internally: simple evaporation of one component, or the vaporization of the products of the reaction between two layers. Examples of these two processes are the evaporation of the substrate, which has been suggested as being responsible for the breakdown of protective oxide film growth on chromium at 800° to 900°C, and the interaction of silica and silicide layers to produce the volatile silicon monoxide responsible for the bubbling of silica films at high temperatures.

"Coating-substrate reactions are necessary for the formation of a good bond, but they could also form volatile or liquid phases or change the composition of the external oxide film formed. Even if the reactions do not have these harmful effects, they decrease the effective coating thickness.

"Some conclusions as to the factors controlling coating-substrate reactions can be drawn. The most important of these is that diffusion kinetics are so fast at 2000°C and above that any thermocynamically favored reaction will occur to an appreciable extent in a rather short time.

"Unfortunately, high-temperature thermodynamic data for many reactions of interest are unknown and can be found only by hazardous extrapolations.

"Our ability to estimate the likelihood of reactions in actual systems at high temperatures is far from satisfactory. So many unknown factors may have an influence that it is most difficult to predict the course of a reaction. When the totally unexpected occurs in a high-temperature process, calculations are meaningless--there is no substitute for experimental studies.

"The data available indicate that the upper temperature limit of silicide coatings is probably 2000°C or lower. This limitation is set by the rate of silica vaporization, reactions between silica and the silicide coating at 1900° to 2000°C, the melting points of the silicides, and the decreasing viscosity of silica with increasing temperature.

"Since most successful coating systems are usually intermetallic compounds, thorides etc. are logically the most promising types of materials for ultra-high-temperature coatings."

This concludes the quotation taken from the October 1963 Journal of Metals (Reference 4-4).

The possibility of the coating material substantially altering the thermocouples thermoelectric properties and hence changing the EMF versus temperature curves should be investigated.

4.1.8 Post Experimental Effort

A design for a thermocouple-probe support expected to be used for the 2 in. by 6 in. combustor tests is shown in Figure 4.1-8.

Cylindircal probes, to be installed in the above support, are shown in Figure 4.1-9. These probes are 1/8 in. dia and 2 in. long. Coaxial and bare-bead types with W/WR_e couples and BeO and MgO insulation are shown.

Cylindrical probes, installed parallel to the gas flow with an L/D ratio of about 10 and an outside diameter of 0.125 in., have been designed and fabricated for the combustor test sensor configuration (see Figure 4.1-9). The designs result from constraints imposed by the cooled sting where the sensor must be mounted, and the physical and thermal requirements of the temperature sensor. Figure 4.1-10 shows two probes for the combustor tests. Figure 4.1-11 shows two probes with different wall thickness, 0.010 and 0.030, that were fabricated for the time response and thermal conduction testing. The basic design of these probes is similar to that shown in Block D in Figure 4.1-9. Tungsten has been used as the supporting body in the fabricated sensors. This material is exceedingly difficult to fabricate into intricate parts where metal joining and drilling is required. Straight cylindrical design simplifies the construction. Other materials, such as tantalum, that can withstand the temperatures, are being considered but no fabrication or physical evaluation work has been undertaken.

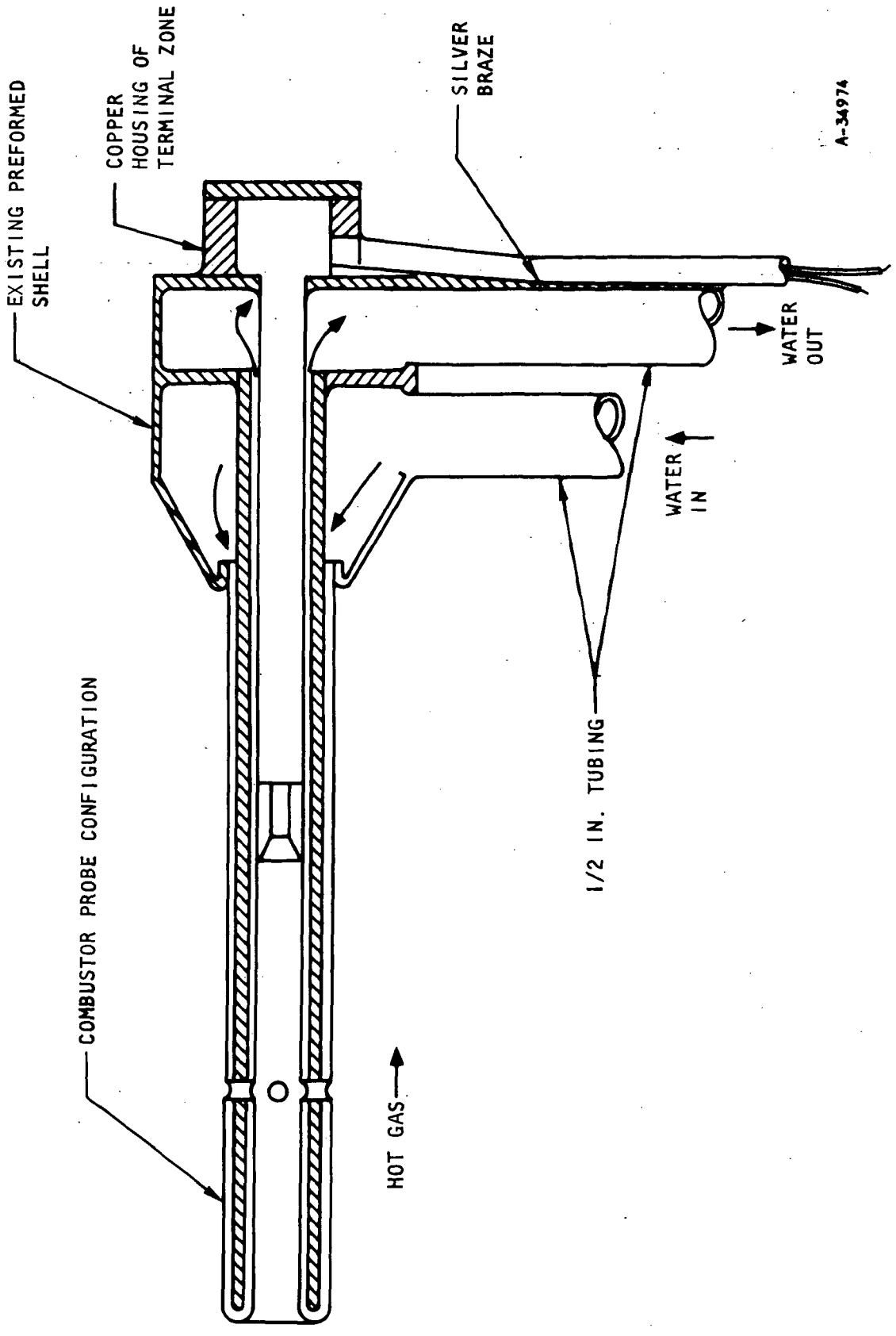

Figure 4.1-8. Thermocouple Test Probe Support Fixture

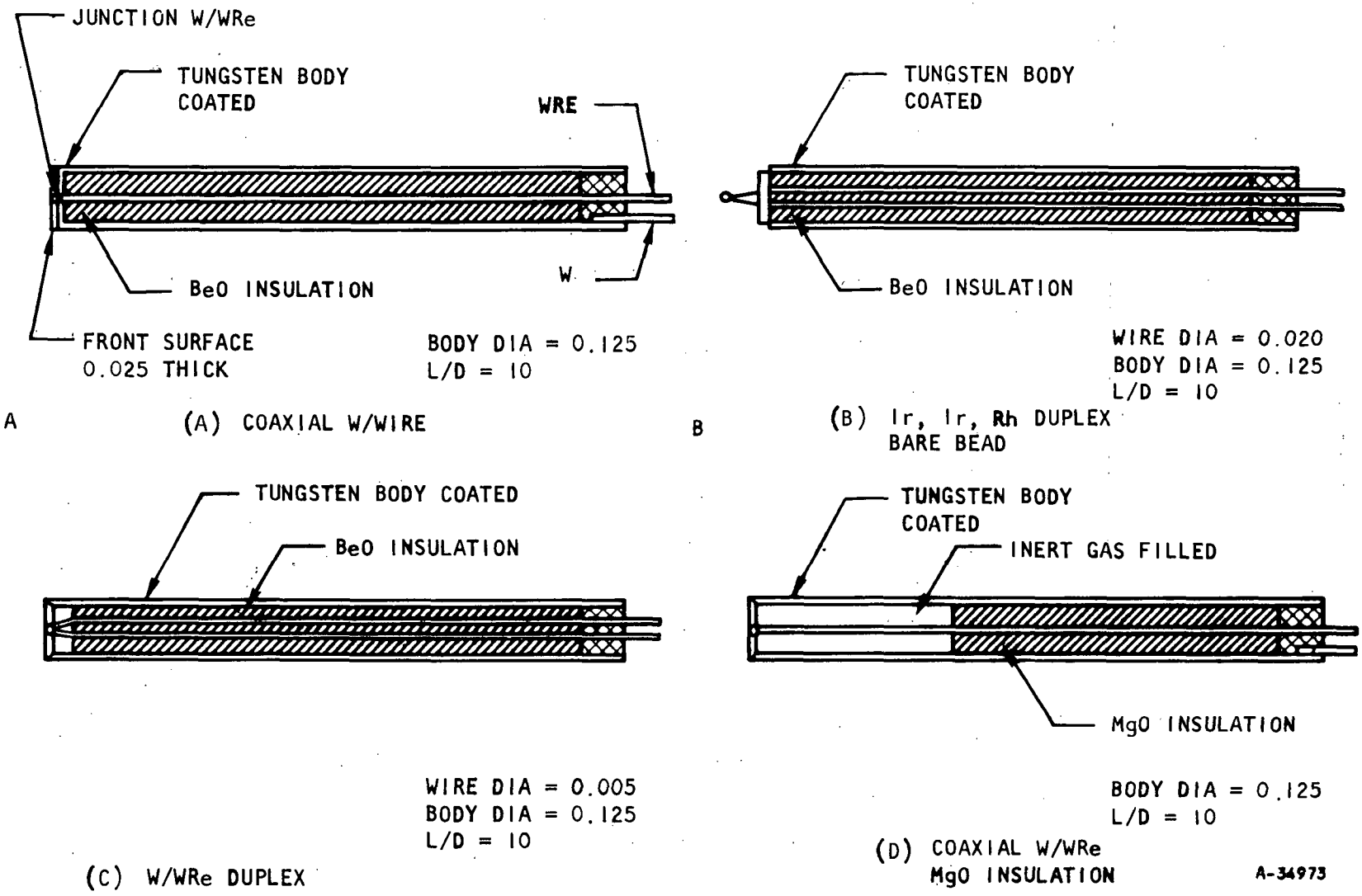

Figure 4.1-9. Basic Probe Designs

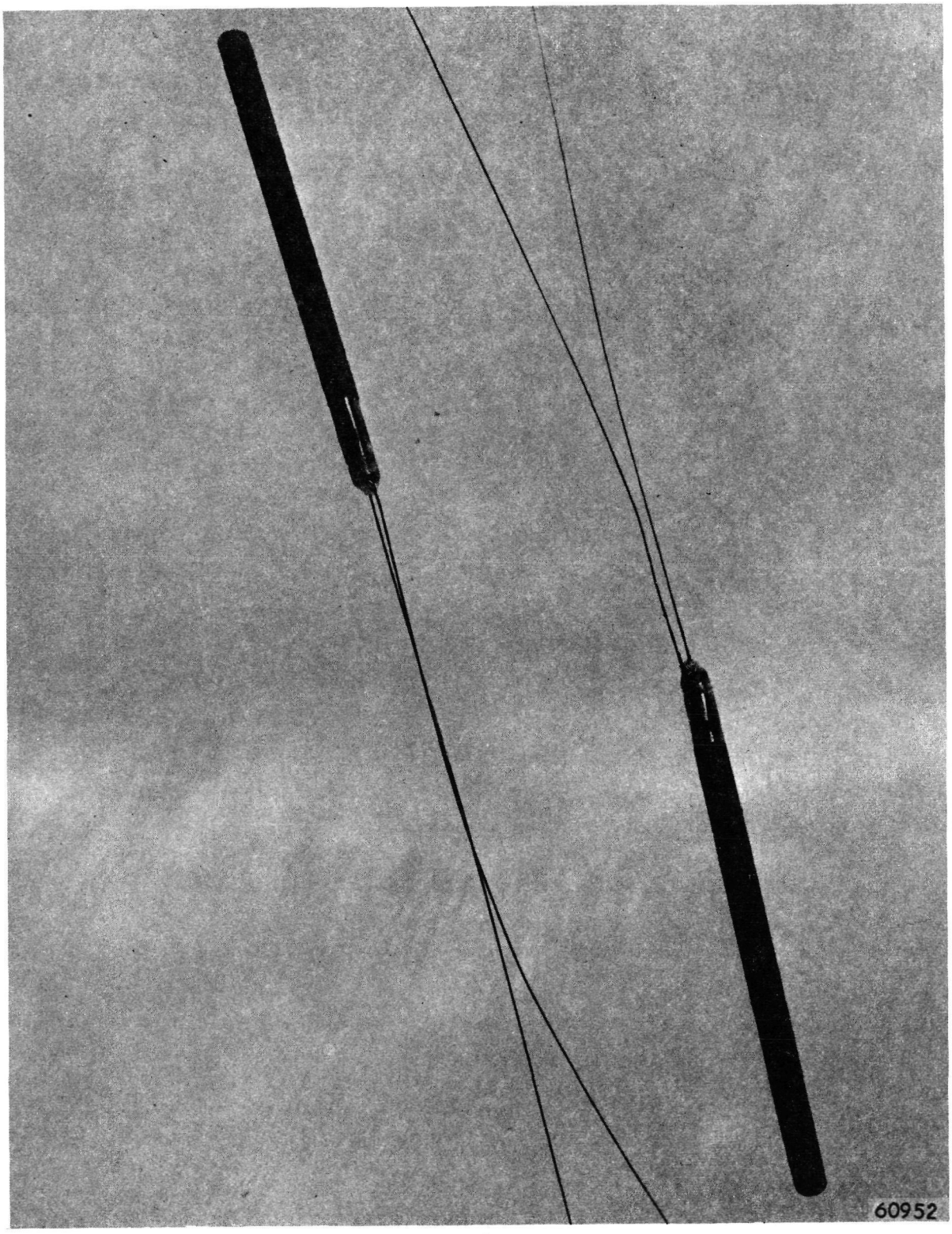

Figure 4.1-10. Combustor Test Probes

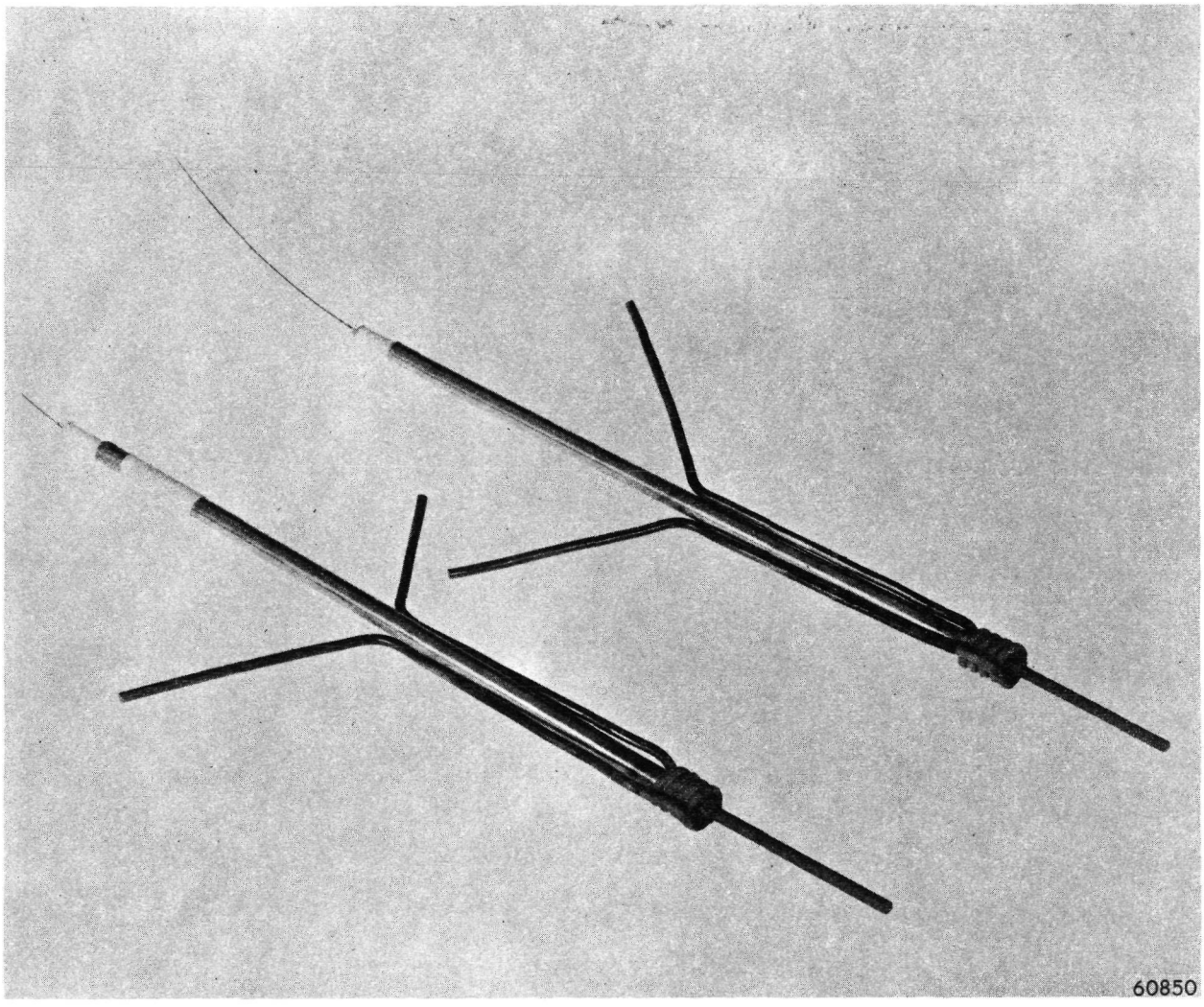

Figure 4.1-11. Time Response and Thermal Conduction Test Probes

4.1.9 Experimental Effort

Several preliminary tests have been made using both hydrogen and air and hydrogen and oxygen mixtures to assess any limitations imposed by the test facility. Temperature measurements taken with a Radiometer on supported wire test specimens in cross flow indicate metal temperatures of 3700°F when subjected to an oxy-hydrogen flame (see Figure 4.1-18) and 2300°F when subjected to an air-hydrogen flame (see Figure 4.1-17). These are indicated temperatures. The temperature would have been hotter if radiation and conduction losses were absent. Radiation errors of 1000°F are indicated for a nonluminous gas environment. Conduction errors will be assessed by radiometric scanning over the length of the probe being tested.

A probe with a diameter of 0.125 in. and a wall thickness of 0.010 in. was coated with about 0.010 in. of silicon. This probe was subjected to the maximum acetylene and oxygen flame temperature in cross flow; Figure 4.1-13 shows the result.

Figure 4.1-14 shows the results of subjecting the same probe to the maximum hydrogen-oxygen flame temperature in axial flow for 20 sec. Radiometric measurement of the coated tip of the probe indicates a temperature of 4000°R. The emissivity setting of the radiometer was based on the emissivity of the coating materials; the value used for emissivity was 0.4 for both the tungsten and the silicon. In the event that different emissivities apply to the coating and the underlying metal, the question arises as to what emissivity should be used in the radiometer setting. The emissivity that should be used depends on the transmission of the coating to the wavelength that the radiometer sees originate from the metal, and depends on whether the radiation from one side of the coating originates partly from within the coating or even from the opposite surface. As a point of interest, the spectral transmission curve for a slab of silicon 0.2 in. thick is shown in Figure 4.1-15.

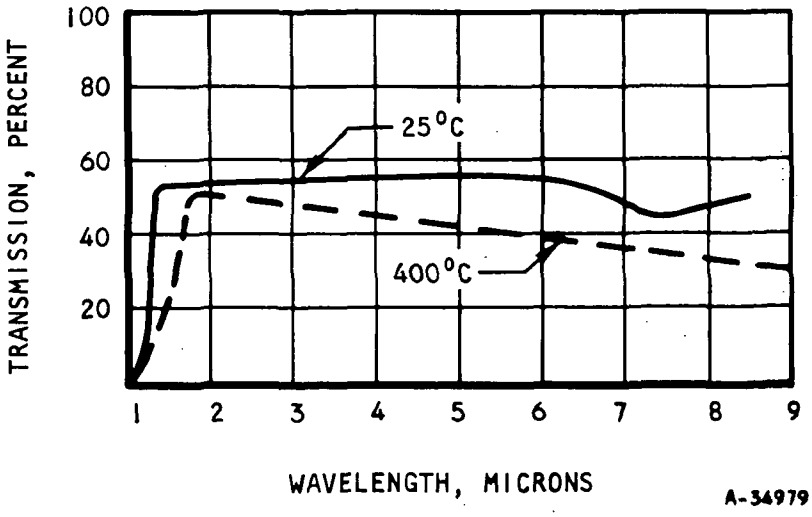

Figure 4.1-15. Spectral Transmission of Silicon (Reference 4-5)

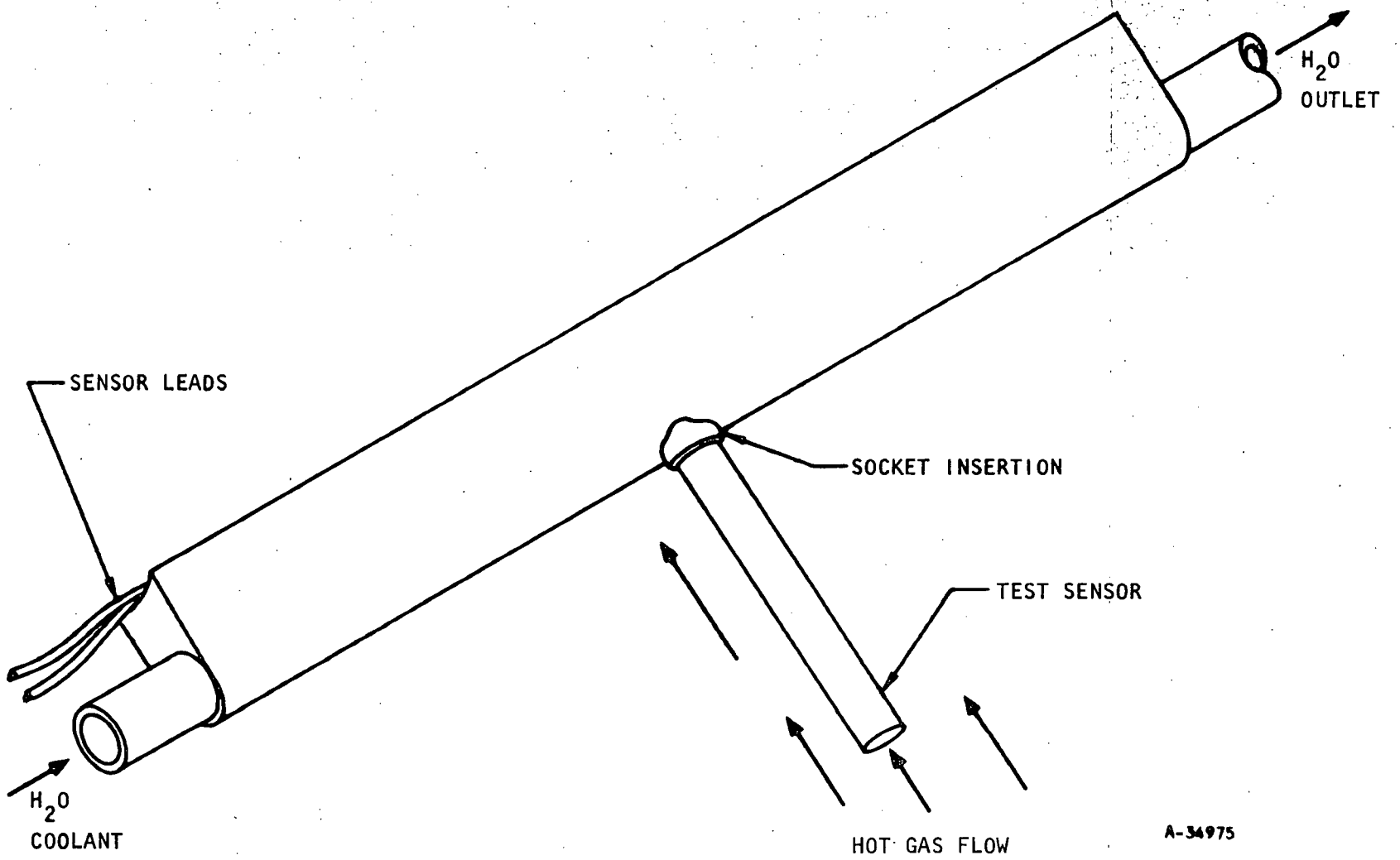

Figure 4.1-12. Probe Evaluation Test Fixture

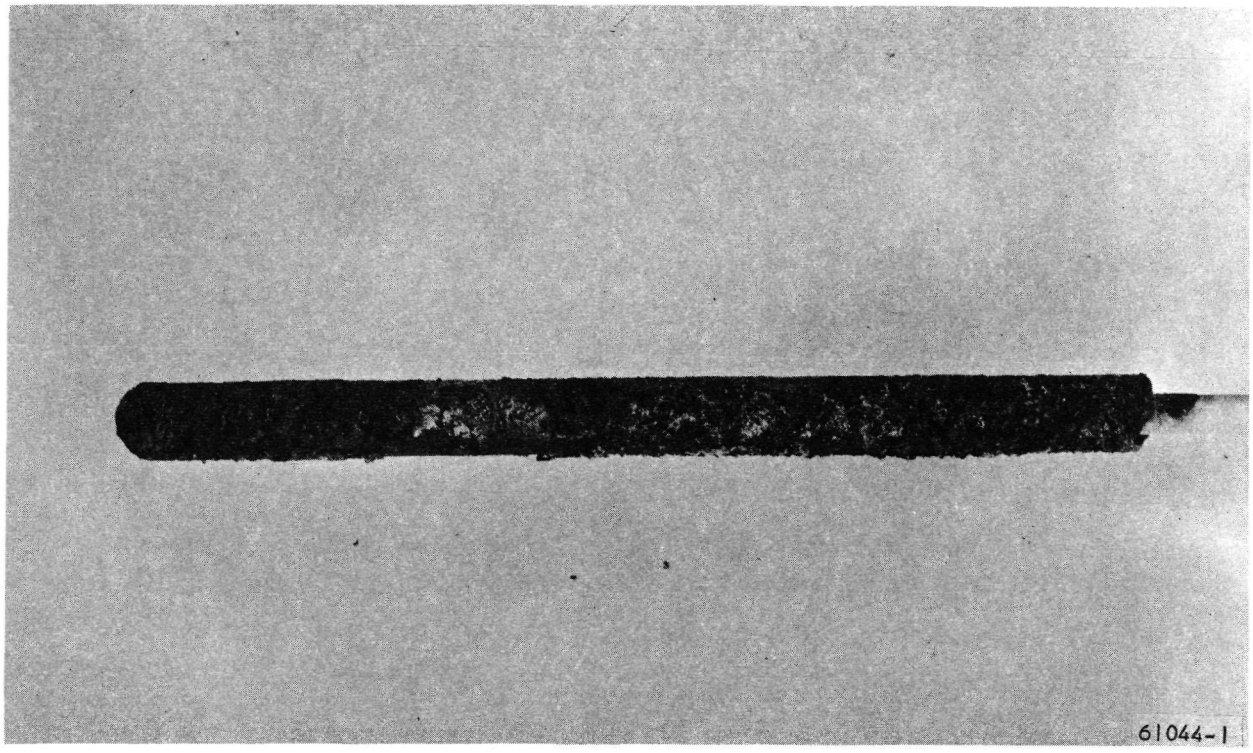

Figure 4.1-13. Silicon-Coated Tungsten Probe After Subjection to Oxygen-Acetylene Combustion Temperature

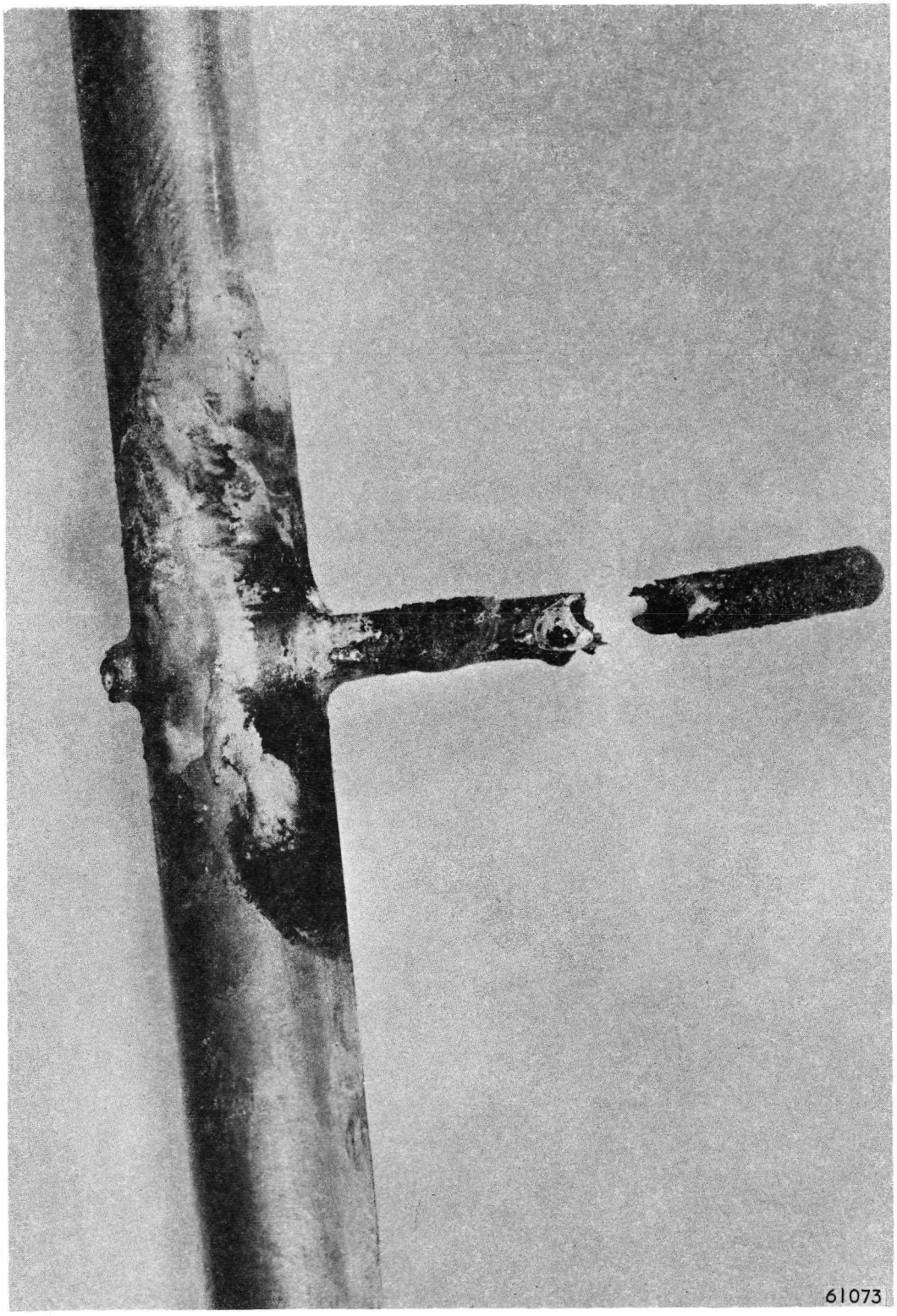

Figure 4.1-14. Silicon-Coated Tungsten Probe After Subjection to Maximum Oxygen-Hydrogen Combustion Temperature

A bare-wire thermocouple, W/WRe_{26} was suspended in a hydrogen air flame in cross flow; it lasted 55 sec. The thermoelectrically determined temperature was about 3000°F. The wire was 0.020 in. in diameter.

4.1.9 Sensor Response Evaluation

After the ACL probes were used in the Phase I boilerplate tests at OAL Daingerfield, they were intact except for a coating deterioration at the probe tip. The No. 2 probe from Test Run 6129 was recoated with silicon applied by plasma-spray techniques, and evaluated for response under bench test conditions using a hydrogen-and-air combustion environment. Time response test results are shown on Figure 4.1-16. The temperature of the probe was monitored with a small target radiometer with an applied emissivity correction of 0.4. Indicated temperatures from the probe were monitored and maintained near the level encountered in the OAL tests. Indicated gas temperatures were set and a step function applied to the thermocouple by inserting a barrier between the hot gas stream and thermocouple. The thermocouple temperature was allowed to decay and reach equilibrium before the barrier was removed; time response was measured from the recorded data.

4.1.10 Future Action

At high temperatures, electrical insulators separating the thermocouple wires become poor insulators; this results in a shunting effect across the thermocouple. If this shunting effect is found to be significant, means will be taken to account for it.

The effect of coating materials on the emissivity of the base material will be investigated, as well as the ability of some coatings to extend the life of sensors.

The effect of shields on the junction temperatures will be experimentally determined; a model of modular design will be used. The shields will be varied in number and in location. See Figure 4.1-1.

4.1.11 Time Response Measurements

Tests on bare-wire configurations were made to evaluate short-lived thermocouples and their response to step transient inputs. Figures 4.1-17 and 4.1-18 show the results of a 0.020-dia W/WRe_{26} thermocouple in cross flow with both hydrogen and air and hydrogen and oxygen combustion gas streams. Their lives extended to over 12 sec in the hydrogen and oxygen flame and lasted up to 55 sec in the hydrogen and air flame.

The graph of Figure 4.1-17 shows that the final temperature of the thermocouple in the hydrogen-air combustion was 2300°F; the thermocouple lasted 55 sec in this environment. Similarly, Figure 4.1-18 shows that the final temperature of the thermocouple in the hydrogen-oxygen combustion was 3700°F; the thermocouple lasted 13 sec in this environment.

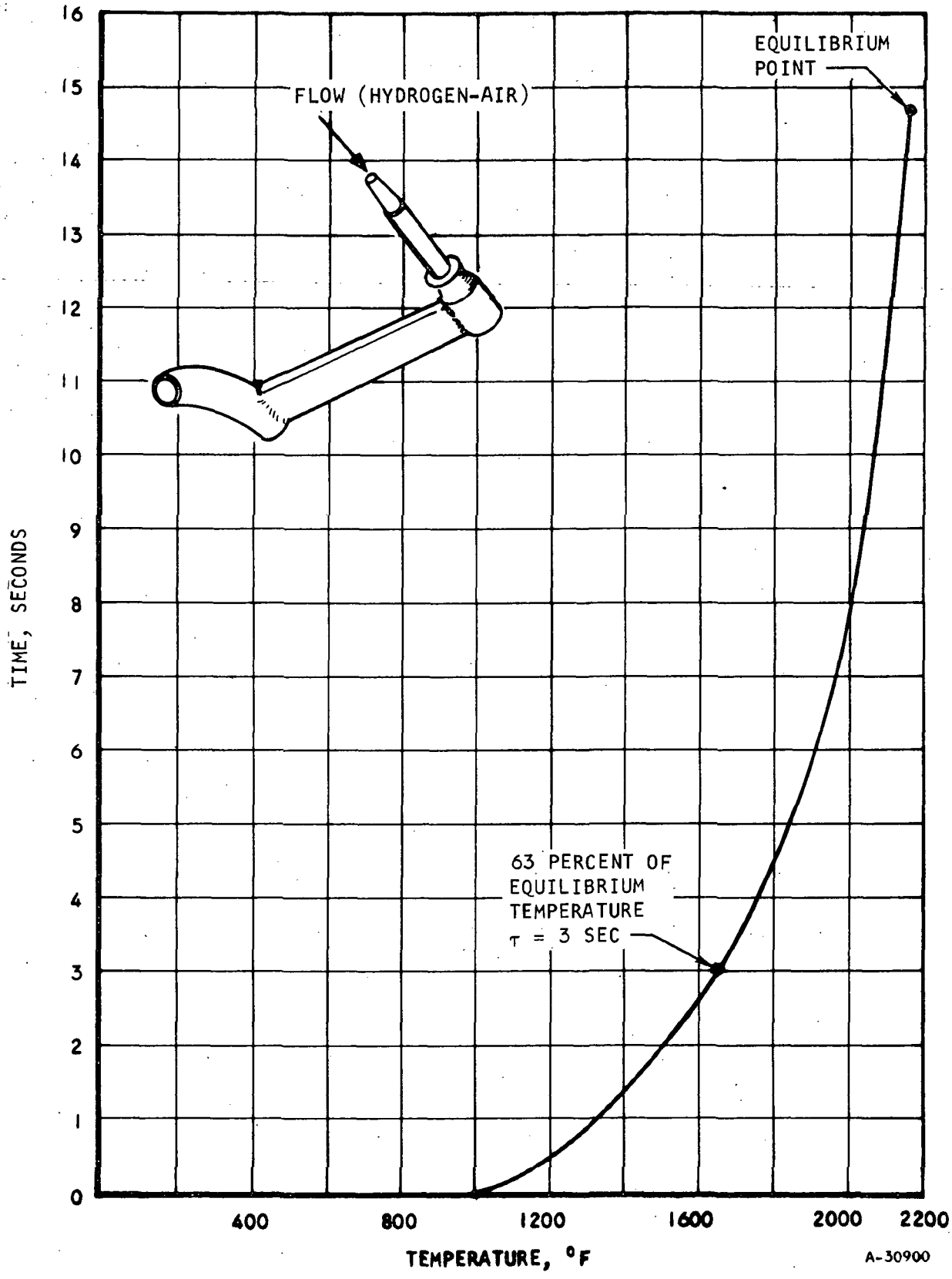

Figure 4.1-16. Time Response OAL Test Probe No. 2 Hydrogen-Air Bench Test

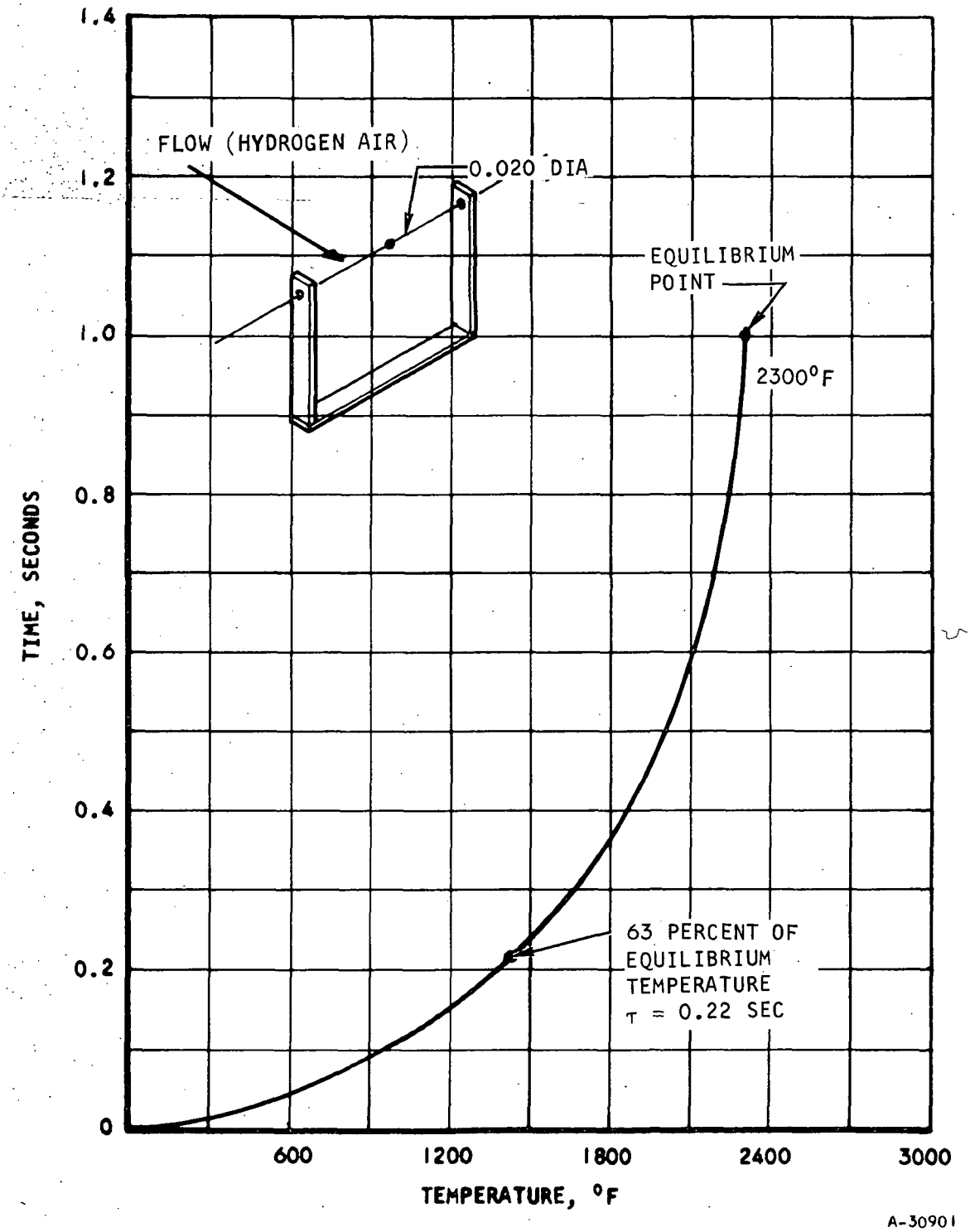

Figure 4.1-17. Time Response 0.020 Diameter W/WRe_{26} T/C in Crossflow Hydrogen-Air Combustion

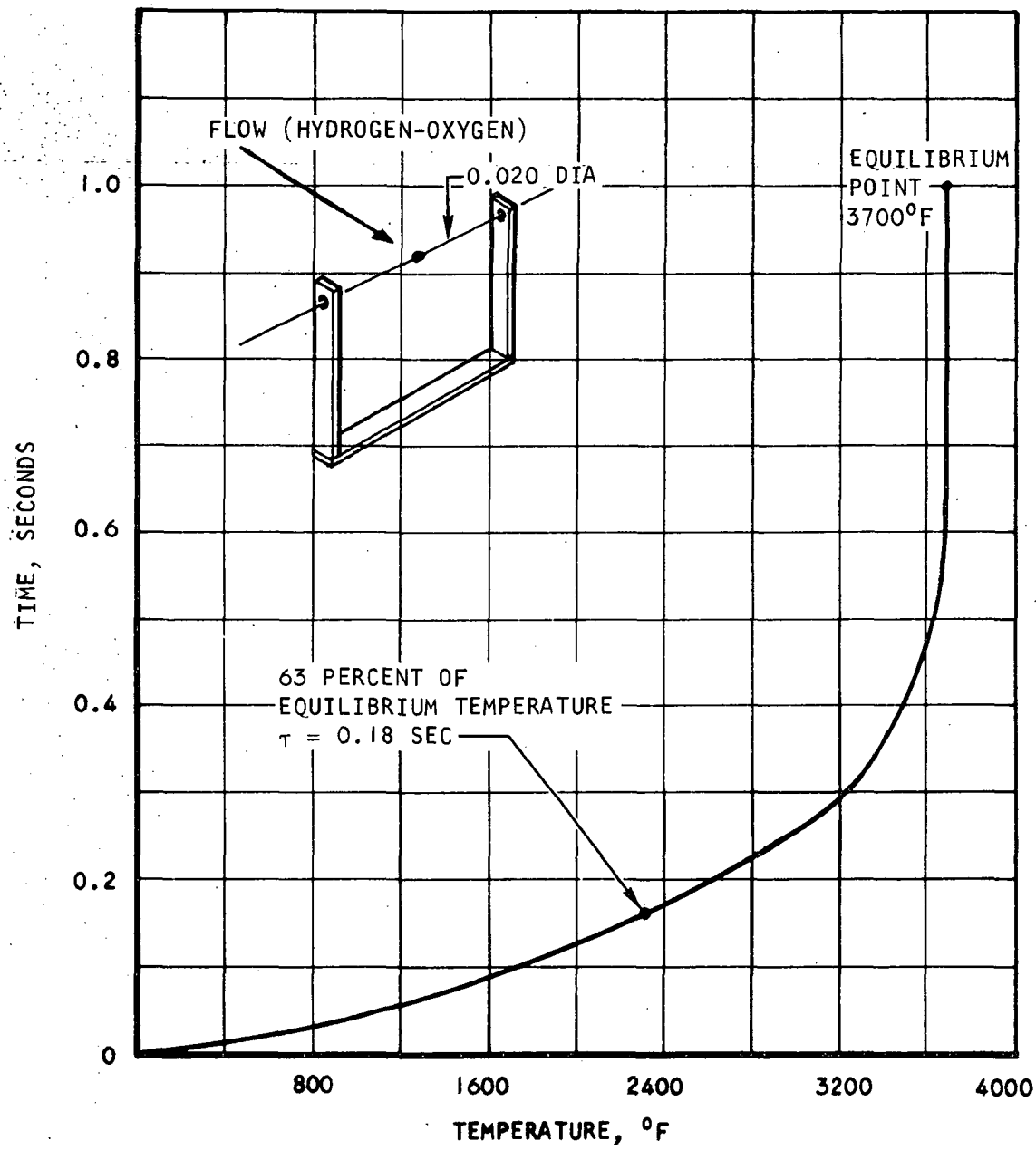

Figure 4.1-18. Time Response 0.020 Diameter W/WRe$_{26}$ T/C in Crossflow Hydrogen-Oxygen Combustion

4.2 OPTICAL TECHNIQUES

The International Practical Temperature Scale (IPTS) of 1948 defines the temperature, t, above the temperature of equilibrium between solid and liquid gold (gold point), T_{Au}, by the equation

$$\frac{N_{b\lambda}(t)}{N_{b\lambda}(t_{Au})} = \frac{e^{\frac{C_2}{\lambda(t_{Au} + T_o)}} - 1}{e^{\frac{C_2}{\lambda(t + T_o)}} - 1} \qquad (4.2\text{-}1)$$

where C_2 and the gold point, t_{Au}, are defined to be 1.438 cm deg and 1063°C, respectively; and T_o is 273.15 deg.

Temperature-measuring instruments calibrated at the National Bureau of Standards (NBS) are calibrated in terms of the IPTS; therefore, temperature calibrations above the gold point are based on Equation (4.2-1)

If it were possible to use Equation (4.2-1) directly, little more would be required concerning the basic theory and practice of optical pyrometry. However, this cannot be done because any visually observable radiation consists of a finite spectral band, and the question arises as to what wavelength to use in Equation (4.2-1). In fact, to have sufficient energy for the eye to see, most instruments used for this purpose require a large spectral bandwidth.

Since it is convenient to discuss this in terms of a particular instrument, the main features of the instrument commonly used will be given at this time. Nevertheless, the presentation will be sufficiently general to apply, with minor modification, to any such instrument, visual or photoelectric.

The instrument that is usually used to realize the IPTS above the gold point is the disappearing filament optical pyrometer. A schematic diagram of this instrument is shown in Figure 4.2-1.

4.2.1 The Disappearing Filament Pyrometer

The disappearing filament pyrometer is essentially a low-power telescope containing a red filter. An evacuated tungsten filament lamp is mounted in the focal plane, and appears as a silhouette superimposed on the field of view. To determine the temperature of a glowing object, it is viewed through the telescope and an electric current through the lamp filament, and is adjusted until the lamp filament flows with an equal brightness as the "target" or object being viewed. When both the lamp filament and the target are adjusted to an equal brightness, as viewed through the red filter, the filament image appears to blend into the target image and disappear. The lamp current under conditions of disappearance can be calibrated as a function of target temperature by using a black body of known temperature (Figure 4.2-2) as a reference standard.

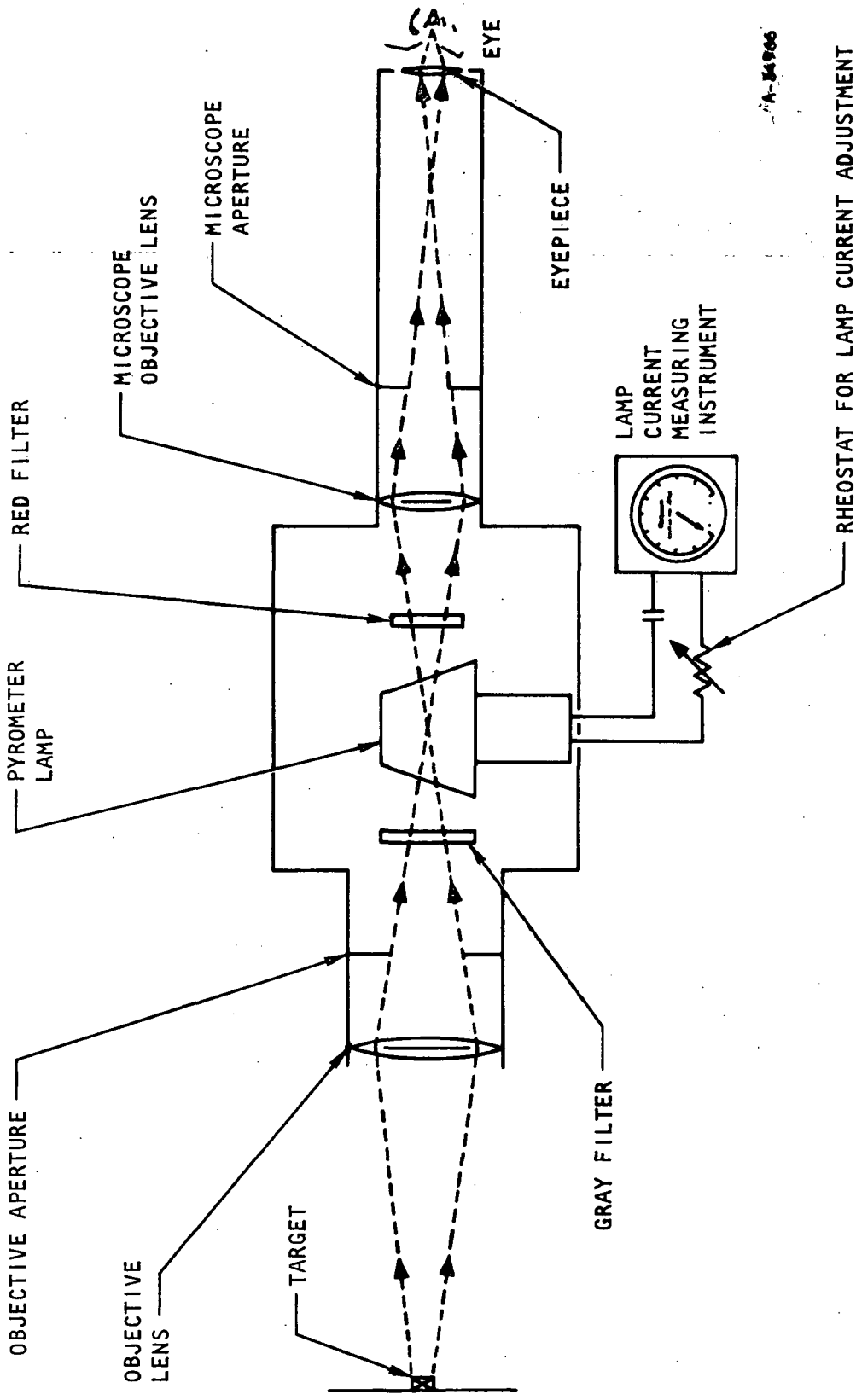

Figure 4.2-1. Conventional Disappearing-Filament Pyrometer

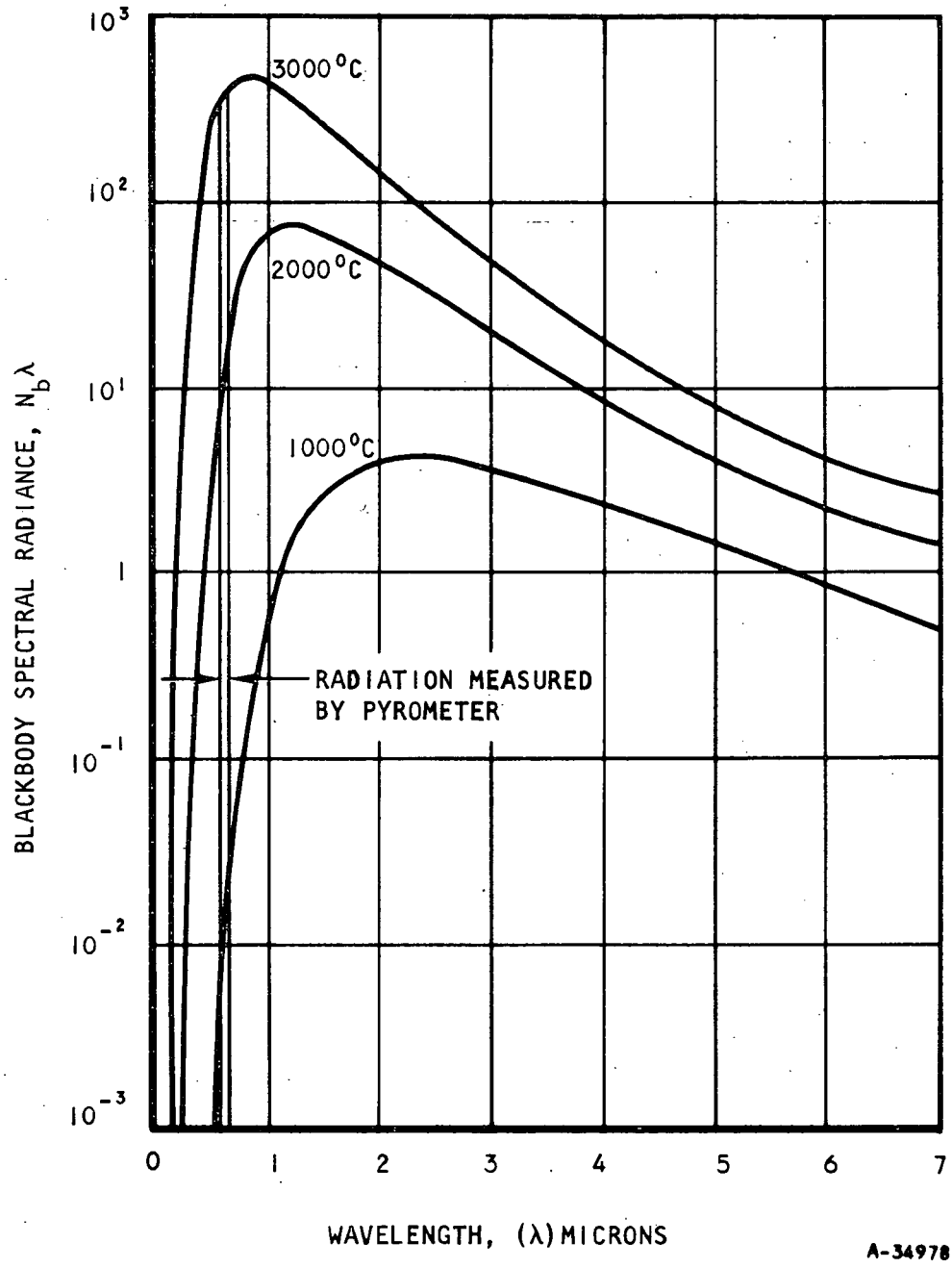

Figure 4.2-2. Planck's Black Body Radiation Distribution Function

The freezing point of gold has been accurately determined by means of gas thermometry, and serves as a reference point by which other temperatures are determined through the use of Planck's radiation law (Figure 4.2-2) that relates the spectral radiance to the temperature.

Spectral radiance is defined as the energy radiated by a body in a particular direction per unit time, per unit wavelength, per unit projected area of the body and per unit solid angle.

Black-body spectral radiance as a function of temperature and wavelength is characterized by

$$N_{b\lambda} = \frac{C_1 \lambda^{-5}/\pi}{e^{C_2/\lambda T} - 1} \qquad (4.2\text{-}2)$$

where $N_{b\lambda}$ = spectral radiance

C_1 = the first radiation constant

C_2 = 1.438 cm^0K, the second radiation constant

λ = wavelength of electromagnetic radiation

T = absolute temperature of the black body

Since intensities are not readily calculable from Planck's law, Wien's law has long been used for practical calculations. When, as at high temperatures, accuracy requires the use of Planck's law, calculation may be facilitated by the use of tables*.

Figure 4.2-3 is a comparison of intensity values calculated from Planck's, Wien's, and Rayleigh-Jeans' laws for a temperature of 1600^0K. It is apparent that the Rayleigh-Jeans law does not give accurate results except for extreme

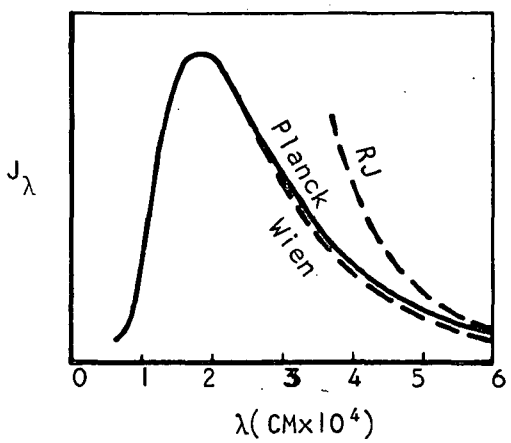

Figure 4.2-3. Comparison of Intensity Values Calculated from Planck's, Wien's, and Rayleigh-Jean's Laws for Temperature of 1600^0K

*A. N. Lowan and G. Balnch, J. Optical Soc. Am., 30, 70 (1940)

values of λT. It is apparent from the form of this law that its curve has no maximum and hence suggests radiation of an infinite amount of energy from a given radiator, which certainly is not in accord with experience.

A simpler approximate form is known as Wien's law:

$$N_{b\lambda} = \frac{C_1 \lambda^{-5}/\pi}{e^{C_2/\lambda T}} \qquad (4.2\text{-}3)$$

Although Equation (4.2-1) is used to define the IPTS, the accuracy of Equation (4.2-3) is more than adequate for most calculations involved for pyrometry. At approximately $3000^{\circ}K$, the additional inaccuracy from this consideration is $< 1^{\circ}K$.

The maximum temperature to which a pyrometer can operate is limited by the image brightness that can be comfortably tolerated by the eye and by the changes that occur in the lamp calibration at the higher temperatures.

To have a very stable pyrometer lamp, a vacuum lamp is usually used. However, to assure long-term stability, a tungsten vacuum lamp is usually not used above a brightness temperature of about $1350^{\circ}C$. Higher temperature calibrations can be attained, however, by the use of sectored disks as part of the calibrated instrument. As seen through a sectored disk having a transmittance of 0.7 percent, a $2280^{\circ}C$ black body appears to have the brightness at 6500 A of a $1350^{\circ}C$ black body. Therefore an optical pyrometer calibrated from 1063° to $1350^{\circ}C$ together with sectored disks can be used to measure temperatures higher than $1350^{\circ}C$.

There are two usual disadvantages in doing this. One is the inconvenience of using sectored disks. The other is that temperatures cannot be realized much higher than $2280^{\circ}C$ without incurring large errors from the uncertainty of the sectored disk transmittance. Although it might be possible to design and construct sectored disks with an angular opening of the disk that can be determined to better than 1 min of arc, this has not yet been done. For a 0.007-transmittance, necessary to achieve $2280^{\circ}C$, an uncertainty of 1 min of arc amounts to an uncertainty of $2.0^{\circ}C$.

A means to circumvent this dilemma is achievable by using a filter rather than a sectored disk to reduce the brightness of the source. Such a filter is called an absorbing glass and is usually inserted between the objective lens and the pyrometer lamp. The primary calibration of the pyrometer for temperature ranges using an absorbing glass would proceed as follows: the temperature t of a black body with a temperature higher than $1350^{\circ}C$ but lower than $2280^{\circ}C$ would be determined as described in the previous paragraph. Then, the sectored disk would be removed, the absorbing glass inserted, and a brightness match made.

The current in the pyrometer lamp at the match, together with the absorbing glass constitutes a calibration point at the temperature t. Since a sectored disk with a very small transmittance can be used with each absorbing glass, the observer is able to proceed to even high temperature than 2280°C.

As of May 1961, optical pyrometers are calibrated up to 2400°C at the National Bureau of Standards using tungsten-strip lamp sources. Usually for instruments used to 2800° or 3200°C, actual observations are not made above 2400°C. In some optical pyrometers, the range to 4200°C is reached by using two absorbing glasses in series.

4.2.2 The Primary Calibration at the Gold Point

A primary calibration is the calibration of an optical pyrometer in which an attempt is made to realize the IPTS directly rather than from a calibrated pyrometer or source. The first step in the primary calibration of an optical pyrometer is a brightness match at the gold point. The spectral brightness of a gold-point black body, $\beta_\lambda(t_{Au})$, as seen through such a typical optical pyrometer, is shown in Figure 4.2-4. The area under β_λ is equal to the brightness and to the integrals in the defining equivalence relation.

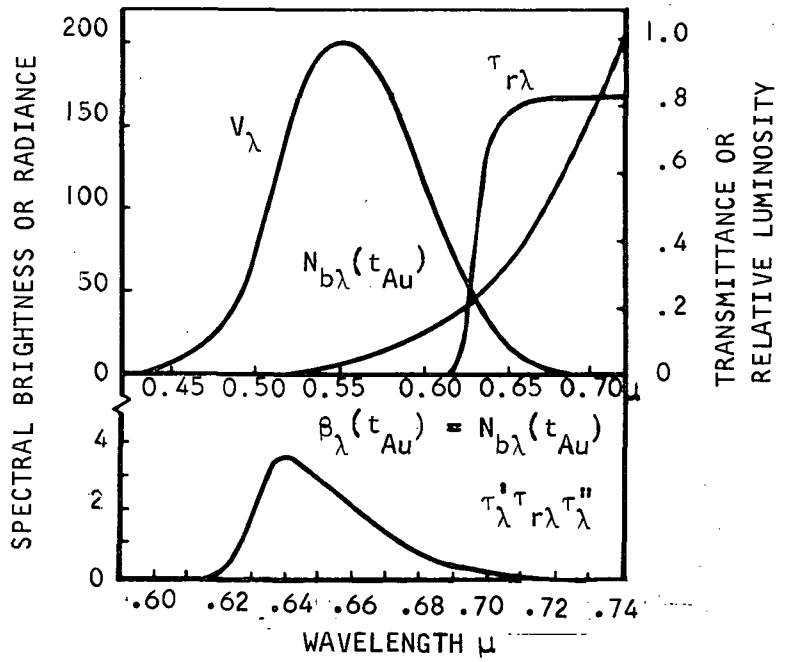

$\beta_\lambda(t_{Au})$ as observed by an observer with a relative luminosity function

V_λ as observed through an optical pyrometer having spectral transmittances

$\tau_{r\lambda}$ as observed for the red glass

$T_\lambda = 0.8$ and $T''_\lambda = 0.7$ for all the optical elements preceding and following the pyrometer lamp filament, respectively, excluding the red

Figure 4.2-4. The Spectral Brightness of a Gold-point Black Body

$$\int_0^\infty N_{b\lambda}\,(t_{Au})\,\tau_\lambda'\,\tau_{\tau\lambda}\,\tau'\lambda'\,V_\lambda d\lambda = \int_0^\infty N_\lambda\,(t_1)\,\tau_{\tau\lambda}\,\tau'_\lambda'\,V_\lambda d\lambda$$

When the brightness match is made, measurement of the current in the pyrometer lamp realizes the primary calibration at the gold point. It should be emphasized that the temperature of the pyrometer lamp t_1, or the lamp current at the match, depends on the particular transmittances and the observer's relative luminosity factor. In general, changing any of these will change the calibration. In the 1960 NBS data where five observers were used, the standard deviation of the primary calibration observations was estimated to be 0.4^0C.

4.2.3 Traceability of Accuracy

The NBS estimates of the accuracy of the primary calibrations have been made by comparing them with the mean of similar calibrations from other national laboratories throughout the world.

It is felt that the results of the 1958 primary calibration at NBS (Table 4.2-I) is about the best that can be expected from visual optical pyrometry. The remaining major limitations are the sensitivity of the eye to differences in brightness, and the knowledge of the mean effective wavelengths.

4.2.4 Secondary Calibrations

The International Practical Temperature Scale that is realized and maintained at the National Bureau of Standards is distributed throughout the United States through the NBS calibration and test services.

Ideally, the uncertainties stated on certificates of calibrations are relatable to the estimated standard deviation of t. Since adequate information has not been obtained to make this sufficiently quantitative it is not meaningful. Thus, until sufficient data are obtained, preliminary NBS "judgment type" estimates of the sum of the constituent determination errors are stated on the calibration certificates.

These are termed maximum uncertainties. For optical pyrometers, they are usually given at $\pm4^0C$ at 800^0C, $\pm3^0C$ at 1063^0C, $\pm8^0C$ at 2800^0C, and about $\pm40^0C$ at 4000^0C.

An uncertainty error of about 15^0F at 5000^0F is therefore the best that is presently certifiable for optical pyrometers by the NBS. It must be reemphasized that these errors are associated with static temperature determinations in a black-body cavity and are generally not approachable for dynamic measurements.

For dynamic temperature determinations, such as is required in the elevated total temperatures of the ramjet streams, errors that accrue from application, however, far overshadow the static NBS limits, and are more often than not, an order of magnitude or more greater.

The absolute temperature traceability is required through optical pyrometry in accordance with the general discussion presented herein.

TABLE 4.2-1

NBS PRIMARY OPTICAL PYROMETER CALIBRATIONS AT THE GOLD POINT USING A GLASS PRISM AND AN APPARENT TEMPERATURE OF 1323.9°K

Observer	1957				1958				1960(a)			
	L_t Pyrometer Lamp Current (b)	Number of Freezes	Standard Deviation(c)		L_t Pyrometer Lamp Current (b)	Number of Freezes	Standard Deviation(c)		L_t Pyrometer Lamp Current (b)	Number of Freezes	Standard Deviation(c)	
			S_t	S_2			S_t	S_2			S_t	S_2
	ma		ma		ma		ma	ma	ma		ma	ma
RDL	104.465	9	0.023		104.450	17	0.019		104.484	3	0.029	
RCH									104.457	1		
RCG					104.426	16	0.036		104.427	2	0.028	
HJK									104.410	1		
EL									104.573	2	0.018	
ATH					104.522	12	0.042					
Mean of all observers	104.465				104.466			0.049	104.470			0.059

(a) The 1960 data were obtained using a horizontal black body, and therefore the glass prism used with the vertical black body was not required.. As a result, for comparison purposes, the 1960 data were normalized to 1323.9°K.
(b) 0.05 ma is equivalent to 0.3°C.
(c) S_t is the sample standard deviation of an individual's freezing point, determinations about his own mean. S_2 is the sample standard deviation of individual observer's mean determinations about the mean of the determinations of all observers.

4.3 DOUBLE-SONIC ORIFICE TOTAL-TEMPERATURE/PRESSURE PROBE

4.3.1 Problem Statement

Devices are needed to measure the total temperature and total pressure in the internal supersonic flow field of a hypersonic ramjet engine. These devices must be able to operate in a temperature of up to about 5800°R, a high velocity stream of about Mach 3, an oxygen-rich atmosphere, and the effluent gases of an oxygen and hydrogen burner. These devices must be suitable for installation and use in a variety of test configurations for a hypersonic ramjet engine test program.

4.3.2 Topical Background

To determine combustor performance and how it is influenced by injector geometry, jet penetration, spreading, and mixing, total temperature and total pressure at several points in the combustor must be measured while the engine is operating. The probe concept and size are affected by the necessity of keeping the combustor duct unblocked so it will not become choked. Also, the probe must be cooled to attain sufficient life to make the tests.

Obtaining temperature and pressure measurements from a supersonic oxygen and hydrogen burner involves many factors. The probes and supporting systems must be cooled. The coolant selected must be compatible with the test facility, installation, and test objectives. In the cases discussed here, the test objectives have necessitated circulation of the coolant through the probe. Further, the test facilities and configurations using the probe will allow the use of two alternate coolant fluids, hydrogen and water.

4.3.3 Overall Approach

One gas aspirating cooled probe design will be tested and fabricated. The probe shown in Figure 4.2-1 of Reference 4-5 will be used in the Phase II segmented combustor test rig. The probe is internally cooled to a temperature compatible with structural requirements and the aspirated air is cooled to about 2300°R or less.

The probe detects the total temperature by two independent methods: the two-sonic orifice method, and the calorimetric method. The working principles of these methods are described in Reference 4-6. Both method of temperature measurement are incorporated in the same physical probe. Evaluation of the total temperature from the two-sonic orifice method requires measurements of the total pressure in the inlet nozzle and total pressure and temperature in the second nozzle. The calorimetric method requires the total pressure and total temperature in the second nozzle, a mass flow rate of the coolant, the inlet and outlet temperature of the coolant, and a check valve for stopping the gas aspiration to take tare measurements.

Since the flow of gas through the probe must be deadheaded to make a tare measurement of heat flux, due to the external freestream flow around the probe, a pressure transducer will be used to measure total pressure. The freestream total pressure may then be computed by using the Rayleigh equation as solved for a real gas. It is possible therefore, to make three determinations with the probe; total temperature by the double-sonic orifice method, total temperature by the calorimetric method, and total pressure.

4.3.4 Double-Sonic Orifice Probe Status

Fabrication of the double-sonic orifice probe has been successfully completed. The following calibration and development tests have been successfully completed:

Proof pressure and leak tests

Coolant circuit ΔP at the required flow rate

Calibration of each sonic orifice for determination of discharge coefficient

Future tests include:

Verification of the cooling system design by exposing the entire probe to hot gas conditions and comparing the actual coolant ΔT's with the predicted values.

Calibration tests of the double-sonic orifice and calorimetric temperature measuring systems under hot gas conditions using the glowbody and optical pyrometry technique.

4.3.5 Analytical Design

The following paragraphs include the analytical technique, results, and discussion of an error analysis of the double-sonic orifice and calorimetric techniques.

4.3.5.1 Double-Sonic Orifice Error Analysis Method

The double-sonic orifice equation used for the computation of T_{T_t} is as follows:

$$T_{T_t} = T_{T_2} \left(\frac{C_{D_t} A_t P_{T_t}}{C_{D_2} A_2 P_{T_2}} \right)^2 \frac{A}{B}$$

where: $A = \sqrt{\frac{\gamma_1}{R_1}\left(\frac{2}{\gamma_1+1}\right)^{\frac{\gamma_1+1}{\gamma_1-1}}}$

$B = \sqrt{\frac{\gamma_2}{R_2}\left(\frac{2}{\gamma_2+1}\right)^{\frac{\gamma_2+1}{\gamma_2-1}}}$

The measurand errors may be expressed as follows:

From mathematics the exact differential of a function $Y = f(X_1, x_2, \cdots x_n)$ of n variables is

$$dY = \sum_{i=1}^{n} \frac{\partial f}{\partial X_i} dX_i$$

$$\frac{\partial T_{T_1}}{\partial T_{T_2}} = \left(\frac{P_{T_1} C_{D_1} A_1}{P_{T_2} C_{D_2} A_2}\right)^2 \frac{A}{B}$$

$$\frac{\partial T_{T_1}}{\partial P_{T_1}} = 2T_{T_2}\left(\frac{P_{T_1} C_{D_1} A_1}{P_{T_2} C_{D_2} A_2}\right)\left(\frac{C_{D_1} A_1}{P_{T_2} C_{D_2} A_2}\right)\left(\frac{A}{B}\right)$$

$$= \frac{2T_{T_1}}{P_{T_1}}$$

$$\frac{\partial T_{T_1}}{\partial C_{D_1}} = \frac{2T_{T_1}}{C_{D_1}}$$

$$\frac{\partial T_{T_1}}{\partial A_1} = \frac{2T_{T_1}}{A_1}$$

$$\frac{\partial T_{T_1}}{\partial P_{T_2}} = 2T_{T_2}\left(\frac{P_{T_1} C_{D_1} A_1}{P_{T_2} C_{D_2} A_2}\right)(-1)\left(\frac{P_{T_1} C_{D_1} A_1}{C_{D_2} A_2}\right) P_{T_2}^{-2}\left(\frac{A}{B}\right)$$

$$= \frac{-2T_{T_1}}{P_{T_2}}$$

$$\frac{\partial T_{T_1}}{\partial C_{D_2}} = \frac{-2T_{T_1}}{C_{D_2}}$$

$$\frac{\partial T_{T_1}}{\partial A_2} = \frac{-2T_{T_1}}{A_2}$$

$$\frac{dT_{T_1}}{T_{T_1}} = \frac{dT_{T_2}}{T_{T_2}} + \frac{2dP_{T_1}}{P_{T_1}} - \frac{2dP_{T_2}}{P_{T_2}} + \frac{2dC_{D_1}}{C_{D_1}} - \frac{2dC_{D_2}}{C_{D_2}} + \frac{2dA_1}{A_1} - \frac{2dA_2}{A_2}$$

The measurand errors are then combined as shown below:

$$\frac{\Delta T_{T_1}}{T_{T_1}} = \left[\left(\frac{\Delta T_{T_2}}{T_{T_2}}\right)^2 + 4\left(\frac{\Delta P_{T_1}}{P_{T_1}}\right)^2 + 4\left(\frac{\Delta P_{T_2}}{P_{T_2}}\right)^2 + 4\left(\frac{\Delta C_{D_1}}{C_{D_1}}\right)^2 + 4\left(\frac{\Delta C_{D_2}}{C_{D_2}}\right)^2 + 4\left(\frac{\Delta A_1}{A_1}\right)^2 + 4\left(\frac{\Delta A_2}{A_2}\right)^2\right]^{1/2}$$

By inserting the values and the errors for each measurand shown in Table 4.3-I and allowing each measurand to vary linearly over its range (all varying at the same rate) the error curve shown in Figure 4.3-I is obtained.

4.3.5.2 Calorimetric Technique Error Analysis Method

The calorimetric technique equation used for the computation of T_{T_1} is as follows:

$$T_{T_1} = \left(\frac{C_{Pc}}{C_{Pg}}\right)\frac{\dot{m}_c\left(\Delta T_{on} - \Delta T_{off}\right)}{\dot{m}_g} + T_{T_2}$$

where $\dot{m} = f\left(P_{T_2}, A_2, T_{T_2}\right)$

$$= \sqrt{\frac{\gamma_2}{gR_2}\left(\frac{2}{1+\gamma_2}\right)^{\left(\frac{\gamma_2+1}{\gamma_2-1}\right)}}\frac{C_{D_2} P_{T_2} A_2}{\sqrt{T_{T_2}}} = k\, C_{D_2}\, P_{T_2}\, A_2\, T_{T_2}^{-1/2}$$

The measurand errors may be expressed as follows:

$$dT_{T_1} = \frac{\partial T_{T_1}}{\partial \dot{m}_c} d\dot{m}_c + \frac{\partial T_{T_1}}{\partial \Delta T_{on}} d\left(\Delta T_{on}\right) + \frac{\partial T_{T_1}}{\partial \Delta T_{off}} d\left(\Delta T_{off}\right) +$$

$$\frac{\partial T_{T_1}}{\partial T_{T_2}} d\,T_{T_2} + \frac{\partial T_{T_1}}{\partial P_{T_2}} d\,P_{T_2} + \frac{\partial T_{T_1}}{\partial A_2} dA_2 + \frac{\partial T_{T_1}}{\partial C_{D_2}} d\,C_{D_2}$$

$$\frac{\partial T_{T_1}}{\partial \dot{m}_c} = \frac{C_{Pc}}{C_{Pg}}\frac{\left(\Delta T_{C,on} - \Delta T_{C,off}\right)}{\dot{m}_g} = \frac{T_{T_1} - T_{T_2}}{\dot{m}_c}$$

TABLE 4.3-1

DOUBLE-SONIC ORIFICE PROBE
ERROR ANALYSIS INPUT

Segmented Combustor Test Rig Application:

				3σError, Percent FS
P_{T_1}	60-280 psia			±2.0
P_{T_2}	41-225 psia			±2.0
T_{T_2}	900-1300°R			±1.0
$\dot{w}\ H_2O$	8 gpm			±2.0
$\Delta T\ H_2O_{off}$	60-33°F			±2.0
$\Delta T\ H_2O_{on}$	82-45°F			±2.0
C_{D_1}	0.964			±0.5
C_{D_2}	0.960			±0.5
A_1	0.0295 $in.^2$			±0.5
A_2	0.0201 $in.^2$			±0.5
	T_{T_1}=5400	T_{T_1}=2900		
γ_1	1.15	1.35		±0
γ_2	1.30	1.40		±0
R_1	64.00	53.30	$\frac{FT\text{-}LB_f}{LB_m\ ^oR}$	±0
R_2	64.00	53.30	$\frac{FT\text{-}LB_f}{LB_m\ ^oR}$	±0
C_{Pgas}	$\frac{R_2}{1-\frac{1}{\gamma_2}} \times \frac{1}{778}\ \frac{BTU}{LB_m\ ^oR}$			±0
$C_{P\ H_2O}$	$1.0\ \frac{BTU}{LB_m\ ^oR}$			±0

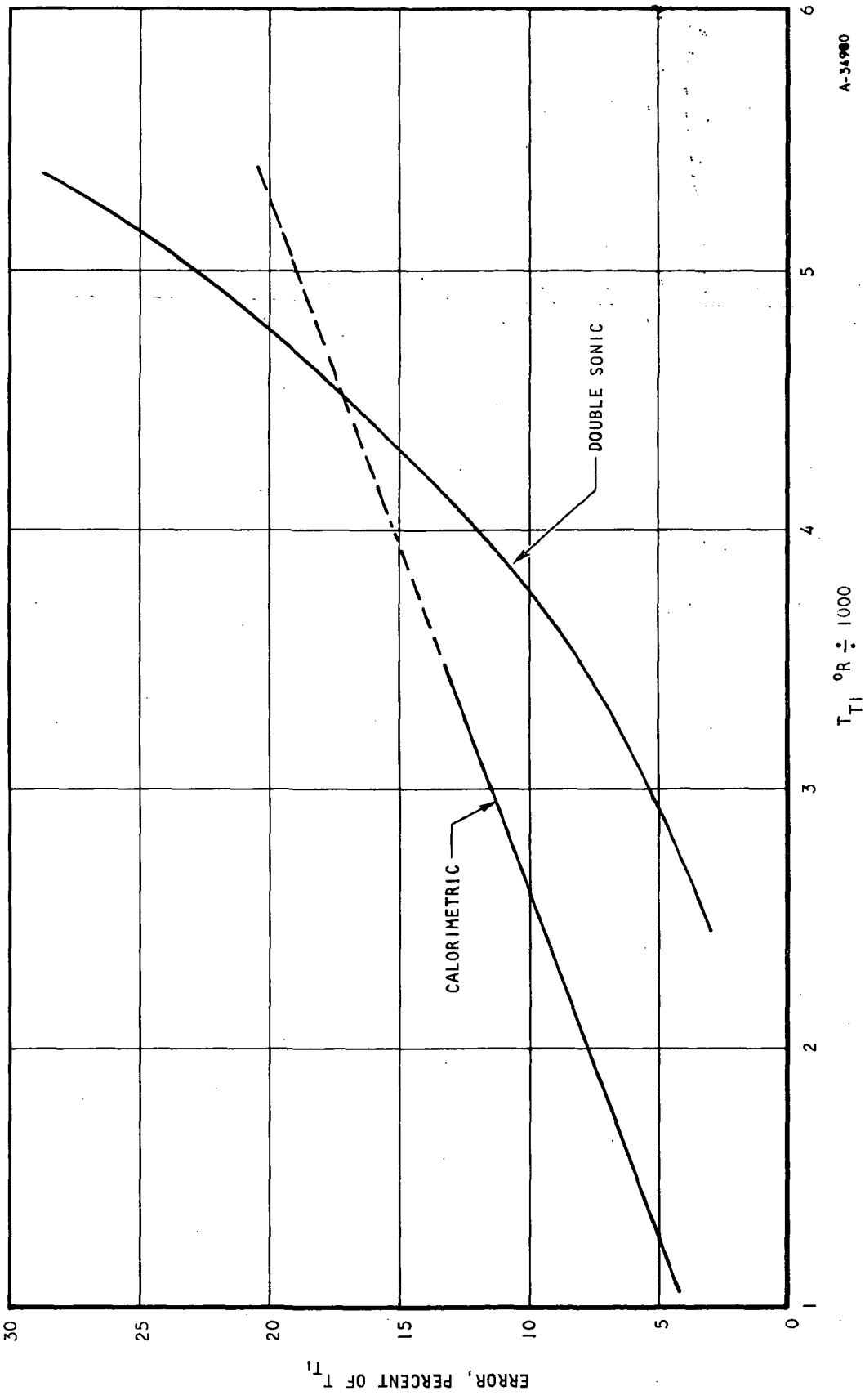

Figure 4.3-1. Calorimetric Versus Double-Sonic Orifice Technique Random Error in T_{T_1}

$$\frac{\partial T_{T_1}}{\partial T_{on}} = \frac{C_{Pc}}{C_{Pg}} \frac{\dot{m}_c}{\dot{m}_g} = \frac{T_{T_1} - T_{T_2}}{\Delta T_{on} - \Delta T_{off}} \; ; \; \frac{\partial T_{T_1}}{\partial T_{off}} = \frac{-C_{Pc}\,\dot{m}_c}{C_{Pg}\,\dot{m}_g} = - \frac{T_{T_1} - T_{T_2}}{\Delta T_{on} - \Delta T_{off}}$$

$$T_{T1} = \frac{\dot{m}_c\, C_{Pc}\, (\Delta T_{c,on} - \Delta T_{c,off})\, \sqrt{T_{T_2}}}{C_{Pg}\, P_{T_2}\, C_{Pg}\, A_2\, \sqrt{f(\gamma, R)}} + T_{T_2}$$

$$\frac{\partial T_{T_1}}{\partial T_{T_2}} = 1 + \frac{C_{Pd}\, m_c\, (\Delta T_{c,on} - \Delta T_{c,off})\, (-1)\, (-1/2)\, k\, P_{T_2}\, A_2}{C_{Pg}\, m_g^2\, \sqrt{T_{T_2}}\, T_{T_2}}$$

$$= \frac{T_{T_2} + T_{T1}}{2\, T_{T_2}}$$

$$\frac{\partial T_{T_1}}{\partial C_{D_2}} = \left(\frac{C_{Pc}}{C_{Pg}}\right) \frac{\dot{m}_c\, (\Delta T_{c,on} - \Delta T_{c,off})\, (-1)}{m_g^2}\, k\, P_{T_2} \cdot A_2\, T_{T_2}^{-1/2} = \frac{T_{T_2} - T_{T_1}}{C_{D_2}}$$

$$\frac{\partial T_{T_1}}{\partial P_{T_2}} = \frac{C_{Pc}}{C_{Pg}} \frac{\dot{m}_c \left(\Delta T_{c,on} - \Delta T_{c,off}\right)}{(-\dot{m}_g^2)}\, K\, A_2\, T_{T_2}^{-1/2}$$

$$= - \frac{C_{Pc}}{C_{Pg}} \frac{\dot{m}_c \left(\Delta T_{c,on} - \Delta T_{c,off}\right)}{\dot{m}_g} \frac{1}{P_{T_2}}$$

$$= \frac{T_{T_2} - T_{T_1}}{P_{T_2}}$$

$$\frac{\partial T_{T_1}}{\partial A_2} = \frac{C_{Pc}}{C_{Pg}}\, \dot{m}_c\, (\Delta T_{c,on} - \Delta T_{c,off})\, (-1)\, \dot{m}_g^{-2}\, K\, P_{T_2}\, T_{T_2}^{-1/2}$$

$$= \frac{C_{Pc}}{C_{Pg}} \times \frac{\dot{m}_c}{\dot{m}_g} (\Delta T_{c,on} - \Delta T_{c,off}) \frac{1}{A_2}$$

$$= \frac{T_{T_2} - T_{T_1}}{A_2}$$

The measurand errors are then combined as follows:

$$\frac{\Delta T_{T_1}}{T_{T_1}} = \frac{1}{T_{T_1}} \left\{ \left[\frac{\left(T_{T_1} - T_{T_2}\right)}{\dot{m}_c} \Delta \dot{m}_c \right]^2 + \left[\frac{\left(T_{T_1} - T_{T_2}\right)}{\Delta^2 T_c} \Delta T_{on} \right]^2 + \left[\frac{\left(T_{T_1} - T_{T_2}\right)}{\Delta^2 T_c} \Delta T_{off} \right]^2 + \right.$$

$$\left. \left[\frac{\left(T_{T_1} + T_{T_2}\right)}{2T_{T_2}} \Delta T_{T_2} \right]^2 + \left[\frac{\left(T_{T_1} - T_{T_2}\right)}{P_{T_2}} \Delta P_{T_2} \right]^2 + \left[\frac{\left(T_{T_1} - T_{T_2}\right) \Delta A_2}{A_2} \right] \right\}^{1/2}$$

$$= \left(\frac{T_{T_1} - T_{T_2}}{T_{T_1}} \right) \left[\left(\frac{\Delta \dot{m}_c}{\dot{m}_c} \right)^2 + \left(\frac{\Delta T_{on}}{\Delta^2 T_c} \right)^2 + \left(\frac{\Delta T_{off}}{\Delta^2 T_c} \right)^2 + \left(\frac{\Delta P_{T_2}}{P_{T_2}} \right)^2 + \left(\frac{\Delta A_2}{A_2} \right)^2 + \right.$$

$$\left. \left(\frac{\Delta C_{D_2}}{C_{D_2}} \right)^2 + \left(\left(\frac{T_{T_1} + T_{T_2}}{T_{T_1} - T_{T_2}} \right) \frac{\Delta T_{T_2}}{2T_{T_2}} \right)^2 \right]^{1/2}$$

Inserting the values from Table 4.3-I as before, the error curve shown in Figure 4.3-I is obtained.

4.3.5.3 Discussion and Conclusions

From the curves it can be seen that up to about 4500°R the double-sonic orifice technique yeilds less error in determination of T_{T_1} than the calorimetric technique. Above 4500°R the calorimetric technique is the more accurate. At 3000°R the error in T_{T_1} is 6 percent using the double-sonic orifice technique and 10.6 percent using the calorimetric technique. At 4500°R the error in T_{T_1} is 16.8 percent for both methods and at 5400°R the error in T_{T_t} is 28 percent for the double-sonic orifice technique and 19.6 percent for the calorimetric technique.

An examination of the two error equations reveals that the coefficients of the error terms in the double-sonic orifice error equation causes the quadratic shape of the error curve for the range of T_{T_t} shown. Also, the double-sonic orifice equation contains fewer measurands and therefore fewer sources of errors than the calorimetric equation, even though the error increases at a faster rate, making the double-sonic orifice technique more desirable below 4500°R freestream total temperature.

Due to the decrease in total pressure recovery factor and pitot total pressure with increasing Mach number which causes the error in percent of reading for the pressure measurands to increase, the error in T_{T_t} generally increases with increasing temperature. This would be the case if the probe were used for freestream total temperature measurement.

See Figure 4.1-6 for the format listing and a sample of the output for the computer program used for this error analysis.

4.3.6 Design Effort

No further design effort was required or performed during this reporting period.

4.3.7 Manufacturing

Primary effort during this reporting period was directed toward the fabrication of the probe that was completed in December 1967.

4.3.8 Testing

The preliminary tests performed on the initial gas sampling probe and outlined in Reference 4-6, Paragraph 3.2.7 were also successfully performed on the double-sonic orifice probe.

4.3.9 Future Action

Tests will be performed to demonstrate mechanical integrity of the probe, adequate cooling capability, and freedom from flutter. Calibration tests of the double-sonic orifice and calorimetric temperature measurement features under simulated combustor conditions will also be performed after completion of the development tests.

4.3.10 Questions Raised by NASA

The following items are in reply to previous questions raised by NASA.

Double-Sonic Orifice Method--In the double-sonic orifice probe sketch shown in Figure 4.2-1 of Reference 4-1, the second sonic orifice is removable, this allowing calibration of each orifice separately at choked conditions. Measuring static pressure as suggested in NASA letter L/HRE-089 (JDM) is then unnecessary and even undesirable; errors up to 40 percent in throat static pressure measurement in a converging-diverging symmetric nozzle operating at or near choked conditions have been reported (Reference 4-7). For this reason, each orifice will be calibrated separately at choked conditions.

Calorimetric Method--The probe coolant ΔT's predicted for the internal gas flow on and off are shown in Table 4.3-2.

TABLE 4.3-2

PROBE COOLANT ΔT's

	Hot Gas Conditions Upstream of Probe	Inlet Coolant Conditions	Outlet Coolant Conditions			
			Internal Gas Flow On		Internal Gas Flow Off	
			Probe Coolant	Support Coolant	Probe Coolant	Support Coolant
Double-sonic orifice total-temperature probe	M = 1.8 p_T = 52 psia T_T = 5400°R	$\dot{w}$ = 8 gpm T = 70°F	$\dot{w}$ = 3 gpm T = 152°F	$\dot{w}$ = 5 gpm T = 155°F	$\dot{w}$ = 3 gpm T = 130°F	$\dot{w}$ = 5 gpm T = 150°F
Gas sampling probe (maximum heat load)	M = 2.9 p_T = 275 psia T_T = 4700°R	$\dot{w}$ = 7 gpm T = 70°F	$\dot{w}$ = 2 gpm T = 255°F	$\dot{w}$ = 5 gpm T = 170°F	$\dot{w}$ = 2 gpm T = 211°F	$\dot{w}$ = 5 gpm T = 165°F
Gas sampling probe (minimum heat load)	M = 3 p_T = 100 psia T_T = 2200°R	$\dot{w}$ = 6 gpm T = 70°F	$\dot{w}$ = 1 gpm T = 120°F	$\dot{w}$ = 5 gpm T = 83°F	$\dot{w}$ = 1 gpm T = 101°F	$\dot{w}$ = 5 gpm T = 82°F

NOTE: See Reference (4-7) for probe geometries and cooling systems.

5.0 FUEL-COOLANT WEIGHT FLOW RATE MEASUREMENTS

5.1 PROBLEM STATEMENT

There are two reasons for measuring the flow rate of fuel to the engine: the determination of the internal specific impulse of the engine; and the determination of flight fuel flow so that the experiment may be programmed for a fuel-to-air ratio. The determination of specific impulse requires a greater accuracy in the measurement of fuel-flow rate than the flight fuel measurement.

The internal specific impulse I_{si} is given by

$$I_{si} = \frac{T_{int}}{\dot{W}_f} \qquad (5.1\text{-}1)$$

where T_{int} is the internal thrust and $\dot{W}_f$ is the fuel flow rate to the burners. I_{si} must be measured as accurately as possible; an error of less than ±5 percent is the objective.

5.2 TOPICAL BACKGROUND

There are two methods under consideration for measuring in-flight fuel flow. A third method is limited to ground evaluation only of the engine. The three methods are as follows:

(a) Measure the fuel flow to the burners using the fuel injector ports as calibrated orifices. This is the original method proposed, and has the advantage of requiring only one flow determination. The conceptual disadvantage is that variation in the discharge coefficient may adversely affect the accuracy.

(b) Measure the inlet fuel flow to the pump and all the fuel dumped overboard. The difference is the combustion fuel. This method has two important disadvantages. First, in some cases the combustion fuel is the difference of two nearly equal fuel-flow rates; therefore, the relative error in combustion fuel flow would be large even though the individual relative errors of the two measurements were small. Second, measurements are made at two or more different points in the flow stream. Except during steady-flow conditions, the computation of combustion fuel flow would be difficult and subject to large error.

(c) Calibrate the fuel valves and use position indicator readings as an indication of volume f ow. This method is limited to ground evaluation of the engine, and is based upon knowing how the discharge coefficient depends on the total pressure and temperature upstream from the valves.

5.3 OVERALL APPROACH

To achieve temperature control, the overall approach measures the difference between $\dot{W}_T$, the total weight flow to the engine, and $\dot{W}_D$, the flow of all the unburned fuel dumped overboard. The dump flow consists of two parts. A small portion of it powers the turbine that drives the pump. These parts are denoted $\dot{W}_{D1}$, main dump flow, and $\dot{W}_{D2}$, turbine flow. Thus

$$\dot{W}_D = \dot{W}_{D1} + \dot{W}_{D2} \qquad (5.3\text{-}1)$$

The combustion-fuel weight-flow rate, $\dot{W}_f$, is the difference between the total fuel flow and the dump flow, and is given by

$$\dot{W}_f = \dot{W}_T - \dot{W}_{D1} - \dot{W}_{D2} \qquad (5.3\text{-}2)$$

The measurement system proposed for determining $\dot{W}_f$ is shown schematically in Figure 5.3-1. The weight flow rate of liquid hydrogen to the pump is the total rate $\dot{W}_T$ and is determined from three measurements. These are the volume-flow rate, the pressure, and the temperature, given by the transducers FX-1, PX-1, and TX-1. The main dump flow rate $\dot{W}_{D1}$ is determined by the stagnation pressure and stagnation temperature at the inlet of the choked sonic nozzle, given by transducers PX-2 and TX-2. The turbine weight flow rate is given by the discharge coefficient of the turbine nozzles and the stagnation pressure and temperature at the turbine inlet. The turbine inlet pressure and temperature are given by transducers PX-3 and TX-3.

This method of measuring the volume flow rate through the turbine $\dot{W}_{D2}$ was chosen for the following reasons:

(a) The hydrogen gas at the turbine inlet will be about 1200°F. There are no commercially available flow transducers that can be used at that temperature.

(b) Even though the method may lead to a large relative error in $\dot{W}_{D2}$, the absolute error and the resulting error of $\dot{W}_f$, will be small due to the size of $\dot{W}_{D2}$.

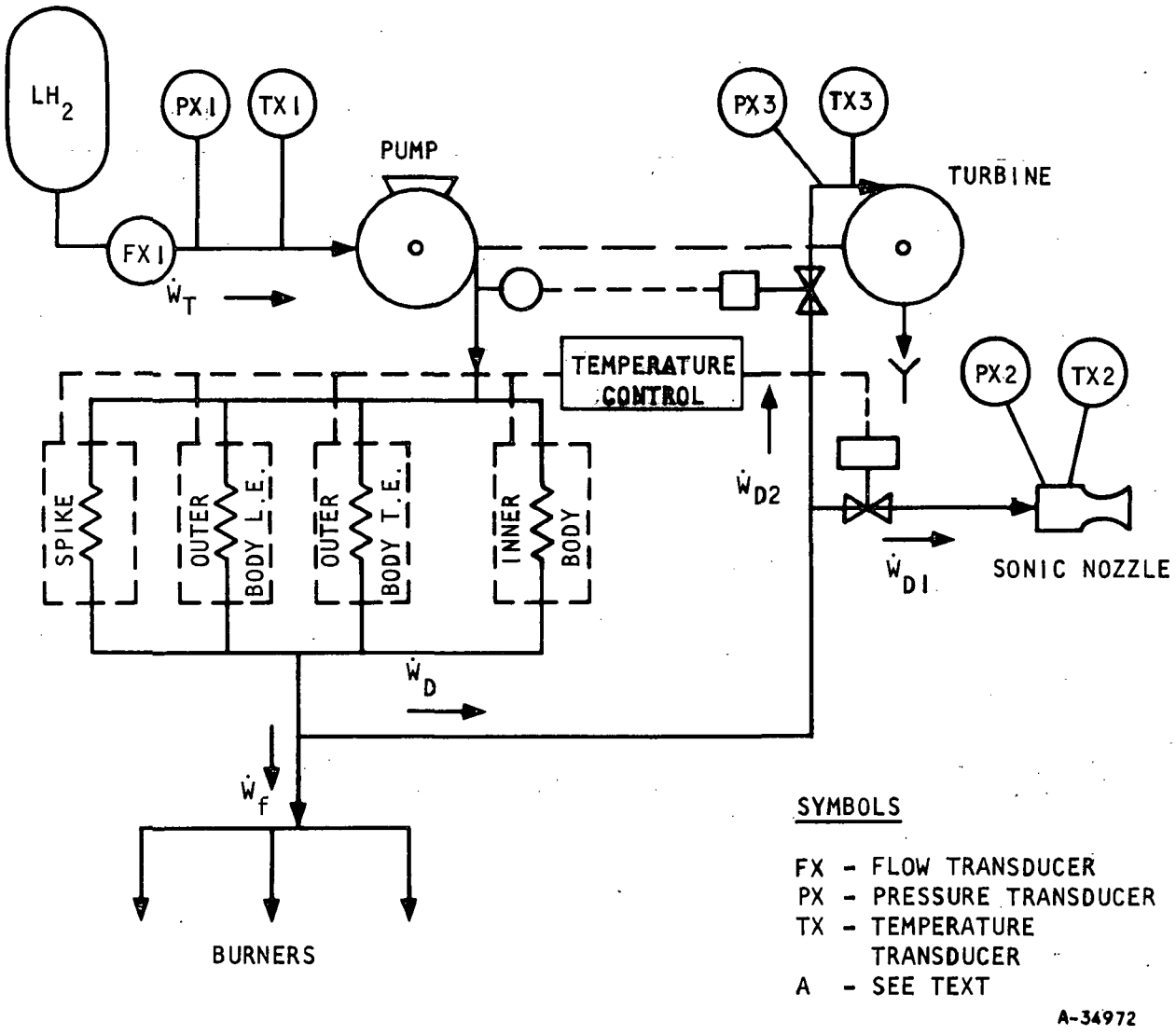

Figure 5.3-1. Schematic of Hydrogen Weight-Flow Rate Measurement System

5.4 ANALYSIS

The analysis given below is valid only during steady flow. Since $\dot{W}_T$, $\dot{W}_{D1}$, and $\dot{W}_{D2}$ are measured at different points in the flow stream, Equation (5.3-2) is invalid if the flow varies. In the case of variable flow, additional terms must be added to Equation (5.3-2) to account for the change in the system's mass of hydrogen between the measurement points.

5.4.1 Total Flow Measurement

The total flow, $\dot{W}_T$, is given by the following equation:

$$\dot{W}_T = \dot{Q}_T \rho \qquad (5.4\text{-}1)$$

where

$\dot{W}_T$ is the total weight flow rate

$\dot{Q}_T$ is the total volume flow rate

ρ is the density of liquid hydrogen

The volume flow rate is measured by the transducer FX-1, a turbine flowmeter. The density ρ is deduced from the pressure P and the temperature R by means of the tabulated thermodynamic properties of liquid hydrogen (Reference 5-1). The pressure and temperature are measured by means of transducers PX-1 and TX-1, as explained above.

The error in determining $\dot{W}_T$ is caused by errors in measuring $\dot{Q}_T$, P, and T. The error in $\dot{Q}_T$ has been calculated to be ±1.58 percent of full scale (Reference 5-2). The errors in P and T are each about ±1.5 percent of the transducer range. For pressure, the transducer range is 0 to 100 psia, or 100 psia. The error is ± (1.5 percent) x (100 psia) = ±1.5 psia. For temperature, the transducer range is 35°R to 60°R, or 25°F. The error in temperature is ± (1.5 percent) x (25°R) = ±0.375°R.

These temperature and pressure errors generate an error in the density ρ. If we assume random, independent errors with normal probability distributions, the error in density is given by the following expression:

$$\Delta P = \left\{ \left(\frac{\partial \rho}{\partial P} \Delta P \right)^2 + \left(\frac{\partial \rho}{\partial T} \Delta T \right)^2 \right\}^{1/2} \qquad (5.4\text{-}2)$$

We shall evaluate Equation (5.4-2) by using the following values for $\partial_\rho/\partial P$ and $\partial_\rho/\partial T$, taken from Reference 5-1, pp 15 and 16:

$$\frac{\partial \rho}{\partial P} = 0.002 \quad \frac{lb/ft^3}{psia} \quad \text{at } T = 53^0R,\ P = 112.5 \text{ psia}$$

$$\frac{\partial \rho}{\partial T} = -0.05 \quad \frac{lb/ft^3}{\text{degree R}} \quad \text{at } T = 43.5^0R,\ P = 115 \text{ psia}$$

Substituting these values and the values $\Delta T = 0.375^0R$, $\Delta P \approx 1.5$ psia into Equation (5.4-2) yields the following value for the density error, $\Delta\rho$:

$$\Delta\rho = \left\{ \left[(0.002)(1.5)\right]^2 + \left[(0.05)(0.375)\right]^2 \right\}^{1/2} = 0.019 \text{ lb/ft}^3$$

The density at the expected operating conditions is 3.36 lb/ft^3. The relative error in density is

$$\frac{\Delta\rho}{\rho} = \frac{0.019}{3.36} = 0.00565$$

The error in $\dot{W}_T$ is obtained by combining the error in density, $\Delta\rho$, with the error in volume flow rate, $\Delta\dot{Q}_T$, as follows:

$$\frac{\Delta\dot{W}_T}{\dot{W}_T} = \left\{ \left(\frac{\Delta\dot{Q}_T}{\dot{Q}_T}\right)^2 + \left(\frac{\Delta\rho}{\rho}\right)^2 \right\}^{1/2} \qquad (5.4\text{-}3)$$

Using the values $\Delta\dot{Q}_T/\dot{Q}_T = \pm .0158$ and $\Delta\rho/\rho = \pm .00565$, we obtain:

$$\frac{\Delta\dot{W}_T}{\dot{W}_T} = \left\{ (.0158)^2 + (.00565)^2 \right\}^{1/2}$$

$$= \pm .01678$$

Thus, the total weight flow rate can be measured with an accuracy of about ±1.7 percent.

5.4.2 Measurement of Temperature Control Dump Flow

The measurement of $\dot{W}_{D1}$, the hydrogen dumped for temperature control, is is to be accomplished by means of a critical flowmeter or choked sonic nozzle. The advantages of this device are:

No need for differential measurement

Weight flow nearly linear with inlet pressure

Weight-flow measurement range equivalent to inlet pressure measurement range

The disadvantages are:

A ratio of inlet pressure to outlet pressure that is greater than a minimum value (about 2) required to maintain sonic flow

The necessity for measuring stagnation temperature

The following error analysis of a critical flowmeter (sonic nozzle) is tentative; the results are subject to later revision. The analysis is based on the usual equations for weight-flow rate through a choked sonic nozzle (Reference 5-3).

$$\dot{W}_{DI} = C\, a\, P\, T^{-1/2} \qquad (5.4\text{-}4)$$

where

C = a coefficient of discharge defined in Equation (5.4-5)

a = cross section of orifice at the location of sonic velocity

P = inlet stagnation pressure

T = inlet stagnation temperature

Equation (5.4-4) is an approximate expression for the weight-flow rate through the flowmeter. The effects of pressure and temperature at the discharge side of the nozzle have been neglected. In addition, the flowing gas is assumed to follow the ideal gas law. These approximations lead to systematic errors that are not considered in the present error analysis.

The discharge coefficient is assumed to be a function of γ, the ratio of specific heats of the gas, Z, the compressibility factor, and F, an empirical connections factor due to distortion of the flow stream by the temperature probe. The equation for C is

$$C = F\, f(\gamma)\sqrt{\frac{g}{ZR}} \qquad (5.4\text{-}5)$$

The quantity R/g in Equation (5.4-5) is the gas constant for hydrogen in engineering units. The compressibility factor Z is assumed to be unity. The

empirical factor F must be determined by experiment. The function f (γ) is as follows:

$$f(\gamma) = \gamma^{1/2}\left(\frac{2}{\gamma+1}\right)^{\frac{\gamma+1}{2(\gamma-1)}} \qquad (5.4\text{-}6)$$

$\dot{W}_{DI}$ is assumed to be determined by three independent measurements: F, P, and T. There is an uncertainty associated with each measurement. The uncertainity in F is a calibration error and is assumed to be systematic. The uncertainties in P and T are assumed to be random. These uncertainties or errors are combined as follows:

$$\Delta\dot{W}_{DI} = \left| \frac{\partial \dot{W}_{DI}}{\partial F} \Delta F \right| + \left\{ \left(\frac{\partial \dot{W}_{DI}}{\partial T} \Delta T \right)^2 + \left(\frac{\partial \dot{W}_{DI}}{\partial P} \Delta P \right)^2 \right\}^{1/2} \qquad (5.4\text{-}7)$$

The partial derivative $\partial \dot{W}_{DI}/\partial F = 1$. It is assumed that F can be determined experimentally to ± 0.5 percent. Hence, an error of 0.5 percent of F causes an error of 0.5 percent in $\dot{W}_{DI}$.

Temperature effects $\dot{W}_{DI}$ in three ways. First, T appears explicitly in Equation (5.4-4) to the power of - 1/2. Second, γ is a function of T. Third, the area "a" depends on the temperature of the nozzle material. The nozzle material is assumed to be at the temperature of the incoming gas, so that "a" is a function of T. Hence,

$$\frac{1}{\dot{W}_{DI}} \frac{\partial \dot{W}_{DI}}{\partial T} = -\frac{1}{2T} + \frac{1}{C}\frac{dC}{d\gamma}\frac{d\gamma}{dT} + \frac{1}{a}\frac{da}{dT} \qquad (5.4\text{-}8)$$

From Equations (5.4-5) and (5.4-6), we have

$$\frac{1}{c}\frac{dc}{d\gamma} = \frac{1}{f}\frac{df}{d\gamma} = \frac{\log\left(\frac{\gamma+1}{2}\right)}{(\gamma-1)^2} - \frac{1}{2\gamma(\gamma-1)} \qquad 5.4\text{-}9)$$

For hydrogen at 1200°F, γ = 1.4 we see that

$$f(1.4) = 0.687$$

$$\frac{1}{f}\frac{df}{d\gamma} = 0.245$$

According to Reference 5-1, at 1200°F,

$$\frac{d\gamma}{dT} = 5 \times 10^{-5} \text{ per deg F}$$

Hence,

$$\frac{1}{c}\frac{dC}{d\gamma}\frac{d\gamma}{dT} = 1.225 \times 10^{-5} \text{ per deg F}$$

Because of the coefficient of thermal expansion, the nozzle throat area "a" varies with temperature. If α is the coefficient of linear-thermal expansion at 1200°F, then

$$\frac{1}{a}\frac{da}{dT} = 2\alpha$$

A typical value for this quantity is 50×10^{-6} per deg F (Reference 5-4, p. 113).

Finally, the operating temperature T is assumed to be 1620°R. Hence,

$$\frac{1}{2T} = 3.08 \times 10^{-4} \text{ per deg F.}$$

The preceding numerical values are substituted in Equation (5.4-8) and absolute values are added.

$$\left| \frac{1}{\dot{W}_{DI}} \frac{\partial \dot{W}_{DI}}{\partial T} \right| = \left\{ 308 + 50 + 12 \right\} \times 10^{-6}$$

$$= 3.70 \times 10^{-4} \text{ per deg F}$$

If $\Delta T = \pm 20^{\circ}F$, then

$$\frac{1}{\dot{W}_{DI}} \frac{\partial \dot{W}_{DI}}{\partial T} \Delta T = .0074$$

The error in pressure is assumed to be 1.5 percent of full scale. In the most favorable case of minimum error, the measured pressure is at full scale, and

$$\frac{1}{\dot{W}_{DI}} \frac{\partial \dot{W}_{DI}}{\partial P} \Delta P = \frac{\Delta P}{P} = .015$$

According to Equation (5.4-7), by combining the effects due to errors ΔF, ΔT, and ΔP we obtain the following result:

$$\frac{\Delta \dot{W}_{D1}}{\dot{W}_{D1}} = .005 + \left\{ (.0074)^2 + (.015)^2 \right\}^{1/2}$$

$$= .005 + .0167 = .0217$$

The preceding calculation indicates that the dump flow might have an error as low as 2.2 percent. It is important to recall that this is a tentative result, based on neglecting certain known effects that are hard to handle mathematically. In addition, it is a best-case calculation, in which the temperature and pressure transducers are both indicating at or near full scale. More work on this error analysis will be performed during the next quarter.

A preliminary value has been determined for the area and diameter of the nozzle. A maximum flow rate of 2.7 lb/sec at 400 psia maximum pressure and $1600^{\circ}R$ was assumed. By substituting these numerical values in Equation (5.4-4) with C given by Equation (5.4-5), we obtain the following numerical result:

$$a = 1.872 \text{ in.}^2$$

The diameter of the nozzle is 1.54 in.

5.4.3 Measurement of Turbine Flow

The turbine weight-flow rate, $\dot{W}_{D2}$, is measured by using the turbine as a calibrated orifice. We can not assume that the turbine will always behave as a choked nozzle. In addition to uncertainty in the discharge coefficient of the turbine, other effects contribute. $\dot{W}_{D2}$ can be measured with an error no greater than 10 percent. As pointed out before, $\dot{W}_{D2}$ is a small quantity; hence, even a large relative error in $\dot{W}_{D2}$ does not produce a large relative error in $\dot{W}_f$.

Thus,

$$\frac{\Delta \dot{W}_{D2}}{\dot{W}_{D2}} = 0.10$$

5.4.4 Total Error in Measurement of $\dot{W}_f$.

$\dot{W}_f$ is composed of the three independently measured weight-flow rates $\dot{W}_T$, $\dot{W}_{D1}$, and $\dot{W}_{D2}$. The error equation is as follows:

$$\Delta\dot{W}_f = \left\{(\Delta\dot{W}_T)^2 + (\Delta\dot{W}_{D1})^2 + (\Delta\dot{W}_{D2})^2\right\}^{1/2} \qquad (5.4\text{-}10)$$

The following weight-flow rates represent a typical operating condition of the engine:

$$\dot{W}_T = 3.0 \text{ lb/sec}$$

$$\dot{W}_{D1} = 1.6 \text{ lb/sec}$$

$$\dot{W}_{D2} = 0.2 \text{ lb/sec}$$

Hence,

$$\dot{W}_f = 1.2 \text{ lb/sec}$$

Using the values obtained previously for $\Delta\dot{W}_T/\dot{W}_T$, $\Delta\dot{W}_{D1}/\dot{W}_{D1}$, and $\Delta\dot{W}_{D2}/\dot{W}_{D2}$, we obtain the following estimated errors:

$$\Delta\dot{W}_T = \dot{W}_T\left(\frac{\Delta\dot{W}_T}{\dot{W}_T}\right) = (3.0)(.017) = .051 \text{ lb/sec}$$

$$\Delta\dot{W}_{D1} = (1.6)(.022) = .035 \text{ lb/sec}$$

$$\Delta\dot{W}_{D2} = (0.2)(.10) = .020 \text{ lb/sec}$$

Hence,

$$\Delta\dot{W}_f = \left\{(.051)^2 + (.035)^2 + (.020)^2\right\}^{1/2}$$

$$= .065 \text{ lb/sec}$$

The relative error is

$$\frac{\Delta\dot{W}_f}{\dot{W}_f} = \frac{.065}{1.2} = .054 = 5.4 \text{ percent}$$

6.0 FIRST QUALIFICATION ENGINE TEMPERATURE AND PRESSURE MEASUREMENTS SYSTEM

6.1 PROBLEM STATEMENT

An integrated instrumentation system is required to determine performance parameters and structural behavior of the qualification engine during ground testing and of the flightweight engine during flight testing. The instrumentation must enable parameters and measurands to be evaluated within defined accuracies and must be capable of withstanding ground and flight operating environments.

The system is to be used with pulse-coded modulation (PCM) equipment during both ground and flight testing. When installed in the flight configuration, this system must be compatible with the engine jettisoning requirements.

The system must be qualified under Phase IIA qualification test conditions and operated, as far as possible, while the environments are being imposed. In addition, the system must meet electomagnetic interference requirements and must be compatible with the engine/airplane interface and recording requirements.

6.2 TOPICAL BACKGROUND

Instrumentation systems are to be provided for the three major engine test configurations of boilerplate qualification, ground qualification, and flightweight tests. The boilerplate engine will be tested to evaluate its aerodynamic and thermodynamic behavior. Results of thest tests will be correlated with qualification engine testing, in which the integrated engine structural characteristics will be assessed. This testing will also be used to finalize flightweight engine measurements.

The environmental conditions inside and outside the engine and onboard the X-15 airplane influence the design and development of special instrumentation and the selection of commercial items when special problems occur in areas adjacent to coolant pipes and hot walls.

The following parameters will be determined:

Internal thrust coefficient

Internal specific impulse

Engine air flow

Engine fuel flow

Engine inlet total temperature

Engine structural temperatures

Fuel temperatures

These determinations require accurate evaluation and recording of indicated thrust, acceleration, angle of pitch, inlet airflow, injected fuel flow, drag, and effective inlet area. Engine control measurements include real time evaluation of inlet total temperature and pressure. Such parameters and measurands necessitate the development of the specialized instrumentation covered in the other sections of this report.

6.3 OVERALL APPROACH

6.3.1 System Development

The task of developing the qualification engine instrument system will be performed in six phases: (1) definition of the system requirements; (2) preliminary system design; (3) hardware development and verification; (4) detailed design, fabrication, and procurement; (5) installation, and (6) qualification testing. These phases are discussed in the following paragraphs.

6.3.1.1 Definition of System Requirements

Quantity, type, and characteristics of the measurands necessary for performance analysis, structural behavior, and control purposes will be defined. Distinction will be made between instrumentation required for qualification ground testing and flight testing. Definitions of measurands will include response, measurement range, overall range, accuracy, location, and environment. In addition, the types of sensors will be determined.

6.3.1.2 Preliminary System Design

Layout drawings showing important dimensions, such as pressure tap configuration, orifice size, tube diameter, and length will be prepared in addition to drawings showing the location of sensor, transducers, cables, etc., within the engine and interface items, such as the thrust deflection block and umbilical connectors. The flight instrumentation system is shown in block diagram form in Figure 6.3-1.

6.3.1.3 Hardware Development and Verification

In addition to the development of the special instrumentation described elsewhere in this report, commercially available hardware will be selected for use in the instrumentation system. Testing to prove suitability for design function and environmental conditions will be performed. These tests will include response, vibration, temperature, and EMI.

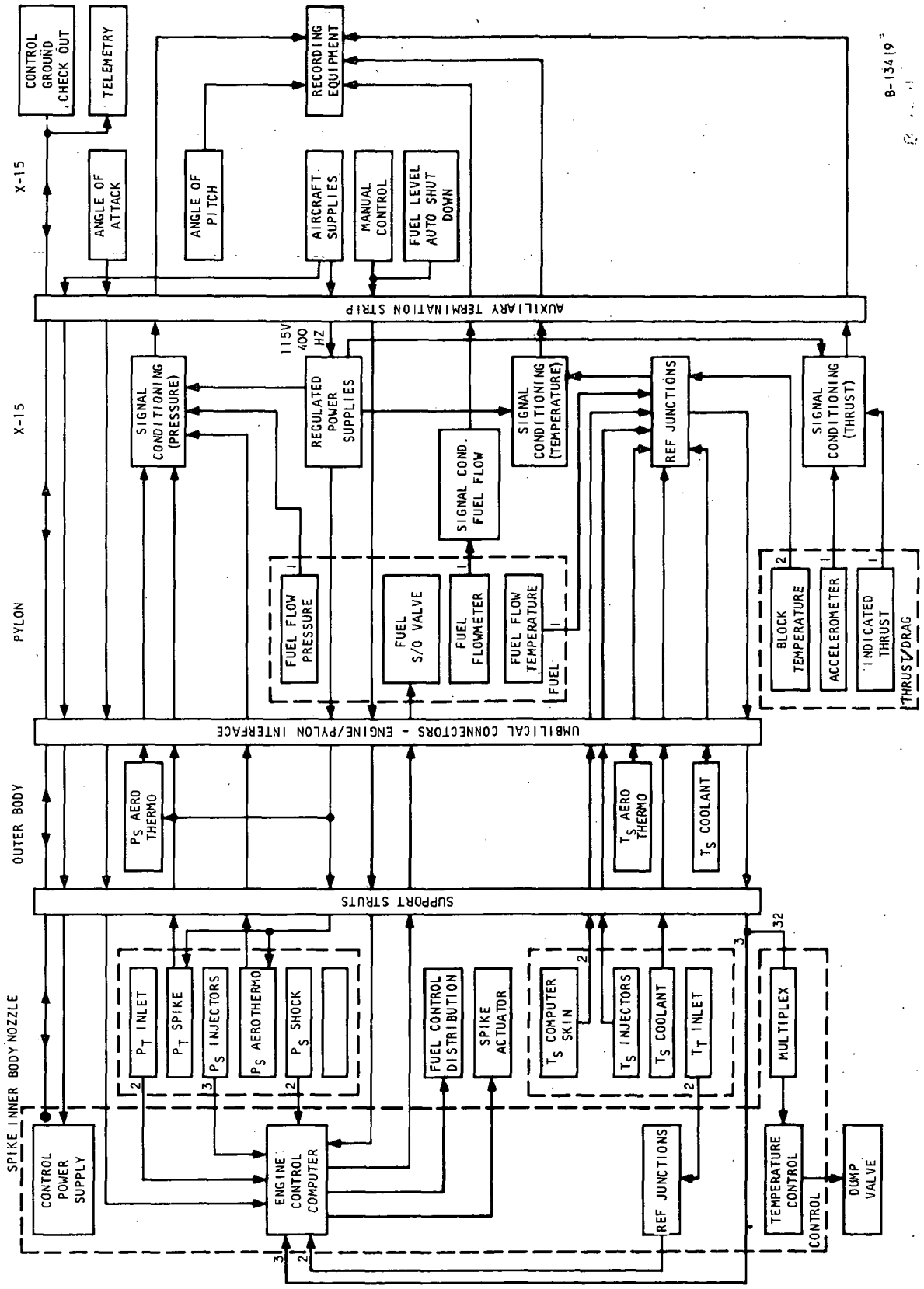

Figure 6.3-1. Preliminary Block Diagram of Flight Instrumentation System

6.3.1.4 Detailed Design, Fabrication, and Procurement

Detailed design and fabrication of in-house hardware and procurement of commercially available signal conditioning items with long lead times will commence during the hardware development and verification phase, and will continue as requirements become more definitive. The system ground and flight configurations, including X-15 requirements such as onboard signal conditioning equipment, data recording, power supplies, etc., will be available.

6.3.1.5 Installation

Installation of flight instrumentation on the engine will be followed by a system check out. Items that are not mounted on the engine, such as thrust block signal conditioning equipment are to be suitably accommodated for system qualification tests. A preliminary space envelope for the instrumentation system is shown in Figure 6.3-2.

6.3.1.6 Qualification Testing

While being operated, the flight instrumentation system will be subjected to structural integrity tests and vibration with hot-gas flow.

6.3.2 Subsystem Development

6.3.2.1 Temperatures Measurements Subsystem

The temperature measuring system will employ Chromel/Constantan and Geminol P and N thermocouple materials. The Chromel/Constantan will be used in the control circuits where maximum sensitivity is required over limited ranges. The Geminol P and N and Chromel/Constantan will be used for recording information to be used by the PCM system onboard the test aircraft.

6.3.2.1.1 Basic Sensor Constraints

Constraints placed upon the temperature sensor selection by the engine fabrication procedures generally limits the basic selection to the thermocouple-type sensor. Temperature sensors must be capable of withstanding the temperature excursions encountered during the several braze cycles the engine will go through. Experience has shown that resistive devices that are compatible with this type of installation cannot be subjected to brazing cycles of 2000°F without extreme calibration shifts. Physically the thermocouple sensor is the only type that will readily adapt to the hot skin surface temperature measurement configuration. Most measurement locations within the engine require that the sensors be installed during the engine assembly. To retain leak-free integrity in the gas and coolant flow paths, it is preferable to install the sensors during the construction of the engine. If the sensors are installed after the engine is complete, leak-integrity requirements can be satisfied only by placing the sensors in wells. A sensor in a well has a response time constant that is too long for the measurement system to achieve the desired system time constant. In view of the fabrication constraints imposed on the measuring system, the initial effort in the subsystem temperature measurement investigation has been the adaptability of the thermocouple to satisfy the measurement requirement. In general, the flight engine is the design goal, with the temperature instrumentation compatible with the PCM input requirements.

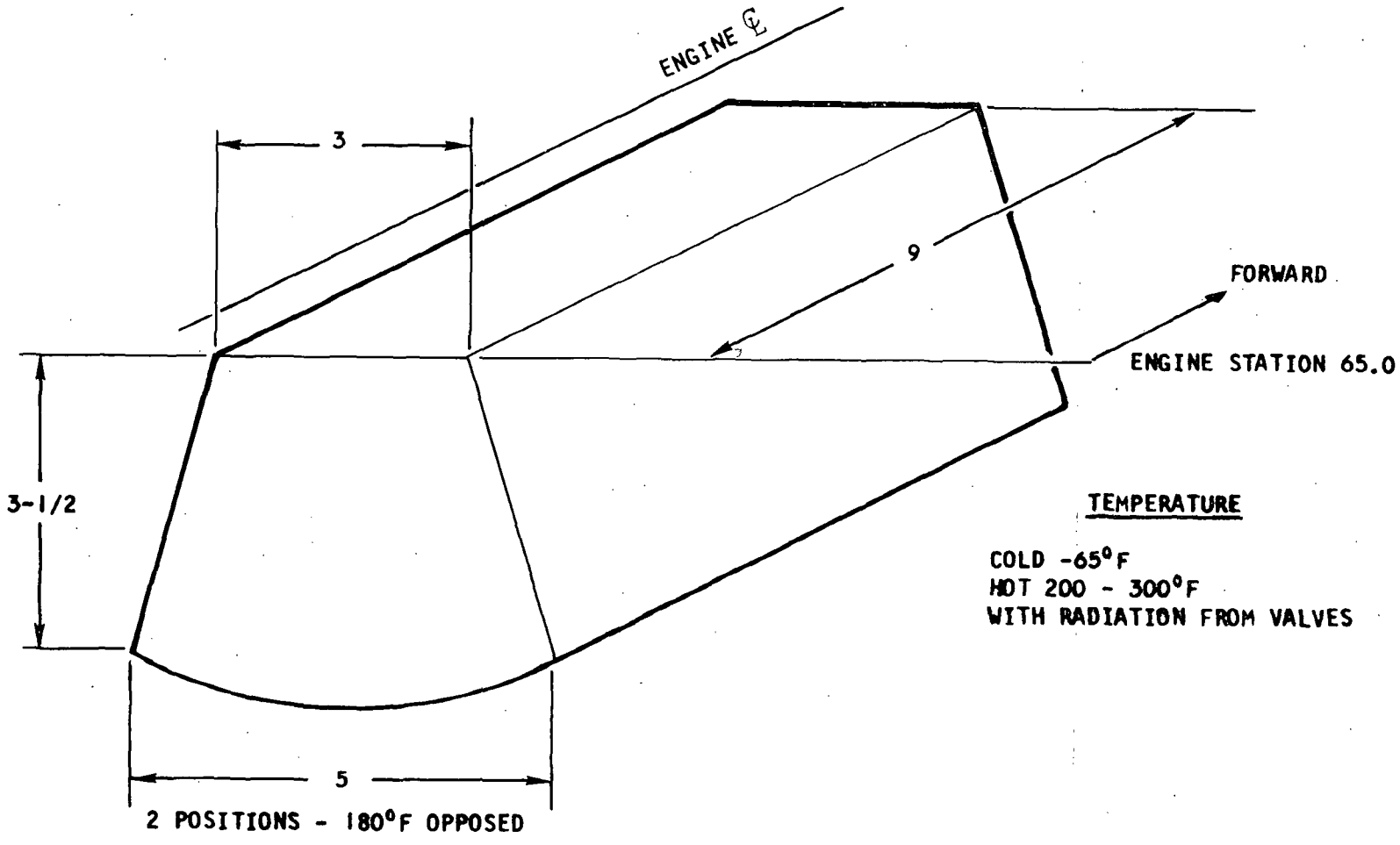

Figure 6.3-2. Preliminary Instrumentation Space Envelope for First Qualification Engine

6.3.2.1.1.1 Thermocouple Material

The thermocouple material has been selected to satisfy the range and accuracy requirement to the readout system aboard the aircraft. Several avenues are considered to meet the above requirements.

(a) Select a thermocouple material and attenuate the output by electrical means to satisfy the range requirement. This approach will require an attenuation circuit for each channel.

(b) Select a thermoelectric material combination that will closely fit the full-scale output of the temperature ranges desired.

(c) Select a thermoelectric material combination that is optimized for a desired range and use over this specified span for a particular sensor.

If the resolution and accuracy could be maintained over the full span, item (b) above would be the ideal combination. Unfortunately this is not true and the sensitivity of the sensor rapidly falls off in the cryogenic regions. This forces a tradeoff between range and accuracy in the lower temperature regions. The accuracy of the cryogenic measurements cannot duplicate those of the higher temperature range; however, they can be improved by the thermoelectric material selection and partial span ranging as noted in item (c) above.

The proposed thermocouple installation will use swaged MgO-insulated thermocouple material from sensor-end fabrication to the reference-junction sensor end and the lead length between the sensing point and the reference junction. Sheath material, encased in a high-density-pack MgO, will be 0.040-in.-diameter Inconel with 0.005-in.-diameter wires. The high-density pack should be in excess of 90 percent of its theoretical value. The Inconel sheath material is compatible with the thermocouple fabrication and the required brazing environments. The thermal coefficient of Inconel expansion closely matches those of the available thermoelectric material of Chromel, Alumel, Constantan, and Geminol. The high-density pack, with closely matched sheath and wire thermal coefficients of expansion, optimize the structural characteristics to thermal shock.

The thermoelectric materials noted above have environmental capabilities to suit the HRE temperature measurement task (see Table 6.3-1). Of the combinations listed, Chromel/Constantan has the largest thermoelectric power. This indicates its advantage for accuracy and resolution, especially in the cryogenic regions.

The thermoelectric powers for three thermoelectric combinations at 40°R are listed below.

Chromel/Constantan	5.2 μ V/°R
Chromel/Alumel	2.5 μ V/°R
*Geminol P and N	1.0 μ V/°R

*Geminol P and N is a Nickel-Silicon (negative) versus a Nickel-Chromium (positive) thermocouple combination and is manufactured by Driver Harris Company of Harrison, New Jersey.

The signal levels are high enough in the upper temperature ranges that the stated accuracy requirements can be met by any of the combinations above.

TABLE 6.3-I

MATERIAL MELTING POINTS AND COMPOSITION

Material	Melting Point, °F	Nominal Composition, percent by weight
Chromel P	2600	90 Ni - 10 Cr
Alumel	2550	95 Ni - 2 Mn - 2 Al
Constantan	2320	45 Ni - 55 Cu
Geminol N	2590	96.5 Ni - 2.75 Si
Geminol P	2550	79 Ni - 18 Cr - 1 Nb
Inconel 610	2570	72 Ni - 16 Cr - 8 Fe

6.3.2.1.1.2 Thermocouple Installation

During engine buildup, installation of the thermocouple assemblies will be made in the second and third braze cycles. The sequence of the brazing cycles for the engine covers the following cycles.

No. 1 - Palniro No. 4 2175°F

Shell assembly buildup

No. 2 - Palniro No. 1 2070°F

Machine and braze in injector plugs

No. 3 - Palniro No. 7 1925°F

Machine the instrumentation holes by EDM methods. Install instrumentation bosses and thermocouple assemblies; spot weld assemblies in place and braze. Cold skin surface thermocouples are installed in areas that are inaccessible following the third braze cycle. In the nozzle area, the plug and adapter inserts can be installed during the second braze cycle. Temperature sensors will be brazed during the third brazing cycle.

Two basic support inserts are required for the temperature sensor installation. These supports are dimensioned and machined to fit the local skin, fin, and cold-wall-thickness requirements of the sensing area. Figures 6.3-3 and 6.3-4 illustrate the installation concept of the temperature sensors that apply to the cooled-skin instrumentation areas of the engine. Cold-skin-temperature sensors are spot-welded by capacitance discharge welding to the

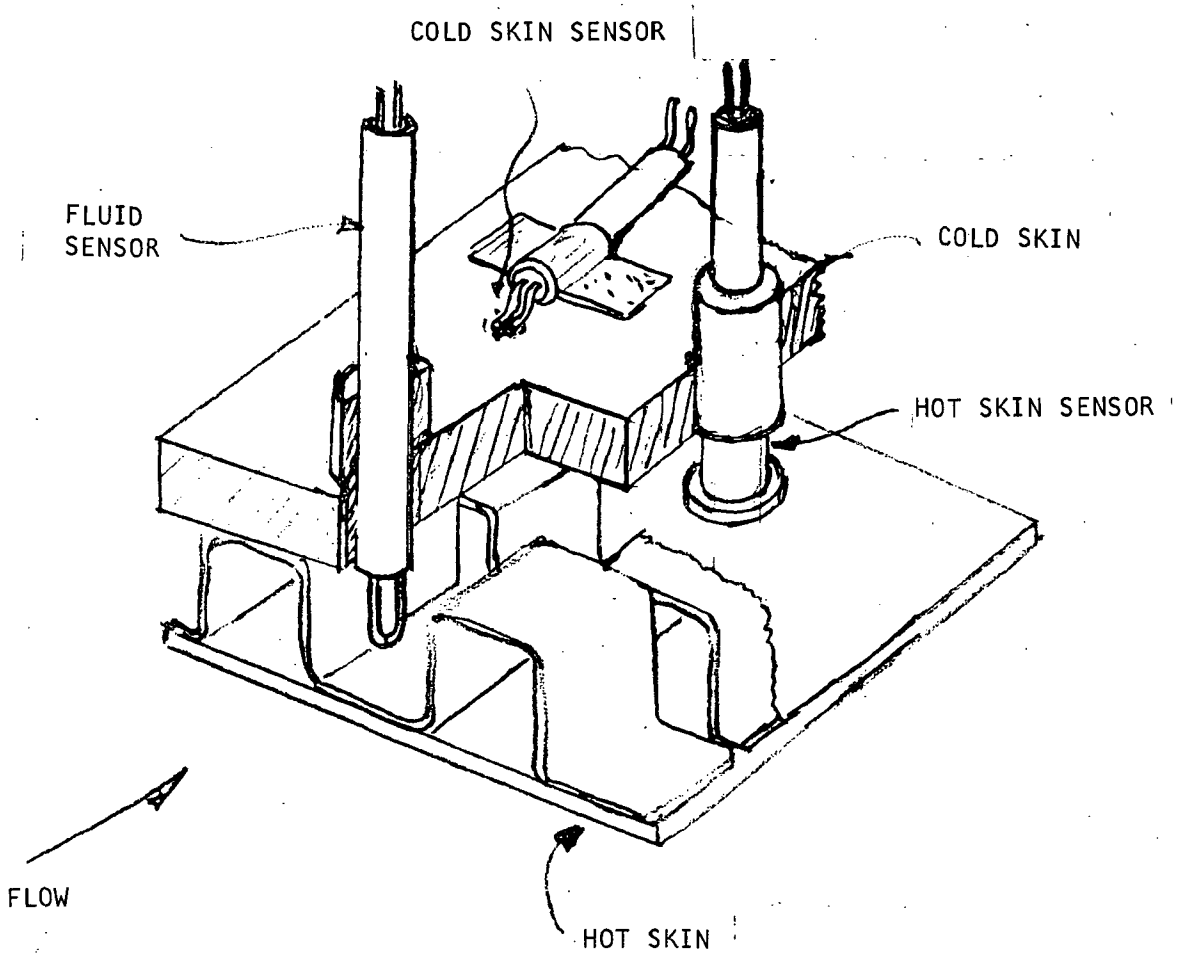

Figure 6.3-3. Instrumentation for Structure Temperature

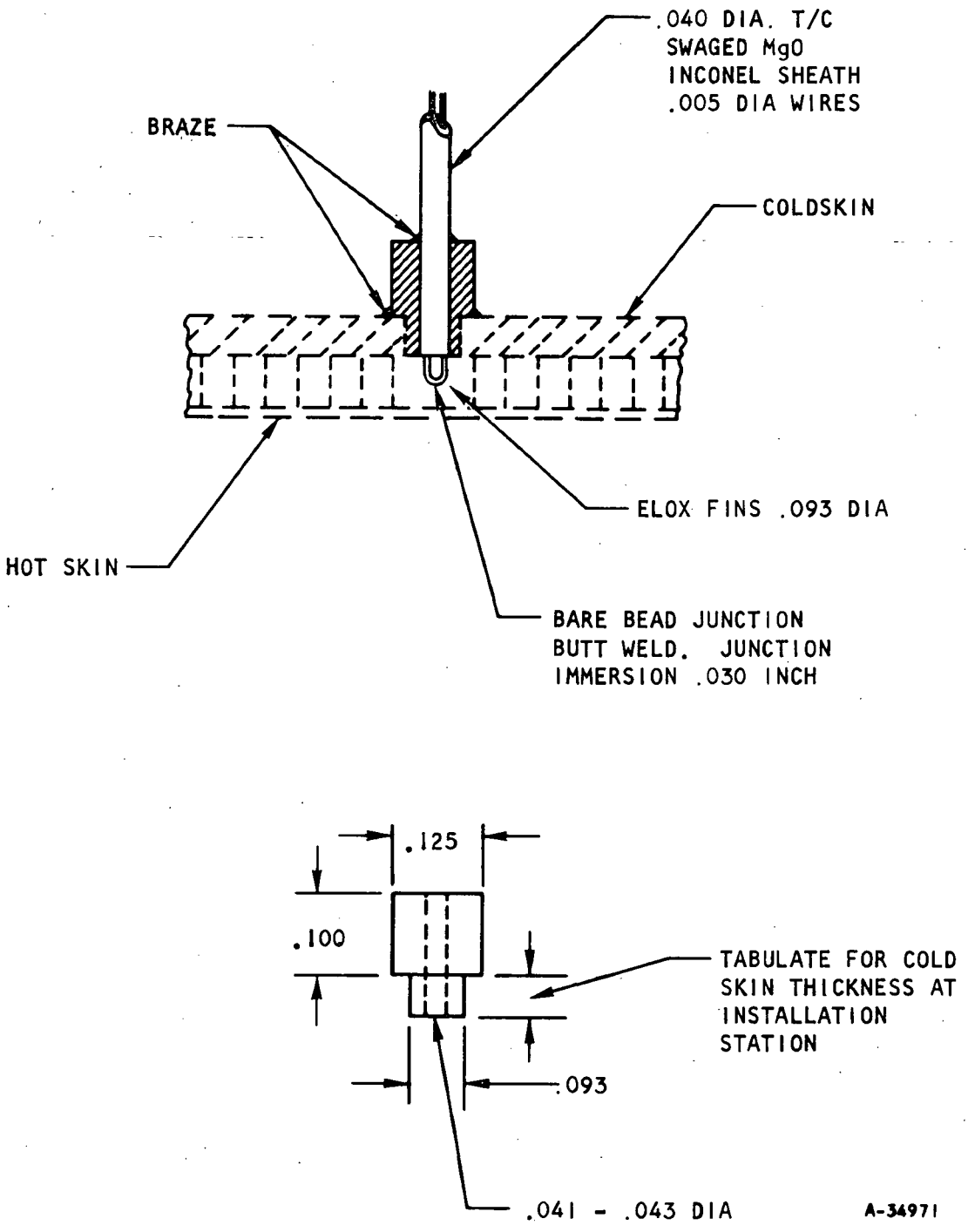

Figure 6.3-4. Hot Gas Thermocouple Installation

cold-skin surfaces. Where possible, installation of the cold-skin sensors will be made after the third brazing cycle. The cold-wall sensor installation includes protective cover (Figure 6.3-5) of thin Inconel to guard against sensor damage and thermal influence. Thermocouple installation in the manifold section will be made during the third braze cycle. The wall of the manifold sections are thick enough that a support insert is not required. Manifold sensors are of closed-end thermocouples configuration. Immersion depths are available that make this kind of thermocouple applicable to the manifold installation

6.3.2.1.1.3 Thermocouple Environment Compatibility

With the sensor used in an open-element configuration, the compatibility of the Chromel material of the temperature sensor with the hot hydrogen gas was questioned. Hoskins Manufacturing Company of Detroit, the prime suppliers of the Chromel material, was contacted regarding this compatibility question; they anticipated no detrimental exposure effect to the dry hydrogen gas environment in the engine application. Fabrication procedures for this material often employ a high temperature - dry hydrogen environment for annealing the cold worked material. Generally, any concern over reactions are based on extremely long-term exposures to the environment.

Since it is necessary to have an exposed junction thermocouple in the high-pressure hydrogen stream, there is a possibility of hydrogen leaking through the porous MgO-packed thermocouple material. Specific information is lacking on probable leak rates related to time, temperature, pressure, and size as a function of a particular gas. Leak-rate tests of the high-density swaged material will be made on samples simulating the pressure, temperature, gas, and time relationship to which they may be exposed. Figure 6.3-6 is a schematic of the proposed leak-rate test for selected samples of the swaged material.

6.3.2.1.1.4 Thermocouple Calibration Stability

Calibration stability of thermocouple combinations are generally based on long-term calibration shifts that accompany the time-temperature-environment relationship involving time periods extending into several hundred hours. This is not equivalent to the environmental conditions to which the thermocouple sensors will be subjected in the engine. Performance and qualification testing of the engine comprises 70 cycles lasting at least 2 min each. This condition approximates a little more than 2 hr of sensor environmental exposure.

Since environmental exposure time is small, the resultant calibration shifts are insignificant. Inhomogeneity of the thermocouple wire, especially in the hot-skin sensors where large temperature gradients can exist over relatively short distances, can account for errors greater than any possible calibration shift. It is difficult to assign numerical values to these errors. The practical approach is to use material with minimal inhomogeneity characteristics. AiResearch ran extensive tests on thermoelectric materials testing for this particular characteristic. These tests have shown that the Geminol

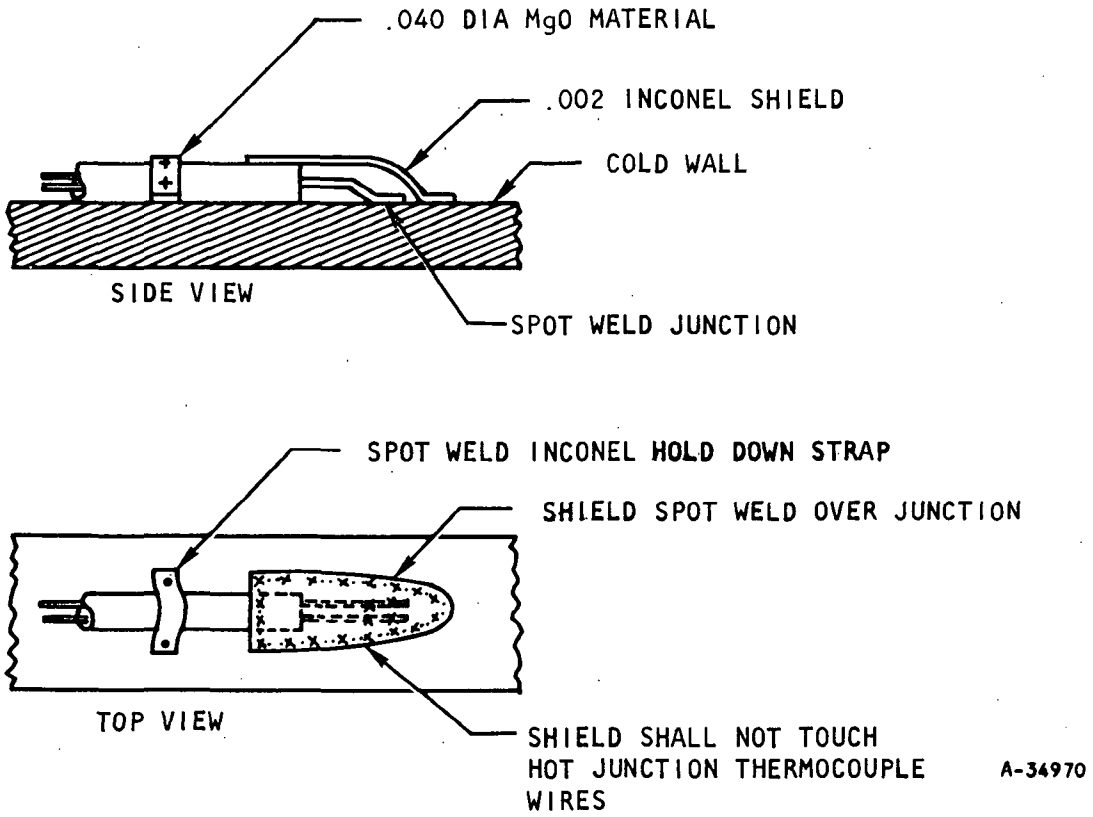

Figure 6.3-5. Cold Skin Temperature Sensor Installation

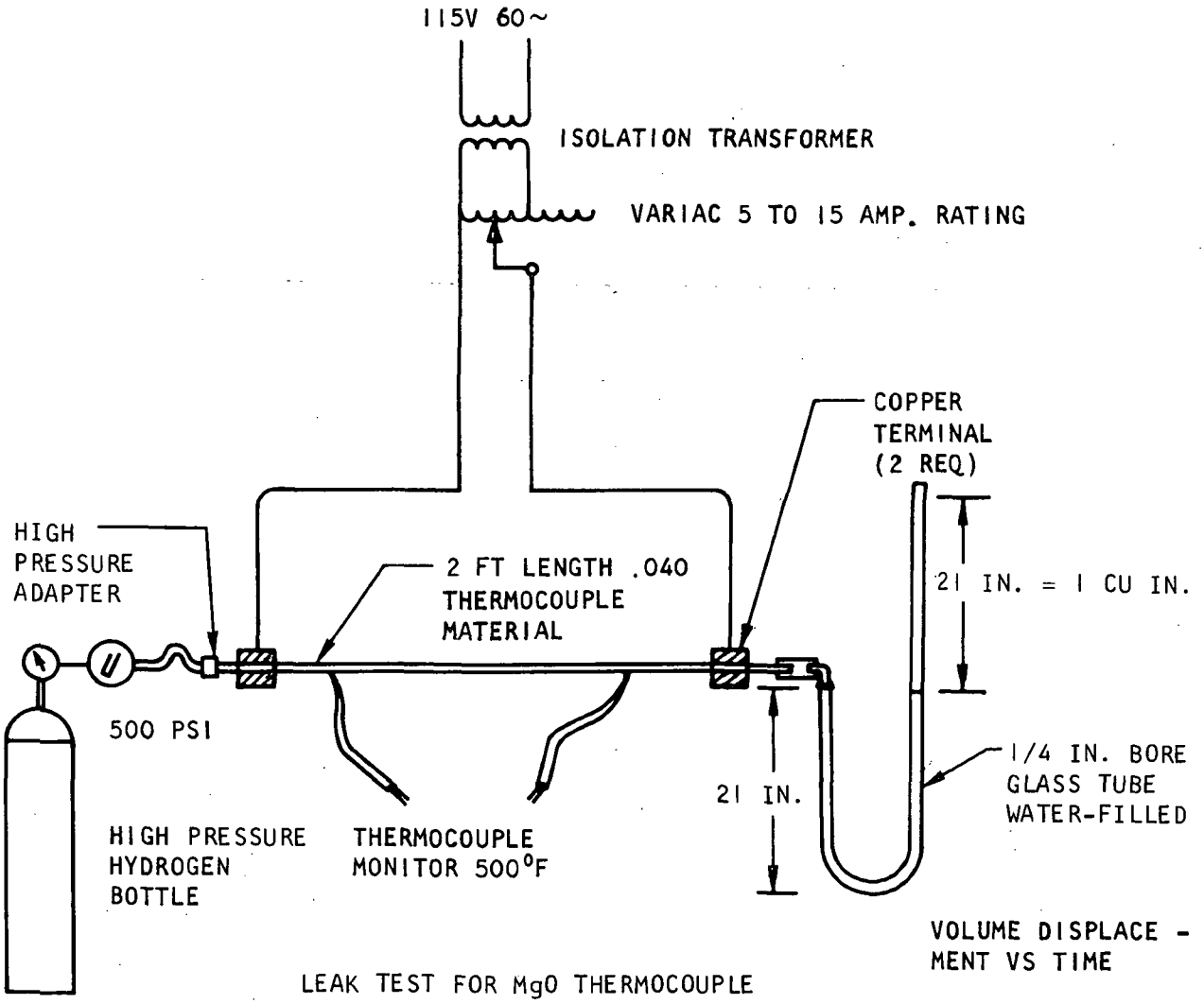

Figure 6.3-6. Swaged MgO Leak Test at Elevated Temperature

P and N combination are superior to other base metal thermocouples. Drift characteristics (calibration) are also shown to be less for the Geminol combination.

The calibration shift and possible inhomogeneity characteristics of any of the base metal thermocouples referred to above will be lost in the uncertainties of the installation to the environment except for the cold skin temperature sensing.

6.3.2.1.1.5 Ranging

The constraints placed on the signal level of the thermocouple output by the ±15-mv input requirement to the PCM aboard the test aircraft limits the sensitivity and resolution capabilities of the temperature sensors. Full-scale range is desirable; however, the sensitivity and resolution of any sensor capable of this range shows extremely poor output in the lower cryogenic region. Geminol P and N is the only commercially available thermoelectric combination that will closely satisfy the total range requirements during engine operation. The lack of sensitivity and the resultant small resolution capabilities in the cryogenic region indicate that this material cannot satisfy the accuracy requirement in the lower ranges. Chromel/Constantan, which has the largest thermoelectric power, will satisfy the accuracy and resolution requirement in the cryogenic region, but only over a limited temperature span equivalent to the ±15-mv input to the PCM.

To meet the accuracy requirement it is necessary to divide the sensor output of the engine into at least two ranges. One range extends from 40^{0} to $1200^{0}R$ using the Chromel/Constantan combination. The other range extends from 500^{0} to $2200^{0}R$ using Geminol P and N materials. These two ranges give the widest latitude and overlap.

Tabulated below are the optimized ranges ±15 mv for the three available thermoelectric materials.

Chromel/Constantan

40^{0} to $1200^{0}R$	Reference level	$645^{0}R$
1000^{0} to $1675^{0}R$	Reference level	$1340^{0}F$
1550^{0} to $2236^{0}R$	Reference level	$1887^{0}R$

Geminol P and N

500^{0} to $2200^{0}R$	Reference level	$1460^{0}R$

Chromel/Alumel

910^{0} to $2200^{0}R$	Reference level	$1547^{0}R$

The tabulated structures instrumentation temperature charts (see Appendix A) show the designated temperature ranges and materials applicable to the range selected.

6.3.2.1.1.6 Structures Instrumentation

The measurement points and related information for the subsystem temperatures are tabulated on the sheet covering each engine section (see Appendix A). Also included are the sensors required for control applications, and a summary sheet of all sensors. The total number of sensors related to the various test engines are summarized in the right hand columns. The column under static error ^{0}R is the largest allowable error; the adjacent column on the right is the worst-case static error expected from the instrumentation. The double asterisk indicates that further analyses and test will be required to assign a definitive value to these sensors. The single asterisk refers to control values that are determined by the control activity. The control sensor points are for control application only and are not intended to be recorded as a part of the temperature subsystem measurements.

The requested ranges are those estimated for the engine. The actual range is covered by the instrumentation. As shown, the total range of temperature excursion is covered by two ranges of two thermocouple materials. The temperature errors noted are static values and do not include the application errors that can accompany the installation.

6.3.2.1.1.7 Thermocouple Configuration

Four basic thermocouple configurations (shown in Figure 6.3-7) will satisfy the structures instrumentation requirement; this includes those configurations needed for the control application.

Except in the case of the hot skin sensor where close control and position of the hot junction location must be known, the junction fabrication of these sensors does not depart from routine thermocouple construction techniques. Two approaches to the fabrication of this sensor have been made: (1) the welded junction; and (2) the plasma-spray junction.

The welded junction is fabricated by conventional TIG welding procedures. A 0.040-in. depth of the insulating MgO material is removed from the end and the wires and swaged body are welded together. The welded junction end is X-rayed and the junction depth and weld condition is determined.

An uncertainty in this hot junction fabrication technique is the effect of the metal alloy diffusion at the weldment on the thermal EMF relationship in a region of steep thermal gradients. Routine calibration will not reveal the effects of junction diffusion.

The plasma-spray junction is fabricated by plasma-spray coating the hot junction end of the thermocouple assembly with a layer of Inconel material. This procedure allows a better control of initial junction thickness and eliminates the possible diffusion problem as encountered in the weldment technique. X-ray methods of checking the hot junction thickness are available.

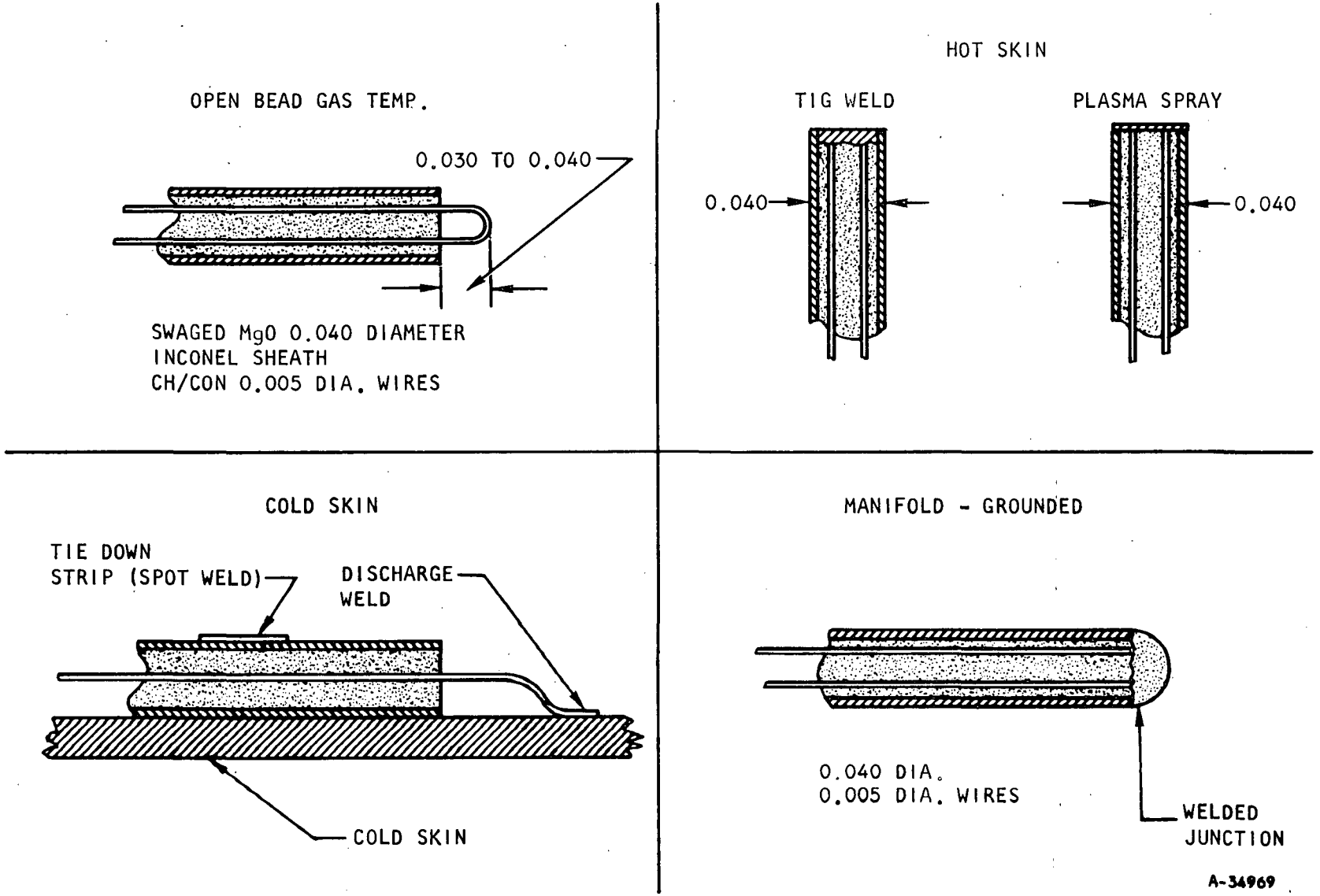

Figure 6.3-7. Configurations of Thermocouples to be Used on Structures

The cold wall sensors are spot-welded (capacitance discharge) in position. To retain the assembly body to the cold wall, an Inconel strap is used to fasten the hot junction end of the thermocouple assembly to the cold wall (see Figure 6.3-5). The hot junction is fabricated when the thermocouple wires are each welded to the cold wall. A protective shield covering the hot junction weldment and the wires leading from the MgO material is made from 0.002-in. thick Inconel material and spot-welded in place. This shield firmly attaches the terminal end of the thermocouple assembly, provides the thermocouple assembly from extraneous thermal influences and protects the small wires of the hot junction from physical damage.

6.3.2.1.1.8 Reference Junction

The temperature instrumentation system including the reference junction subsystem is grouped into four basic regions; each region satisfies the temperature instrumentation reference requirements in that portion of the engine. This approach makes it possible to reference the thermocouple circuits and have sensor output leads without crossing interface disconnects that are potential thermoelectric error sources in areas of large temperature gradients. As shown in Figure 6.3-8, the power supply is accessible through the aft end of the nozzle section.

The reference junction error associated with the anticipated large ambient temperature changes are responsible for a major part of the overall inaccuracy of the measurement, particularly in the lower cryogenic regions. Several possible approaches may be taken to reduce the error.

> Stabilize the reference junction body so that it does not see the large temperature excursion. With this approach, the limited excursion of the reference temperature will allow a smaller percentage error factor to be applied. Instead of 1 percent of the ambient excursion, a 0.5-percent factor would be applicable. This approach also requires the use of temperature control devices resulting in system complication and additional power. The error reduction, however, is direct and requires no further processing in the information.
>
> Monitor each reference junction's block by a thermocouple sensor and apply a correction to the data information. Treat the temperature versus error of the reference junction block as a systematic error based on reference junction environmental tests. This approach is readily adaptable to the thermocouple system as planned.

At temperatures less than $100^{\circ}R$, the reflected errors of the compensating reference junction ambient-temperature excursion reach necessary corrective magnitudes. The present temperature measurand layout indicates a total of 10 measurements in four engine areas below $100^{\circ}R$ and will need correction to meet the desired accuracy.

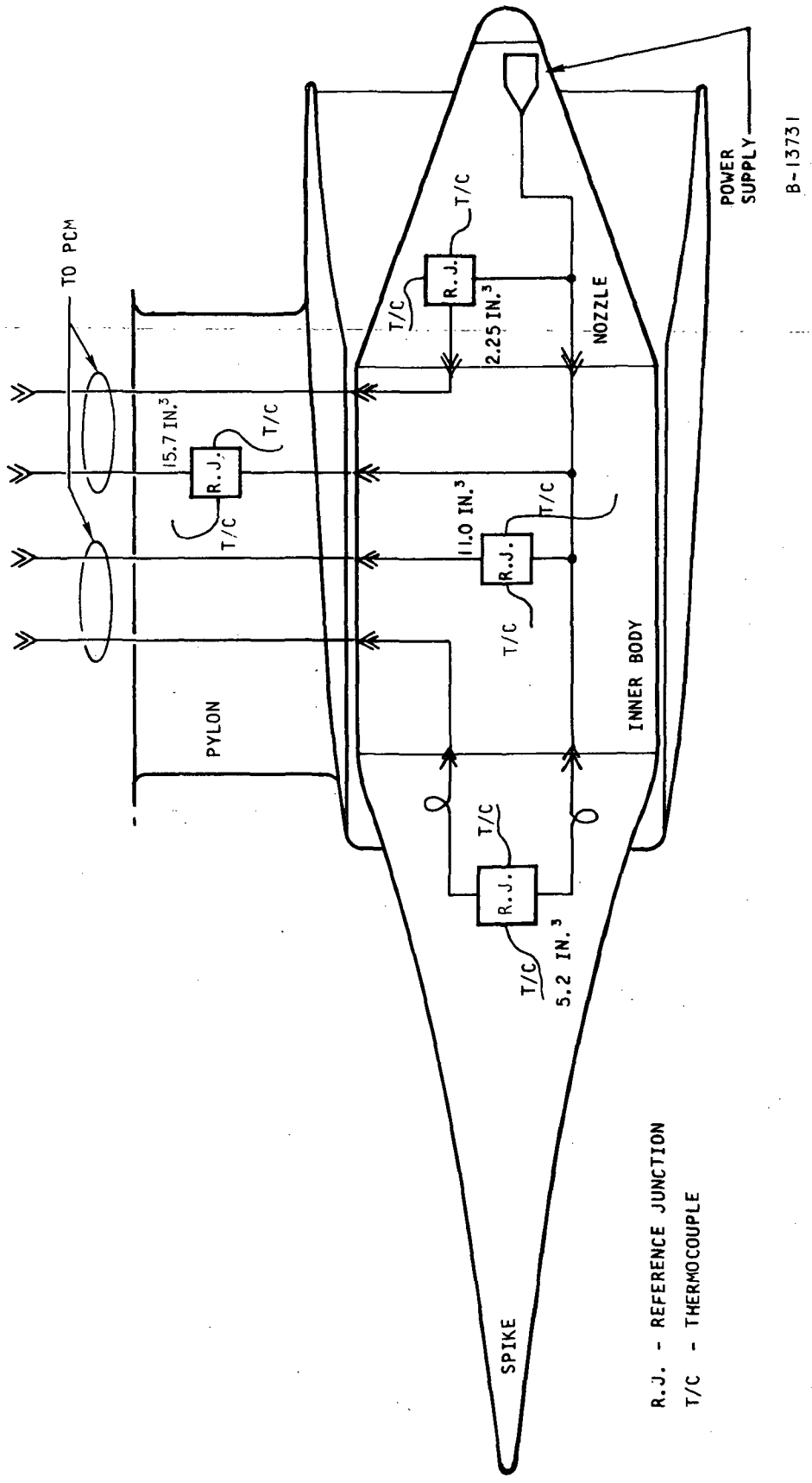

Figure 6.3-8. Thermocouple System, HRE Flight Engine

Review of the reflected error due to the compensating junction is shown below. The interest here lies in the Chromel/Constantan systems that are the low temperature sensors.

Reference junction excursion	=	395^0 to 760^0R (error = 1 percent of excursion)
Reference junction set point	=	645^0R
Thermoelectric power at set point	=	0.036 mv/^{0}R
1 percent of 365 x 0.036 mv	=	0.131 mv
Thermoelectric power at 40^0R	=	0.0052 mv/^{0}R
Reflected temperature equivalent at 40^0R	=	0.131/0.0052 = 25^0R
Thermoelectric power at 100^0R	=	0.011 mv/^{0}R
Reflected temperature equivalent at 100^0R	=	0.131/0.011 = 12^0R

Using an added circuit to monitor the temperature of the reference junction package to within 50^0R will permit the application of a systematic error correction to 1 percent of 50^0 or 0.5^0R.

0.5^0R = 0.018 mv at 645^0R (Reference level)

Reflected temperature equivalent at 40^0R = 0.018/0.0052 = 3.4^0R

Reflected temperature equivalent at 100^0R = 0.018/0.011 = 1.6^0R

A review of the static error contributions by basic system components in the critical cryogenic region is as follows:

PCM = 0.5 percent of 15 mv	=	75 μv
Wire calibration	=	6^0R
Reference junction	=	131 μv
At 40^0R (worst case)	=	57^0R (uncorrected)
40^0R (worst case)	=	24.4^0R (corrected)
At 100^0R	=	26^0R (uncorrected)
	=	15.1^0R (corrected)

Reduction and/or correction for the attributed reference junction error can reduce the errors in the cryogenic region to the values listed above. Thermocouple sensors with maximum sensitivity are being used and optimum ranging for the sensors is being applied. Further reduction must come from a close analysis of system component parts and their relation to a possible systematic error correction.

6.3.2.1.1.9 Instrumentation and Control Interface

Using the same temperature sensors for control and readout was considered, but because of possible interface problems, this approach was dropped. The major drawbacks to the approach are:

Control systems sensors must be ungrounded

Range is not compatible

Possible system feedback between control and instrumentation circuits when in parallel affecting the reliability of the system

Time constant requirements are different

Sensor sensitivity requirements are not compatible

To satisfy the circuit requirements, individual sensors and circuitry compatible to each system requirements are to be used with the duplication of the applicable sensors in discrete areas, when required.

6.3.2.1.1.10 Resistance Sensors

The apparent large errors associated with thermocouple sensors in the cryogenic areas, prompts one to look to other sensor types that may be better low-temperature characteristics and are compatible to the total instrumentation plan. The brazing-cycle temperatures the engine encounters during build-up will generally rule out both the semiconductor and metal resistive devices. Resistance sensors are not contemplated in the temperature subsystem task for engine metal temperatures.

6.3.2.2 Engine Metals and Coolant Temperatures

The transient temperature response of HRE panel structures, hydrogen coolant, and a coolant hydrogen temperature sensor at the start of Mach 6.5 (local) engine operation was investigated. The objectives were twofold: (1) to determine whether the thermal response of the cold wall inner surface near a flow route outlet is indicative of the thermal response of adjacent outer wall and fins, and (2) to evaluate the response of a temperature sensor immersed in the hydrogen coolant near a flow route outlet. It was initially planned that thermocouples measuring the cold wall inner surface temperature near a flow route outlet would control coolant flow rate. However, results in Figure 6.3-9 indicate that the cold wall inner surface temperature response (T70) is not indicative of the adjacent fins (T64) and outer wall (T58)

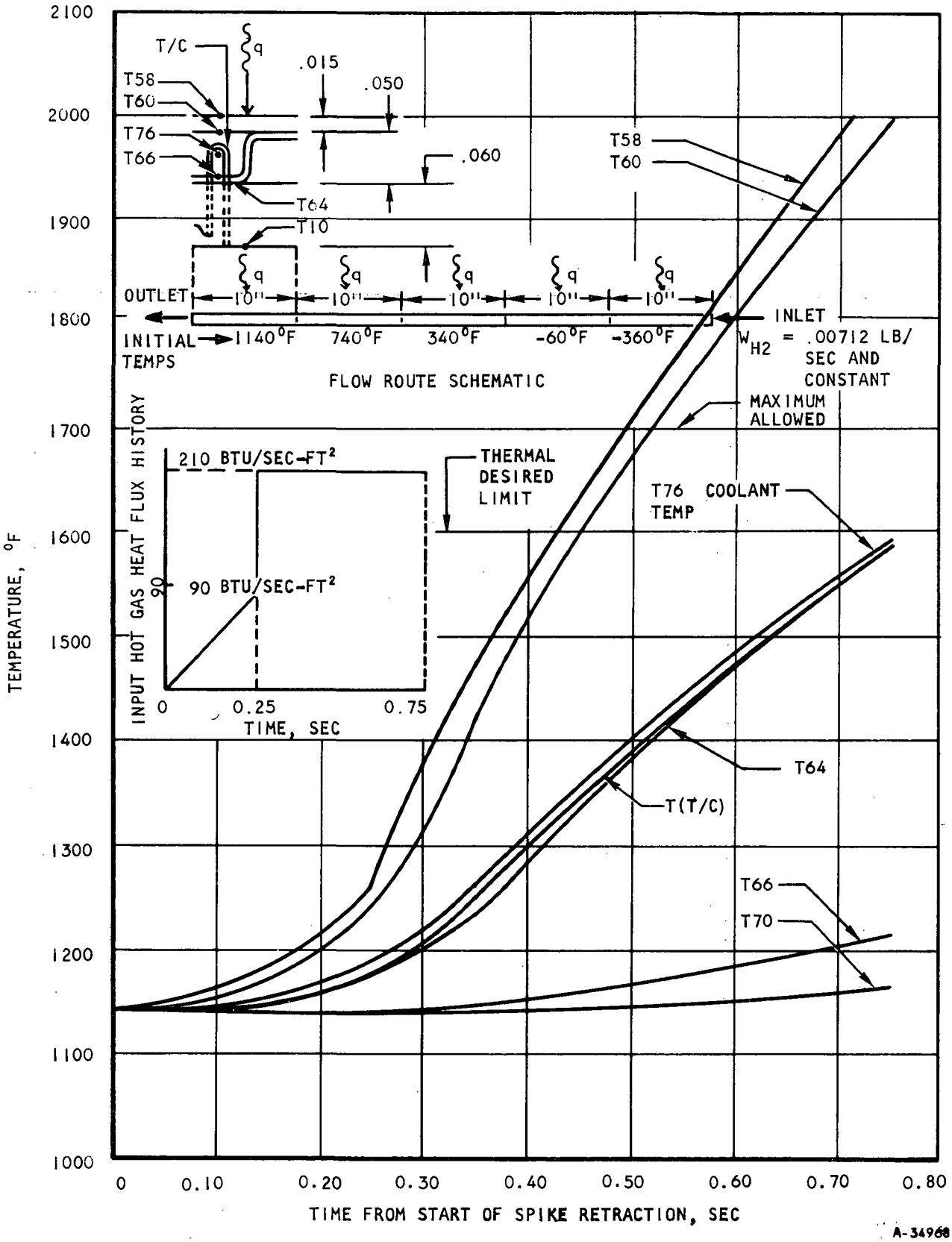

Figure 6.3-9. Results of Transient Thermal Analysis of Panel Cross Section and Hydrogen Coolant Thermocouple

temperature histories at the start of operation. The temperature of the outer wall near the outlet of the analyzed flow route (typically the inner body or outer body) increased from 1140°F to the maximum of 1700°F in the first one-half sec from the start of spike retraction. In the same one-half sec period the cold structure wall inner surface temperature increased from 1140° to 1145°F. Because of this slow structural wall response, the thermal response of a thermocouple bead immersed in the coolant fin passages near flow route outlet was investigated as a possible means of controlling coolant flow rate. A sketch of the thermocouple analyzed here is presented in Figure 6.3-10. Figure 6.3-9 indicates that the thermocouple bead response is almost equal to the response of the hydrogen coolant in the finned passages. The maximum difference between bead and coolant is 15°F. The coolant temperature increase near the outlet in the first half-second is approximately half of the outer wall temperature increase of 575°F.

The panel structures analyzed and the hot gas conditions used in the analysis are typical of the inner body or outer shell flow routes for combustion at Mach 8 (Mach 6.5 local), 88,000 ft. The required coolant rate in these routes just prior to spike retraction is about 5 percent of the design combustion values because the only heat load on these routes is from hot gas leaking through the 0.060-in. (nominal) gap between spike and leading edge. When the spike is retracted (minimum elapsed time for retraction is about 1/4 sec) and combustion starts (about 8 μsec from the time fuel is injected), coolant rate must increase to the design value so that design metal temperature limits are not exceeded. Use of a longer spike retraction period of up to 1 sec would not have changed the conclusions of the analyses. It was initially planned that thermocouples monitoring the cold structure inner surface temperature near a flow route outlet would control the coolant rate. The coolant rate would be adjusted to maintain the monitored temperature within a band. The band size was to be selected to avoid hot wall surface temperatures higher than 1700°F and structural wall temperatures higher than 1140°F. Thermocouples attached to the structure inner surface are preferred over coolant or outer wall temperature sensors because installation is much easier.

6.3.2.2.1 Panel Cross Section Analysis

The structure panels transient analysis was performed on the thermal analyzer computer program (H2800). The aft engine flow route analyzed was idealized into a cylinder 60 in. in circumference and 50 in. in length. The plate-fin panels (28R-0.050-0.100(0)-0.006 rectangular offset fins) of the flow route were divided into five 10-in. segments along the flow length. Each lengthwise segment was incremented into 14 cross-section nodes. A constant Hastelloy-X thermal conductivity evaluated at 340°F of 7.2 Btu/hr ft °F was used to calculate conductances between cross section nodes. The input coolant hydrogen flow rate was held constant at 0.00712 lbm/sec throughout the analysis. This is the flow rate required to dissipate the leak flow heat load on the innerbody flow route just prior to spike retraction and increase coolant temperature from -360°F (100°R) to 1140°F (1600°R). Coolant flow rate was intentionally held constant at the low precombustion value of 0.00712 lbm/sec to investigate thermal responses of all panel cross-section

NOTE: ALL DIMENSIONS IN INCHES

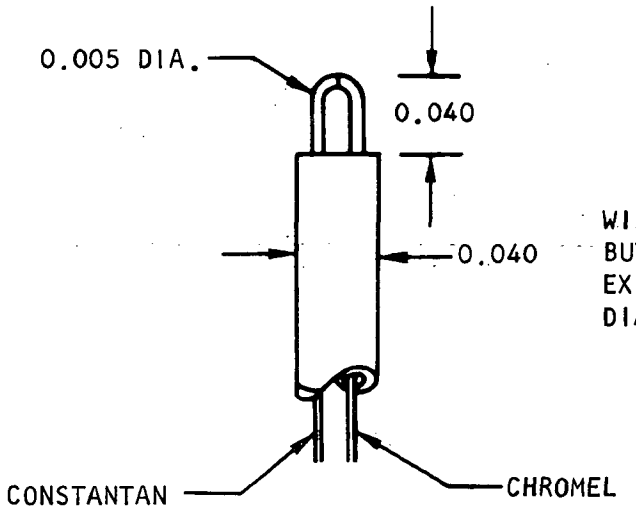

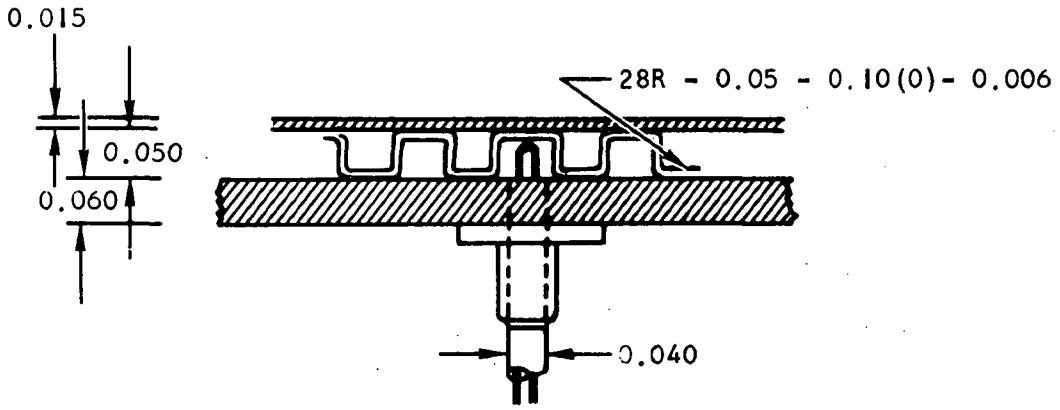

PROPERTIES	CHROMEL	CONSTANTAN	JUNCTION
SPECIFIC HEAT, $\frac{BTU}{LBM\ ^0F}$	0.107	0.094	0.1005*
DENSITY, LB/IN^3	0.315	0.322	0.3185*
EMISSIVITY			0.5**

*THE AVERAGE VALUE BETWEEN THOSE OF CHROMEL AND CONSTANTAN WAS TAKEN

**ASSUMED VALUE

A-34967

Figure 6.3-10. Thermocouple Details

locations near outlet to combustion heating conditions and precombustion cooling conditions. These conditions will indicate which candidate thermocouple location can quickly sense the hot gas heating and thus increase the coolant rate accordingly.

The initial temperatures of each segment (metal and hydrogen coolant) are shown in Figure 6.3-9. A linear coolant and metal temperature increase from -360°F at inlet (first segment) to 1140°F at outlet (filler segment) was assumed. The initial metal and coolant temperatures were assumed equal at each segment because the low hot gas heat flux prior to combustion will create low temperature differences across the panel. Each of the five panel segments were subjected to the same hot gas heat flux history shown in Figure 6.3-9. The ramp change in the heat flux from zero to 90 Btu/sec ft^2 in the first 1/4 sec represents the buildup in the heat flux due to spike retraction. A flux of 90 Btu/sec ft^2 is the estimated average hot gas heat flux on inner body surfaces for spike open, no combustion at Mach 6.5 (local), 88,000 ft. The step change in heat flux from 90 to 210 Btu/sec ft^2 represents the instantaneous (actually estimate 8 μsec) start of combustion. A flux of 210 Btu/sec ft^2 is the estimated average hot gas heat flux on inner body surfaces for spike open with combustion at Mach 6.5 (local), 88,000 ft.

Transient temperature responses of the metal cross section and coolant of the fifth lengthwise segment are shown in Figure 6.3-9. Only temperatures of the fifth segment are shown because they represent the outlet of the flow route where coolant flow control sensors will be located. In the first 1/2-sec the outer wall temperature (T58) increases from 1140° to 1715°F while the structural inner wall temperature (T70) increases from 1140° to 1145°F. An outer wall temperature of 1700°F (2160°R) is the maximum metal service temperature and is 100°F over the maximum design temperature of 1600°F (2060°R). Coolant flow must be increased to the design value for combustion of 0.42 lbm/sec on the inner body of Mach 6.5 local conditions from the precombustion flow of 0.00712 lbm/sec in less than 1/2 sec from the start of spike retraction if design temperatures are not to be exceeded. If coolant rate is increased instantaneously at 1/2 sec, there will be an outer wall temperature overshoot higher than 1715°F before steady-state design thermal conditions will exist. An estimate of the maximum allowance time from start of spike retraction until coolant must increase to maintain acceptable temperature will require further analysis.

6.3.2.2.2 Hydrogen Coolant Thermocouple Analysis

The transient analysis of the thermocouple was performed on the thermal analyzer computer program (H2800) by setting up an energy balance among the thermocouple, hydrogen coolant, and surrounding walls. The time-dependent temperature variations of the hydrogen coolant and surrounding walls shown as T(76), T(60), T(64) and T(66) in Figure 6.3-9 were used as forcing functions for the thermocouple response. The average heat-transfer coefficient of 0.415 Btu/sec ft^2 °F was obtained between the thermocouple and the hydrogen coolant for the specified coolant flow rate of 0.00712 lb/sec and given flow geometry. Radiation between the thermocouple and surrounding walls was included in the analysis, while conduction through the thermocouple wire was neglected because

the lengthwise thermal gradient is believed to be negligible and the cross-sectional area of the thermocouple wire through which heat may be conducted away is very small. The result shown at T(T/C) in Figure 6.3-9 shows that the thermocouple follows the coolant temperature quite closely, implying that convective heat transfer is the main mechanism of heat transfer to the thermocouple. In fact, with convective heat transfer alone and no radiation, a maximum deviation of 1^{0}F occurs at a time of 0.75 sec. This indicates that the radiation effect is negligible for coolant and surrounding wall conditions under consideration.

If longer than 35 sec, the time lag between the coolant temperature and the thermocouple response is fairly constant where the coolant temperature undergoes approximately a ramp change. This time lag is about the same as the time constant of the thermocouple, which is about 0.0139 sec for the present thermocouple under given coolant conditions (see Subsection 6.3.2.2.2.1 for definition of the time constant of the thermocouple). These facts are clearly shown in Subsection 6.3.2.2.2.1 in the hope that they may be used for other thermocouples for which convection is the major heat-transfer mechanism and a ramp change in fluid temperature is to be measured.

6.3.2.2.2.1 Thermocouple Response to Ramp Change in Fluid Temperature

For a system with a thermocouple that receives heat from the surrounding fluid by convection, an energy balance leads to

$$Wc \frac{dT_J}{dt} = h_c A_s (T_G - T_J)$$

or

$$\frac{dT_J}{dt} = \frac{1}{\tau_o} (T_G - T_J) \qquad (6.3\text{-}1)$$

where

W = mass of thermocouple junction or bead

c = specific heat of junction material

h_c = convective heat-transfer coefficient

A_s = heat transfer area of junction

T_J = junction temperature

T_G = gas or fluid temperature

t = time

$\tau_o = \frac{Wc}{h_c A_s}$ = time constant of thermocouple for step change in T_G (time for T_J to reach 63.3 percent of step change in T_G)

Initially, the system is assumed to be at a uniform temperature.

$$T_G = T_J = T_o \qquad (6.3\text{-}2)$$

when

$$t = 0$$

For a ramp change in fluid temperature,

$$T_G = T_o + bt \qquad (6.3\text{-}3)$$

where b is the ramp slope and a constant.

The solution to the governing differential Equation (6.3-1), subject to side conditions (6.3-2) and 6.3-3, is

$$T_J = T_o + bt - b\tau_o \left(1-e^{-t/\tau_o}\right) \qquad (6.3\text{-}4)$$

or

$$T_J = T_G - b\tau_o \left(1-e^{-t/\tau_o}\right)$$

Equation (6.3-2) is graphically interpreted as follows:

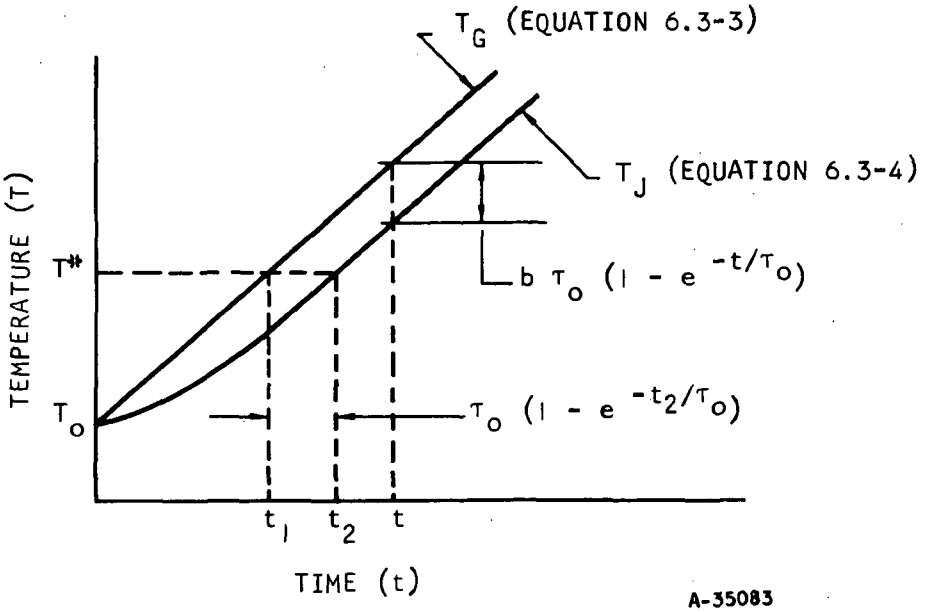

A-35083

As can be seen from Equation (6.3-4) or from the figure, the thermocouple reading difference below the fluid temperature is

$$T_G - T_J = b\tau_o \left(1-e^{-t/\tau_o}\right) \qquad (6.3\text{-}5)$$

and asymptotically approaches the steady-state reading difference

$$T_G - T_J = b\tau_o \quad \text{as } t \to \infty \quad \text{or when } t \gg \tau_o \qquad (6.3\text{-}6)$$

Use of Equation (6.3-6) is recommended when $t \geq 3\ \tau_o$ with an error of 5 percent or less.

As for the thermocouple response, the fluid temperature, at time = t_1, of

$$T^* = T_o + bt_1 \qquad (6.3\text{-}7)$$

is sensed by the thermocouple at time = t_2, i.e.,

$$T^* = T_o + bt_2 - b\tau_o \left(1-e^{-t_2/\tau_o}\right) \qquad (6.3\text{-}8)$$

Equating Equations (6.3-7) and (6.3-8) and rearranging them, one obtains the time lag of the thermocouple response as follows:

$$t_2 - t_1 = \tau_o \left(1-e^{-t_2/\tau_o}\right) \qquad (6.3\text{-}9)$$

As $t_2 \to \infty$ or when $t_2 \gg \tau_o$, the steady-state time lag asymptotically approaches

$$t_2 - t_1 = \tau_o \qquad (6.3\text{-}10)$$

Use of this equation is recommended when $t_2 \geq 3\ \tau_o$ with an error of 5 percent or less.

Equation (6.3-10) indicates that the thermocouple reading at a certain time represents the fluid temperature at the time one time constant back when $t \gg \tau_o$. The time constant τ_o is defined as the time for T_J to reach 63.3 percent of a step change in T_G and thus is indicative of the thermocouple response. The response time for T_J to reach 99 percent of a step change in T_G is about 4.6 times the time constant. This indicates that the response time for a ramp change in T_G is about 4.6 times as short as that for a step change in T_G when $t \geq 3\tau_o$ and that the response time becomes even shorter than this for the initial time in which $t < 3\ \tau_o$.

So far, the case under discussion has been for a positive ramp slope, but similar discussion can be made for a negative ramp slope simply by reversing the sign of b.

6.3.2.3 Pressure Measurements Subsystem

6.3.2.3.1 Problem Statement

Pressure measurements are required at many points in the HRE system. Of particular concern are measurements at points at which it is impractical or impossible to mount a transducer, so that pressure must be transmitted from the point to the transducer through a pipe. The pipe acts as a low-pass filter, so that the transducer cannot respond properly to rapid changes in pressure. It is necessary to design the pressure measuring system so that the frequency band pass and accuracy will be adequate at all operating conditions of the engine.

6.3.2.3.2 Approach

A combination of analysis and experimentation is being used to design a pressure transmitting pipe. The analysis of linear oscillations of gas in pipes is well developed and forms a major part of the theory of acoustics. Iberall has published a comprehensive discussion of the theory of oscillations in instrument lines, in which the pipe and the transducer volume at one end are treated as a damped Helmholtz resonator (Reference 6-1). A short summary of Iberall's results, useful for practical calculations, has been given by Humphreys (Reference 6-2). Another approximation of the instrument and the line, valid in the limit of very small instrument volumes, is a simple pipe, closed at one end. Both approximations yield results that are qualitatively similar but that differ in detail.

The experimental approach is to measure the response of the pipe and transducer by means of a laboratory pneumatic function generator. This instrument will produce pressure oscillations whose frequency, waveform, and amplitude can be controlled. The measurements will be conducted at static pressures covering the range of atmospheric pressure between sea level and 115,000 ft.

There are two important reasons for carrying out these experiments. First, it is not clear whether a linear acoustic model, either a damped Helmholtz resonator or a damped closed pipe, provides an adequate model of an instrument at the end of a line. The pressure variations about a mean pressure are large enough that nonlinear efforts, which are neglected in linear acoustic theory, may be important. Second, the experiment will provide a calibration of the measurement system in terms of amplitude and phase angle as a function of frequency. This kind of information is not generally available for a pressure measuring system.

6.3.2.3.3 Analysis

The linear acoustic model of an instrument at the end of a pipe leads to a linear second-order differential equation of the following familiar form:

$$\ddot{X} + 2\zeta_n \dot{X} + \omega_n^2 X = F(t) \qquad (6.3\text{-}11)$$

If ζ, the damping ratio, and ω_n, the natural angular frequency are known, then the response of the instrument, X(t), can be calculated for any driving function, F(t). Particularly useful and well-known solutions are those for a sinusoidal diving function and for a step function.

The Helmholtz resonator theory of Iberall predicts the following relations for ω_n and ζ in the simple case where acoustic delay between the open end of the pipe and the instrument can be neglected (Reference 6-2):

$$\omega_n = \sqrt{\frac{\pi\gamma r^2 P_o}{VL\rho}} = C\sqrt{\frac{\pi r^2}{VL}} \qquad (6.3\text{-}12)$$

$$\zeta = \frac{4\mu}{P_o r^3}\sqrt{\frac{VLP_o}{\pi\gamma\rho}} = \frac{4\mu}{P_o C r^3}\sqrt{\frac{VL}{\pi}} \qquad (6.3\text{-}13)$$

where γ = ratio of specific heats, 1.4 for air

P_o = static or mean pressure, psia

r = pipe radius, in.

V = volume of transducer, cu in.

L = length of pipe, in.

ρ = density of gas, slugs/cu in.

C = speed of sound, in. per sec

μ = viscosity of gas, lb-sec/sq in.

Equations (6.3-12) and (6.3-13), together with the graphical solutions of Equation (6.3-1), can be used to predict the frequency response of a transducer at the end of a pipe. A simple computer program has been generated to facilitate the required numerical calculations. An important property of the freqency behavior of the system is that the damping factor, ζ, is a reciprocal function of the pressure. Thus, at an altitude of 100,000 ft, the damping factor is about 100 times as great as at sea level.

The usual criterion for a measurement system is that the response at any frequency within the defined useful frequency range shall be within one percent of the zero-frequency response. Generally, no criterion is imposed on the phase angle; obviously, the phase angle should be small if complex waveforms are to be preserved. If ω is the angular frequency of the oscillating pressure to be measured and ω_n is the natural frequency defined by Equation (6.3-12), the relative amplitude of the pressure at the transducer is

$$A = \frac{\omega_n^2}{\sqrt{(\omega_n^2-\omega^2)^2 + 4\zeta^2\omega^2\omega_n^2}} = \frac{1}{\sqrt{(1-\beta^2)^2 + 4\zeta^2\beta^2}} \qquad (6.3\text{-}14)$$

where $\beta = \omega/\omega_n$, the frequency ratio. If A is limited by

$$0.99 < A < 1.01$$

then Equation (6.3-14) can be used to find the maximum permissible value of n (or frequency) for a given damping factor. For example, if $\zeta = 1$ (critical damping), then β must not exceed 0.10. That is, the highest frequency to be measured must not exceed 10 percent of the resonant frequency. For $\zeta = 0.707$, $\beta \leq 0.3779$. For $\zeta^2 >> 1$, the limiting value of β is given approximately by

$$\beta \leq \frac{0.0714}{\zeta} \qquad (6.3\text{-}15)$$

For example, at $\zeta = 10$, β must not exceed 0.00714, or about one-fourteenth the value for critical damping.

The effect of finite pressure excursions is to invalidate the assumption of linear acoustics that products of small changes in pressure and density can be neglected. Iberall has treated the case of a moderate departure from linearity in which the effect can be described in terms of the generation of harmonics of the fundamental frequency (Reference 6-1). Larger pressure excursions lead to more severe departures from linear behavior. The analysis of such pressure excursions and the resulting pressure variation at the transducer can be handled only by techniques developed for nonlinear mechanics (References 6-3 and 6-4). The experimental results which are scheduled to be obtained during the next quarter should provide an indication as to which mathematical model will be most useful in the analysis.

6.3.2.3.4 Planned Activity During the Fifth Quarter

During the next quarter of the program, the analysis will be continued and extended to cover the case of the linear, damped, closed pipe. In addition, other frequency compensation techniques such as electrical compensation of the transducer output will be investigated. If a nonlinear theory is required to explain the experimental results, the theory of nonlinear oscillations will be reviewed.

The tests of transducers and pipes with the laboratory pneumatic function generator will begin. As these results become available, they will be used to determine which analytical approach will be most useful.

6.3.2.3.4.1 Power Supplies

The current planning for the pressure measurement subsystem is to incorporate two electronically controlled power supplies with external voltage sensing leads to supply to 20-vdc power for the strain-gage pressure transducers. It is desirable to have the regulated power supply in the instrumentation bay of the X-15A-2 where there is 115-v, 400-Hz power from the airplane

supply. Eight wires, four for dc power transmission and four for voltage sensing and control will pass from the X-15A-2 airframe into the HRE via the engine pylon. Suitable power supplies for this application are available from Technipower, a Benrus subsidiary.

6.3.2.3.4.2 Pressure Transducers

The current planning for pressure transducers is as follows:

(a) The external compensating resistors will be omitted for the pressure transducer strain-gage bridge because of restraints imposed by a lack of space for additional wiring required for the zero-drift compensation. In addition to this, it is almost a certainty that the EMF generated in this additional wiring and caused by the high-temperature gradients present in the wireway spaces, along with the poor homogeneity of the metal alloy of this wiring, will result in an unacceptable equivalent zero shift. Therefore, measures will be taken to ensure long-term zero hold stability for the pressure transducer strain gage.

(b) All pressure transducers will be mounted on thermal masses with high thermal conductance. The absolute temperatures of the thermal masses will be continuously monitored and recorded.

(c) The pressure transducers will be mounted in the HRE after pressure calibrations and zero drift versus temperature response characteristics are thoroughly checked out.

(d) There will be no pressure lines to the pressure transducer other than the one pressure sensing line associated with each pressure transducer. There will be no calibration checking lines because of the degradation in dynamic response caused by the additional volume of these lines. It will be possible to check the calibration of those pressure transducers with accessible pressure sensing ports by applying an external pressure source to the sensing port with a suction connection or by enclosing the entire engine in a pressure chamber and varying the chamber pressure.

The pressure transducer currently being considered for this system is the Statham Model PA 856, which is a scaled down version of the PA 822 described in Reference 6-5. It is unique in that its pressure diaphragm is coated with an electrical insulating material, and it has a resistance strain-gage vacuum deposited on the insulating surface. This construction technique has several advantages over the old bonded strain-gage construction methods which were described in Reference 6-5. A description of the Statham Model PA 856 is included in Appendix A.

6.3.2.3.4.3 Pressure Transducer Locations

The following charts indicate the physical quantity of pressure sensors available at each engine station on each of the engine components and the

actual number of sensors used for each of the following requirements:

No. 1 - Vibration Test Flightweight Engine

No. 2 - Functional Test Flightweight Engine

No. 3 - Flight Engine

Cont - Data to Digital or Analog Computer for Control Purposes

Nomenclature:

A	-	Air	H_e	-	Helium
H_2	-	Hydrogen	LH_2	-	Liquid Hydrogen
N_2	-	Nitrogen	COMB	-	Combustion

TABLE 6.3-2

NUMBER OF TAPS USED IN EACH TEST

Spike Pressure Instrumentation								
Sta	Fluid Measure	Description	No. of Taps Available	Range, psia	No. of Taps Used			
					No. 1	No. 2	No. 3	Cont
0.5	A	Spike tip	1		-	1	1	1
5.2	H_2	Spike tip plenum	1	0 to 1100	-	1	1	-
24.0	A	Outside diameter	4		-	4	4	4
35.7	A	Outside diameter	4		-	4	4	4
42.5	A	Outside diameter (combustion control)	4		-	4	4	4
43.0	H_2	Injector manifold No. 1	2		-	2	2	1
44.3	A	Outside diameter (shock sensor)	1		-	1	1	1
46.0	H_2	Outlet manifold	2		-	2	1	-
Subtotal			19		0	19	18	15

TABLE 6.3-2 (Continued)

Inner Shell Pressure Instrumentation								
Sta	Fluid Measure	Description	No. of Taps Available	Range, psia	No. of Taps Used			
					No. 1	No. 2	No. 3	Cont
51.0	H_2	Coolant outlet (inner)	2		-	2	2	-
55.67	H_2	Injector manifold No. 2	2			2	2	1
59.0	Comb Prod	Outside diameter	4		-	4	1	-
59.53	H_2	Injector manifold No. 3	2		-	2	2	1
62.0	Comb Prod	Outside diameter (combustion control)	4		-	4	4	4
64.89	H_2	Coolant inlet (inner)	1		-	1	1	-
65.0	Comb Prod	Outside diameter	1		-	1	1	-
65.7	H_2	Strut manifold	1		-	1	1	-
66.4	H_2	Coolant outlet (No. 2)	1		-	1	1	-
76.5	Comb Prod	Outside diameter	4		-	4	4	-
80.0	H_2	Coolant inlet (No. 2)	1		-	1	1	-
81.4	Comb Prod	Outside diameter	2		-	2	2	-
Subtotal			25			25	22	6

TABLE 6.3-2 (Continued)

Leading Edge and Forward Outer-Shell Pressure Instrumentation								
Sta	Fluid Measure	Description	No. of Taps Available	Range, psia	No. of Taps Used			
					No. 1	No. 2	No. 3	Cont
36.395	A	Outside diameter	4		-	4	4	-
37.395	A	Inside diameter	2		-	2	2	2
37.895	A	Outside diameter	4		-	4	4	-
38.200	A	Inside diameter	4		-	4	-	-
38.70	A	Outside diameter	4		-	4	4	-
38.895	A	Outside diameter	1		-	1	1	-
39.2	A	Inside diameter	4		-	4	-	-
39.895	A	Outside diameter	1		-	1	1	-
40.2	A	Inside diameter	4		-	4	-	-
41.2	A	Inside diameter	4		-	4	-	-
41.445	H_2	Coolant inlet manifold	2	0 to 1100	-	2	2	-
41.7	A	Outside diameter	4		-	4	-	-
42.8	H_2	Coolant outlet manifold	1	0 to 600	-	1	1	-
44.1	H_2	Coolant outlet manifold	1		-	1	1	-
48.5	H_2	Injector No. 1	2		-	2	2	-
Subtotal			42		0	42	22	2

TABLE 6.3-2 (Continued)

Outer Shell Pressure Instrumentation								
Sta	Fluid Measure	Description	No. of Taps Available	Range, psia	No. of Taps Used			
					No. 1	No. 2	No. 3	Cont
51.0	A	Inside diameter	4		-	4	1	-
52.0	H_2	Coolant outlet manifold	2	0 to 600	-	2	2	-
54.5	A	Inside diameter (combustion control)	4		-	4	4	4
54.6	H_2	No. 2 injector manifold	2	0 to 400	-	2	2	-
56.5	Comb Prod	Inside diameter	4		-	4	-	-
59.4	H_2	No. 3 injector manifold	2	0 to 400	-	2	2	-
60.0	Comb Prod	Inside diameter	4		-	4	4	-
72.24	H_2	Coolant inlet (nozzle)	1	0 to 1100	-	1	1	-
		Subtotal	23		0	23	16	4
Miscellaneous Pressure Sensors								
	H_e	S/O and purge valve inlet	1		-	1	-	-
	H_2	S/O and purge valve inlet	1	0 to 150	-	1	-	-
	H_e-H_2	S/O and purge valve outlet	1	0 to 150	-	1	1	-
	LH_2	Pump inlet	1	50 to 150	-	1	1	-
	LH_2	Pump discharge	1	50 to 1100	-	1	1	-
	H_2	Dump valve inlet	1		-	1	1	-

TABLE 6.3-2 (Continued)

Miscellaneous Pressure Sensors (Continued)								
Sta	Fluid Measure	Description	No. of Taps Available	Range, psia	No. of Taps Used			
					No. 1	No. 2	No. 3	Cont
	H_2	Dump valve outlet	1		-	1	1	-
	H_2	Turbine inlet	1		-	1	1	-
	H_2	Turbine discharge	1		-	1	1	-
	H_2	Fuel plenum	1		-	1	1	-
	N_2	Nitrogen	1	3000 to 6000	-	1	1	-
			1	1500 to 3000	-	1	1	-
	A	Double-sonic 1st orifice	1		-	1	1	1
	A	Double-sonic 2nd orifice	1		-	1	1	1
	Hydr	Actuator piston	1		-	1	1	-
	Hydr	Actuator cylinder	1		-	1	1	-
	N_2	Nitrogen (valves)	1		-	1	1	-
	H_e	Helium (valves)	1		-	1	1	-
Subtotal			18		0	18	18	2

REFERENCES

2-1 Engineering Staff, Hypersonic Ramjet Engine Project Phase IIA Instrumentation Program, Third Interim Technical Data Report, Item No. 55-8.03, AiResearch Report No. AP-67-3020, Dec. 21, 1967.

2-2 Engineering Staff, Hypersonic Ramjet Experiment Project Phase I, Conceptual and Preliminary Design of the Instrumentation for the Ground and Flight Test, AiResearch Report No. AP-66-0167, Sept. 1966.

2-3 Langley Research Center, Statement of Work Hypersonic Ramjet Engine Project for the Phase IIA, Langley Research Center Report No. L-4947-B, Jan. 15, 1967.

2-4 Engineering Staff, Hypersonic Ramjet Engine Project Phase IIA X-15-A-2 Integration Program, Second Interim Technical Data Report, AiResearch Report No. AP-67-2384, Nov. 22, 1967.

2-5 Michel, D. J., R. M. Mains, R. L. George, and N. H. Wood, Instrumentation Design Study for Testing a Hypersonic Ramjet Engine On the X-15A-2, prepared under Contract NASA-715 for NASA, March 1965.

3-1 Hypersonic Research Engine Project-Phase IIA, Instrumentation Program, Third Interim Technical Data Report, AP-67-3020, AiResearch Mfg Co, Sept. 25, 1967.

4-1 Hypersonic Research Engine Project-Phase IIA, Instrumentation Program, Second Interim Technical Data Report, Item No. 55-8.02, AP-67-2579, AiResearch Mfg Co, Sept. 25, 1967.

4-2 Cho, S. M., Analysis of High-Temperature Probe, AiResearch Mfg Co, Office Memo to A. Vigilante, May 12, 1967.

4-3 Cho, S. M., Thermocouple Error Analysis, AiResearch Mfg Co, Office Memo to G. Sawyer, Feb. 5, 1968.

4-4 Dickenson, et al., "Protective Coatings for Tungsten," Journal of Metals, Oct. 1963, Vol. 15, No. 10, Page 787.

4-5 Kruse, P. W., Elements of Infrared Technology, John Wiley and Son, New York, 1962.

4-6 Hypersonic Research Engine Project - Phase IIA, Instrumentation Program, Third Interim Technical Data Report, Item No. 55-8.03, AP-67-3020, AiResearch Mfg Co, 21 Dec. 1967.

4-7 Back, L. H., et al., "Comparison of Experimental with Predicted Wall Static Pressure Distributions in Conical Supersonic Nozzles," JPL-TR No. 32-654, Jet Propulsion Laboratory Technical Report.

5-1. Thermodynamic and Transport Properties of Para-Hydrogen, Vol. II, 67-2268-2, June 26, 1967.

5-2. Midterm Report, L-9544.

5-3. Shapiro, A. H., The Dynamics and Thermodynamics of Compressible Fluid Flow, Vol. I, p 85, Ronald Press, New York, 1953.

5-4. Fluid Meters, 5th Edition, A.S.M.E., 1959.

6-1. Iberall, A. S., Attenuation of Oscillatory Pressures in Instrument Lines, Nation Bureau Standard Research Paper RP 2115, Vol. 45, July 1950.

6-2. Humphreys, J. D., "Pressure Sensing Calculations," Tele-Tech and Elect. Ind., pp 82-ff, April 1953.

6-3. Minorsky, N., Introduction to Non-Linear Mechanics, Edwards Brothers, Ann Arbor, Michigan, 1947.

6-4. Cunningham, J. W., Introduction to Non-Linear Analysis, McGraw-Hill Book Co., New York, New York, 1958.

6-5. Third Interim Technical Data Report Instrumentation Program, AP-67-3020, AiResearch Manufacturing Company, December 21, 1967.

APPENDIX A

TEMPERATURE INSTRUMENTATION REQUIREMENTS

TABLE A-1

MEASURAND SUMMARY - TEMPERATURE

	Vibration Test Flightweight Engine	Wind Tunnel and Flight Test	Flight Engine	Controls
Spike	0	10	10	6
Inner shell	4	16	16	6
Outer shell	7	15	15	18
Nozzle	0	7	7	
Leading edge	0	12	12	6
Fuel system	0	21	21	5
Instrumentation	4	22	22	1
Total	15	103	103	42

TEMPERATURE INST.
FUEL SYSTEM

XX CONTROLS DEPARTMENT

STA.	DESCRIPTION	TYPE	DESIRED RANGE °R	RESPONSE °R/SEC	ERROR °R	ERROR °R INST.	°R ACTUAL RANGE	T/C MTL.		VIB.	TEST FLT.	WIND TUNNEL	FLIGHT ENGINE CONTROLS
43.0	INJECTOR #1	H_2	800-1700		XX	XX	800-2200	CA/PON		0	0	0	1
93.0	INJECTOR #1	H_2	800-1700			10	800-2200	CHROMEL		0	X	2	0

H.S. - HOT SKIN
C.S. - COLD SKIN
H_2 - HYDROGEN

TEMPERATURE SENSE
FUEL SYSTEM

xx CONTROLS DETERMINATION

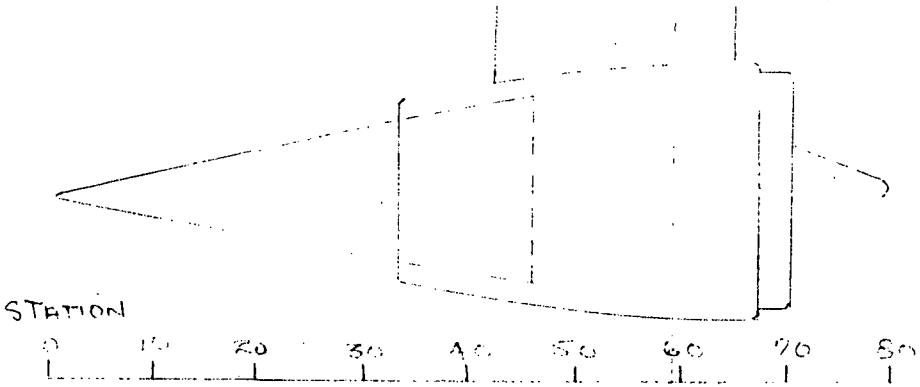

T.C. NO.	DESCRIPTION	TYPE	DESIRED RANGE °R	RESPONSE °R/SEC	ERROR °R	ERROR °R/MIN.	°R ACTUAL RANGE	T/C MTL.		VIB. TEST	FLT. WT. ENG. WIND TUNNEL	FLT. ENGINE CONTROLS	
X-15 R/C	SHUT OFF * PURGE VALVE INLET	H_e	-100 - 200		4						1	1	1
X-15 R/C	SHUT OFF * PURGE VALVE INLET	H_2	36.5-45		0.16*			SPARE			1	1	0
59.16	PUMP INLET	H_2	36.5-45		0.16*			SPARE			1	1	0
63.25	PUMP DISCHARGE	H_2	40-60		0.4*			SPARE			1	1	0
55.3	FUEL PLENUM	H_2	100-150		2*						1	1	0
53.0	TURBINE INLET	H_2	400-1800		1*	"					1	1	1
51.2	TURBINE DISCHARGE	H_2	300-1600		1*	"					1	1	1
8 MON	PUMP VALVE INLET	H_2	400-1800		1*	"					1	1	1
MON	PUMP DISCHARGE	H_2	400-1800		1*	"					1	1	1
48.5	INJECTOR #1	H_2	500-1600		10	10	500-2200	COMP/CH		0	2	2	0
54.6	INJECTOR #2	H_2	800-1700		10	10	"	"		0	2	2	0
59.4	INJECTOR #3	H_2	800-1700		10	10	"	"		0	2	2	0
55.2	INJECTOR #2	H_2	800-1700		10**	10**		CH/CON					2
58.6	INJECTOR #1	H_2	800-1700		10	10	500-2200	SPARE		0	2	2	0
62.55	INJECTOR #3	H_2	800-1700		10**	10**		CH/CON		0	2	2	2
52.53	INJECTOR #5	H_2	800-1700		10	10	500-2200	COMP		0	1	1	0

H.S. - HOT SKIN
C.S. - COLD SKIN
H_2 - HYDROGEN

TEMPERATURE INST.

STRUCTURE

NOZZLE

* SUBJECT TO ENGINE [illegible]

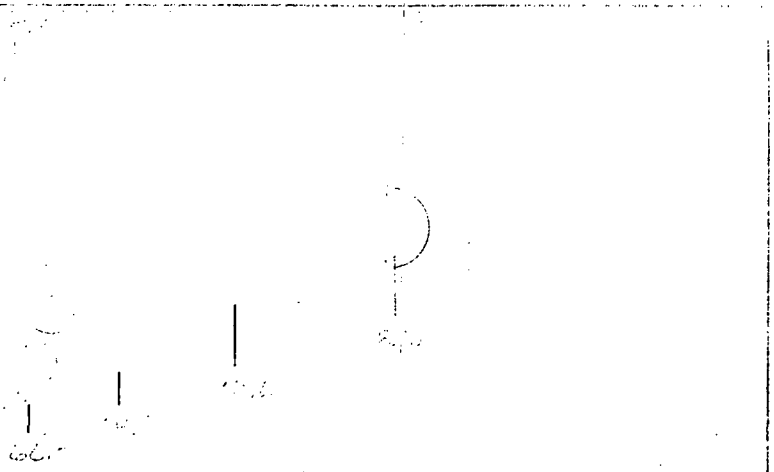

STA.	DESCRIPTION	TYPE	DESIRED RANGE °R	RESPONSE °R/SEC	ERROR °R	REPEAT. °R INST.	°R ACTUAL RANGE	T/C MTL.		VIB.	TEST FLT. WING WIND TUNNEL FLT.	FLIGHT ENGINE CONTROLS	
65.6	ACCUMULATOR TANK	CS	350-600	50	20	15	40-1200	CHROMEL		0	1	1	0
66.0	CROSS OVER MANIFOLD	H_2	200-800	500	10	10	[illegible]	"		0	1	1	0
68.6	JACKET	H.S.	500-1400	*	20	*	500-2200	ALUMEL		0	1	1	0
66.6	"	CS	200-700	200	20	15	40-1200	CHROMEL		0	1	1	0
75.6	"	HS	300-900	*	20	*	40-1200	"		0	1	1	0
75.6	"	CS	40-500	200	10	25	[illegible]	"		[illegible]	[illegible]	[illegible]	[illegible]
92.2	NOZZLE [illegible]	H_2	40-200	200	50	10	40-1200	"					

H.S. - HOT SKIN
C.S. - COLD SKIN
H_2 - HYDROGEN

TEMPERATURE INST.

LEADING EDGE

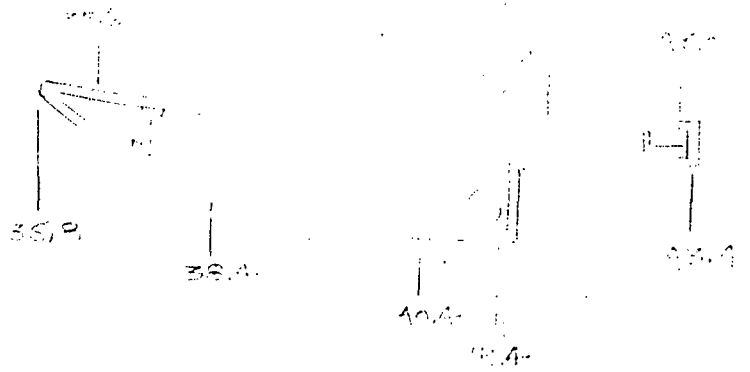

STAT. NO.	DESCRIPTION	TYPE	DESIRED RANGE °R	RESPONSE °R/SEC	ERROR °R	REPEAT. °R	INST. H	°R ACTUAL RANGE	T/C MTL.		VIB.	TEST FLT, WT. ENG., WIND TUNNEL, ETC. FLIGHT TEST CONT.			
37.6	INSIDE JACKET	CS	40-400	200	20	25		40-1200	CH/CON		0	1	1	0	H.S. - HOT SKIN C.S. - COLD SKIN H_2 - HYDROGEN FOR EVALUATION PURPOSES ONLY -65°F TO 900°F
38.4	OUTSIDE JACKET	HS	100-400	*	20	*		"	"		0	1	1	0	
38.4	" "	CS	40-400	200	20	25		"	"		0	1	1	0	
40.4	180° APART	HS	100-400	*	20	*		"	"		0	1	1	0	
40.4	180° APART	CS	40-400	200	20	25		"	"		0	1	1	0	
41.4	180° APART INLET MANIFOLD	H_2	40-200	200	10	25		"	"		0	1	1	0	
41.9	INSIDE JACKET	H_2	200-300	200	XX	XX		"	"		0	0	0	6	
43.0	180° APART OUTLET MANIFOLD	H_2	250-700	200	10	15		"	"		0	1	1	0	
43.4	OUTLET MANI. FLANGE	CS	200-1000	100	20	15		"	"		0	1	1	0	

XX CONTROLLED BY [illegible]

XX CONTROLLED BY [illegible]

TEMPERATURE INST.

STRUT

SPIKE

* SUBJECT TO ANALYSIS
** CONTROLS DEPENDENT

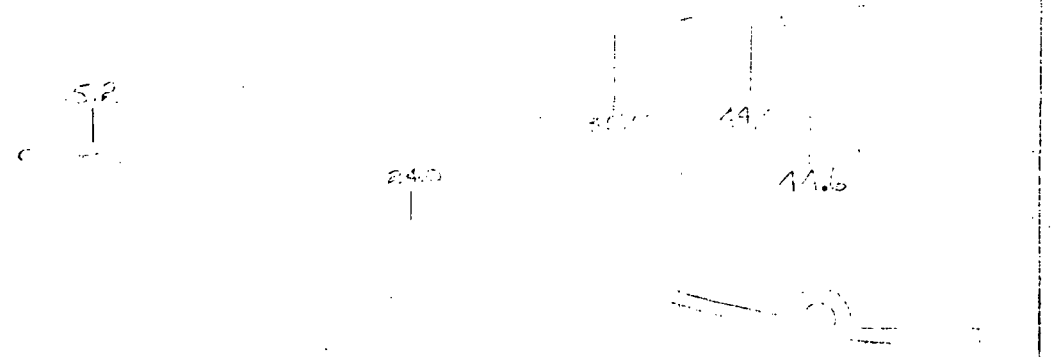

STA.	DESCRIPTION	TYPE	DESIRED RANGE °R	RESPONSE °R/SEC	ERROR °R	ERROR @ INST. °R	°R ACTUAL RANGE	T/C MTL.		VIB.	TEST FLT. WIND TUNNEL FLIGHT CONT.	WE ENG.	
5.2	SPIKE TIP PLENUM	H_2	40-200	200	10	25	40-1200	H/CON		0	1	1	0
24.0	JACKET	C.S.	100-600	200	10	25	40-1200	"		0	1	1	0
24.0	"	H.S.	100-900	*	10	*	40-1200	"		0	1	1	0
35.7	"	C.S.	100-600	200	10	25	40-1200	"		0	1	1	0
35.7	"	H.S.	300-1000	*	10	*	40-1200	"		0	1	1	0
44.3	"	C.S.	200-1000	200	10	10	40-1200	"		0	1	1	0
44.3	"	H.S.	500-1500	*	15	*	500-2200	Chromel		1	1	1	0
46.0	Coolant Out Manif.	H_2	500-1500	500	10	10	500-2200	"		0	2	2	0
47.5	BELLOWS	C.S.	500-1600	200	20	20	500-2200	"		0	1	1	0
49.0	JACKET	H_2	600-1500	800	**	**	500-2200	CHROMEL		0	1	1	0
										0	10	7	0

H.S. - HOT SKIN
C.S. - COLD SKIN
H_2 - HYDROGEN

REF. JUNCTION AMBIENT -65°F to 300°F

#1
#2 (USED)
#3

TEMPERATURE LIST
STRUCTURE

INNER SHELL

Ⓢ IN LINE 1.5" FROM START OF
* SUBJECT TO INNOVATIVE'S
** DEPENDS ON

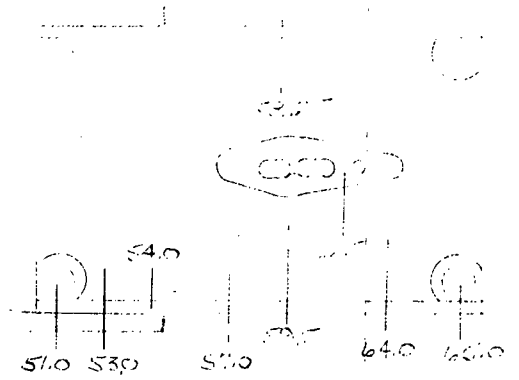

STA	DESCRIPTION	TYPE	DESIRED RANGE °R	RESPONSE °R/SEC	ERROR °R	ERROR °R/FT	°R ACTUAL RANGE	T/C MTL.		VIB. TEST FLT. WIND TUNNEL FLIGHT ENGINE CONTROLS #1	#2	#3	
51.0	OUTER MANIFOLD	H_2	800-1700	500	10	10	500-2200	CHROMEL ALUMEL		0	2	2	0
52.0	JACKET	H_2	800-1700	800	**	**	500-2200	"		0	0	0	6
53.0	JACKET IN LINE WITH STRUT ℄ 80°	HS	1200-2200	*	20	*	500-2200	CHROMEL ALUMEL		0	1	1	0
53.0	JACKET	CS	800-1700	200	20	10	500-2200	"		0	1	1	0
54.0	JACKET	HS	1200-2200	*	20	*	500-2200	"		0	1	1	0
54.0	JACKET	CS	800-1700	200	20	10	500-2200	"		0	1	1	0
57.0	STRUT SOCKET	CS	800-1600	100	10	10	500-2200	"		1	1	1	0
57.25	JACKET Ⓢ	HS	1200-2200	*	20	*	500-2200	"		0	1	1	0
57.25	JACKET Ⓢ	CS	800-1600	200	20	10	500-2200	"		0	1	1	0
58.25	JACKET Ⓢ	HS	1200-2200	*	20	*	500-2200	"		0	1	1	0
58.25	JACKET Ⓢ	CS	800-1600	200	20	10	500-2200	"		0	1	1	0
59.5	ACTUATOR FRAME	CS	300-800	50	15	10	40-1200	CHROMEL ALUMEL		1	1	1	0
62.5	ACTUATOR TUBE	CS	350-600	50	15	10	40-1200	"		1	1	1	0
64.0	ACTUATOR MOUNT	CS	300-800	50	15	15	40-1200	"		1	1	1	0
65.0	CROSSOVER MANIFOLD	H_2	800-1700	500	10	10	40-2200	"		2	2	2	0
								SUM	TOT.	7	16	16	6

H.S. - HOT SKIN
C.S. - COLD SKIN
H_2 - HYDROGEN

REF JUNCTION AMBIENT -65°F TO 300°F

#1, #2, #3 - USAGE

TEMPERATURE INST.
STRUCTURE

OUTER SHELL

* SUBJECT TO FURTHER STRUT INSTRUMENT DETAIL VARIATION

STAT.	DESCRIPTION	TYPE	DESIRED RANGE °R	RESPONSE °R/SEC	ERROR LIMIT °R	ERROR LIMIT °R	°R ACTUAL RANGE	T/C MTL.		VIB. TEST	FLT. WT. RNG.	WIND TUNNEL	FLIGHT	CONTROLS
44.0	CROSSOVER DUCT	H_2	250-1700	200	10	15	400-1700	CH/ALUM		0	1	1	1	0
50.25	IN LINE STRUT & JACKET	H.S.	1200-2200	*	20	*	500-2200	CHROMEL/ALUMEL		0	1	1	1	0
50.25	JACKET 90° APART	C.S.	700-1600	200	20	10	500-2200	"		2	2	2	2	0
50.25	JACKET 180° APART	H_2	500-1700	800	**	**	500-2200	CH/ALUM		0	0	0	0	6
51.5	OUTLET MANIFOLD	H_2	800-1700	500	10	10	800-1700	"		2	2	2	2	0
51.5	OUTLET MANIFOLD	C.S.	500-1700	100	20	10	500-1700	"		1	1	1	1	0
53.8	IN LINE STRUT & JACKET	H.S.	1200-2200	*	20	*	500-2200	"		0	1	1	1	0
53.8	JACKET 90° APART	C.S.	700-1600	200	20	10	500-2200	"		2	2	2	2	0
53.8	JACKET	H_2	800-1700	800	**	**	500-2200	CH/ALUM		0	0	0	0	6
62.3	JACKET	H.S.	1200-1500	*	20	*	"	"		0	1	1	1	0
62.3	JACKET	C.S.	700-1500	200	20	15	500-2200	"		0	1	1	1	0
64.9	KEEL SUPPORT MACH	H_2	250-700	200	10	15	"	"		0	1	1	1	0
67.6	COOLANT IN MANIFOLD	H_2	40-200	200	5	25	40-1700	"		0	0	0	0	0
58.0	STRUT SURFACE	H_2	800-1500	500	10	**				0	0	0	0	6
										1	1	1	1	5

H.S. - HOT SKIN
C.S. - COLD SKIN
H_2 - HYDROGEN

PER JUNCTION
[illegible]
[illegible] '30's

#1
#2 [illegible]
#3

TEMPERATURE INST.

ENGINE

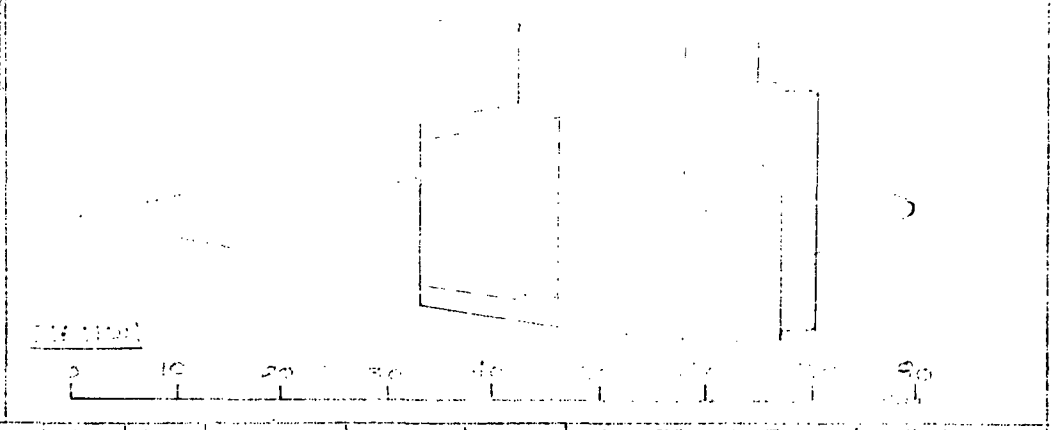

STN.	DESCRIPTION	TYPE	DESIRED RANGE °R	RESPONSE °R/SEC	ERROR °R	TEMP. °R INST.	°R ACTUAL RANGE	T/C MTL.		VIB. TEST FLT. WIND TUNNEL FLIGHT ENGINE CONTROLS			
										#1	#2	#3	
40	REF. JUNCTION MONITOR	C.S.	350-700	10	50	10	40-1200	CH/CON	SPIKE	1	1	1	—
56	"	C.S.	350-700	10	50	10	40-1200	CH/CON	INNER BODY	1	1	1	—
74	"	C.S.	350-700	10	50	10	40-1200	CH/CON	NOZZLE	1	1	1	—
50	"	C.S.	350-700	10	50	10	40-1200	CH/CON	PYLON	1	1	1	—
52	THRUST BEAM	C.S.	350-1000	10	10	10	40-1200	CH/CON	PYLON	5	5	5	—
79	INST. FAIRING	C.S.	350-700	10	10	10	40-1200	CH/MIN	NOZZLE	1	1	1	—
30	STREAM TOTAL TEMP.	A						SPECIAL		1	1	1	1
X-15 P/C	FLOWMETER	LH_2	36-60		0.4					1	1	1	—
*	TEMP. IGNITION	C.S.	350-700	10	25	10	40-1200	CH/CON		10	10	10	—

H.S. - HOT SKIN
C.S. - COLD SKIN
H_2 - HYDROGEN
A - AIR
#1, #2, #3 } USAGE

APPENDIX B

THIN-FILM STRAIN-GAGE PRESSURE TRANSDUCER MODEL PA 856

THIN FILM STRAIN GAGE PRESSURE TRANSDUCER
MODEL PA856

1. DESCRIPTION

This transducer is the culmination of several years of extensive research and development in thin film strain gage techniques. The sensing element of the Model PA856 utilizes a vacuum deposited, fully active strain gage bridge. The diaphragm materials used in the Model PA856 are Types 17-4 PH and 17-7 PH stainless steel.

The units utilize a beam-diaphragm assembly with the ceramic film deposited onto the beam to provide electrical insulation for the bridge elements. Four strain gages are vacuum deposited onto the insulator and are electrically connected into a bridge circuit. The strain gage material is a specially developed alloy which exhibits the excellent stability, gage factor, and resistance characteristics required in a strain gage transducer.

The instrument's flush-diaphragm construction permits direct exposure to pressure media, and produces a system response flat to one-fifth the transducer's natural frequency. Either light-weight aluminum or corrosion-resistant steel adapters may be used to convert the PA856 to a cavity-type instrument. Adapters are available in a variety of pipe and tube fittings.

2. SPECIFICATIONS

2.1 Model Designation, Typical Pressure Ranges, Maximum psia, Natural Frequency, and Static Acceleration Response: (The acceleration response quoted represents the output of the transducer due to stimulus applied in the sensitive axis, including vibration at frequencies up to approximately 20% of the natural frequency. Above this frequency, the response will increase in accordance with the behavior of an undamped single-degree-of-freedom system.)

Model Designation	Range (psia)	Maximum (psia)	Approx. Natural Frequency (Hz)	Static Response (% FS/g)
PA856-15	0- 15	30	3,000	0.06
PA856-25	0- 25	50	4,000	0.04
PA856-50	0- 50	100	5,000	0.02
PA856-100	0- 100	200	9,000	0.015
PA856-150	0- 150	300	10,000	0.01
PA856-250	0- 250	375	11,000	0.01
PA856-500	0- 500	750	13,000	0.01
PA856-1M	0-1000	1500	17,500	0.01
PA856-2M	0-2000	3000	24,000	0.01
PA856-5M	0-5000	7500	37,000	0.01

2.2	Pressure Media:	Fluids compatible with Types 17-4 PH and 17-7 PH stainless steel
2.3	Transduction:	Resistive, balanced, thin film, fully active strain gage bridge
2.4	Nominal Bridge Resistance:	350 ohms
2.5	Excitation:	10 V DC or AC (rms) through carrier frequencies
2.6	Full-scale Output (open circuit):	3 mV/V nominal
2.7	Resolution:	Infinitesimal
2.8	Non-linearity & Hysteresis:	Less than ±0.25%FS
2.9	Ambient Temperature Limits:	-65 to +250°F
2.10	Thermal Sensitivity Shift:	0.01%/°F
2.11	Thermal Zero Shift:	0.01%FS/°F
2.12	Pressure Connection:	Flush diaphragm; adapters are available for conversion to chamber-type pickup
2.13	Electrical Connection:	Four numbered terminal pins; an electrical disconnect assembly, Model DC12, is available
2.14	Weight:	Approximately 0.6 oz.
2.15	Identification:	The model designation, serial number, range, maximum excitation, and manufacturer are on each unit.
2.16	Dimensions:	See Outline Drawing No. 52221
2.17	Calibration:	Statham pressure transducers are calibrated individually by qualified technicians using specialized equipment of laboratory accuracy. Pertinent data are furnished at time of shipment.

3. All correspondence relating to the equipment described herein must reference this Specification Number 17157.

KAP:mt
3/7/68

52221

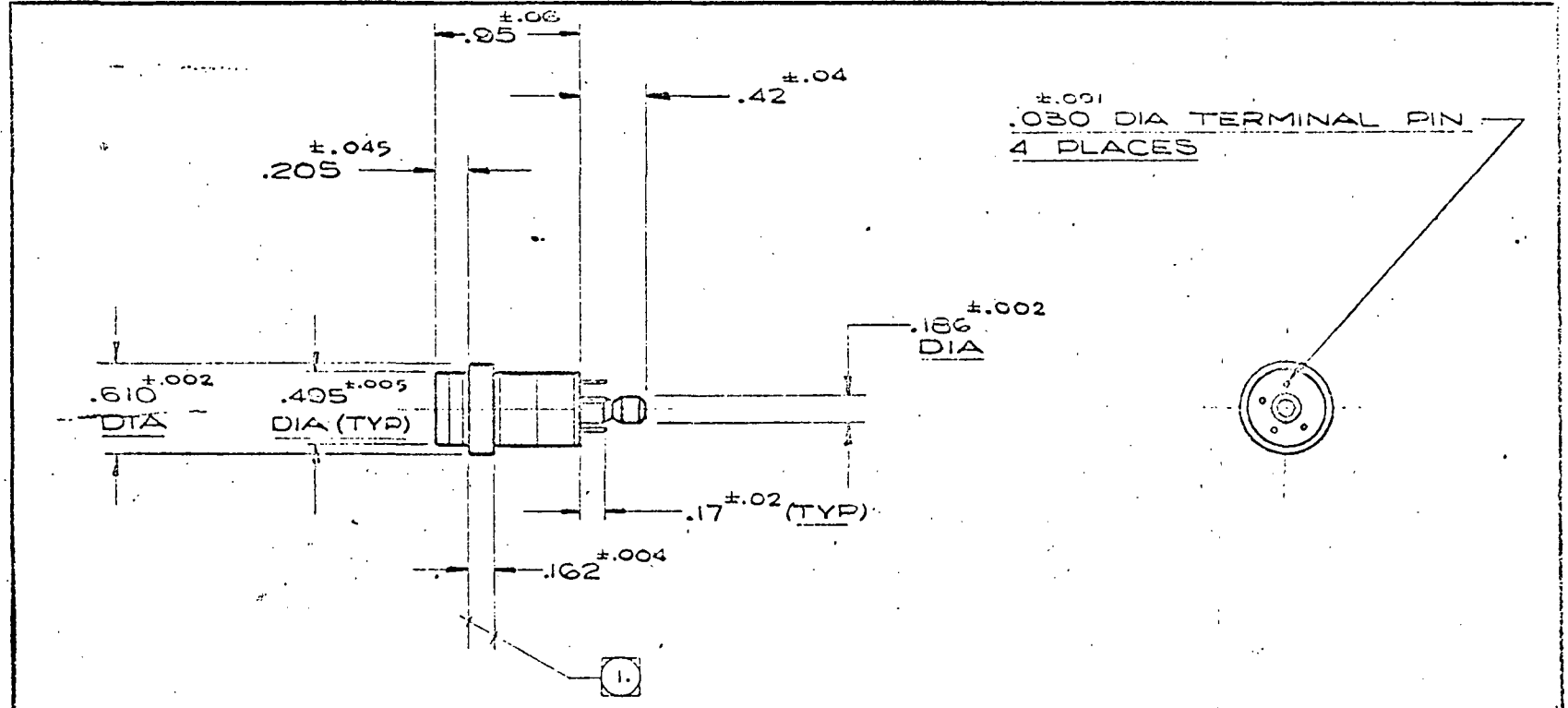

NOTES:
1. CLAMP ON THESE SURFACES ONLY

REVISION	BY	DATE	CHK.	APP.	TOLERANCE UNLESS NOTED: FILLET MAX. .010 BREAK EDGE .005 - .010 MACH. FINISH 63 RMS	STATHAM INSTRUMENTS, INC. LOS ANGELES 64, CALIFORNIA	SCALE 1/1		
					STOCK	DRAWN Ron Bowlin 1/3/69			
					MATERIAL	CHECKED [illegible] 1-3-69			
					HEAT TREAT	PROJECT ENGINEER R. HELIN		PS56J 51950	
					FINISH	APPROVED [illegible]	MODEL	NEXT ASSEMBLY	NO. REQ
					OUTLINE – TRANSDUCER, ABSOLUTE PRESSURE	CODE IDENT. NO. 57187	52221		

LA 1872